Nanostructured complex hydride systems for solid state hydrogen storage

by

Minchul Jang

A thesis

presented to the University of Waterloo

in fulfilment of the

thesis requirement for the degree of

Doctor of Philosophy

in

Mechanical Engineering

Waterloo, Ontario, Canada, 2011

Abstract

The present work reports a study of the effects of the formation of a nanostructure induced by high-energy ball milling, compositions, and various catalytic additives on the hydrogen storage properties of $LiNH_2$-LiH and $LiNH_2$-MgH_2 systems. The mixtures are systematically investigated using X-ray diffraction (XRD), Fourier transform infrared spectroscopy (FT-IR), scanning electron microscopy (SEM), differential scanning calorimetry (DSC), thermogravimetric analysis (TGA), and a Sieverts-type apparatus.

The results indicate that microstructural refinement (particle and grain size) induced by ball milling affects the hydrogen storage properties of $LiNH_2$-LiH and $LiNH_2$-MgH_2 systems. Moreover, the molar ratios of the starting constituents can also affect the dehydrogenation/ hydrogenation properties.

In the $LiNH_2$-LiH system, high-energy ball milling is applied to the mixtures of $LiNH_2$ and LiH with molar ratios of 1:1, 1:1.2 and 1:1.4 LiH. The lowest apparent activation energy is observed for the mixture of $LiNH_2$-LiH (1:1.2) milled for 25 h. The major impediment in the $LiNH_2$-LiH system is the hydrolysis and oxidation of LiH, which causes a fraction of LiH to be inactive in the intermediate reaction of $NH_3+LiH \rightarrow LiNH_2+H_2$. Therefore, the $LiNH_2$-LiH system always releases NH_3, as long as a part of LiH becomes inactive, due to hydrolysis/oxidation, and does not take part in the intermediate reaction.

To prevent LiH from undergoing hydrolysis/oxidation during desorption/absorption, 5 wt. % graphite is incorporated in the ($LiNH_2$+1.2LiH) system. The DSC curve of the mixture does not show a melting peak of retained $LiNH_2$, indicating that graphite can prevent or at least substantially reduce the oxidation/hydrolysis of LiH. Moreover, compared to the mixture without graphite, the mixture with graphite shows more hydrogen capacity, thus this

mixture desorbs ~5 wt.% H_2, which is close to the theoretical capacity. This system is fully reversible in the following reaction: $LiNH_2+LiH \leftrightarrow Li_2NH+H_2$. However, the equilibrium temperature at the atmospheric pressure of hydrogen (0.1 MPa H_2) is 256.8°C for ($LiNH_2$+1.2LiH) mixture, which is too high for use in onboard applications.

To overcome the thermodynamic barrier associated with the $LiNH_2$/LiH system, LiH is substituted by MgH_2; therefore, the ($LiNH_2$+nMgH_2) (n=0.55, 0.6 and 0.7) system is investigated first. These mixtures are partially converted to $Mg(NH_2)_2$ and LiH by the metathesis reaction upon ball milling. In this system, hydrogen is desorbed in a two-step reaction: $[0.5xMg(NH_2)_2+xLiH]+[(1-x)LiNH_2+(0.5-0.5x)MgH_2] \rightarrow 0.5Li_2Mg(NH)_2+1.0H_2$ and $0.5Li_2Mg(NH)_2+MgH_2 \rightarrow 0.5Mg_3N_2+LiH+H_2$. Moreover, this system is fully reversible in the following reaction: $Li_2Mg(NH)_2+2H_2 \leftrightarrow Mg(NH_2)_2+2LiH$. Step-wise desorption tests show that the enthalpy and entropy change of the first reaction is -46.7 kJ/molH_2 and 136.1 J/(molK), respectively. The equilibrium temperature at 0.1 bar H_2 is 70.1°C, which indicates that this system has excellent potential for onboard applications. The lowest apparent activation energy of 71.7 kJ/mol is observed for the molar ratio of 1:0.7MgH_2 milled for 25 h. This energy further decreases to 65.0 kJ/mol when 5 wt.% of n-Ni is incorporated in the system.

Furthermore, the molar ratio of MgH_2/$LiNH_2$ is increased to 1.0 and 1.5 to increase the limited hydrogen storage capacity of the ($LiNH_2$+0.7MgH_2) mixture. It has been reported that the composition changes can enhance the hydrogen storage capacity by changing the dehydrogenation/hydrogenation reaction pathways. However, theoretically predicted LiMgN is not observed, even after dehydrogenation at 400°C. Instead of this phase, $Li_2Mg(NH)_2$ and Mg_3N_2 are obtained by dehydrogenation at low and high temperatures, respectively, regardless of the milling mode and the molar ratio of $MgH_2/LiNH_2$. The only finding is that the molar ratio of $MgH_2/LiNH_2$ can significantly affect mechano-chemical reactions during ball milling, which results in different reaction pathways of hydrogen desorption in subsequent heating processes; however, the reaction's product is the same regardless of the milling mode, the milling duration and their composition. Therefore, the ($LiNH_2$+0.7MgH_2) mixture has the greatest potential for onboard applications among Li-Mg-N-H systems due to its high reversible capacity and good kinetic properties.

Acknowledgements

I would like to express my sincere gratitude to my supervisors, Prof. R. A. Varin and Prof. L. F. Nazar for their guidance, tireless support and continual encouragement throughout this work. I would also like to thank Prof. J. Huot, Prof. E. Croiset, Prof. M. Yavuz and Prof. J. Z. Wen for their constructive criticism.

Dedication

To my parents

&

My lovely wife and daughter

Jaenam and Haneul

Table of contents

Author's declaration -- ii
Abstract -- iii
Acknowledgements -- vi
Dedication -- vii
Table of contents -- viii
List of Tables -- xi
List of Figures -- xiii
Nomenclature -- xix
1. Introduction -- 1
  1-1. Hydrogen storage methods for mobile application -------------------------------- 3
2. Solid state hydrogen storage --- 6
  2-1. Basic concepts of solid state hydrogen storage ----------------------------------- 6
    2-1-1. The metal-hydrogen reaction --- 6
    2-1-2. The Lennard-Jones picture --- 6
    2-1-3. Reaction mechanism --- 7
    2-1-4. The Van't Hoff equation --- 8
    2-1-5. Requirements for solid state hydrogen storage for fuel cells on vehicles -- 11
3. Complex hydrides -- 14
  3-1. Li-N-H system -- 14
  3-2. Li-Mg-N-H system -- 18
4. Nanostructuring of solid state hydrides by mechanical milling ----------------------- 22
  4-1. Thermodynamic and kinetic issues in solid state hydrides ----------------------- 22
  4-2. Nanostructuring of solid state hydrides --- 24
  4-3. Nanostructuring process --- 26
5. Objectives -- 29
  5-1. Nanostructured lithium amide and lithium hydride system ---------------------- 29
    5-1-1. Nanostructured ($LiNH_2$+LiH) mixture --------------------------------------- 29
    5-1-2 Nanostructured Li-N-C-H systems --- 29
  5-2. Nanostructured lithium amide and magnesium hydride system ----------------- 30
    5-2-1. Nanostructured ($LiNH_2$+nMgH_2) (n=0.55, 0.60, and 0.70) mixtures ------ 30
    5-2-2. Nanostructured ($LiNH_2$+nMgH_2) (n=1.0 and 1.5) mixtures ---------------- 31
6. Experimental -- 32
  6-1. Materials -- 32
    6-1-1. Starting hydrides --- 32
    6-1-2. Catalysts --- 32
  6-2. Synthesis of nanostructure hydrides --- 32
    6-2-1. Chemical compositions --- 32
    6-2-2. Milling procedure --- 33
  6-3. Analysis of powder morphology --- 36
    6-3-1. X-Ray diffraction --- 36
    6-3-2. FT-IR --- 37
    6-3-3. Scanning Electron Microscopy --- 37
    6-3-4. BET --- 38
  6-4. Thermal analysis and hydrogen storage properties ------------------------------- 38

    6-4-1. Differential Scanning Calorimeter -- 38
    6-4-2. Thermogravimetric analysis --- 39
    6-4-3. Gas analysis -- 39
    6-4-4. Hydrogen storage properties --- 39
7. Nano-structured ($LiNH_2$+LiH) systems --- 42
  7-1. Effect of milling on the microstructure of hydride mixtures --------------------- 42
  7-2. Thermal behavior of $LiNH_2$ --- 46
  7-3. Thermal behavior of the ($LiNH_2$+LiH) system ----------------------------------- 49
  7-4. Discussion -- 60
    7-4-1. Origin of the ammonia (NH_3) release from the ($LiNH_2$+LiH) mixture ---- 60
8. Li-N-C-H system --- 68
  8-1. Reactions of carbon with $LiNH_2$ -- 68
    8-1-1. ($2LiNH_2$+C) system -- 68
  8-2. ($LiNH_2$+1.2LiH) system incorporated with graphite ------------------------------ 72
    8-2-1. Morphology and microstructure of powder mixtures ------------------------ 72
    8-2-2. Thermal (DSC) behavior -- 74
    8-2-3. Isothermal hydrogen storage behavior -- 77
  8-3. Discussion -- 84
    8-3-1. Enthalpy and entropy change for the hydrogen desorption reaction ------- 84
9. ($LiNH_2$+nMgH_2) (n=0.55, 0.6, and 0.7) -- 88
  9-1. ($LiNH_2$+nMgH_2) (n=0.55, 0.6, and 0.7) without catalysts ----------------------- 88
    9-1-1. Effect of milling on the microstructure of hydride mixtures ---------------- 88
    9-1-2. Thermal behavior of ($LiNH_2$+nMgH_2) (n=0.55, 0.6, and 0.7) ------------- 89
    9-1-3. Reaction pathways occurring during dehydrogenation ---------------------- 92
    9-1-4. Isothermal hydrogen storage behavior -- 98
  9-2. ($LiNH_2$+0.7MgH_2) mixtures with catalysts --------------------------------------- 101
    9-2-1. Morphology and microstructure of powder mixtures ------------------------ 101
    9-2-2. Thermal behavior -- 103
    9-2-3. Isothermal hydrogen storage behavior -- 108
  9-3. Discussion of thermodynamic properties -- 117
10. ($LiNH_2$+1.0MgH_2) system --- 121
  10-1. Hydrogen desorption during ball milling --- 121
  10-2. Morphology and microstructure of powder mixtures ---------------------------- 127
  10-3 Thermal behavior --- 127
  10-4. Dehydrogenation behaviors and reaction pathways ---------------------------- 131
    10-4-1. ($LiNH_2$+1.0MgH_2) mixture milled under the LES6-3B mode for 25 h --- 131
    10-4-2. ($LiNH_2$+1.0MgH_2) mixture milled under the IMP67 mode for 1 h ------- 135
    10-4-3. ($LiNH_2$+1.0MgH_2) mixture milled under the IMP67 mode for 25 h ------ 138
  10-5. Reversibility --- 141
  10-6. Apparent activation energies -- 146
11. ($LiNH_2$+1.5MgH_2) system --- 150
  11-1. Hydrogen desorption during ball milling ------------------------------------ 150
  11-2. Thermal behavior -- 156
  11-3. Reaction pathways occurring during dehydrogenation -------------------------- 158
    11-3-1. The ($LiNH_2$+1.5MgH_2) milled under the LES6-2B mode for 25 h ------- 158
    11-3-2. The ($LiNH_2$+1.5MgH_2) milled under the IMP67 mode for 1 h ---------- 161

11-3-3. The ($LiNH_2$+1.5MgH_2) milled under the IMP67 mode for 25 h ---------- 163
11-4. Reversibility -- 166
11-5. Apparent activation energies -- 170
12. Discussion of ($LiNH_2$+nMgH_2) (n=0.55, 0.6, 0.7, 1.0 and 1.5) ------------------- 173
12-1. Effect of the molar ratio of MgH_2 and $LiNH_2$ on the reaction pathways ------ 173
12-2. Effect of the molar ratio of MgH_2 and $LiNH_2$ on kinetics ---------------------- 177
13. Summary and Conclusions -- 180
13-1. Li-N-H system --- 180
13-2. Li-N-C-H system with graphite --- 181
13-3. ($LiNH_2$+nMgH_2) (n=0.55, 0.6 and 0.7) -- 182
13-3. ($LiNH_2$+nMgH_2) (n=1.0 and 1.5) -- 183
References -- 185
Appendix A --- 194
A-1. Controlled milling modes by changing position of magnets in Uni-Ball Mill 5 --- 194
A-2. Hydrogen storage capacity estimated by pressure variations during milling using a volumetric method -- 194
A-3. Kinetic curves determination by volumetric method in a Sieverts-type apparatus -- 195
A-4. Determination of reaction pathways occurring on ball milling process ----------- 198
Appendix B. Characteristic absorption lines in FT-IR spectra --------------------------- 200
Appendix C. Rehydrogenation behaviour of ($LiNH_2$+LiH) system depending on applied hydrogen pressure --- 202

List of Tables

Table 1-1. Comparison of the major hydrogen storage methods ------------------ 5
Table 2-1. DOE Targets for Onboard Hydrogen Storage Systems for Light-Duty Vehicles -- 13
Table 3-1. Hydrogen storage properties of selected high-capacity hydrides ----- 15
Table 6-1. Composition of powders and Milling parameters ---------------------- 35
Table 7-1. Powder characteristics of the 1:1 molar ratio mixture of ($LiNH_2$+LiH) as a function of ball milling time --------------------------------------- 45
Table 7-2. The amount of NH_3 released from single-phase $LiNH_2$ before and after milling and approximate onset temperatures of the NH_3 release as estimated from TGA -- 48
Table 7-3. Summary of the DSC results for the ($LiNH_2$+LiH) mixture with various molar ratios of constituents ------------------------------------- 51
Table 7-4. Summary of the calculations of the apparent activation energy of reaction (4-2) --- 59
Table 7-5. The calculated and experimental amount of H_2 desorbed from the 1:1 molar mixture ($LiNH_2$+LiH) ball milled for 25 h --------------------- 62
Table 7-6. Comparison of the calculated and experimental amounts of H_2 and NH_3 as a function of milling time and the molar ratio of LiH:$LiNH_2$ assuming a fraction of inactive LiH ----------------------- 66
Table 8-1. The calculated and experimental amount of H_2 desorbed from the 1:1.2 molar mixture ($LiNH_2$+LiH) with and without 5 wt.% graphite (G) milled for 25 h -- 79
Table 9-1. Reaction pathways for the ($LiNH_2$+0.7MgH_2) mixtures milled for 25 h (IMP67 mode) -- 94
Table 9-2. Reversible reaction pathways for the (($LiNH_2$+0.7MgH_2)+5 wt.% n-Ni) mixtures milled for 25 h (IMP67 mode) ------------------------- 116
Table 10-1. Summary of XRD results of the ($LiNH_2$+1.0MgH_2) mixture milled under various milling modes and times -------------------------------- 125
Table 10-2. Summary of XRD results of the ($LiNH_2$+1.0MgH_2) mixture milled for 25 h (LES6-3B) and subsequently dehydrogenated under 1 bar H_2 at various temperatures --------------------------------------- 133
Table 10-3. Summary of XRD results of the ($LiNH_2$+1.0MgH_2) mixture milled for 1 h (IMP67) and subsequently dehydrogenated under 1 bar H_2 at various temperatures --- 136
Table 10-4. Summary of XRD results of the ($LiNH_2$+1.0MgH_2) mixture milled for 25 h (IMP67) and subsequently dehydrogenated under 1 bar H_2 at various temperatures --- 141
Table 10-5. Summary of XRD results of the ($LiNH_2$+1.0MgH_2) mixture milled for 25 h (LES6-3B) and subsequently dehydrogenated under 1 bar H_2 at 175°C and 400°C, respectively, and rehydrogenated under 50 bar H_2 at 175°C -- 145
Table 11-1. Summary of XRD results of the ($LiNH_2$+1.5MgH_2) mixture milled for various milling modes and times --------------------------- 154
Table 11-2. Summary of the XRD results of the ($LiNH_2$+1.5MgH_2) mixture

milled for 25 h (LES6-2B) and subsequently dehydrogenated under 1 bar H_2 at various temperatures --------------------------------------- 161
Table 11-3. Summary of XRD results of the ($LiNH_2$+1.5MgH_2) mixture milled for 1 h (IMP67) and subsequently dehydrogenated under 1 bar H_2 at various temperatures --- 163
Table 11-4. Summary of XRD results of the ($LiNH_2$+1.5MgH_2) mixture milled for 25 h (IMP67) and subsequently dehydrogenated under 1 bar H_2 at various temperatures -- 166
Table 11-5. Summary of XRD results of the ($LiNH_2$+1.5MgH_2) mixture milled for 25 h (LES6-2B) and subsequently dehydrogenated under 1 bar H_2 at 175°C and 400°C, respectively, and rehydrogenated under 50 bar H_2 at 175°C --- 168
Table 12-1. Summary of the reaction pathways ------------------------------------- 174
Table B-1. Summary of the characteristic absorption lines ------------------------ 201

List of Figures

Fig. 1-1 Production and utilization of hydrogen -- 4

Fig. 1-2 Volume of 4kg of hydrogen compacted in different ways, with size relative to the size of a car -- 4

Fig. 2-1 Simple schematic Lennard-Jones potential energy diagram of chemisorption of hydrogen on metals --- 10

Fig. 2-2 Schematic illustration of the different mechanisms involved in the formation of a metal hydride --- 10

Fig. 2-3 a) Idealized pressure-composition temperature (PCT) curve and b) Van't Hoff plot --- 11

Fig. 2-4 Volumetric and gravimetric hydrogen storage densities of different hydrogen storage methods -- 13

Fig. 4-1 Schematic representation of an equiaxed nanocrystalline material distinguishing between crystallite (open circles) and inter-crystalline regions (dark circles) --- 25

Fig. 4-2 Effect of nanostructuring of a) hydrogen absorption and b) desorption temperature of hydrogen --- 25

Fig. 4-3 Motion of balls in a) a planetary and b) a vibrational mill ------------------ 28

Fig. 4-4 Various controlled modes of milling available in the Uni-Ball-Mill 5 ---- 28

Fig. 6-1 A Sieverts-type apparatus custom-built by A.O.C. Scientific Engineering Pty Ltd., Australia, for evaluating hydrogen storage properties ----------- 41

Fig. 7-1 The evolution of the morphology of the (LiH+$LiNH_2$) mixture milled for a) 1 h, b) 5 h, c) 10 h, d) 25 h, e) 50 h and f) 100 h ------------------------- 43

Fig. 7-2 X-ray diffraction patterns of a) as-received LiH, $LiNH_2$ and their 1:1 molar ratio mixture before and after milling for 1 and 5 h. b) The crystallite sizes of $LiNH_2$ and LiH in the 1:1 molar ratio mixture as a function of milling time --- 44

Fig. 7-3 Specific surface area (SSA) of the ($LiNH_2$+LiH) powder mixture vs. milling time -- 45

Fig. 7-4 The desorption behavior of single-phase $LiNH_2$ before and after ball milling for 25 h: a) TGA and b) DSC profiles ------------------------------ 47

Fig. 7-5 TPD spectra for the 1:1 molar ratio mixture --------------------------------- 48

Fig. 7-6 DSC profiles for a) various milling times for the 1:1 molar ratio mixture $LiNH_2$:LiH and b) the molar ratio of LiH to $LiNH_2$ in the mixture milled for 25 h (heating rate of 10°C/min) (Netzsch 404 apparatus). c) the onset and peak temperature of reaction (4-2) vs. the SSA of powder mixture and d) the grain size of $LiNH_2$ in the 1:1 molar ratio mixture ------------------ 50

Fig. 7-7 XRD patterns of the 1:1 molar ratio mixture milled for 5 h and DSC directly after milling and after heating at various temperatures ----------- 53

Fig. 7-8 FT-IR absorption spectra of a) 1:1, b) 1:1.2 and c) 1:1.4 molar ratio mixtures milled for 25 h and heated to various temperatures 1) 200 °C, 2) 225 °C, 3) 250 °C, 4) 275 °C, and 5) 300°C --------------------------------- 54

Fig. 7-9 a) Examples of the DSC profiles at various heating rates (5, 10 and 15°C/min) for the 1:1 molar ratio mixture of $LiNH_2$:LiH. The Kissinger plots of the activation energy for hydrogen desorption (reaction (4-2) goes

to the right) for the milled LiH and $LiNH_2$ mixtures vs. b) milling time and c) the molar ratio of LiH to $LiNH_2$ -------------------------------------- 57
Fig. 7-10 The apparent activation energy of reaction (4-2) as a function of specific surface area (SSA) for the 1:1 molar ratio mixture $LiNH_2$:LiH --------- 58
Fig. 7-11 The apparent activation energy of reaction (4-2) as a function of the molar ratio of LiH to $LiNH_2$ for the mixtures milled for 25 h ----------- 58
Fig. 7-12 a) TGA curve for the 1:1 molar mixture $LiNH_2$:LiH milled for 25 h. Tangent lines 1 and 2 show two distinct weight-loss regimes for H_2 and NH_3, respectively. b) Corresponding DSC curve showing endothermic desorption peaks of H_2 and NH_3 -- 61
Fig. 7-13 Thermal desorption profiles from a) TGA and b) DSC of the 1:1 molar ratio $LiNH_2$:LiH mixture ball milled for 100 h with and without flushing with Ar for 1.5 h before heating --- 64
Fig. 7-14 a) Comparison of the calculated (Eq. (7-3) and (7-4)) and experimental values of NH_3 vs. milling time for 5, 25 and 100 h. The experimental amount of H_2 and NH_3 in the 1:1 molar ratio $LiNH_2$:LiH mixture vs. b) milling time for 5, 25 and 100 h, and c) the molar ratio of LiH to $LiNH_2$ for the mixtures milled for 25 h -- 67
Fig. 8-1 DSC profiles of 1) single-phase $LiNH_2$ milled for 25 h and 2:1 molar ratio mixtures of $LiNH_2$ with 2) carbon black and 3) graphite milled for 25 h --- 69
Fig. 8-2 TGA profiles of 1) single-phase $LiNH_2$ milled for 25 h and 2) 2:1 molar ratio mixtures of $LiNH_2$ with graphite milled for 25 h --------------------- 70
Fig. 8-3 X-ray diffraction patterns of 2:1 molar ratio mixtures of $LiNH_2$ with graphite milled for 25 h heated to various temperatures at a heating rate of 10°C/min in Ar atmosphere (a- 400°C and b- 500°C) ---------------------- 71
Fig. 8-4 a) Backscattered electron (BSE) micrograph of (($LiNH_2$+1.2LiH)+5 wt.% G) and (b) XRD patterns for 1-(($LiNH_2$+1.2LiH) and 2-(($LiNH_2$+1.2LiH) +5 wt.% G), both of which were milled for 25 h ---------------------------- 73
Fig. 8-5 DSC curves at a heating rate of 10°C/min for the ($LiNH_2$+1.2LiH) mixture without and with 5 wt.% graphite, both of which were ball milled for 25 h-- 75
Fig. 8-6 a) DSC curves at various heating rates and b) the Kissinger plot for the apparent activation energy of dehydrogenation (reaction (4-2)) for the milled (($LiNH_2$+1.2 LiH)+5 wt.% G) system ------------------------------ 76
Fig. 8-7 a) Desorption curves of ($LiNH_2$+1.2 LiH) and (($LiNH_2$+1.2 LiH)+5 wt.% G) (1-250°C, 2-275°C, 3-300°C, 4-325°C) under 1 bar H_2 (atmospheric) and milled for 25 h and b) Arrhenius plots for the estimate of the apparent activation energy for mixtures without and with 5 wt.% G ---------------- 78
Fig. 8-8 Comparison of apparent activation energies obtained from the Kissinger and Arrhenius methods for the mixtures without and with 5 wt.% G ----- 80
Fig. 8-9 a) Desorption curve at 325°C under 1 bar H_2 pressure and b) corresponding absorption curves at 325°C under 11 and 35 bar H_2 pressure for the ($LiNH_2$+1.2LiH) mixture ball milled for 25 h. c) Desorption curve at 325°C under 1 bar H_2 pressure and d) corresponding absorption curves at 325°C under 11 and 35 bar H_2 pressure for the (($LiNH_2$+1.2LiH)+5 wt.% G) mixture ball milled for 25 h- 80
Fig. 8-10 Comparison of XRD profiles for a) ($LiNH_2$+1.2LiH) and b)

((LiNH$_2$+1.2LiH)+5 wt.% G) ball milled for 25 h and subsequently desorbed at 325°C under 1 bar H$_2$ pressure -------------------------------- 83
Fig. 8-11 Comparison of XRD profiles for a) ball milled ((LiNH$_2$+1.2LiH)+5 wt.% G), b) desorbed at 325°C under 1 bar H$_2$ pressure after ball milling, and c) absorbed at 325°C under 11 bar H$_2$ pressure after desorption --------- 83
Fig. 8-12 a) Step-wise desorption curves at varying temperatures and b) the corresponding Van't Hoff plot for the (LiNH$_2$+1.2LiH) mixture without graphite. c) Step-wise desorption curve at varying temperatures and d) the corresponding Van't Hoff plot for the (LiNH$_2$+1.2LiH) mixture with 5 wt.% graphite -- 86
Fig. 8-13 Plateau pressure vs. temperature for a) (LiNH$_2$+1.2LiH) and b) {(LiNH$_2$+1.2LiH)+5 wt.% G} mixtures milled for 25 h ------------------ 87
Fig. 9-1 XRD patterns of the (LiNH$_2$+0.7MgH$_2$) mixtures milled for various milling times (IMP67 mode) --- 88
Fig. 9-2 DSC curves of the (LiNH$_2$+nMgH$_2$) mixtures milled for a) 1 h and b) 25 h: n=0.55, 0.60 and 0.70 (IMP67 mode) -------------------------------- 90
Fig. 9-3 DSC curves of the (LiNH$_2$+0.7MgH$_2$) mixtures milled for various milling Times (IMP67 mode) -- 91
Fig. 9-4 a) DSC curves of the (LiNH$_2$+0.7MgH$_2$) mixture milled for 25 h (IMP67 mode), b) XRD patterns at three temperatures and c) FT-IR absorption spectra at two temperatures --- 93
Fig. 9-5 TPD spectra for the (LiNH$_2$+0.7MgH$_2$) milled for 25 h (IMP67 mode) ----- 94
Fig. 9-6 Dehydrogenation curves at various temperatures under 1 bar H$_2$ for the (LiNH$_2$+0.7MgH$_2$) mixtures milled for 25 h (IMP67 mode) -------------- 100
Fig. 9-7 Isothermal dehydrogenation curves at 250°C under 1 bar H$_2$ for the (LiNH$_2$+0.7MgH$_2$) mixture milled for various durations (IMP67 mode) --- 100
Fig. 9-8 a) Secondary electron (SE) micrograph and energy-dispersive X-ray spectroscopy (EDS) mapping for b) Mg, c) N and d) Ni elements of the (LiNH$_2$+0.7MgH$_2$) mixture with 5 wt.% n-Ni milled for 25 h (IMP67) ----- 102
Fig. 9-9 Grain sizes as function of milling times for (LiNH$_2$+0.7MgH$_2$) a) without and b) with 5 wt.% n-Ni (IMP67 mode) ------------------------------------ 102
Fig. 9-10 DSC curves for the (LiNH$_2$+0.7MgH$_2$) mixtures with 5 wt.% n-Ni milled for various durations (IMP67 mode) --------------------------------------- 103
Fig. 9-11 a) DSC curves at various heating rates for the (LiNH$_2$+0.7MgH$_2$) mixture milled for 25 h (IMP67 mode) and b) and c) the Kissinger plots of the apparent activation energies of reaction (9-1) and reaction (9-2), respectively, after the 25 h milled (LiNH$_2$+0.7MgH$_2$) mixtures without and with catalysts -- 105
Fig. 9-12 The apparent activation energies for the (LiNH$_2$+nMgH$_2$) (n= 0.55, 0.60 and 0.70) mixtures milled for various durations (IMP67 mode) --------- 106
Fig. 9-13 Comparison of the apparent activation energy for the (LiNH$_2$+ 0.7MgH$_2$) mixture without and with two types of catalysts (n-Ni and MnCl$_2$) as a function of milling time (IMP67 mode) ------------------------------------ 107
Fig. 9-14 Dehydrogenation curves at various temperatures under 1 bar H$_2$ for the (LiNH$_2$+0.7MgH$_2$) mixtures with 5 wt.% n-Ni milled for 25 h (IMP67) -- 109
Fig. 9-15 Comparison of dehydrogenation curves at various temperatures under 1

bar H_2 for the ($LiNH_2$+0.7MgH_2) mixtures milled for 25 h (IMP67 mode): a) with and without 5 wt.% n-Ni and b) with 5 wt.% n-Ni/$MnCl_2$- 110
Fig. 9-16 Reversibility for the ($LiNH_2$+0.7MgH_2) mixtures with 5 wt.% n-Ni milled for 25 h (IMP67 mode) -- 114
Fig. 9-17 XRD patterns for the (($LiNH_2$+0.7MgH_2)+5 wt.% n-Ni) mixtures milled for 25 h under IMP67 mode and subsequently dehydrogenated at a) 175°C and b) 400°C, respectively, under 1 bar H_2 and then rehydrogenated at 175°C under 50 bar H_2 --------------------------------- 115
Fig. 9-18 a) & c) Step-wise desorption curves at varying temperatures and b) & d) corresponding Van't Hoff plots for the ($LiNH_2$+0.7MgH_2) mixtures; a) & b) without n-Ni and c) & d) with 5 wt.% n-Ni milled for 25 h (IMP67 mode) -- 118
Fig. 9-19 Plateau pressure vs. temperature for the ($LiNH_2$+0.7MgH_2) mixture a) without and b) with 5 wt.% n-Ni milled for 25 h (IMP67 mode) -------- 120
Fig. 10-1 Hydrogen loss of the ($LiNH_2$+1.0MgH_2) during ball milling process in four different milling modes --- 121
Fig. 10-2 a) XRD patterns and b) FT-IR absorption spectra for the ($LiNH_2$+1.0MgH_2) mixtures milled for various times (IMP67 mode) ------ 123
Fig. 10-3 XRD patterns for the ($LiNH_2$ + 1.0MgH_2) milled for 25 h under two different milling modes --- 125
Fig. 10-4 Backscattered electron (BSE) micrographs of the ($LiNH_2$+1.0MgH_2) mixtures milled for 25 h under two different milling modes: a) LES6-2B and b) LES6-3B --- 128
Fig. 10-5 Specific surface areas of the ($LiNH_2$ + 1.0MgH_2) without and with the milling under various milling modes for 25 h ---------------------------- 128
Fig. 10-6 DSC curves at a heating rate of 10°C/min for the ($LiNH_2$+1.0MgH_2) mixtures milled for 25 h under two different milling modes ------------- 129
Fig. 10-7 Comparison of DSC curves for the ($LiNH_2$+1.0MgH_2) mixtures milled for 1 h and 25 h (IMP67 mode) -- 129
Fig. 10-8 TPD spectra for ($LiNH_2$+1.0MgH_2) milled for 25 h (LES6-3B mode) ---- 130
Fig. 10-9 a) Dehydrogenation curves under 1 bar H_2 pressure (atmospheric) at various temperatures and b) the corresponding XRD patterns for the ($LiNH_2$+1.0MgH_2) mixtures milled for 25 h under the LES6-3 mode ----- 134
Fig. 10-10 a) Dehydrogenation curves and b) XRD profiles for the ($LiNH_2$+1.0MgH_2) mixtures milled for 1 h (IMP67 mode) and subsequently dehydrogenated under 1 bar H_2 at varying temperatures --- 137
Fig. 10-11 a) Dehydrogenation curves and b) XRD profiles for the ($LiNH_2$+1.0MgH_2) mixtures milled for 25 h (IMP67 mode) and subsequently dehydrogenated under 1 bar H_2 at varying temperatures --- 140
Fig. 10-12 (a) 1st and 2nd dehydrogenation curves at 175°C under 1 bar H_2 pressure and corresponding rehydrogenation curve at 175°C under 50 bar H_2 pressure and (b) 1st and 2nd dehydrogenation curves at 400°C under 1 bar H_2 pressure and corresponding rehydrogenation curve at 175°C under 50 bar H_2 pressure for the ($LiNH_2$+1.0MgH_2) mixtures milled for 25 h under LES6-3B mode -- 143
Fig. 10-13 XRD patterns for the ($LiNH_2$+1.0MgH_2) mixtures milled for 25 h under

the LES6-3B mode and subsequently dehydrogenated at a) 175°C and b) 400°C, respectively, under 1 bar H_2 and then rehydrogenated at 175°C under 50 bar H_2 -- 144
Fig. 10-14 a) DSC curves at various heating rates for the ($LiNH_2$+1.0MgH_2) mixtures milled for 25 h and b) the corresponding Kissinger plots of the apparent activation energies for the mixtures milled for 1 h (closed) and 25 h (open), respectively (IMP67 mode). c) DSC curves at various heating rates and d) the Kissinger plots of the apparent activation energies for the ($LiNH_2$+1.0MgH_2) mixtures milled for 25 h in the LES6-3B mode --- 148
Fig. 10-15 Comparison of the apparent activation energies for ($LiNH_2$+1.0MgH_2) milled for 1 h and 25 h under IMP67 and for 25 h under the LES6-3B mode, respectively --- 149
Fig. 11-1 Hydrogen loss of the ($LiNH_2$+1.5MgH_2) during ball milling process under four different milling modes -- 150
Fig. 11-2 a) XRD patterns and b) FT-IR absorption spectra for the ($LiNH_2$+1.5MgH_2) milled for various milling times (IMP67 mode) ----- 152
Fig. 11-3 XRD patterns for the ($LiNH_2$ + 1.5MgH_2) mixture milled for 25 h under two different milling modes -- 154
Fig. 11-4 Comparison of DSC curves for the ($LiNH_2$+1.5MgH_2) mixtures milled for 1 h and 25 h under IMP67 and for 25 h under the LES6-2B mode ----- 157
Fig. 11-5 TPD spectra for the ($LiNH_2$+1.5MgH_2) milled for 25 h (LES6-2B mode)- 158
Fig. 11-6 Dehydrogenation curves under 1 bar H_2 pressure (atmospheric) at various temperatures and b) the corresponding XRD patterns for the ($LiNH_2$+1.5MgH_2) mixtures milled for 25 h under the LES6-2B mode --- 160
Fig. 11-7 a) Dehydrogenation curves and b) XRD patterns for 1 h milled ($LiNH_2$+1.5MgH_2) mixtures (IMP67 mode) and subsequently dehydrogenated under 1 bar H_2 at varying temperatures ----------------- 162
Fig. 11-8 a) Dehydrogenation curves and b) XRD patterns for 25-h milled ($LiNH_2$+1.5MgH_2) mixtures (IMP67 mode) that are subsequently dehydrogenated under 1 bar H_2 at various temperatures ------------------ 165
Fig. 11-9 (a) 1st and 2nd dehydrogenation curves at 175°C under 1 bar H_2 pressure and corresponding rehydrogenation curve at 175°C under 50 bar H_2 pressure and (b) 1st and 2nd dehydrogenation curves at 400°C under 1 bar H_2 pressure and corresponding rehydrogenation curve at 175°C under 50 bar H_2 pressure for the ($LiNH_2$+1.5MgH_2) mixtures milled for 25 h under the LES6-2B mode --- 167
Fig. 11-10 XRD patterns for the ($LiNH_2$+1.5MgH_2) mixtures milled for 25 h under the LES6-2B mode and subsequently dehydrogenated at 175°C under 1 bar H_2 and rehydrogenated at 175°C under 50 bar H_2 ------------------- 168
Fig. 11-11 a) DSC curves at various heating rates and b) the corresponding Kissinger plots of the apparent activation energies for the ($LiNH_2$+1.5MgH_2) mixtures milled for 1 h (closed) and 25 h (open) (IMP67 mode). c) DSC curves at various heating rates and d) the Kissinger plots of the apparent activation energies for the ($LiNH_2$+1.5MgH_2) mixtures milled for 25 h under LES6-2B mode ------ 171

Fig. 11-12 Comparison of the apparent activation energies for the ($LiNH_2$+1.5MgH_2) milled for 1 h and 25 h under IMP67 and for 25 h under the LES6-2B mode -- 172
Fig. 11-13 Available hydrogen storage capacity as a function of the molar ratio of $MgH_2/LiNH_2$ --- 176
Fig. 11-14 The peak temperatures corresponding to the first endothermic peak in each DSC curve as a function of various molar ratios of $MgH_2/LiNH_2$ mixtures milled for a) 1 h and b) 25 h (IMP67 mode) ------------------ 176
Fig. 11-15 The apparent activation energies as functions of the molar ratio of the $MgH_2/LiNH_2$ (IMP67 mode) --- 179
Fig. A-1 Milling modes with two magnets in Uni-Ball Mill 5: (a) high energy impact mode with magnets at 6 and 7 o'clock positions (IMP67 mode) and (b) low energy shearing mode with magnets at 6 o'clock position (LES6 mode) -- 194
Fig. A-2 Scheme of Sieverts-type apparatus where: T- transducer, V_H – hydrogen cut off valve, V_{Ar}–argon cut off valve, V_P–vacuum system cut off valve, V_R–reactor cut off valve, V_C–calibrated volume and its cut off valve, V_v-vent valve, R–reactor -- 196
Fig. C-1 Scheme of rehydrogenation behaviours of ($LiNH_2$+LiH) mixture depending on applied hydrogen pressure ------------------------------------ 202

Nomenclature

Solid state hydride

PCI/PCT: pressure-composition isotherm/pressure-composition temperature curve

P_{eq}: plateau pressure

Milling modes and parameters

LES6: low energy shearing mode with one magnet at 6 o'clock position

IMP67: impact mode with two magnets at 6 and 7 o'clock positions

BPWR: ball-to-powder weight ratio

WD: working distance

Grain size calculation

L: mean dimension of the nanograin (crystallite) composing the powder particle

K: constant (≈ 1)

e: maximum microstrain

λ: wave length

θ: position of the analyzed peak maximum

$\delta(2\theta)$: instrumental broadening-corrected "pure" XRD peak profile breadth

B: breadth of the Bragg peak from the XRD scans of the experimental powder

b: the breadths of Bragg peak from the XRD scans of the reference powder

FWHM: the full-widths at half maximum

Hydrogen capacity estimated by the volumetric method

ΔP: the total pressure change of H_2 (Pa) during the test

m: weight of absorbed H_2 (g)

M_H: molar mass of H_2 (g/mol)

T: temperature (K)

R: gas constant (8.314J $(mol)^{-1}K^{-1}$)

M: initial powder mass (g)

1. Introduction

The industrialized countries rely heavily on fossil fuels. In fact 87% of the world energy consumption in year 2003 was from fossil fuels and the rest mainly comes from nuclear power, hydro power, and burning of waste and wood. Although energy consumption from sustainable energy sources such as wind electricity are rapidly increasing (increased by a factor of 5 from 1989-2003) the overall contribution is only 0.11% [1-3].

We consume fossil fuels for a wide variety of purposes from heating our houses, cooking of our food to transportation and manufacturing of consumer goods - the list could be continued and it is long and exhaustive. In fact almost every aspect of human life in the modern world is associated with the use of fossil fuels - the result is an ever increasing energy consumption caused by population growth and a general increase in living standard. The world population has been projected to increase from approx. 6.4 billion today to approx. 9 billion by year 2050 [1-3] and especially the explosive development in Asia, in particular in China, requires massive amounts of energy.

In order to support the growing demand for fossil fuels new reserves needs to be discovered. However, oil discovery already peaked in the 1962 with 40 billion barrels being found and have declined ever since. In 1997 only 6 billion barrels of oil was found in comparison with the production of 26 billion barrels [4-8]. Someday, we will inevitably run out of fossil fuels, although it may not happen in our lifetime due to relatively large reserves of natural gas and coal.

Another issue which might become critical even before we run out of fossil fuels is the global warning issue potentially threatening the life of many people due to rising sea levels and increasingly harsh weather conditions. Increasing levels of atmospheric CO_2 originating from the burning of fossil fuels correlate with the increasing global temperature [9-10]. Therefore, the emission of carbon dioxide (CO_2), the main greenhouse gas from human activities, is the most sensitive subject of a world-wide debate about energy sustainability and the stability of global climate in the recent years.

A possible way of addressing both the global warming issue and to keep a sustainable energy supply after the fossil fuels have been depleted is a gradual transformation of our present fossil fuel based society to a hydrogen based society viz. a society in which hydrogen is the primary energy carrier [11-14].

According to many studies in the scientific community we are now at the verge of a new hydrogen age [15,16]. Energy is first produced from renewable sources and stored in the form of hydrogen. Hydrogen is transported and distributed to final applications such as transportation, and electric power generation for industrial and residential use. The process is shown schematically in Fig. 1-1.

Extensive research efforts are laying down the foundation of the next industrial revolution in the application of hydrogen as the fuel of the future. Some focus on contributions that hydrogen can make to sustainable development [17-19]. Others focus on hydrogen's potential to resolving environmental issues [20-22].

Recently, investigations of hydrogen storage systems have become important. As the studies point out, there are still problems in the realization of renewed hydrogen, but the market supply and the cost of hydrogen do not impede the utilization of hydrogen in practical applications. The biggest and the only roadblock for using hydrogen commercially, especially in vehicular applications, is the storage of hydrogen [15, 16, 22-25].

1-1. Hydrogen storage methods for mobile application

For on-board energy storage, vehicles need compact, light, safe and affordable containment. Modern cars are burning about ~24 kg of gasoline for a range of 400 km in a combustion engine. To cover similar range, 4 kg of hydrogen are needed for an electric car with a fuel cell [1, 15, 22, 26]. Since 4 kg of hydrogen has a volume of 45 m^3 at room temperature and atmospheric pressure, a tank with considerable storage space would be needed. This volume corresponds to a balloon of 5 m in diameter, which is hardly a practical solution for the mobile applications.

Fig. 1-2 shows a comparison of the volume of 4 kg of hydrogen, which is required for ~400 km travel range for a modern electric car powered by a fuel cell, compacted in different ways with the size relative to the size of a car [26]. As shown in Fig. 1-2, storage of hydrogen is a critical challenge in mobile application.

The most common hydrogen storage systems are high pressure gas cylinders, liquid hydrogen in cryogenic tanks and solid state hydrides as shown in Table 1-1 [1, 22, 26]. With the newly developed light weight composite cylinders which support pressure up to 80 MPa, the hydrogen volumetric density can reach ~40 kg m^{-3} [26]. However, the concern in respect to use of the pressurized cylinders is a problem especially in the regions with high population. Liquid hydrogen is stored in cryogenic tanks at -252^{o}C and ambient pressure. The volumetric density of liquid hydrogen is ~71 kg m^{-3} [22]. Due to the low critical temperature of hydrogen (-241 ^{o}C [22], above this temperature hydrogen is gaseous), liquid hydrogen can only be stored in open systems to prevent strong overpressure, thus it results in the thermal loss.

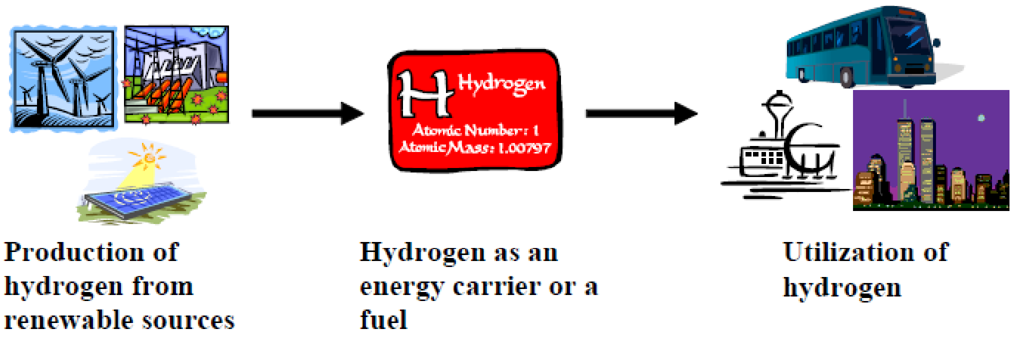

Fig. 1-1 Production and utilization of hydrogen

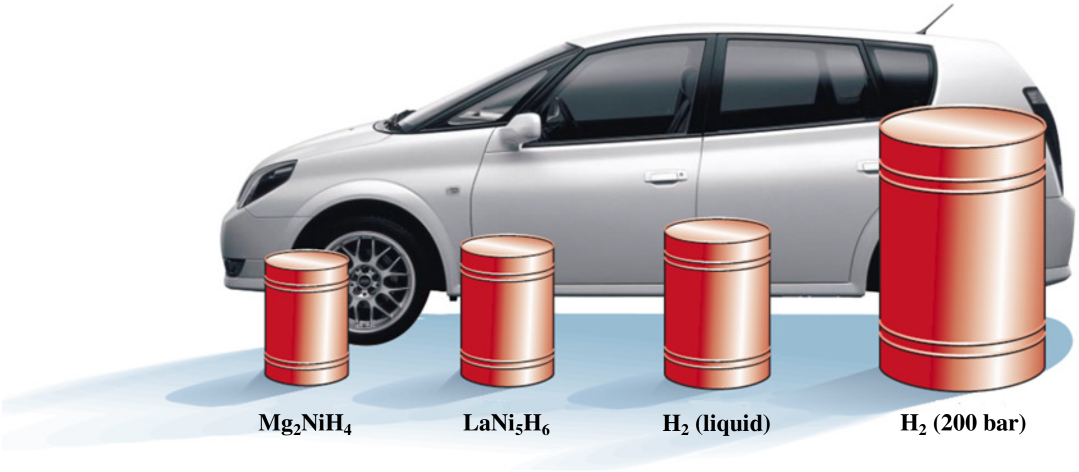

Fig. 1-2 Volume of 4kg of hydrogen compacted in different ways, with size relative to the size of a car [26]

Solid state hydrides which include metal/intermetallic and complex (chemical) hydrides are characterized by the highest volumetric capacities and they do not suffer drawbacks as those experienced by compressed and liquid hydrogen. Because of the low pressures involved in metal hydride technologies and the fact that the release of hydrogen takes place via an endothermic process, this method of hydrogen storage is the safest of all. Moreover, the hydrogen released from a metal hydride is of very high purity and therefore, can be used directly to feed a PEM fuel cell [1]. It is clear that hydrogen storage requires a major technological breakthrough, and this is most likely to occur in the most viable alternative to compressed and liquid hydrogen, namely the storage of hydrogen in solids. The development of new sold-state hydrogen storage materials could herald a step change in the technology of hydrogen storage and would have a major impact on the transition to a hydrogen economy.

Table 1-1. Comparison of the major hydrogen storage methods [1, 22, 26]

Storage system	**Volumetric density ($kg\ H_2\ m^{-3}$)**	**Drawbacks**
Compressed hydrogen gas under 80 MPa pressure	~40	1) Safety problem since enormous pressures are required 2) Cost of pressurization 3) Large pressure drop during use 4) Hydrogen embrittlement of storage Tanks
Liquid hydrogen at cryogenic tank at −252°C (21 K)	~71	1) Large thermal losses (open system) 2) Safety 3) Cost of liquefaction
Solid state hydrides	~80-160	***None of above two***

2. Solid state hydrogen storage

2-1. Basic concepts of solid state hydrogen storage

2-1-1. The metal-hydrogen reaction

Hydrogen-metal system can be generalized to some degree, although numerous deviations and exceptions to those generalizations can be found. Metal hydrides as candidates for storage applications can be formed reversibly by direct interaction of metals or intermetallics with hydrogen at proper temperature and pressure according to the general reaction [23]:

$M\ (s) + xH_2\ (g) \leftrightarrow MH_x(s) + \boldsymbol{Q}$ (2-1)

where Q is the released heat during reaction.

2-1-2. The Lennard-Jones picture

The reaction between gas phase H_2 and a metal surface is schematically illustrated in Fig. 2-1 [26-28] where the one-dimensional Lennard-Jones potential of atomic H and molecular H_2 is shown. Far from the surface, two potentials are separated by the hydrogen dissociation energy which is 218 kJ/mol H. A H_2 molecule moving towards the surface will at some point feel a weak attractive force in the range of approx. 0-20 kJ/mol H (van der Waals forces) corresponding to molecular physisorption (point 1 in Fig. 2-1). If the molecule is moved closer to the surface, the potential energy will increase due to repulsion. At some point, the potential energy of the H_2 molecule will intersect with the potential energy of the H atom. After this point, it is energetically more favourable for the two H atoms to be separated and bonded to the metal surface rather than bonded to each other. Hence dissociation will occur. If this intersection is at a potential energy larger than zero relative to gas phase H_2 (point 2), dissociation is said to be activated and the height of point 2 determines the activation barrier.

If the intersection is located at approximately zero potential energy, dissociation is said to be non-activated (point 3). In the former case only the fraction of H_2 molecules with an energy larger than the activation barrier will be able to dissociate. After dissociation the H atoms find a potential energy minimum shown as point 4 (chemisorption) which corresponds to the H atoms being bonded to the metal surface. If the H-M bond is stronger than the H-H bond, chemisorption is said to be exothermic. Likewise if the H-H bond is the strongest, chemisorption is said to be endothermic.

2-1-3. Reaction mechanism

A schematic visualization of the interaction of hydrogen with a metal is depicted in Fig. 2-2. In contrast to Fig. 2-1 which was an energy representation, Fig. 2-2 shows all the individual reaction steps including bulk processes. The formation of the metal hydride can be divided into the following elementary reactions [28-31].

Dissociation/adsorption: The first step is the dissociative adsorption of hydrogen on the metal/hydride surface. This is shown as point 1 in Fig. 2-2.

Surface penetration: From the surface the hydrogen atoms can penetrate into the sub-surface (point 3).

Bulk diffusion: From the sub-surface, the hydrogen atoms can diffuse into the bulk or from the bulk and further in (point 4).

Hydride formation: Hydrogen atoms in the bulk (corresponding to a solid solution) can create a hydride nuclei which can grow to larger hydride grains by trapping of additional hydrogen atoms (point 6). The formation of a hydride phase complicates the picture somewhat since hydrogen diffusion can also take place through the hydride (point 5).

For dehydrogenation the process is the reverse. A reaction mechanism can be proposed on the basis of the above reversible elementary reactions. When reviewing the hydrogenation/ dehydrogenation kinetic properties, the rate determining step can roughly be divided into two major classes; one is either a surface process such as dissociation or bulk diffusion mechanism limiting the overall kinetics and the other is a nucleation and growth mechanism limiting the overall kinetics. However, the mechanism which determines the overall kinetics has not been still understood well. Recently a lot of efforts have been devoted to improving the slow kinetics of solid state hydrides. Among new strategies, the most promising results are shown in the studies of catalysts and nano-structure.

2-1-4. The Van't Hoff equation

The thermodynamic aspects of the hydride formation from gaseous hydrogen can be described by pressure-composition temperature (PCT) curves, which is also called pressure-composition isotherm (PCI) [1, 26]. An idealized PCT curve is shown in Fig. 2-3 a). As discussed previously, H_2 molecule will dissociate on the surface of the metal according to the dissociative chemisorption reaction $H_2 \rightarrow 2H$ and then H atoms will diffuse into the metal lattice to form a solid solution (α-phase). As the concentration of dissolved H is increased, at some pressure or composition, nucleation and growth of the ordered hydride phase β start. While the two phases, α and β coexist, the isotherms show a plateau, the length of which determines the amount of hydrogen that can be stored reversibly with small pressure variations. As the plateau is traversed by adding more and more hydrogen, the β phase grows as the expense of the α phase. In the pure β phase, hydrogen pressure rises steeply with the concentration. The two phase region ends in a critical point T_c. The dotted line in Fig. 2-3 a) defines the limit of the two-phase coexistence region on a PCT phase diagram. As temperature increases plateau width decreases and the plateau pressure increases. The plateau pressure (P_{eq}) strongly depends on temperature. The equilibrium pressure (P_{eq}) as a function of temperature is related to the changes ΔH and ΔS of enthalpy and entropy, respectively, by the Van't Hoff equation [1, 26]:

$$\ln P_{eq} = \frac{\Delta H}{RT} - \frac{\Delta S}{R} \qquad (2\text{-}2)$$

As shown in Fig. 2-3 b), a plot of ln P_{eq} vs. 1/T tends to be a straight line with the slope equal to ΔH and intercept (1/T=0) equal to ΔS. The knowledge of enthalpy change is important to the heat management required for hydride storage devices and is also a measure of the strength of the M-H chemical bond [11,31]. The entropy term corresponds mostly to the change from molecular hydrogen gas to dissolved solid hydrogen. It is approximately equal to the standard entropy of hydrogen (-130 $JK^{-1}mol^{-1}$) for all of the metal hydrogen systems [11]. The Van't Hoff plot is a convenient way to graphically represent hydride thermal stability, especially to compare different solid state hydrogen storage systems.

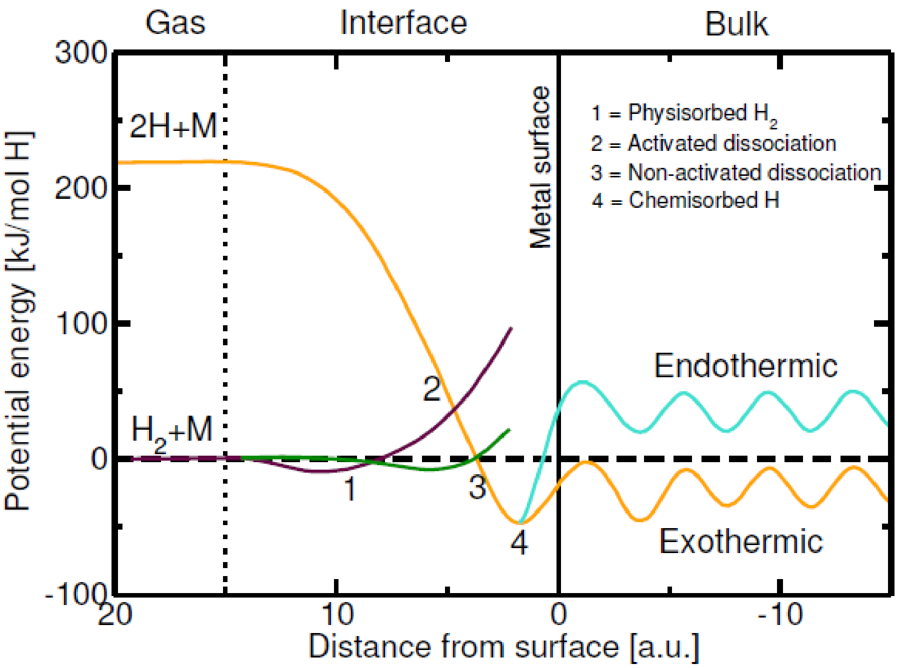

Fig. 2-1 Simple schematic Lennard-Jones potential energy diagram of chemi-sorption of hydrogen on metals [26-28]

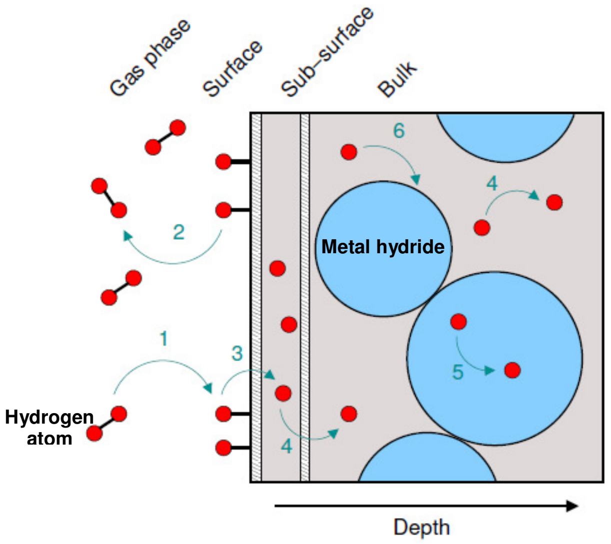

Fig. 2-2 Schematic illustration of the different mechanisms involved in the formation of a metal hydride [28-31]

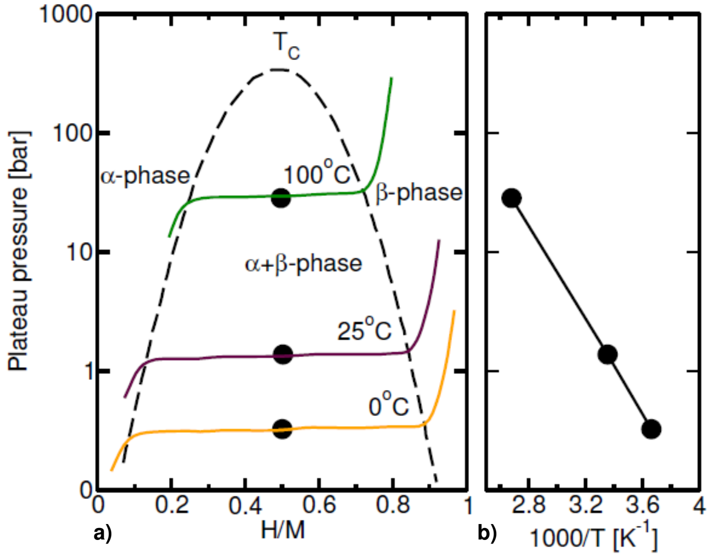

Fig. 2-3 (a) Idealized pressure-composition temperature (PCT) curve and (b) Van't Hoff plot [26]

2-1-5. Requirements for solid state hydrogen storage for fuel cells on vehicles

For stationary systems, the weight and volume of the system used for hydrogen storage is not a key factor. However, for mobile applications, such as fuel cell electric vehicles (FCEV) or hydrogen-fuelled (internal combustion) cars, hydrogen storage system has to be compact, lightweight, safe and affordable. In 1996, the International Energy Agency (IEA) established the "hydrogen storage task force" to search for innovative hydrogen storage methods and materials. The U.S. Department of Energy (D.O.E.) Hydrogen Plan has set a standard for this discussion by providing a commercially significant benchmark for the amount of reversible hydrogen absorption. Specially, the U.S. Department of Energy (D.O.E.)

introduced a number of targets for on-board hydrogen storage systems within the frame work of its FreedomCar program [1]. Recently, the on-board hydrogen storage system targets have been revised to reflect knowledge gained in hydrogen-fueled vehicles since the original release of the targets as shown in Table 2-1. Among these targets, the two criteria that are most often considered are gravimetric and volumetric storage capacities. These two criteria have been developed using guidelines from the auto industry that reflect consumers' expectations about the performance of cars without causing exceptionally large changes in automobile design. Fig. 2-4 shows the gravimetric and volumetric energy densities of hydrogen stored using various storage methods. It can be seen that neither cryogenic nor high-pressure hydrogen storage options can meet the mid-term D.O.E. targets for transportation application. It is becoming increasingly accepted that solid state hydrogen storage using ionic-covalent hydrides of light elements, such as lithium, boron, sodium, magnesium and aluminum (or some combination of these elements), represents the only method enabling one to achieve the necessary gravimetric and volumetric target densities.

Table 2-1. D.O.E. Targets for Onboard Hydrogen Storage Systems for Light-Duty Vehicles [33]

Targeted factor	**2015**	**2015**	**Ultimate**
	Old	**new**	**new**
System Gravimetric Density [wt.%] **(kWh/kg)**	[9] (3.0)	**[5.5]** **(1.8)**	**[7.5]** **(2.5)**
System Volumetric Density [g/L] **(kWh/L)**	[81] (2.7)	**[40]** **(1.3)**	**[70]** **(2.3)**
System fill time for 5-kg fill [min] **(kgH_2/min)**	[2.5] (2.0)	**[3.3]** **(1.5)**	**[2.5]** **(2.0)**
System cost [$/$kgH_2$] **($/kWh_{net})**	[67] (2)	**TBD**	**TBD**

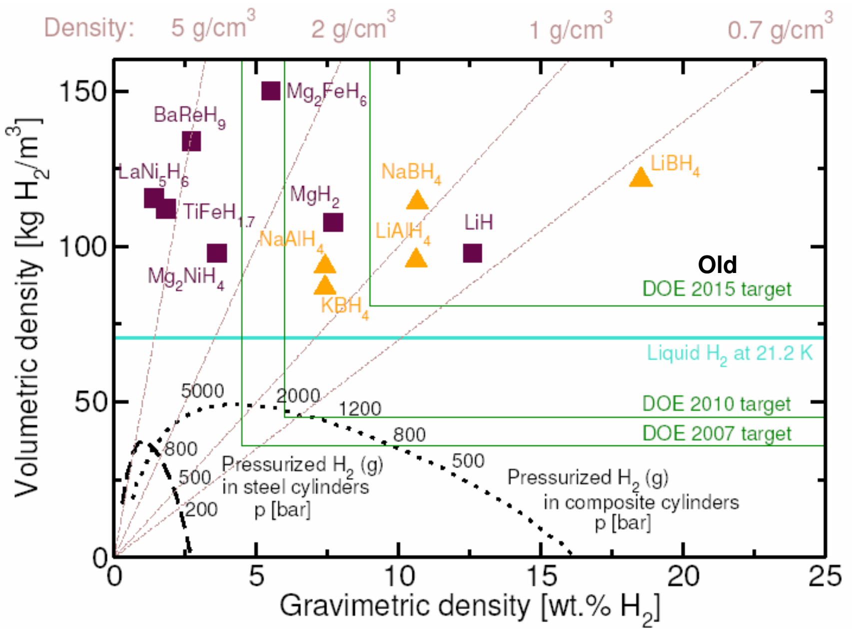

Fig. 2-4 Volumetric and gravimetric hydrogen storage densities of different hydrogen storage methods [1]

3. Complex hydrides

Group I and II salts of $[AlH_4]^-$, $[NH_2]^-$, and $[BH_4]^-$ (alanates, amides and borohydrides) have recently received considerable attention as potential hydrogen storage materials [34-40]. These materials have high hydrogen gravimetric densities [15, 27, 42] as seen in Fig. 2-4 and Table 3-1. Thus, they would seem to be viable candidates for application as practical on-board hydrogen storage materials. However, all of these materials are plagued by high kinetic barriers to dehydrogenation and/or hydrogenation in the solid state. Traditionally, it was thought that it would be impossible to reduce the barrier heights to an extent that would give reaction rates that even approached those that would be required for vehicular applications. Thus, until recently, complex hydrides were not considered as candidates for application as rechargeable hydrogen carriers. This situation has been changed by Bogdanovic and Schwickardi [44], who show that the addition of Ti catalyst to the complex hydride $NaAlH_4$ made it reversibly release and take up 3.7 wt.% of hydrogen under moderate temperature-pressure conditions with an enhanced hydriding kinetics. This breakthrough has led to a worldwide effort to develop doped alanates as practical hydrogen storage materials, which has been quickly expanded to include amides and borohydrides.

3-1. Li-N-H system

Lithium nitrides are considered to be one of the most promising hydrogen storage materials that could achieve practical hydrogen storage due to their light weight, high theoretical capacity (10.4 wt.% H_2) and relatively low decomposition temperature (e.g. as compared to MgH_2 [45-45]) [56-69].

Table 3-1. Hydrogen storage properties of selected high-capacity hydrides [1, 15, 26, 27, 35, 38, 41-43]

Hydride	Theoretical maximum H_2 capacity (wt.%)	Theoretical reversible H_2 capacity (wt.%)	Desorption temperature range (°C)
$LiBH_4$	18.4	~13.8	~ 470
$Mg(BH_4)_2$	14.9	~11.2	~ 300
$NaBH_4$	10.6	10.6	400-600
$LiAlH_4$	10.6	~7.9	110-260
$Mg(AlH_4)_2$	9.3	~7.0	110-160
Li_3N ($LiNH_2$+LiH)	10.4	~6.5	150–280
MgH_2	7.6	7.6	300-400
$NaAlH_4$	7.5	5.6	229-247

Recently, Chen et al. reported that Li_3N can absorb and desorb hydrogen by the following 2 step reversible reactions [56, 70]:

$$Li_3N + H_2 \leftrightarrow Li_2NH + LiH \qquad (3\text{-}1)$$

$$Li_2NH + H_2 \leftrightarrow LiNH_2 + LiH \qquad (3\text{-}2)$$

These two reaction steps correspond to a total hydrogen storage potential of 10.4 wt.% H_2. While this maximum storage capacity has been demonstrated by several groups, its practical application is limited since full desorption to Li_3N from Li_2NH (reaction (3-1)) requires temperatures greater than 320°C in dynamic vacuum. Only reaction (3-2) is considered to be suitable for a hydrogen storage system because the latter reaction has a smaller enthalpy change and still possesses a large amount of 6.5 wt.% H_2 [71-92]. The desorption enthalpy change of reaction (3-2) has been calculated to be -44.5 kJ/mol H_2 [56, 70], but a recent measurement [65] suggests that it might be -65.6 kJ/mol H_2, which is higher than the previous theoretical value.

In spite of its potential for reversible storage of 6.5 wt.% H_2 for automobile applications, there exists two critical barriers to the practical utilization of these materials [57]. The first is its high operational temperature for the hydrogen absorption/desorption. This barrier may come from both thermodynamic and kinetic issues. The second is the release of NH_3 during the desorption, which can be poisonous for the polyelectrolyte membrane of a conventional PEM fuel cell, even at trace levels, so at present even the smallest release of ammonia in the hydrogen gas cannot be tolerated in the system [1].

To address these problems, a lot of efforts have been devoted to developing new strategies such as i) partial substitution of Li by elements with larger electro-negativity such as Mg [74, 75, 77, 81-88], ii) search for effective catalysts [59, 75, 79, 80] and iii) high energy ball milling [1]. The first approach has been shown to be effective in reducing the hydriding and dehydriding temperature to around 200°C with a hydrogen pressure of 30 bars [83-86]. However, the second approach has not borne much fruit yet even though a wide range of potential catalysts, such as Ni, Fe, Co, VCl_3, $TiCl_3$, TiO_2, Ti, Mn, MnO_2, V, and V_2O_5, have been investigated [58, 59, 75, 79]. The best result appears to show less than 50°C reduction in the peak temperature for hydrogen desorption when the $LiNH_2$ and LiH mixture with and without catalysts are compared [58, 59, 75, 79]. The third approach exhibits some promising results, showing a decrease in the peak temperature for the desorption reaction from 350 to

270°C without and with ball milling, respectively [58, 59]. However, the dependence of the hydrogen absorption/desorption properties of the $LiNH_2$ and LiH mixture on the degree of mechanical activation has not been systematically investigated and reported in the literature.

To date, few works have been dedicated to the NH_3 escaping issue. Nevertheless, recently, it has been shown that the release of NH_3 can be prevented by high energy ball milling as shown by Yao et al [59]. In spite of this, several other groups [58, 70, 80] have reported the presence of NH_3 in the effluent gas from the $LiNH_2$/LiH mixture. The discrepancy among different groups has not been explained yet. Another issue is the mechanism of reaction (3-2). It has not been clearly understood. Some reports suggest that $LiNH_2$ may directly react with LiH to produce H_2 according to reaction (3-2). Others propose that NH_3 is evolved as a transient gas by followed by reactions (3-3) and (4-4) [57-62]:

$$2LiNH_2 \leftrightarrow Li_2NH + NH_3 \qquad (3\text{-}3)$$

$$NH_3 + LiH \leftrightarrow LiNH_2 + H_2 \qquad (3\text{-}4)$$

with the enthalpy change of +84 kJ/molNH_3 and −42 kJ/molH_2, respectively.

In these reactions $LiNH_2$ decomposes into Li_2NH and NH_3, and then the emitted NH_3 quickly reacts with LiH to form $LiNH_2$ and H_2. The newly formed $LiNH_2$ decomposes again and repeats the cycle of reactions (3-3) and (3-4). Such successive reactions continue until all $LiNH_2$ and LiH completely transform to Li_2NH and H_2. It has been shown that reaction (3-4) takes place very fast in the order of the microseconds. However, even with such high reaction rates, escaping of NH_3 from the hydrogen storage system has been reported and used as the evidence to support the mechanism defined by reaction (3-3) and (3-4). Several recent studies have also provided evidence supporting a two-step elementary reaction mechanism. However, so far there is no direct evidence to support a two-step elementary reaction mechanism.

Recently, another approach has been reported by Xie et al. to improve the kinetic properties and remove NH_3 release [64]. They synthesized Li_2NH hollow nano-spheres to decrease the diffusion distance to nanometers and increase the specific surface area. These hollow nanospheres have diameters ranging from 100 to 400 nm and 20 nm shell thickness. In addition, the specific surface area is 79.4 m^2/g and the crystallite sizes are about 15 nm. They have shown that the desorption onset and peak temperature of the reaction (3-2) as measured by Differential Scanning Calorimetry (DSC) is reduced to 179 and 230°C, respectively. Furthermore, they have reported that the activation energy for the hydrogen absorption in the reaction (3-2) is reduced to 106 kJ/mol due to the large specific surface area and shorter diffusion distance of the nanometric hollow structure. In spite of the short diffusion distance, this newly designed Li_2NH hollow nano-spheres doesn't show significantly improved hydrogen storage kinetics compared to the nano-structured ($LiNH_2$+LiH) mixture processed by the high energy ball milling. Therefore, the investigation of the main kinetic control parameters will be critical to further improve hydrogen storage properties of ($LiNH_2$+LiH) system.

3-2. Li-Mg-N-H system

The kinetic and thermodynamic properties of Li-N-H system require further improvement for practical applications [56, 58, 59, 65, 70-80]. The strongly endothermic nature of the reactions mentioned above requires high operation temperatures. To lower the temperature, the thermodynamic properties of the reaction must be improved. Nakamori et al. [83-87, 93-

96] noted that the dehydrogenation reaction of $LiNH_2$ can be promoted by substituting Li with Mg, which is the element with larger electronegativity. Recent studies [69, 81, 82, 88, 89, 97-102] revealed that the Li-Mg-N-H ternary system has improved thermodynamic properties compared to the $LiNH_2$-LiH system. It was found that $2LiNH_2/MgH_2$ and $Mg(NH_2)_2/2LiH$ systems could reversibly store 5.5 wt.% H_2 at 180°C by the following reaction [83, 86, 87, 94, 96]:

$$LiNH_2 + 0.5MgH_2 \rightarrow 0.5Li_2Mg(NH)_2 + H_2 \qquad (3\text{-}5)$$

$$0.5Li_2Mg(NH)_2 + H_2 \leftrightarrow 0.5Mg(NH_2)_2 + LiH \qquad (3\text{-}6)$$

After an initial dehydrogenation, the 2:1 $LiNH_2/MgH_2$ mixture was transformed into a novel phase with a suggested composition of $Li_2Mg(NH)_2$. In the subsequent rehydrogenation process, this phase was hydrogenated to $Mg(NH_2)_2$ and LiH, rather than the initial $LiNH_2/MgH_2$ mixture. Therefore, the reversible reaction is actually processed between $[Li_2Mg(NH)_2+2H_2]$ and $[Mg(NH_2)_2+2LiH]$ as described in equation (3-6). The heat of the endothermic hydrogen desorption reaction measured by differential scanning calorimetry has been reported to be 44.1 kJ/mol H_2, which is favorable for PEM Fuel Cell application. However, the relatively high activation energy (E_a= 102 kJ/mol) sets a kinetic barrier [84, 87].

Further efforts have been devoted to the composition adjustments for obtaining higher hydrogen capacities. Leng et al. reported that the $3Mg(NH_2)_2/8LiH$ mixture absorbed/desorbed reversibly 6.9 wt.% of hydrogen through the following reaction [Eq. (3-7)]:[95]

$$Mg(NH_2)_2 + \frac{8}{3}LiH \leftrightarrow \frac{4}{3}Li_2NH + \frac{1}{3}Mg_3N_2 + \frac{8}{3}H_2 \qquad (3\text{-}7)$$

When the molar ratio of $Mg(NH_2)_2$ to LiH was adjusted to 1:4, the hydrogen storage capacity of the mixture was increased to 9.1 wt.% H_2 as shown below [Eq. (3-8)]:[97]

$$Mg(NH_2)_2 + 4LiH \leftrightarrow \frac{4}{3}Li_3N + \frac{1}{3}Mg_3N_2 + 4H_2 \qquad (3\text{-}8)$$

It indicates that the composition changes can enhance the hydrogen-storage capacity of the Li-Mg-N-H system due to the change of dehydrogenation/hydrogenation reaction pathways.

Recently, a novel $LiNH_2/MgH_2$ system with a molar ratio of 1:1 attracted our attention due to its higher hydrogen capacity and improved thermodynamics. Alapati et al [103]. first predicted the thermodynamic feasibility of the following reaction by first-principles calculations based on density function theory (DFT) [Eq. (3-9)]:

$$LiNH_2 + MgH_2 \rightarrow LiMgN + 2H_2 \qquad (3\text{-}9)$$

The desorption enthalpy change calculated is 29.7 kJ/mol of H_2 at 0 K, which is an acceptable value for on-board hydrogen-storage applications. Further first-principles calculations showed that the reaction between $LiNH_2$ and MgH_2 at a molar ratio of 1:1 might be a multistep reaction as follows [Eq. (3-10)]:[104]

$$\begin{aligned}
&LiNH_2 + MgH_2 \rightarrow \frac{1}{2}Mg(NH_2)_2 + LiH + \frac{1}{2}MgH_2 \\
&\rightarrow LiH + \frac{1}{4}Mg(NH_2)_2 + \frac{1}{4}Mg_3H_2 + H_2 \\
&\rightarrow \frac{1}{2}LiH + \frac{1}{4}Li_2Mg(NH)_2 + \frac{1}{4}Mg_3H_2 + \frac{3}{2}H_2 \\
&\rightarrow LiMgN + 2H_2
\end{aligned} \qquad (3\text{-}10)$$

However, Osborn et al. found experimentally that the $LiNH_2/MgH_2$ (1:1) mixture milled for 3 h followed a new reaction pathways at 210°C instead of the originally predicted reactions in Equations (3-9) and (3-10), as described below [Eq. (3-11)]:[105]

$$LiNH_2 + MgH_2 \rightarrow \frac{1}{3} Li_2Mg_2(NH)_3 + \frac{1}{3} MgH_2 + \frac{1}{3} LiH + H_2 \qquad (3\text{-}11)$$

Although Lu et al [106]. reported that approximately 8.1 wt.% H_2, a theoretical value of hydrogen desorption for the reaction in Equation (3-9), was observed by means of thermo-gravimetric analysis (TGA) from the sample milled for 24 h, the effects of the co-product of NH_3 have not been eliminated, and hence the details of structural information of the solid products need to be further ascertained. Unlike the previous investigations, Liang et al. reported that four sequential reactions proceeded during 36 h of ball milling and the subsequent heating process for the $LiNH_2/MgH_2$ (1:1) mixture [Eq. (3-12)]:[107, 108]

$$\begin{aligned} & LiNH_2 + MgH_2 \xrightarrow{milled\ \ for\ \ 12h} \frac{1}{2} Mg(NH_2)_2 + LiH + \frac{1}{2} MgH_2 \\ & \xrightarrow{milled\ \ for\ \ 36h} LiH + \frac{1}{4} Mg(NH_2)_2 + \frac{1}{2} MgNH + \frac{1}{4} MgH_2 + \frac{1}{2} H_2 \\ & \xrightarrow{heated\ \ to\ \ 220^o C} \frac{1}{2} LiH + \frac{1}{4} Li_2Mg(NH)_2 + \frac{1}{2} MgNH + \frac{1}{4} MgH_2 + H_2 \\ & \xrightarrow{heated\ \ to\ \ 390^o C} \frac{1}{4} Mg_3N_2 + + \frac{1}{4} Li_2Mg(NH)_2 + \frac{1}{2} LiH + \frac{3}{2} H_2 \end{aligned} \qquad (3\text{-}12)$$

However, the ternary nitride product, LiMgN, which was predicted by Akbarzael et al. [104], has not been obtained even though the sample was heated up to 390°C. Therefore, the above theoretical and experimental findings have not reached an agreement on the dehydrogenation reaction pathways of $LiNH_2/MgH_2$ (1:1) system due to its complexity and sensitivity to experimental conditions, specifically ball milling conditions. Understanding the effects of experimental conditions will be critical for determining the reaction pathways.

4. Nanostructuring of solid state hydrides by mechanical milling

4-1. Thermodynamic and kinetic issues in solid state hydrides

Hydrogen storage in solid-state metal hydrides has been investigated extensively because, compared with other technologies such as gas compression or liquefaction, solid state materials can store hydrogen at relatively low pressures and ambient temperatures as mentioned earlier. Particular attention has focused on light element binary hydrides such as LiH and MgH_2 and complex metal hydrides such as $NaAlH_4$, $LiAlH_4$, $LiBH_4$ and $LiNH_2$ because high capacity storage can be achieved in these materials [1, 109]. However, there are problems with high thermodynamic stability and slow kinetics that must be addressed before light element hydrides can be used for on-board transportation applications as listed in Table 3-1. Specifically, in contrast to the delocalized metallic hydrides, the chemical bonds in light-element based hydrides are predominately covalent or ionic [109]. These bonds are often strong, resulting in unacceptably high thermodynamic stability and, consequently, low equilibrium hydrogen pressures. In addition, the high directionality of the covalent/ionic bonds in these systems leads to large activation barriers for atomic motion, resulting in slow hydrogen absorption/desorption kinetics and limited reversibility [109-110].

Two primary approaches are being used to address the thermodynamic constraints imposed by the high bond strengths in light-element based hydrides. The first focuses on the discovery of new single phase materials in which atomic substitution or alloying is used to decrease the thermodynamic stability. That work encompasses a wide range of ternary and quaternary compounds whose thermodynamic properties make them potentially acceptable as practical hydrogen storage media [93, 111]. The second approach utilizes existing binary and complex hydrides in combinations to form new compounds or alloys upon dehydrogenation [112-121]. This approach can lower the overall enthalpy for dehydrogenation, increase equilibrium hydrogen pressures and effectively destabilize the component hydrides. Although alloy formation in the dehydrogenated state can be used to reduce the overall reaction enthalpy, this approach does not remedy the problems of slow hydrogen exchange kinetics in light-element based hydrides.

To improve kinetic properties, a lot of efforts have been devoted to developing new strategies. Generally two approaches have been shown to be effective in improving kinetic properties on dehydrogenation/rehydrogenation reaction. The first approach involves addition of catalysts, which has dramatically improved the rates of hydrogen exchange in systems such as MgH_2 [45] and has enabled reversibility in $NaAlH_4$ [44]. The second approach is related to nanotechnology. Nano-structured materials have a lot of potentials in hydrogen storage because of their unique features such as adsorption on the surface, inter- and intragrain boundaries, and bulk absorption [1, 122, 123]. Nanostructured and nanoscale materials strongly influence the thermodynamics and kinetics of hydrogen absorption and desorption by increasing the diffusion rate as well as by decreasing the required diffusion length. Specially, in contrast to bulk materials, the nano-scale materials [124, 125] can offer several advantages for the physicochemical reactions, such as surface interactions, adsorption in addition to bulk absorption, rapid kinetics, low temperature desorption, hydrogen atom dissociation, and molecular diffusion via the surface. The intrinsically large surface areas and unique adsorbing properties of nano materials can assist the dissociation of gaseous hydrogen.

4-2. Nanostructuring of solid state hydrides

The nanostructuring process is one promising candidate of nano-technologies in the hydrogen storage. Nanostructured materials (also referred to as “nanocrystalline” or “nanophase” materials) are single-phase or multi-phase polycrystals with the grain sizes from a few nanometers to 100 nm in at least one dimension [1, 126]. Recently, researches have concentrated on nanocrystalline materials, which are expected to find applications based on their improved mechanical, magnetic, and other properties. In a powder form, nanostructured/nanocomposite means that each phase present in the individual powder particle is in the form of grains with nanometer size. One particle is one nano-polycrystal.

A schematic representation of a hard sphere model of an equiaxed nanostructured material formed by only one kind of atoms is showed in Fig. 4-1. Two types of atomic structures can be distinguished: the crystallites (atoms represented by open circles) and the boundary regions/intercrystalline regions (dark circles). The atomic structure of all crystallites is identical. The only difference between them is their crystallographic orientation. In the boundary regions, the average atomic density, interatomic spacing and the coordination between nearest neighbour atoms deviates from the ones in the crystallites and differs from region to region. The presence of these two structural constituents (crystallites and boundaries) of comparable volume fractions and with typical crystal sizes of a few nanometers is crucial for the properties of nanocrystalline materials. Generally nanostructuring by ball milling introduces a variety of defects, vacancies, dislocations, stacking faults besides the grains and grain boundaries.

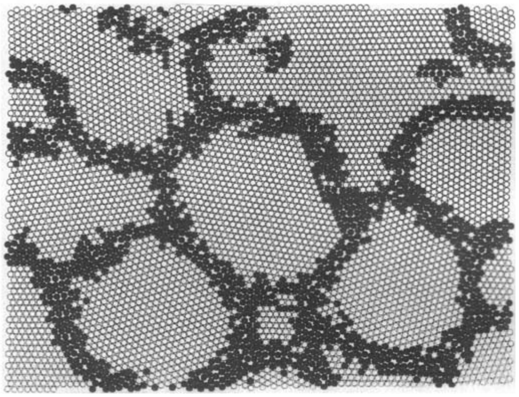

Fig. 4-1 Schematic representation of an equiaxed nanocrystalline material distinguishing between crystallite (open circles) and inter-crystalline regions (dark circles) [126]

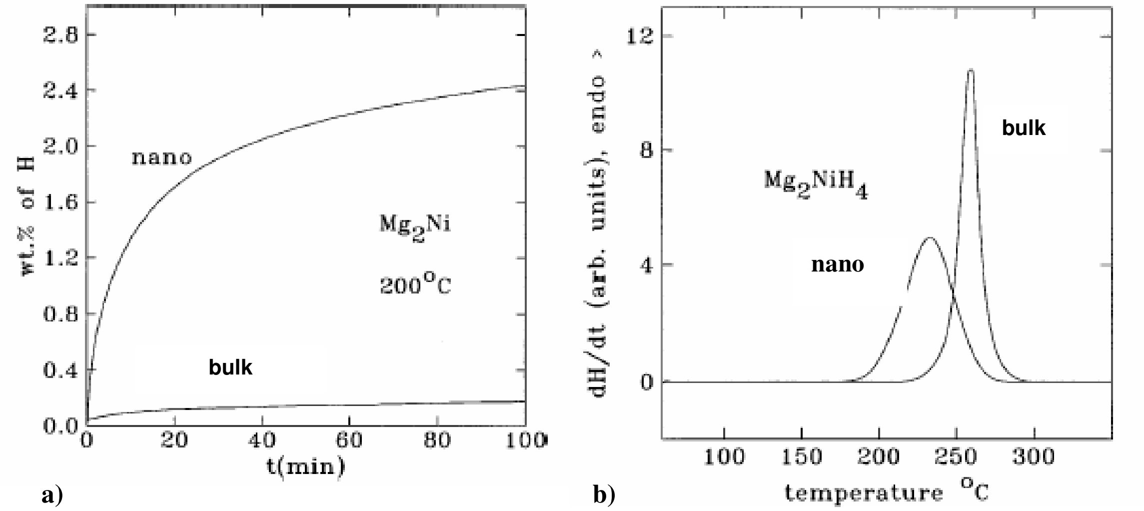

Fig. 4-2 Effect of nanostructuring of (a) hydrogen absorption and (b) desorption temperature of hydrogen [51]

These defects can raise the free energy of the system making it accessible to formation of thermodynamically metastable phases. Also, defects can lower the activation energy of reactions limited by poor kinetics [1]. Therefore, the nano-structured materials are the best and easiest solution to address both thermodynamic and kinetic problem in hydrogen storage. Numerous experiments indicate that in practically all solid state hydrides, the kinetics of both absorption and desorption can be improved by reducing the grain size of the compound [55]. An example for the improvement of absorption is shown in Fig. 4-2 (a) for Mg_2Ni. It can be seen that the bulk sample does not exhibit any significant hydrogen absorption at 200°C, whereas the nanocrystalline sample absorbs hydrogen relatively quickly. Fig. 4-2 (b) shows an example of the enhancement in hydrogen desorption for Mg_2NiH_4. A reduction in desorption temperature is found as the grain size of the hydride is brought to nanoscale. Zaluska et al. [127] reported the improvement of the reaction kinetics by mechanical milling in decomposition of $NaAlH_4$. Therefore, nanocrystalline materials have properties markedly different from their conventional crystalline counterparts and can be promising candidates for hydrogen storage in solid state hydrides.

4-3. Nanostructuring process

High-energy ball milling is the only nanotechnology top-down approach for the synthesis of nanoparticles. There are many different designs of ball mills, which can be used for processing of advanced materials. In conventional ball mills (planetary or shakers), the trajectories of grinding balls are rather chaotic (Fig. 4-3). This creates a continuous and erratic change of various mechanical modes of milling from shearing to impact during the same milling cycle. However, in the magneto-mill, Uni-Ball-Mill Model 5, the trajectories of the balls are controlled by the magnetic field created by strong FeNdB permanent magnet (Fig. 4-4). The milling mode can be then adjusted from shearing to impact by changing the angular position of the external magnets, as shown in Fig. 4-4.

Ball milling is a complex process which involves optimization of milling parameters to achieve the desired product microstructure and properties. The important parameters are [1]:

(1) Milling mode

(2) Number of balls used for milling

(3) Milling speed

(4) Milling time

(5) Milling atmosphere

(6) Ball-to-powder-ratio

(7) Working distance (WD)

The above process variables are not completely independent. For example, in Uni-Ball-Mill, the milling mode depends on milling speed and working distance. Also, milling time depends on milling mode and ball-to-powder-ratio.

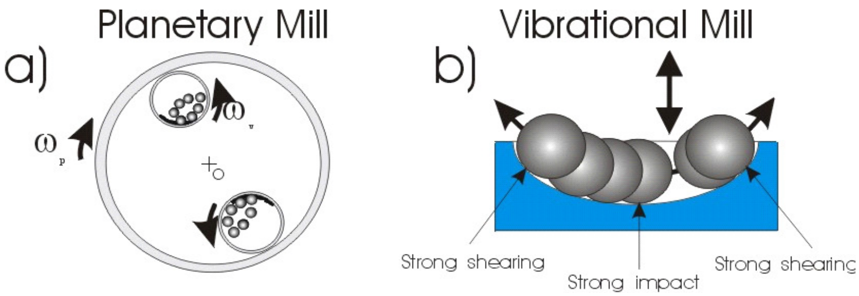

Fig. 4-3 Motion of balls in (a) a planetary and (b) a vibrational mill [1, 128]

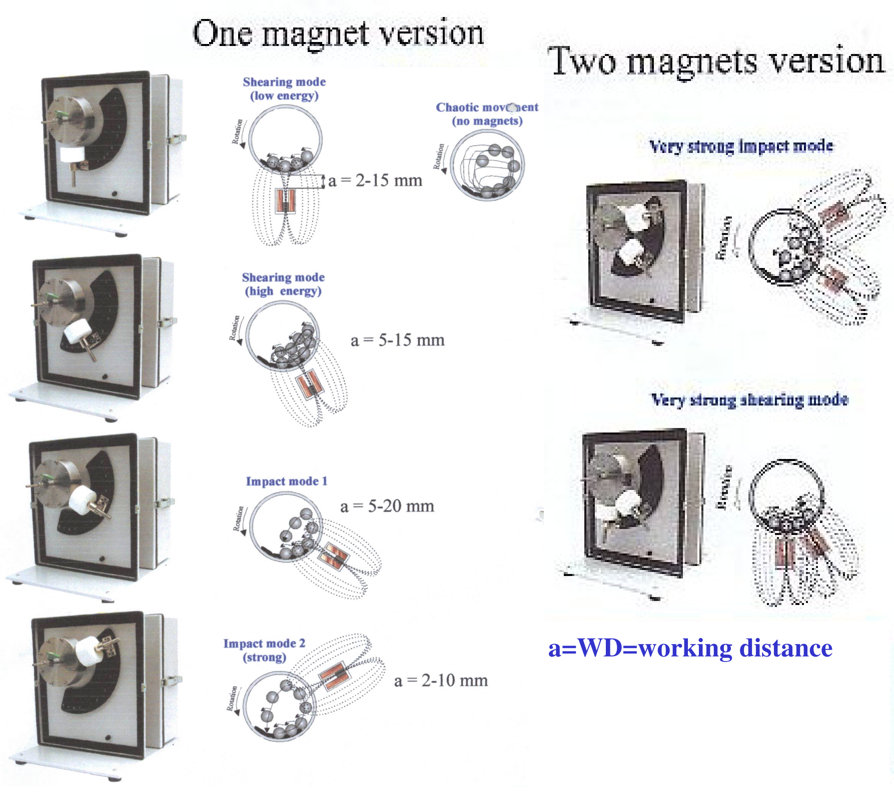

Fig. 4-4 Various controlled modes of milling available in the Uni-Ball-Mill 5 [1,129]

5. Objectives

In this thesis, nanostructured lithium complex hydrides are investigated to develop a breakthrough material in the field of solid-state hydrogen storage. The primary motivation for studying Li complex hydrides is their potential ability to store large amounts of hydrogen. However, there are still thermodynamic and kinetic barriers to the practical utilization of these materials. To address two critical barriers, the present study investigates the dependence of the thermodynamic and kinetic properties of Li complex hydrides on their chemical composition and degree of mechanical activation.

To accomplish these objectives, the goal of each topic is outlined as follows.

5-1. Nanostructured lithium amide and lithium hydride system

5-1-1. Nanostructured ($LiNH_2$+LiH) mixture

In this study, the effect of ball milling and different molar ratios of constituents $LiHN_2$ and LiH in the mixture are investigated systematically to explore the role of nanostructure and the influence of chemical composition on hydrogen desorption properties. In particular, the role of LiH is studied in detail to understand the desorption behavior of the mixture. The relationship between the release of NH_3 and the partial contamination of LiH is also demonstrated and discussed.

5-1-2. Nanostructured Li-N-C-H system

In the ($LiNH_2$+LiH) mixture, LiH does not fully react with $LiNH_2$ because part of the LiH becomes inactive, due to hydrolysis/oxidation. Thus, a large amount of NH_3 is emitted, and hydrogen capacity is lost. This study focuses on two approaches employed to solve the problems mentioned above:

1) The substitution of LiH by graphite in the reaction $2LiNH_2+C \rightarrow Li_2CN_2+2H_2$, proposed by the theoretical model, is clarified and discussed.

2) The ($LiNH_2$+LiH) mixture with 5 wt. % graphite and the mechanism by which it prevents LiH from oxidation/hydrolysis and thus mitigates the escape of NH_3 are investigated.

3) The equilibrium plateau pressure is investigated; moreover, the enthalpy change of the dehydrogenation reaction is estimated from the Van't Hoff equation to understand the hydrogen storage properties of the ($LiNH_2$+LiH) mixture with and without graphite.

5-2. Nanostructured lithium amide and magnesium hydride system

5-2-1. Nanostructured ($LiNH_2$+nMgH_2) (n=0.55, 0.60, and 0.70) mixtures

Research in this phase focuses on investigating the thermodynamic and kinetic properties of ($LiNH_2$+nMgH_2) (n=0.55, 0.60, and 0.70) mixtures:

1) The equilibrium plateau pressure as a function of temperature is investigated; moreover, the enthalpy change of the dehydrogenation reaction is also estimated from the Van't Hoff equation and compared with the ($LiNH_2$+LiH) system.

2) The role of nanostructure and the influence of chemical composition on hydrogen desorption properties are systematically investigated by comparing the apparent activation energies as functions of the molar ratio of $MgH_2/LiNH_2$ and the degree of mechanical activation.

3) Reversibility and reaction pathways at various temperatures are explored.

4) Catalytic effects are studied by comparing the kinetic properties of the desorption reactions.

5-2-2. Nanostructured ($LiNH_2$+nMgH_2) (n=1.0 and 1.5) mixtures

The molar ratios of MgH_2/$LiNH_2$ are increased further to 1.0 and 1.5 to increase the hydrogen storage capacity because it has been reported that composition changes can enhance the hydrogen storage capacity by changing the dehydrogenation/hydrogenation reaction pathways. Furthermore, investigations of the ball-milled $LiNH_2$-MgH_2 (1:1) mixture by several research groups have shown different dehydrogenation processes. Therefore, the main motivation is to understand the underlying mechanisms of the chemical reaction between $LiNH_2$ and MgH_2 with the two different molar ratios of 1:1 and 1:1.5:

1) Hydrogen loss and phase changes during ball milling are investigated as a function of milling time and milling mode.

2) The correlation between mechanical ball milling and the dehydrogenation reactions of the $LiNH_2$/MgH_2 (1:1 and 1:1.5) mixtures is studied.

3) Reversibility and reaction pathways are explored at various temperatures.

4) The effect of chemical composition on the kinetic properties is understood by comparing the apparent activation energies of the two compounds.

6. Experimental

6-1. Materials

6-1-1. Starting hydrides

95% pure lithium amide($LiNH_2$) and 95% pure lithium hydride (LiH) and 98% pure magnesium hydride (MgH_2) from ABCR GmbH & Co.KG from were used in this thesis.

6-1-2. Catalysts

A synthetic graphite (G) powder (particle size <20 μm) from Sigma-Aldrich and carbon black produced as experimental batches from Columbian Chemical company were added in Li-N-H systems. Nanometric Ni (n-Ni, $60.46 m^2/g$) produced as experimental batches by Vale Inco Ltd., 99.99% pure and ultra dry manganese(II) chloride ($MnCl_2$) from Alfa Aesar were used for catalysts for Li-N-Mg-H systems.

6-2. Synthesis of nanostructure hydrides

6-2-1. Chemical compositions

In the Li-N-H system, the mixtures of $LiNH_2$:LiH having the molar ratio 1:1, 1:1.2 and 1:1.4 were investigated. In the Li-N-C-H system, the following combinations of starting materials were used:

(1) The mixtures of $LiNH_2$:C (graphite or carbon black) having the molar ratio 2:1

(2) The mixture of {($LiNH_2$+1.2LiH)+5wt.% Graphite}

In the Li-N-Mg-H system, the following combinations of starting materials were used:

(1) The mixtures of ($LiNH_2$+nMgH_2) (n=0.55, 0.60, 0.70, 1.00 and 1.50)

(2) The mixtures of ($LiNH_2$+nMgH_2)(n=0.55 and 0.70) with 5wt.% n-Ni

(3) The mixture of {($LiNH_2$+0.70MgH_2) with 5wt.% $MnCl_2$}

6-2-2. Milling procedure

Syntheses of nanostructured hydrides were implemented by controlled mechanical milling (CMM) in the magneto-mill, Uni-Ball-Mill 5 manufactured by A.O.C. Scientific Engineering Pty Ltd, Australia [1, 129]. In this particular ball mill the milling modes with varying milling energy can be achieved by using one or two strong NdFeB magnets, changing their angular positions and changing the number of hard steel balls (25mm in diameter each) in a milling vial. Fig. A-1 shows a set up for a strong impact mode with two magnets positioned at 6 and 7 o'clock, at the distance of ~10 and ~2 mm, respectively, from the milling vial (working distance – WD) and 4 hard steel balls in the vial (referred to hereafter as an IMP67), while a set up for a low energy impact mode with one magnet positioned at 6 o'clock at the distance of ~10mm from the milling vial and 2, 3 or 4 hard steel balls in the vial referred to LES6-2B, LES6-3B or LES6-4B, respectively.

The ball-to-powder weight ratio (R) was ~40 and the rotational speed of milling vial was ~200 rpm. After loading with powder, an air-tight milling vial with an O-ring, equipped with a pressure valve mounted in the lid, was always first evacuated and then purged several times with ultra-high purity argon (Ar) gas (99.999% purity) before final pressurization with H_2. The pressure of high purity hydrogen (purity 99.999%: O_2< 2 ppm; H_2O< 3 ppm; CO_2< 1 ppm; N_2< 6 ppm; CO< 1 ppm; THC< 1 ppm) in the vial was always kept constant at ~ 600 kPa during the entire milling process. Through the entire milling process the milling vial was continuously cooled with an air fan. All the powder handlings before and after milling were performed in a purged glove box under overpressure of high purity argon (purity 99.999%) in order to minimize any possible contamination by moisture or oxygen from air. Additionally, pressure drops during milling were recorded to estimate the amount of hydrogen loss. A volumetric method was used to calculate the amount of hydrogen absorbed during milling. The details of calculation are given in Appendix A-2. The composition of powders and the processing parameters applied during controlled milling are summarized in Table 6-1.

Table 6-1 Composition of powders and Milling parameters

System	Composition	Milling mode	Ball to Powder ratio	# of Balls	Milling Time (h)
Li-N-H	$LiNH_2$+1.0LiH	IMP67	40	4	1, 5, 10, 25, 50,100
	$LiNH_2$+1.2LiH	IMP67	40	4	25
	$LiNH_2$+1.4LiH	IMP67	40	4	25
Li-N-C-H	2$LiNH_2$+C (C: graphite or carbon black)	IMP67	40	4	25
	{($LiNH_2$+1.2LiH) +5wt.% G} (G: graphite)	IMP67	40	4	25
Li-N-Mg-H	($LiNH_2$+nMgH_2) (n=0.55, 0.60 and 0.70)	IMP67	40	4	0.5, 1, 5, 10, 25
	{($LiNH_2$+nMgH_2) +5wt.% n-Ni or $MnCl_2$} (n=0.55 and 0.70)	IMP67	40	4	0.5, 1, 5, 10, 25
	($LiNH_2$+nMgH_2) (n=1.0 and 1.5)	IMP67	40	4	0.5, 1, 5, 10, 25
		LES6	40	2,3,4	0.5, 1, 5, 10, 25

6-3. Analysis of powder morphology

6-3-1. X-Ray diffraction

The crystal structure of powders was characterized with a Bruker D8 powder diffractometer using monochromated CuKα_1 radiation at an accelerating voltage of 40 kV and a current of 30 mA. One powder sample was simply placed on an aluminum substrate and sealed with a Mylar tape to prevent contact with air during XRD scans. However, since Mylar tape gives a diffuse peak around 2θ=27° which superimposes a graphite peak, we decided to use a home-made environmental brass holder with a Cu plate for powder support which was loaded in a glove box filled with Ar. One powder sample was simply placed on an aluminum substrate and sealed with a Mylar tape to prevent contact with air during XRD scans. However, since Mylar tape gives a diffuse peak around 2θ=27° which superimposes a graphite peak, we decided to use a home-made environmental brass holder with a Cu plate for powder support which was loaded in a glove box filled with Ar. Upper and lower part of the environmental holder is sealed through a soft-rubber O-ring and tightened using threaded steel bolts with nuts. The scan range was from 2θ = 10° to 90° and the rate was 1.2° min^{-1} with a step size of 0.02°. The nanograin size of phases was calculated from the broadening of their respective X-ray diffraction peaks. Since the Bragg peak broadening in an XRD patterns is due to a combination of grain size and lattice strains, it is customary to use computing techniques by means of which one can separate these two factors. The separation of crystallite size and strain was obtained from a Cauchy/Gaussian approximation by a linear regression plot according to the following equation [130]:

$$\frac{\delta^2(2\theta)}{\tan^2\theta} = \frac{K\lambda}{L}\left(\frac{\delta(2\theta)}{\tan\theta\ \sin\theta}\right) + 16e^2 \qquad (6-1)$$

where the term *K λ/L* is the slope, the parameter L is the mean dimension of the crystallite, K is a constant (≈1) and e is the so-called 'maximum' micro-strain (calculated from the intercept), λ is the wavelength and θ is the position of the analyzed peak maximum. The term $\delta(2\theta) = B\left(1 - \frac{b^2}{B^2}\right)$ (rad) is the instrumental broadening-corrected "pure" XRD peak profile breadth, where B and b are the breaths in radians of the same Bragg peak from the XRD scans of the experimental and reference powder, respectively. They were automatically calculated by the diffractometer software from the full width at half maximum, FWHM. The powder of the LaB_6 compound, the National Institute of Standards and Technology (NIST) standard reference materials (SRM) 660, was used as a reference for subtracting the instrumental broadening.

6-3-2. FT-IR

The Fourier transform infrared spectroscopy (FT-IR) measurements were performed with a Bruker Tensor 27 at room temperature in the range of 4000-400cm^{-1} to characterize the $LiNH_2$, Li_2NH, $Mg(NH_2)_2$, MgNH, and $Li_2Mg(NH)_2$ phases. The powder samples were ground with KBr and pressed into pellets.

6-3-3. Scanning Electron Microscopy

The analysis of powder morphology was performed with FESEM (LEO 1530) equipped with integrated EDAX (Pegasus 1200 EDS/OIM) and the back-scattered electron mode was used.

6-3-4. BET

The specific surface area (SSA) of powder before and after ball milling was determined through nitrogen adsorption at 77K based on the Brunauer-Emmett-Teller (BET) method using the surface area and pore size analyzer from Quantachrome Corporation (AUTOSORB-1). The measurements were performed after a degassing treatment at room temperature. The reported SSA data were calculated based on 5 points BET method.

6-4. Thermal analysis and hydrogen storage properties

6-4-1. Differential Scanning Calorimeter

The thermal behavior of powders was studied by differential scanning calorimetry (DSC) (Netzsch 404) of ~5 mg samples in an alumina crucible. Samples were heated to 500°C at a heating rate of 5, 10 and 15°C/min in Ar atmosphere to estimate the activation energy by using the Kissinger equation [1]:

$$\frac{d\ln\left(\frac{\beta}{T_p^2}\right)}{d\left(\frac{1}{T_p}\right)} = -\frac{E_A}{R} \qquad (6\text{-}2)$$

where β is the heating rate, T_p is the peak temperature, E_A is the apparent activation energy, and R is the gas constant.

6-4-2. Thermogravimetric analysis

The thermal weight loss (TGA) was analyzed with a TA INSTRUMENT Q600, which also contains a DSC option, using a 5 mg sample heated at 10°C/min under 100 ml/min Ar gas flow.

6-4-3. Gas analysis

Temperature programmed desorption (TPD) studies were carried out with a HTP1-S Hiden Isochema volumetric analyzer equipped with a mass spectrometer.

6-4-4. Hydrogen storage properties

The hydrogen desorption/absorption was evaluated using a second generation volumetric Sieverts-type apparatus custom-built by A.O.C. Scientific Engineering Pty Ltd., Australia as shown in Fig. 6-1. This apparatus built entirely of austenitic stainless steel allows loading of a powder sample in a glove box under argon and its subsequent transfer to the main unit in a sealed austenitic stainless steel sample reactor without any exposure to the environment. The weight of the powder sample in the desorption experiments was in the range of 20-30 mg. The calibrated accuracy of desorbed hydrogen capacity is about ±0.1 wt.% H_2 and that of temperature reading ±0.1°C. Before starting the desorption test, the inner tubing of the apparatus and reactor were evacuated and purged 4 times with argon and then two times with hydrogen. The furnace of the apparatus was heated separately to the desired test temperature and subsequently inserted onto a tightly sealed powder sample reactor inside which a pressure of 1 bar H_2 was kept. Hence, the beginning of the desorption test was in reality pseudo-isothermal before the powder sample temperature reached the desired value.

However, the calibrated time interval within which the powder sample in the reactor reaches the furnace temperature is ~400-600 s in the 100-350°C range, which is negligible compared to the desorption completion time especially at temperatures below 200°C. Therefore, one can consider the test as being "isothermal" for any practical purposes at this range of temperatures. After desorption the powder without removal from the reactor was subjected to absorption at pre-selected temperature and pressure. The amount of desorbed/absorbed hydrogen was calculated from the ideal gas law as described in detail in Appendix A-3 [1]. Hydrogen desorption curves were also corrected for the hydrogen gas expansion due to the increase in temperature. The amount of desorbed/absorbed H_2 expressed in wt.% is calculated with respect to a total weight of powder including the additives.

Equilibrium plateau pressures at various temperatures were obtained in our Sieverts-type apparatus by a step-wise method by increasing pressure at a constant temperature until equilibrium was established. The enthalpy change of the dehydrogenation reaction was estimated from the Van't Hoff equation [1] as mentioned in Chapter 3-1-4.

The apparent activation energy for desorption process was estimated from the obtained volumetric desorption curves at corresponding temperatures using the Arrhenius plot of *k* values with temperature [1]:

$$k = k_o e^{-E_A / RT} \qquad (6\text{-}3)$$

where E_A is the apparent activation energy, *R* is the gas constant and *T* is the temperature. The rate constant *k* was determined using the Johnson-Mehl-Avrami-Kolmogorov (JMAK) equation [1]:

$$\alpha = 1 - e^{-(k \cdot t)^{\eta}} \qquad (6\text{-}4)$$

where η is the reaction exponent (the Avrami exponent) related to the transformation mechanism, taken as a free value characteristic for each individual temperature [1] rather than a fixed value for all temperatures, and α is the desorption fraction at time t.

Fig. 6-1 A Sieverts-type apparatus custom-built by A.O.C. Scientific Engineering Pty Ltd., Australia, for evaluating hydrogen storage properties

7. Nano-structured ($LiNH_2$+LiH) systems

7-1. Effect of milling on the microstructure of hydride mixtures

Fig. 7-1 shows the evolution of the morphology of the $LiNH_2$-LiH mixture with a molar ratio of 1:1 with milling time. After 1 h of ball milling, the particles have a non-uniform particle size distribution with small and large particle populations. However, after 5 h of milling, the population of large particles is substantially reduced. After milling for 50 and 100 h, an agglomeration of smaller particles into larger aggregates becomes more pronounced (Fig. 7-1 e) and f)).

Fig. 7-2 a) shows the XRD profiles of the as-received $LiNH_2$ and LiH and their 1:1 molar ratio mixture before and after ball milling for 1 and 5 h. XRD testing was performed shortly after the milling processing was terminated. According to JCPDS file No. 09-0189 and No. 85-1327 for LiH and Al, respectively, the diffraction peaks of LiH and Al overlap except for two peaks at $2\Theta=64.2$ and 77.5° for LiH. Therefore, these peaks are assumed to be indicators of the presence of the LiH phase in the mixture. As-received LiH powder contains LiOH, whereas $LiNH_2$ contains both Li_2O and LiOH. Because the powders were packed into the environmental holder, Li_2O and LiOH are probably inherent impurities of the as-received materials. No other phases are present. Therefore, both constituents remain separated in the ($LiNH_2$+LiH) mixture and do not react with each other during ball milling.

The grain sizes and lattice strains of $LiNH_2$ and LiH after milling were estimated from XRD patterns in Fig. 7-2 a), and the results are summarized in Table 7-1 and Fig. 7-2 b). It can be seen that the crystallite size of $LiNH_2$ and LiH decreases to 10 nm after ball milling for 100 h, and the lattice strains are negligible.

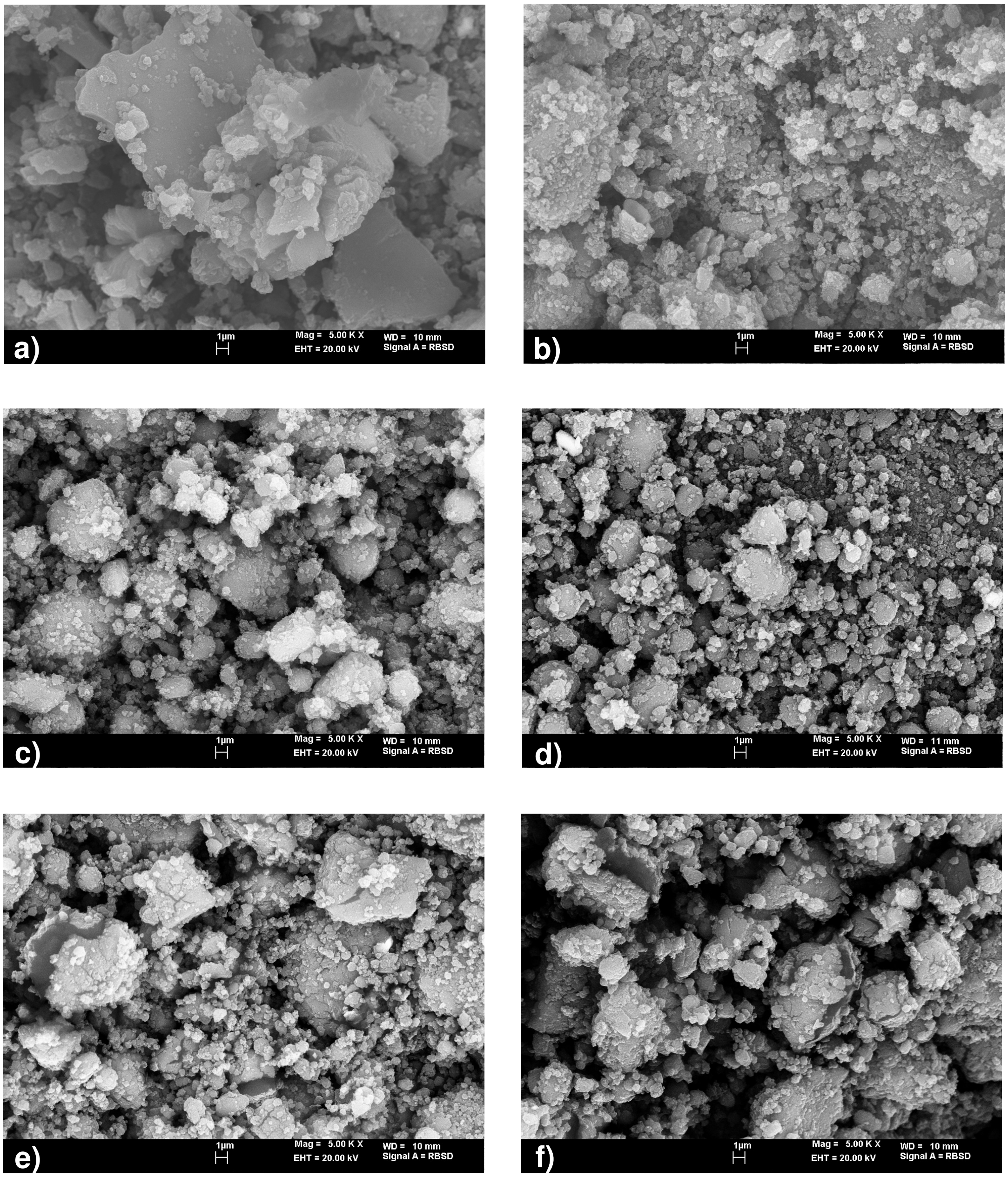

Fig. 7-1 The evolution of the morphology of the (LiH+$LiNH_2$) mixture milled for a) 1 h, b) 5 h, c) 10 h, d) 25 h, e) 50 h and f) 100 h

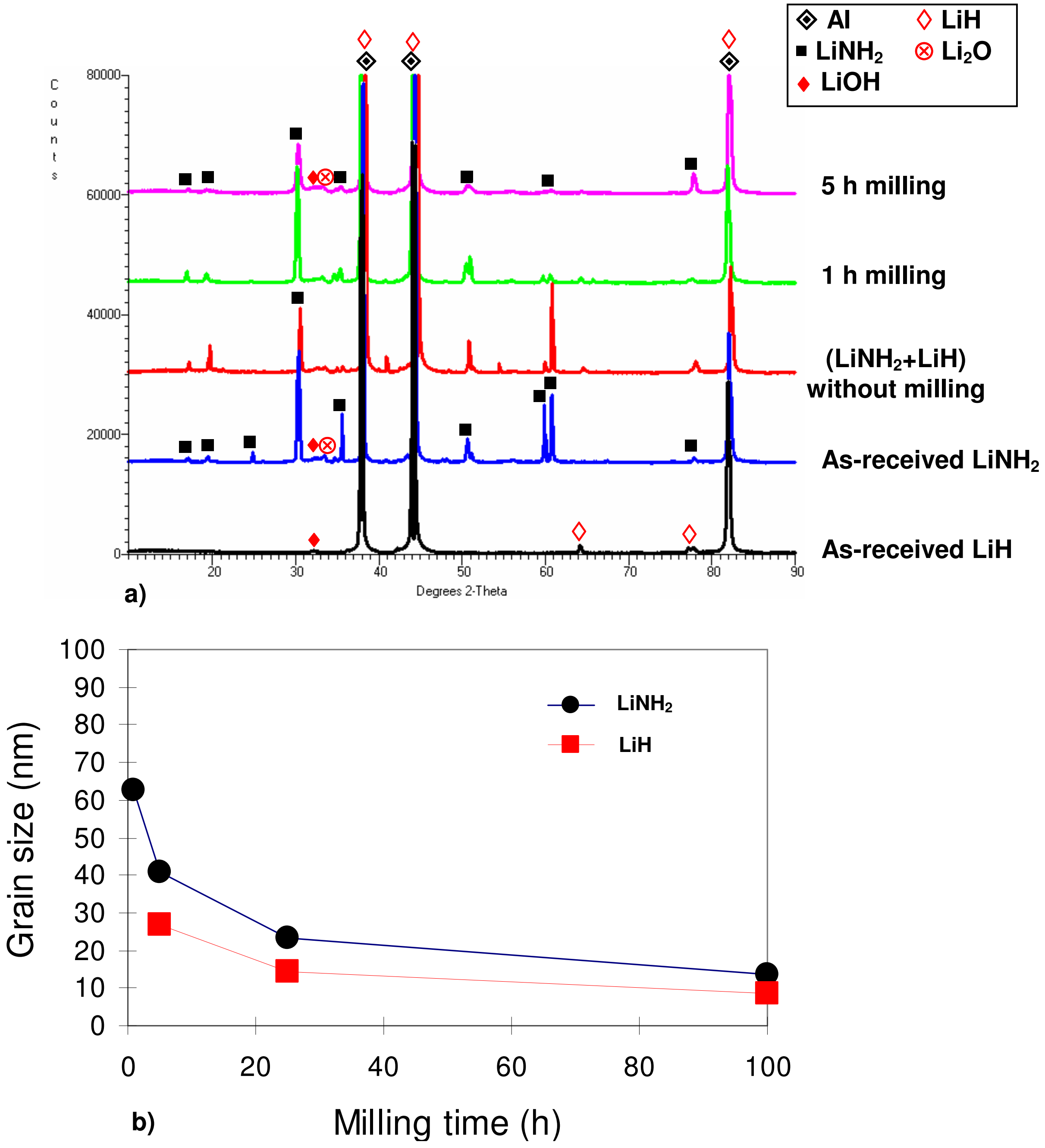

Fig. 7-2 X-ray diffraction patterns of a) as-received LiH, LiNH$_2$ and their 1:1 molar ratio mixture before and after milling for 1 and 5 h. b) The crystallite sizes of LiNH$_2$ and LiH in the 1:1 molar ratio mixture as a function of milling time

Fig. 7-3 shows the specific surface area (SSA) measured from the BET method. It is noticeable that there is a sharp increase in the specific surface area after 5 h of the ball milling. The maximum specific surface area is almost 60 m^2/g after 25 h milling but afterwards the SSA slightly decreases most likely due to the agglomeration occurring for longer milling times (Fig. 7-1 e) and f)).

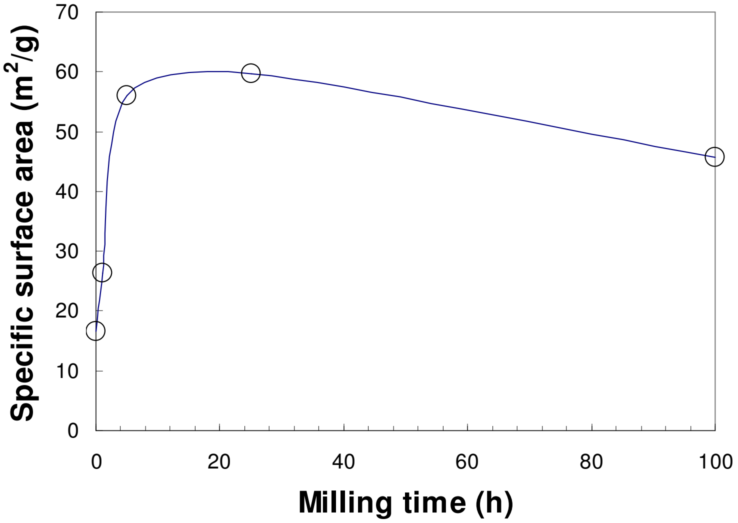

Fig. 7-3 Specific surface area (SSA) of the ($LiNH_2$+LiH) powder mixture vs. milling time

Table 7-1. Powder characteristics of the 1:1 molar ratio mixture of ($LiNH_2$+LiH) as a function of ball milling time

Milling time (h)	Grain size $LiNH_2$/LiH (nm)	Lattice strain $LiNH_2$/LiH	BET specific surface area (m^2/g)
0	> 100*)	0*)	16.5
1	63/NA*)	0/NA*)	26.4
5	41/27	$5.68\times10^{-3}/1.14\times10^{-3}$	56.0
25	23/14	$4.62\times10^{-3}/0$	59.6
100	14/9	$1.77\times10^{-3}/0$	45.6

Note: *)Measured with a Bruker D8-Advantage powder diffractometer; other grain sizes and internal strains were measured with a Rigaku Rotaflex D/Max B rotating anode powder diffractometer

7-2. Thermal behavior of $LiNH_2$

All thermal tests were carried out almost immediately after the termination of ball milling; therefore, the samples were not stored under a protective gas for an excessive period of time. The XRD patterns of samples, which were stored for 3 months under high-purity argon (purity 99.999%), revealed that a fraction of LiH transformed into LiOH, even under such "clean" storage conditions. TGA and DSC profiles are shown in Fig. 7-4 a) and b), respectively, for single-phase $LiNH_2$ before and after 25 h of ball milling. The DSC profile shows a single endothermic peak that corresponds to the melting of $LiNH_2$ at approximately 380°C independently of the degree of mechanical activation by ball milling. Ball milling does not seem to change the character of thermal behavior of $LiNH_2$. It is well-known that a single-phase $LiNH_2$ decomposes through the release of only the ammonia gas (NH_3) [1, 59]. The TGA curve in Fig. 7-4 a) shows that NH_3 is released more slowly when $LiNH_2$ is in the solid state and more rapidly from liquid $LiNH_2$. Assuming that the release of NH_3 begins when the TGA curve starts deviating from linearity, one can estimate that the TGA onset temperature for the release of NH_3 is 150 and 80°C for $LiNH_2$ before and after milling, respectively. From the change in the slope of the TGA curves in Fig. 7-4 a), one can estimate the weight loss that corresponds to the amount of NH_3 when $LiNH_2$ is either solid or liquid as shown in Table 7-2. It can be seen that the as-received $LiNH_2$ releases 8.4 wt.% and 25.7 wt.% NH_3 from the solid and liquid phases, respectively. In turn, the milled powder releases 10.7 wt.% and 22.9 wt.% NH_3 from the solid and liquid phases, respectively. Thus, ball milling slightly enhances the NH_3 release from solid $LiNH_2$. Within the experimental error, the total amount of NH_3 released in Fig. 7-4 a) is in a good agreement with the theoretical value of 37 wt.% NH_3 released through the reaction (3-3).

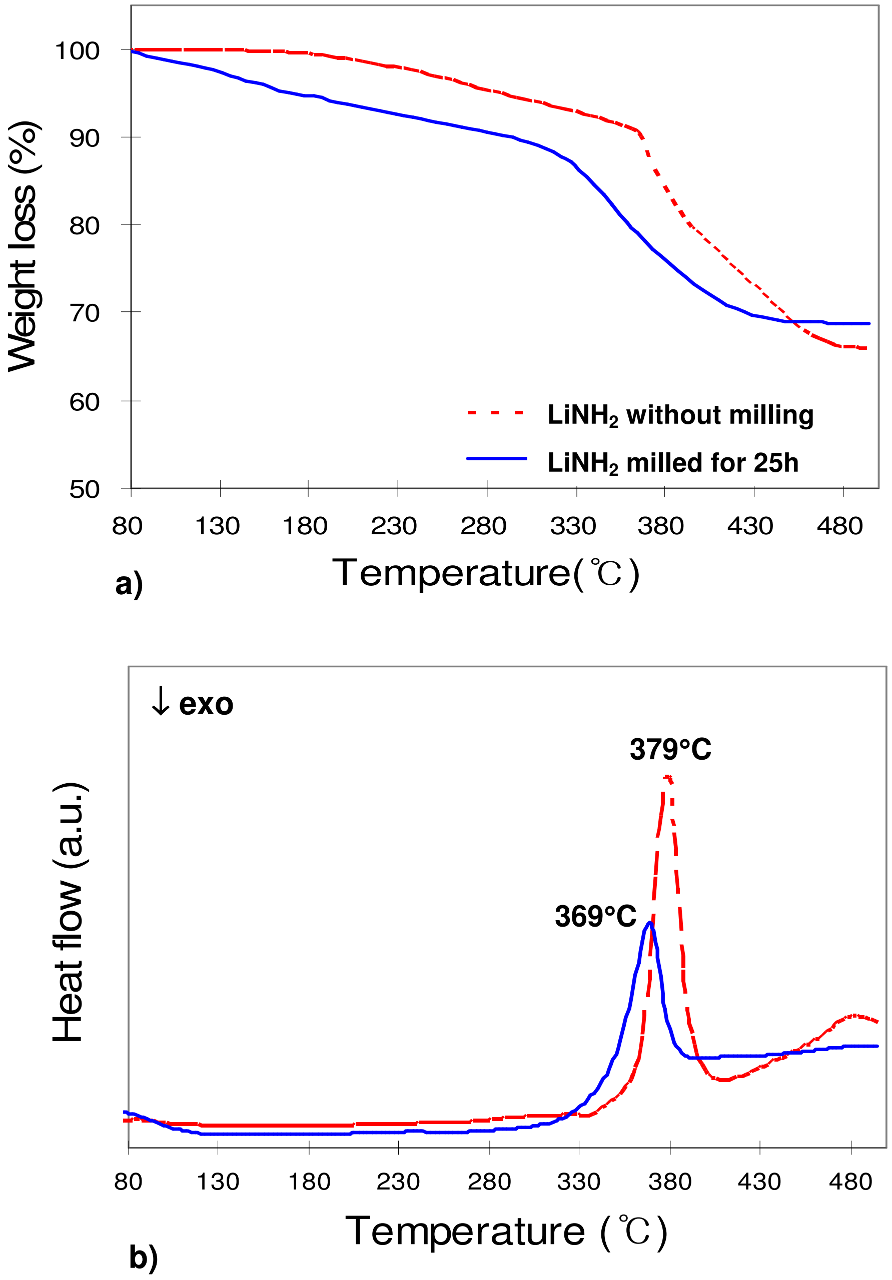

Fig. 7-4 The desorption behavior of single-phase LiNH$_2$ before and after ball milling for 25 h: a) TGA and b) DSC profiles (TA Q600 apparatus)

Table 7-2. The amount of NH_3 released from single-phase $LiNH_2$ before and after milling and approximate onset temperatures of the NH_3 release as estimated from TGA

	The amount of NH_3 released from a single phase $LiNH_2$			
	Solid state (wt.% NH_3)	**Liquid state (wt.% NH_3)**	**Onset temp. (^{o}C)**	**Peak temp. (^{o}C)**
Before milling	~8.4	~25.7	150	379
After milling for 25 h	~10.7	~22.9	80	369

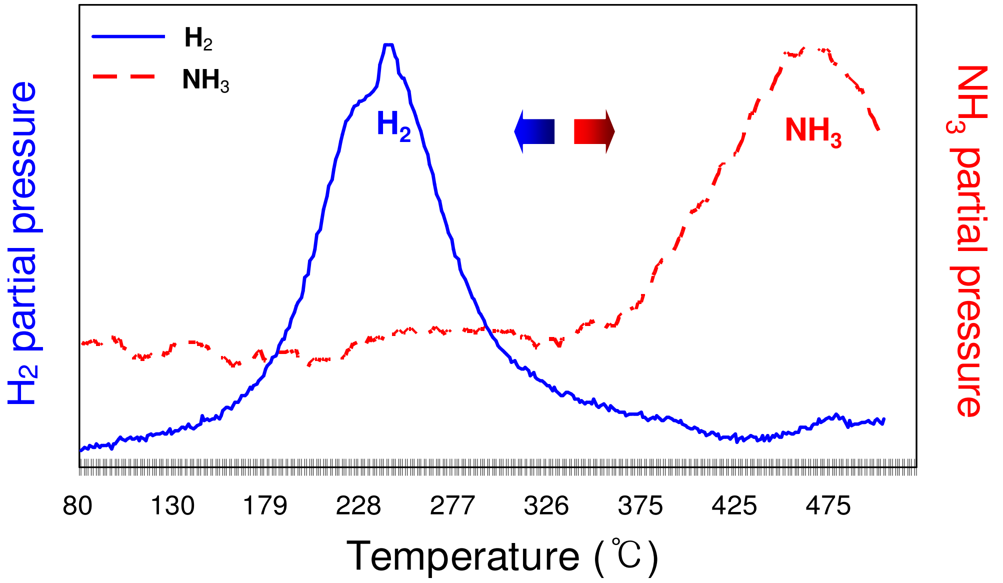

Fig. 7-5 TPD spectra for the 1:1 molar ratio mixture

7-3. Thermal behavior of the ($LiNH_2$+LiH) system

To determine the temperature range for the release of hydrogen and ammonia, a TPD test was performed for the 1:1 molar ratio mixture $LiNH_2$:LiH milled for 25 h, and the result is presented in Fig. 7-5. The majority of hydrogen is released up to ~320°C while there is no measurable release of ammonia at this temperature range from the unreacted $LiNH_2$ in the mixture. Ammonia from the latter is predominantly released when the temperature exceeds 375°C.

Since the hydrogen desorption peak is separated from the ammonia peak, its behavior can be easily analyzed in a DSC. Fig. 7-6 a) and b) show the dependence of DSC curves on the milling time for the 1:1 molar ratio of the $LiNH_2$:LiH mixture and the molar ratio for a milling time of 25 h, respectively. Table 7-3 summarizes the onset and peak temperatures of the hydrogen desorption peak for each DSC curve.

As can be seen in Fig. 7-6 a), the as-received 1:1 molar ratio $LiNH_2$:LiH mixture has two endothermic peaks at temperatures below 400°C. The first broad peak at about 325°C is related to reaction (3-2) in which hydrogen is released, and the second sharp peak at around 370°C results from the melting of the unreacted $LiNH_2$ in the mixture and the release of ammonia. However, all powders processed by ball milling exhibit only a single endothermic reaction peak in this temperature range. The melting peak of unreacted $LiNH_2$ disappears for the mixtures ball milled for even 1 h, which indicates that most of the $LiNH_2$ has reacted with LiH in a DSC test below the melting temperature of $LiNH_2$. Furthermore, the endothermic peak of reaction (3-2) is reduced from 325 for the unmilled 1$LiNH_2$:1LiH mixture to 235°C after milling for 25 h. The onset temperature also decreases from 268 for the unmilled 1$LiNH_2$:1LiH mixture to 180-186°C after ball milling for 25 to 100 h.

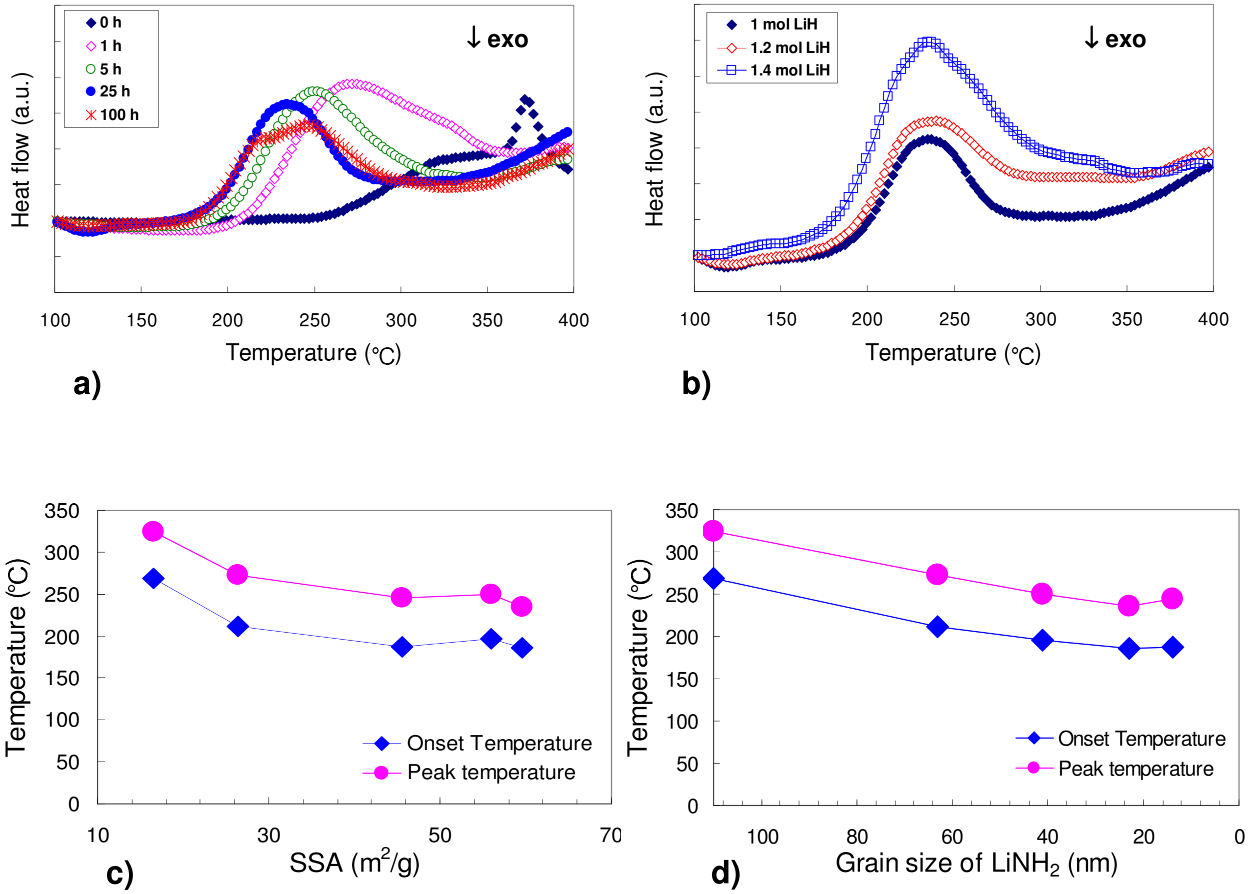

Fig. 7-6 DSC profiles for a) various milling times for the 1:1 molar ratio mixture $LiNH_2$:LiH and b) the molar ratio of LiH to $LiNH_2$ in the mixture milled for 25 h (heating rate of 10°C/min) (Netzsch 404 apparatus). c) the onset and peak temperature of reaction (3-2) vs. the SSA of powder mixture and d) the grain size of $LiNH_2$ in the 1:1 molar ratio mixture

Table 7-3. Summary of the DSC results for the ($LiNH_2$+LiH) mixture with various molar ratios of constituents

Milling time (h)	Molar ratio ($LiNH_2$:LiH)	DSC peaks (℃)	
		T_{ON}	T_{peak}
0	1:1	268.0	324.7 ($LiNH_2$ melting peak 371.6)
1		212.0	272.5
5		196.2	250.2
25	1:1	186.0	235.2
	1:1.2	183.4	239.2
	1:1.4	180.3	234.1
100	1:1	187.2	245.0

In Fig. 7-6 a), it is also evident that the DSC peak broadening is reduced as the milling time increases up to 25 h, but, after 100 h of milling, this peak becomes broader than that observed after 25 h. It is likely that this effect is related to the pronounced powder particle agglomeration process that occurs for a milling time of 100 h as already shown in Fig. 7-1 e) and f).

As can be seen in Fig. 7-6 b) and especially Table 7-3, for the mixtures milled for a constant time of 25 h, the increasing molar ratio of $LiNH_2$/LiH does not measurably affect the peak position of reaction (3-2) but slightly reduces its onset temperature. As shown in Fig. 7-6 c), the onset and peak temperature of reaction (3-2) for the 1:1 molar ratio mixture decreases as the SSA of the powder mixture increases up to about 45 m^2/g (100 h milling), then reaches saturation and again slightly decreases at larger values of SSA. As shown in Fig. 7-6 d), both the onset and peak temperature of reaction (3-2) decrease monotonically with decreasing $LiNH_2$ grain size to about 23 nm (Table 7-1; 25 h milling), and, subsequently, both slightly increase as the grain size of $LiNH_2$ further decreases to 14 nm. Table 7-1 shows that the grain size of LiH in the mixture decreases proportionally to the grain size of $LiNH_2$; therefore, a similar dependence to that in Fig. 7-6 d) is also found for the grain size of LiH. The simultaneous decrease of the grain size of $LiNH_2$ with increasing SSA (Table 7-1 and 7-3) makes it difficult to unambiguously establish which of these two factors is responsible for the observed reduction of the peak temperature of reaction (3-2) in Fig. 7-6 b) and c). Nevertheless, the onset/peak temperature's decrease with increasing SSA observed in Fig. 7-6 c) and increase for the smallest grain size of $LiNH_2$/LiH observed in Fig. 7-6 d) indicate that the controlling factor in the reduction of the reaction (3-2) peak temperature is probably SSA rather than the grain size of the constituents in the ($LiNH_2$+LiH) mixture. Otherwise, it would be difficult to justify the behavior observed in Fig. 7-6 d).

The results of this study can be compared with those obtained for hollow nanospheres [64]. The hollow nanospheres have an SSA of 79.4 m^2/g and had lowered desorption onset and peak temperatures of 179 and 230°C, respectively. From Tables 7-1 and 7-3, a similar reduction of the desorption temperature of the ($LiNH_2$+LiH) expressed by reaction (3-2) can be achieved by ball milling for 5-25 h, which brings about a profound reduction of SSA to 60 m^2/g. Although the hollow nanospheres have 33% greater surface area than the nanostructured ($LiNH_2$+LiH) mixture (59.6 m^2/g), the desorption temperatures of both materials are notably similar. Therefore, the hollowness of the particles of $LiNH_2$/($LiNH_2$+LiH) is not an important factor in reducing their desorption temperature. Instead, the principle factor is the reduction of SSA, which can be achieved with ball milling.

To study the progress of reaction (3-2) during a DSC test in terms of microstructural evolution, the 1:1 molar ratio mixture milled for 5 h was heated to 150, 200, and 300°C with the same heating rate of 10°C/min as used in the DSC tests shown in Fig. 7-6 a) and b). The samples obtained after heating were tested by XRD in an environmental holder. The obtained XRD patterns are presented in Fig. 7-7. Unfortunately, the Bragg peaks of $LiNH_2$ and Li_2NH overlap (the reader is referred to JCPDS file # 06-0418 and 06-0417 for $LiNH_2$ and Li_2NH, respectively) in addition to the aforementioned overlap of those of LiH and Al. This overlap renders the XRD test inconclusive because the presence of Li_2NH cannot be confirmed unambiguously as required by reaction (3-2).

Because of the ambiguity of the XRD tests, the FT-IR technique was used to obtain microstructural information for the mixtures heated to various temperatures as shown above.

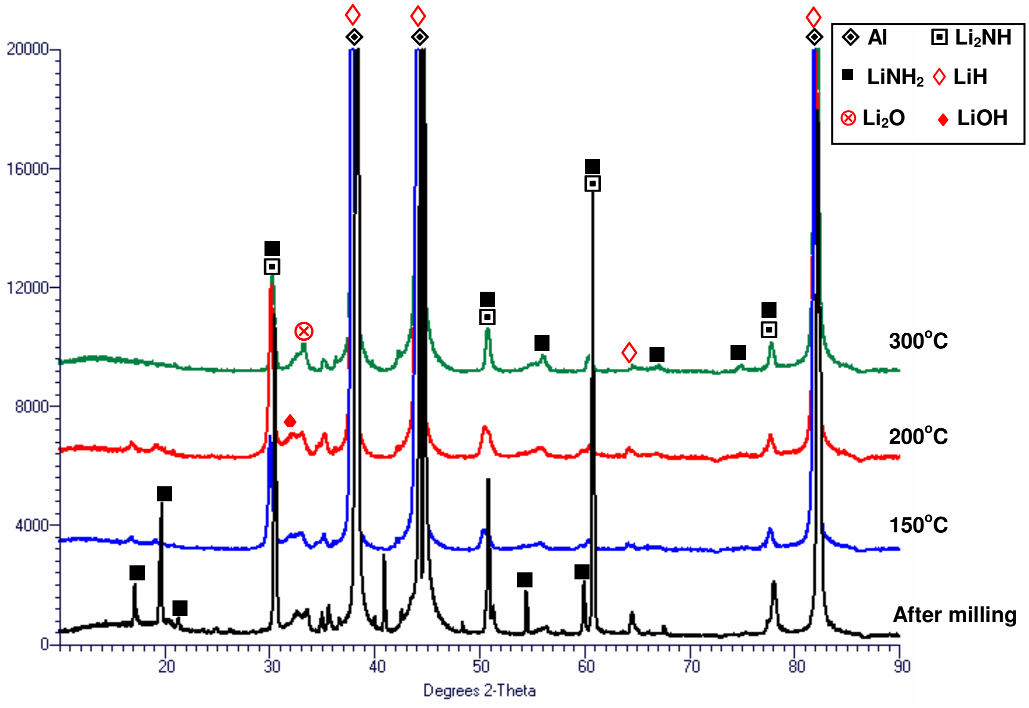

Fig. 7-7 XRD patterns of the 1:1 molar ratio mixture milled for 5 h and DSC directly after milling and after heating at various temperatures

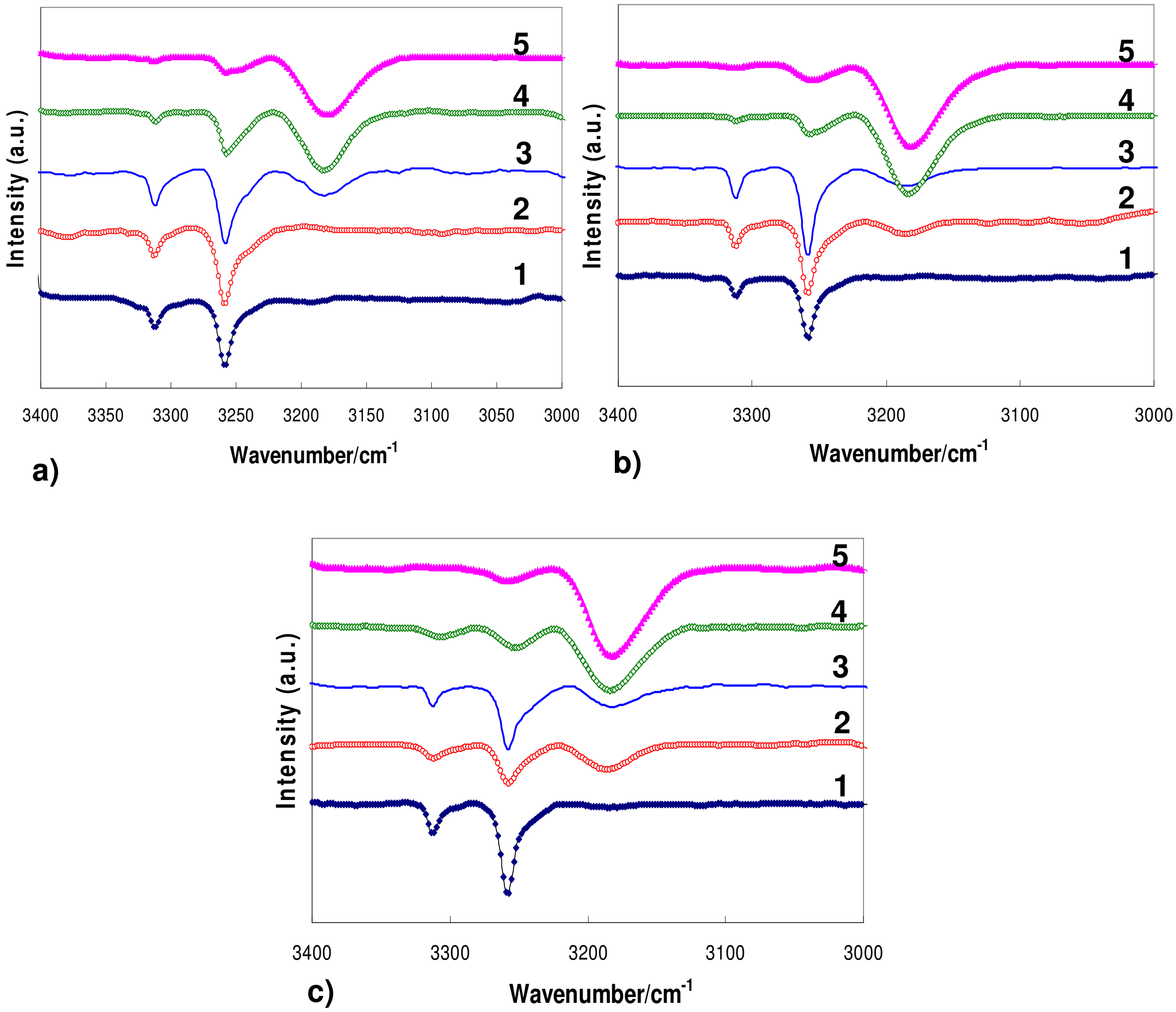

Fig. 7-8 FT-IR absorption spectra of a) 1:1, b) 1:1.2 and c) 1:1.4 molar ratio mixtures milled for 25 h and heated to various temperatures 1) 200 °C, 2) 225 °C, 3) 250 °C, 4) 275 °C, and 5) 300°C

Fig. 7-8 a), b) and c) show the FT-IR absorption spectra for the 1:1, 1:1.2, and 1:1.4 molar ratio mixtures, respectively, which were milled for 25 h and subsequently heated to various temperatures at a heating rate of 10°C/min. $LiNH_2$ has two peaks at 3312 and 3259 cm^{-1}, corresponding to the asymmetric and symmetric stretching of the N-H bonds in $LiNH_2$, respectively. Li_2NH also has two peaks at wavelengths of 3180 and 3250 cm^{-1} [65-67]. Fig. 7-8 shows that the increase of the molar ratio of LiH results in faster transformation of $LiNH_2$ to Li_2NH through more efficient capturing of NH_3 by a larger amount of LiH as required by reactions (3-3) and (3-4). For the 1:1 molar ratio, reaction (3-2) starts at 250°C, and a portion of the $LiNH_2$ phase still remains at 300°C, which agrees with the presence of its melting peak in Fig. 7-6 a). For the 1:1.2 molar ratio, reaction (3-2) starts at 225°C and ends at approximately 300°C. For the 1:1.4 molar ratio, the reaction starts at 225°C and ends between 275 and 300°C.

The measurements of the apparent activation energy of hydrogen desorption according to reaction (3-2) (reaction goes to the right) were conducted using the Kissinger method (Eq. (6-2)). Fig. 7-9 a) shows the effect of various heating rates on DSC profiles, which is an underlying principle of the Kissinger method. The corresponding Kissinger plots are shown in Fig. 7-9 b) for various milling times and in Fig. 7-9 c) for various molar ratios. One should note the excellent correlation coefficients, R^2, obtained for the Kissinger plots in Fig. 7-9 b) and c), which attest to the accuracy of the method. Table 7-4 lists the activation energy data obtained from the Kissinger plots. The apparent activation energy is rapidly reduced after 1 h of ball milling, and further milling only slightly changes the apparent activation energy. In Fig. 7-10, the apparent activation energy is plotted vs. SSA for the 1:1 molar ratio mixture. The lowest energy is obtained after 25 h of milling when the SSA reaches approximately 60 m^2/g. In general, within the range of 45-60 m^2/g, the apparent activation energy changes only moderately. For comparison, the results reported by Xie et al. [64], who investigated hollow nanospheres, are shown in Fig. 7-10. Their apparent activation energy is slightly higher than the values obtained in the present work, even though the nanospheres have higher surface area and possibly lower diffusion depth. However, the results of Xie et al. [64] are for the hydrogen absorption reaction (3-2) (reaction goes to the left); therefore, it is not clear whether their results can be compared directly with those for desorption in the present work. This problem requires further study, especially because the apparent activation energy for the hydrogen absorption in amides/imides is usually lower than that for desorption [57, 68]. Therefore, there are other factors related to ball milling that further reduce the supposedly elevated apparent activation energy for desorption. In Fig. 7-11, the calculated apparent activation energy for hydrogen desorption is plotted vs. the molar ratio of LiH to $LiNH_2$ in the mixtures milled for 25 h. The data reported by Shaw et al. [57, 68] for the 1:1.1 molar ratio and 24-h milling time are also plotted in Fig. 7-11, and the data fit the observed trend well. It is clear that increasing the LiH molar ratio to 1.2 results in a more profound reduction of the apparent activation energy. It is possible that increasing the number of interfaces between LiH and $LiNH_2$ provides many diffusion paths and also increases the reactant energy to a sufficiently high state to reduce the apparent activation energy. However, a further increase of the LiH molar ratio to 1.4 does not lead to any further decrease in the apparent activation energy, suggesting that excessive LiH may be present at the $1LiNH_2$: 1.4LiH molar ratio.

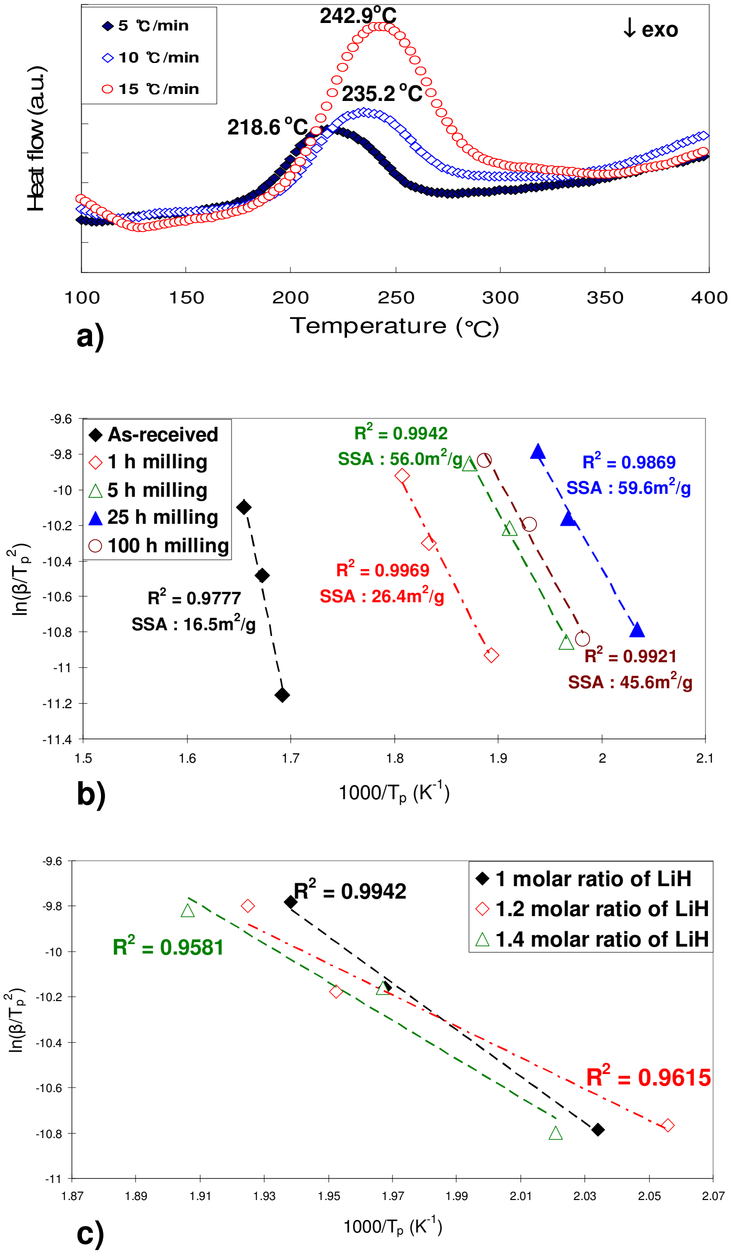

Fig. 7-9 a) Examples of the DSC profiles at various heating rates (5, 10 and 15°C/min) for the 1:1 molar ratio mixture of $LiNH_2$:LiH. The Kissinger plots of the apparent activation energy for hydrogen desorption (reaction (3-2) goes to the right) for the milled LiH and $LiNH_2$ mixtures vs. b) milling time and c) the molar ratio of LiH to $LiNH_2$

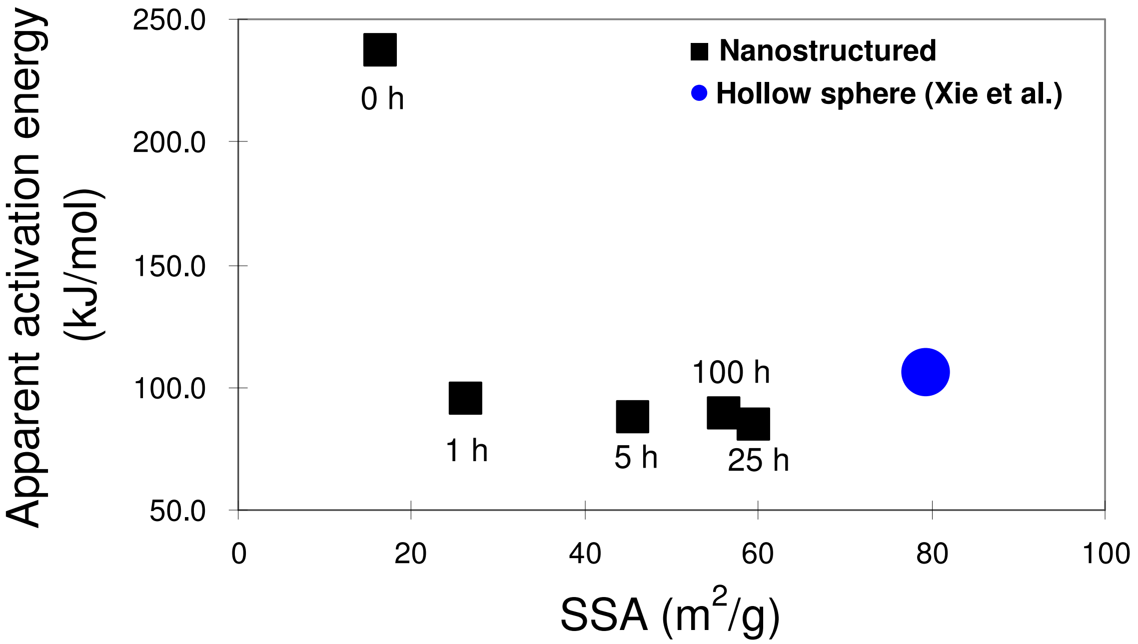

Fig. 7-10 The apparent activation energy of reaction (3-2) as a function of the specific surface area (SSA) for the 1:1 molar ratio mixture $LiNH_2$:LiH

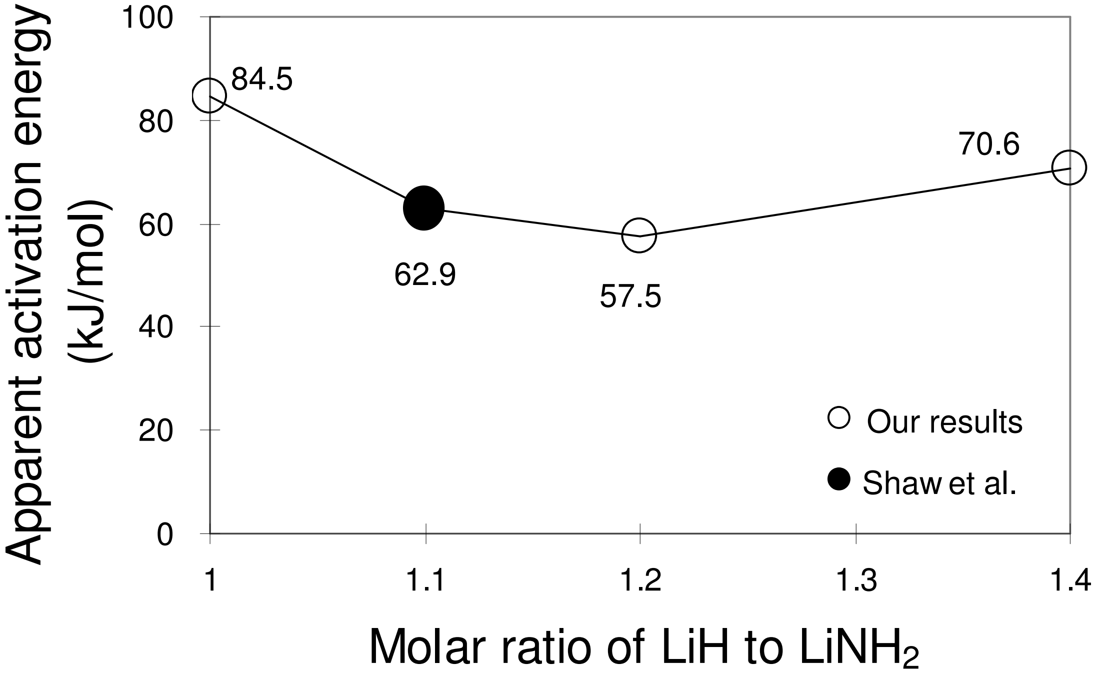

Fig. 7-11 The apparent activation energy of reaction (3-2) as a function of the molar ratio of LiH to $LiNH_2$ for the mixtures milled for 25 h

Table 7-4. Summary of the calculations of the apparent activation energy of reaction (3-2)

Milling time (h)	Molar ratio ($LiNH_2$:LiH)	BET specific surface area (m^2/g)	Apparent activation energy (kJ/mol)
0	1:1	16.5	237.5
1		26.4	94.9
5		56.0	89.5
25	1:1	59.6	84.5
	1:1.2	NA	57.5
	1:1.4	NA	70.6
100	1:1	45.6	88.0

7-4. Discussion

7-4-1. Origin of the ammonia (NH_3) release from the ($LiNH_2$+LiH) mixture

Fig. 7-12 a) and b) show the TGA and corresponding DSC curve, respectively, for the 1:1 molar ratio $LiNH_2$:LiH mixture after milling for 25 h obtained with a TA Q600 combined TGA and a DSC apparatus. The TGA curve shows two distinct weight loss regions with distinctly different slopes, which are delineated by tangent lines 1 and 2 in Fig. 7-12 a). In accordance with the TPD curve in Fig. 7-5, the corresponding DSC curve in Fig. 7-12 b) shows that the first TGA region results from hydrogen desorption, while the second results from the release of ammonia. From the intersection of these two tangent lines in Fig. 7-12 a), the 1:1 molar ratio mixture desorbs approximately 4.4 wt.% H_2 at up to 330°C below the melting temperature of $LiNH_2$, while ammonia is released in a much higher temperature range when the retained $LiNH_2$ melts (also compare with Fig. 7-4).

Based on the estimated amounts of ammonia released from the $LiNH_2$ milled for 25 h in Fig. 7-4 in the solid (10.7 wt.%) and liquid (22.9 wt.%) states as listed in Table 7-5, the theoretical amount of hydrogen released in the solid and liquid states from the 1:1 molar mixture can be estimated as (6.5 wt.% $H_2 \times$ [10.7 wt.%/(10.7+22.9 wt.%)] ≈ 2.1 wt.% H_2 in the solid state of $LiNH_2$ in the mixture and (6.5 wt.% $H_2 \times$ [22.9 wt.%/(10.7+22.9 wt.%)] ≈ 4.4 wt.% H_2 in the liquid, respectively. However, the value of 4.4 wt.% H_2 released in a solid state as shown in Fig. 7-12 a) is twice as high as the theoretical amount expected for the 1:1 molar ratio $LiNH_2$:LiH mixture as summarized in Table 7-5.

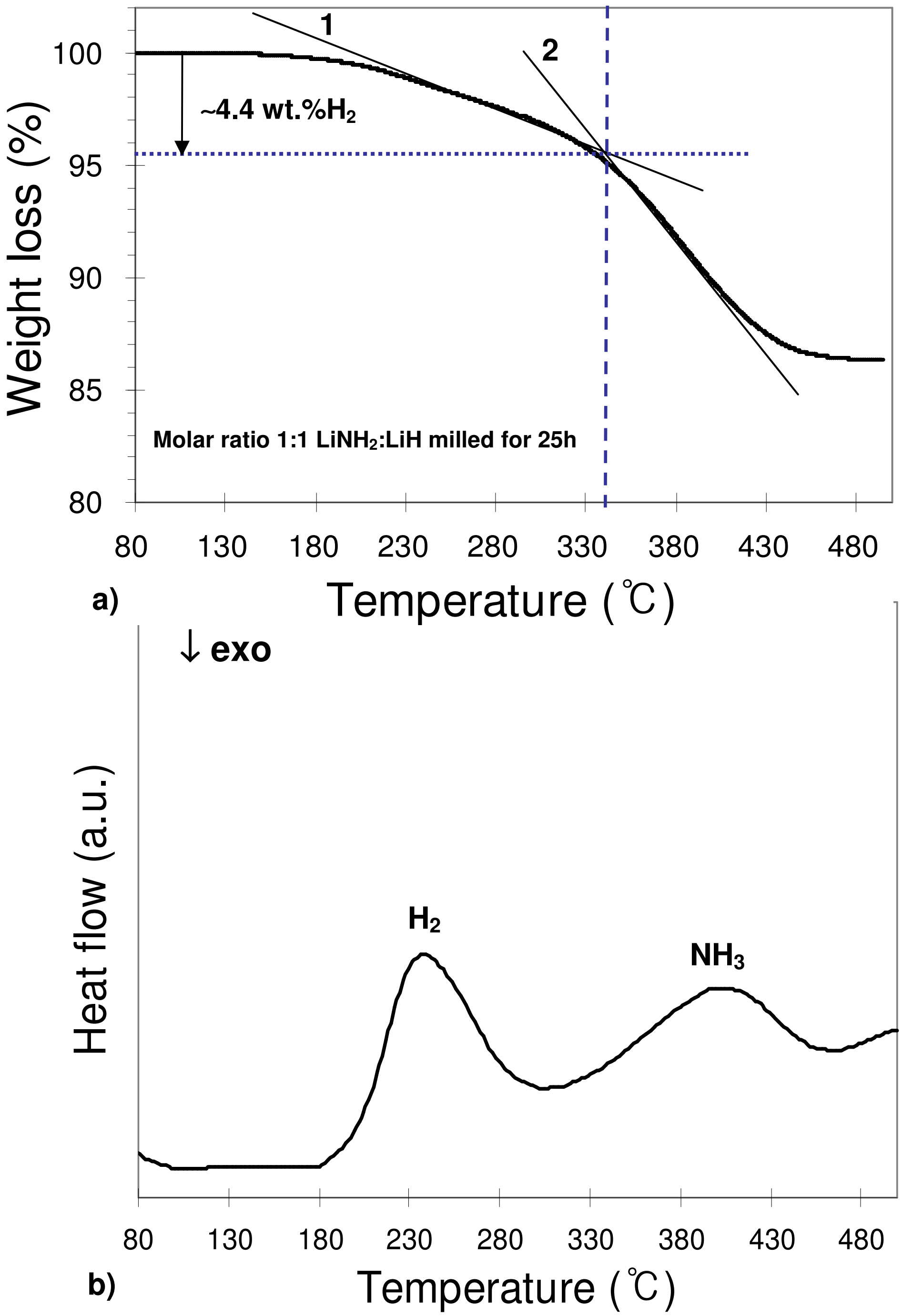

Fig. 7-12 a) TGA curve for the 1:1 molar mixture $LiNH_2$:LiH milled for 25 h. Tangent lines 1 and 2 show two distinct weight-loss regimes for H_2 and NH_3, respectively. b) Corresponding DSC curve showing endothermic desorption peaks of H_2 and NH_3. Data obtained with TA Q600 apparatus

Table 7-5. The calculated and experimental amount of H_2 desorbed from the 1:1 molar mixture ($LiNH_2$+LiH) ball milled for 25 h

The amount of H_2 desorbed from 1 mol $LiNH_2$: 1 mol LiH mixture milled for 25 h			
Theoretical (wt.% H_2)		Experimental (wt.% H_2)	
Solid state of $LiNH_2$	Liquid state of $LiNH_2$	Solid state of $LiNH_2$	Liquid state of $LiNH_2$
2.1	4.4	4.4	0

Therefore, in addition to capturing NH_3, it appears that LiH can accelerate $LiNH_2$ decomposition to Li_2NH and NH_3 at lower temperatures if LiH has intimate contact with $LiNH_2$ due to ball milling. As shown in Fig. 7-6 a), ball milling is absolutely necessary to enhance $LiNH_2$ decomposition in the ($LiNH_2$+LiH) mixture because the unmilled 1:1 molar ratio mixture in Fig. 7-6 a) shows only minimal H_2 desorption before the $LiNH_2$ component melts. Thus, LiH may act as a catalyst for the decomposition of $LiNH_2$.

An important question that arises from these results is why ammonia is persistently released from the ($LiNH_2$+LiH) mixture as seen in Fig. 7-12 a) and b). TGA/DSC experiments were performed after flushing the TA Q600 apparatus with Ar for 1.5 h and subsequently allowing a flow of high-purity Ar. However, the chamber of the TA Q600 apparatus is essentially open, and air contamination of the flowing Ar is quite possible.

Based on this experimental fact, we formulate the hypothesis that contact with moisture in the remnant air in the chamber (or anywhere else, for that matter) hydrolyzes a fraction of the LiH in the mixture into LiOH, which makes this fraction inactive and unable to react with NH_3 according to reaction (3-4). To test this hypothesis, we performed an experiment in which the 1:1 molar ratio $LiNH_2$:LiH mixture ball was milled for 100 h and thermally tested with the TA Q600 apparatus with and without flushing with Ar for 1.5 h. Fig. 7-13 a) and b) show TGA and DSC desorption profiles of the 1:1 molar ratio mixture, respectively. In Fig. 7-13 b), the mixture without Ar flushing shows only one DSC endothermic peak corresponding to the melting of $LiNH_2$. Fig. 7-13 b) also shows a rapid weight loss starting around 350^{o}C. These TGA and DSC curves look similar to the curves registered for single-phase $LiNH_2$ as shown in Fig. 7-4 a) and b). Such behavior provides strong evidence in favor of the hypothesis of the partial hydrolysis/oxidation of LiH accelerated by heating in the presence of an impure Ar atmosphere contaminated by air, which makes a portion of LiH inactive in reaction (3-4). In contrast, after flushing with Ar, the mixture shows two distinct regimes of weight loss with two distinct slopes in a TGA test in Fig. 7-13 b). The regime at low temperatures is related to H_2 desorption, and the regime at high temperatures is related to NH_3 desorption, which is similar to the results presented in Fig. 7-12 a) and b). In a DSC test in Fig. 7-13 b), the argon-flushed mixture shows two endothermic peaks: one related to H_2 desorption (reaction (3-2)) and the other related to the melting of retained $LiNH_2$ and simultaneous NH_3 desorption. The latter is formed from the retained $LiNH_2$ that did not fully react with LiH, due to its partial inactivity. As shown by Ren et al. [69], LiH is sensitive to storage and testing conditions. Therefore, we conclude that the unreacted/retained $LiNH_2$ always releases NH_3 as long as a part of the LiH becomes inactive, due to hydrolysis/ oxidation, and does not take part in the intermediate reaction (3-4).

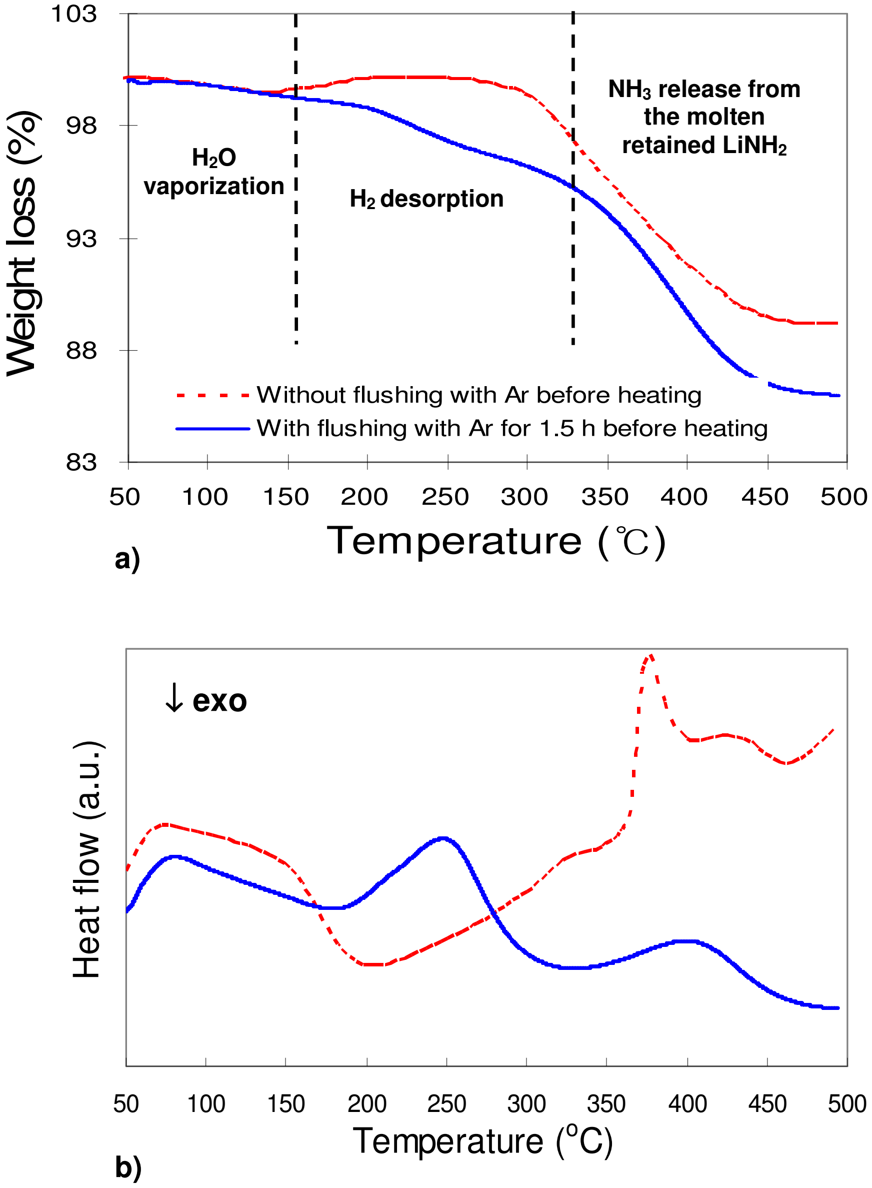

Fig. 7-13 Thermal desorption profiles from a) TGA and b) DSC of the 1:1 molar ratio $LiNH_2$:LiH mixture ball milled for 100 h with and without flushing with Ar for 1.5 h before heating. Data obtained with a TA Q600 apparatus

Assuming that all LiOH comes from LiH, this reaction can be expressed as follows. For the first endothermic peak (H_2),

$LiNH_2 + (1\text{-}x)LiH + x(LiH)_{inactive} \rightarrow (1\text{-}x)Li_2NH + (1\text{-}x)H_2 + xLiNH_2 + x(LiH)_{inactive}$ (7-1)

For the second peak (NH_3),

$xLiNH_2 \rightarrow (x/2Li_2NH_3 + x/2NH_3) + x(LiH)_{inactive}$ (7-2)

where $x(LiH)_{inactive}$ is the fraction of inactive LiH.

In the first step, it is assumed that $xLiNH_2$ is rendered inactive such that $(1\text{-}x)LiNH_2$ reacts with $(1\text{-}x)LiH$, which transforms into $(1\text{-}x)Li_2NH$ and $(1\text{-}x)H_2$. In the second step, this unreacted $xLiNH_2$ decomposes into $(x/2Li_2NH + x/2NH_3)$. Through this modified reaction, we can calculate the amount of NH_3 using the following equations:

$$x(LiH) = A - \frac{Hydrogen\ Capacity_{\ Experimental}}{Hydrogen\ Capacity_{\ Theorectical}} \qquad (7\text{-}3)$$

$$Weight\ percentage\ of\ NH_3 = \frac{\frac{[x-(A-1)]}{2}(Mass\ of\ 1\ mol\ NH_3)}{Total\ mass\ of\ \text{reactants}} \qquad (7\text{-}4)$$

where A is the molar ratio of LiH to $LiNH_2$.

Table 7-6 shows the amounts of inactive LiH calculated above for various molar ratios of $LiNH_2$:LiH together with experimentally estimated amounts of released H_2 and NH_3. Fig. 7-14 a), plotted from data in Table 7-6, shows good agreement between the calculated and experimentally observed amounts of desorbed NH_3, which strongly supports our hypothesis.

Fig. 7-14 b) shows that the amount of hydrogen desorbed slightly decreases as the milling time increases from 5 to 25 and 100 h. Table 7-6 shows that this effect is due to the gradual increase in inactive LiH with increasing milling time for the 1:1 molar ratio $LiNH_2$:LiH.

Table 7-1 and Fig. 7-2 show that the grain (crystallite) size of LiH decreases monotonically with increasing milling time. This observation suggests that with the reduction in grain (crystallite) size, LiH is rendered more sensitive to hydrolysis and the formation of LiOH.

Fig. 7-14 c) shows that the optimal molar ratio of $LiNH_2$:LiH in the mixture is 1:1.2 because the amount of desorbed hydrogen is 5 wt.% at that ratio and, conversely, the amount of NH_3 that is desorbed is the smallest. This result agrees well with the data in Table 7-6, which show that at the molar ratio 1:1.2, the mass of active LiH in the mixture is the largest of all of the compounds.

Table 7-6. Comparison of the calculated and experimental amounts of H_2 and NH_3 as a function of milling time and the molar ratio of LiH:$LiNH_2$ assuming a fraction of inactive LiH

Molar ratio LiH - milling time (h)	**Hydrogen capacity (wt.%)**		**Calculated fraction of inactive LiH (%)**	**Calculated weight of LiH in the mixture (g)**		**Released NH_3 (wt.%)**	
	Theor.	**Exp.**		**Active**	**Inactive**	**Cal.**	**Exp.**
1.0 mol LiH -5 h	6.5	4.6	29.2	5.6	2.3	8.0	7.5
1.0 mol LiH -25 h		4.4	33.1	5.3	2.6	9.1	9.7
1.0 mol LiH -100 h		4.1	37.3	5.0	3.0	10.3	9.6
1.2 mol LiH -25 h	6.2	5.0	33.0	6.4	3.2	5.1	5.8
1.4 mol LiH -25 h	5.9	4.5	53.0	5.2	5.9	5.9	6.2

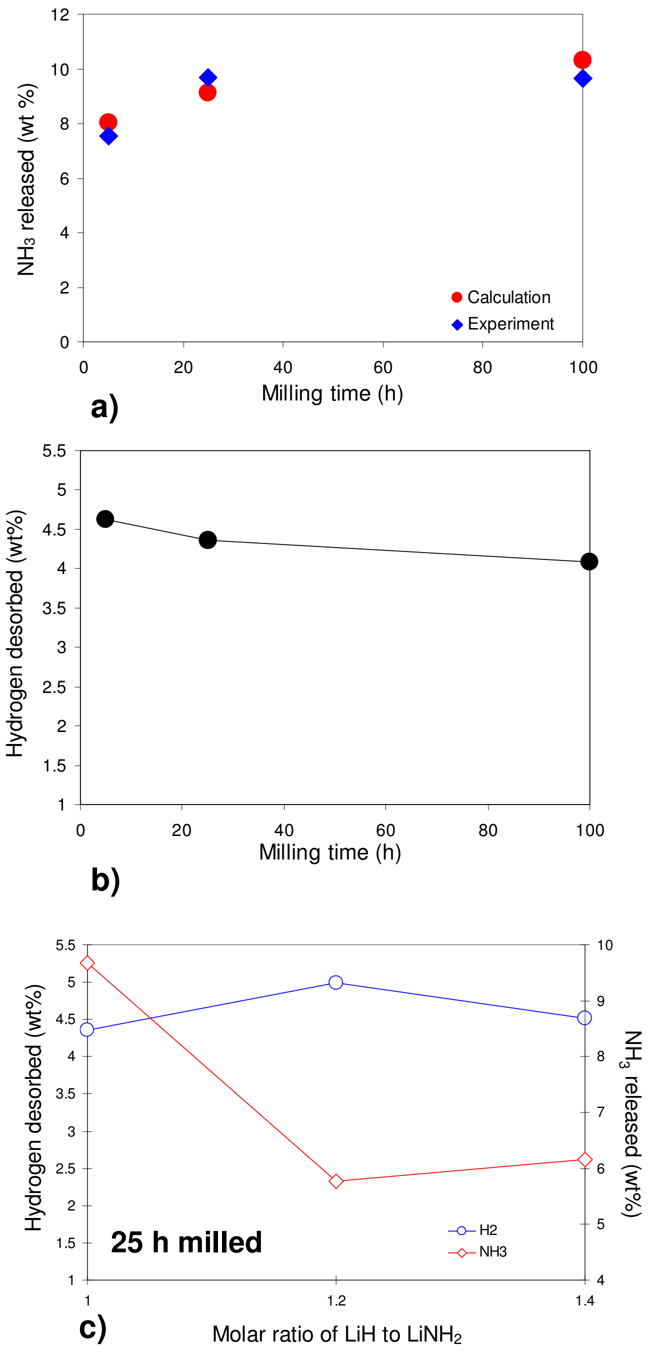

Fig. 7-14 a) Comparison of the calculated (Eq. (7-3) and (7-4)) and experimental values of NH_3 vs. milling time for 5, 25 and 100 h. The experimental amount of H_2 and NH_3 in the 1:1 molar ratio $LiNH_2$:LiH mixture vs. b) milling time for 5, 25 and 100 h, and c) the molar ratio of LiH to $LiNH_2$ for the mixtures milled for 25 h

8. Li-N-C-H system

8-1. Reactions of carbon with $LiNH_2$

Recently, Alapati et al. [132] performed the first principle calculations to identify new destabilized metal hydride reactions. These researchers also suggested attractive reactions containing carbon as a destabilizing agent. One of the suggested reactions shows the destabilization of $LiNH_2$:

$2LiNH_2 + C \rightarrow Li_2CN_2 + 2H_2$ (8-1)

The theoretical model indicates that the standard enthalpy change is -31 kJ/mol H_2 (the negative sign indicates an endothermic reaction) and that the theoretical hydrogen capacity is 7 wt.% H_2. However, no experimental studies of this system have been attempted yet.

8-1-1. ($2LiNH_2$+C) system

Fig. 8-1 compares the DSC curves of single-phase $LiNH_2$ and the ($2LiNH_2$+C) mixtures with two different carbon forms, all of which were milled for 25 h. Carbons in the form of graphite (crystalline) and carbon black (amorphous) were used as destabilizing agents of $LiNH_2$. The DSC curve of single-phase $LiNH_2$ shows a single endothermic peak that corresponds to reaction (3-3) at approximately 370°C, while both mixtures with two different carbon forms show one endothermic peak below 370°C and two exothermic peaks above 450°C. Fig. 8-2 shows the corresponding TGA curves for single-phase $LiNH_2$ and a ($2LiNH_2$+Graphite) mixture, both of which were milled for 25 h. Single-phase $LiNH_2$ releases 33.6 wt.% NH_3 according to reaction (3-3), while the weight loss of the ($2LiNH_2$+Grapite) mixture is approximately 25.2 wt.%. Two findings are particularly interesting. First, the weight loss of the ($2LiNH_2$+Grapite) mixture starts at lower temperatures than that of the $LiNH_2$ and ends below 400°C. Therefore, the weight loss of the mixture of $LiNH_2$-C (graphite) (2:1) is due to the only endothermic peak that appears below 400°C as shown in Fig. 8-1. The two exothermic peaks that appear at approximately 450°C do not contribute to any weight loss.

The second finding is that the amount of weight loss in the 2:1 molar ratio mixture $LiNH_2$:C (graphite) is much larger than our expectation based on reaction (8-1) proposed by Alapati [132], which suggests 7 wt.% H_2 release through a single endothermic reaction. Assuming that graphite is inactive with $LiNH_2$ and that 2 mol of $LiNH_2$ is melted and decomposed into Li_2NH, the mixture can release 29.4 wt.% NH_3, which corresponds to 1 mol of NH_3 per unit formula of the ($2LiNH_2$+C) mixture.

Considering the purity of each material, the result is in good agreement with the experimental value of 25.2 wt.%. Therefore, the reaction pathway of the mixture as it is heated up to 500°C is not processed by reaction (8-1) but follows reaction (3-3), which releases NH_3.

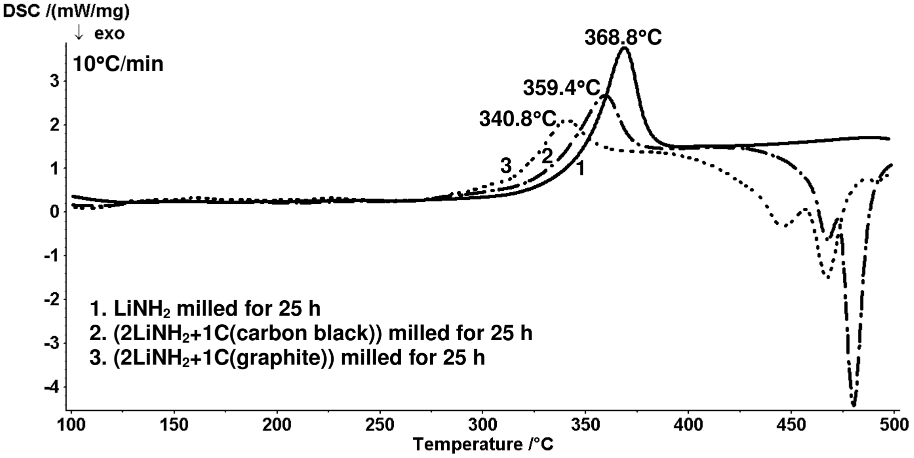

Fig. 8-1 DSC profiles of 1) single-phase $LiNH_2$ milled for 25 h and 2:1 molar ratio mixtures of $LiNH_2$ with 2) carbon black and 3) graphite milled for 25 h

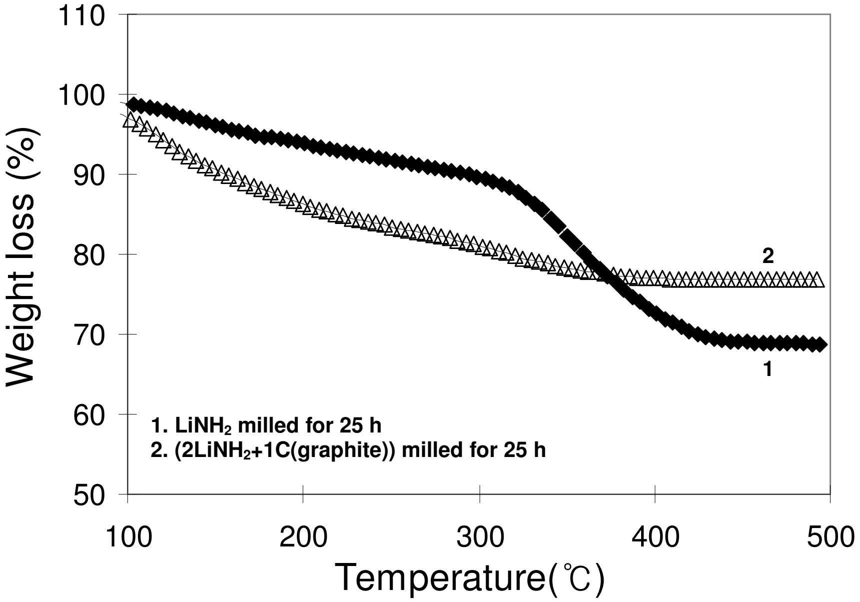

Fig. 8-2 TGA profiles of 1) single-phase $LiNH_2$ milled for 25 h and 2) 2:1 molar ratio mixtures of $LiNH_2$ with graphite milled for 25 h

To clarify the reaction pathways corresponding to one endothermic and two exothermic peaks, as shown in the DSC curves of the ($2LiNH_2$+Grapite) mixture, samples at different DSC stages were collected and analyzed using XRD. XRD analysis was performed with Mylar film to prevent oxidation/hydrolysis during the XRD test. As can be seen in Fig. 8-3, the XRD pattern of the ($2LiNH_2$+graphite) heated to 400°C shows the diffraction peaks of the Li_2NH and Li_2O phases, which indicates that the endothermic peak in the DSC curve of the mixture shown in Fig. 8-1 is related to the melting and decomposition of $LiNH_2$ described in reaction (3-3). Further heating of the sample to 500°C splits the diffraction peak of graphite and forms the $LiOH{\bullet}H_2O$ phase, while XRD patterns of the Li_2NH phase are no longer detectable. Therefore, it is likely that two exothermic reactions are related to the oxidation and hydrolysis of the Li_2NH phase or to the formation of lithiated graphite because the diffraction peak of graphite at 2Θ=26.4° is split after heating at 500°C.

However, it is worth mentioning that the ternary nitride product predicted by Alapati et al. [132], the Li_2CN_2 phase, is not obtained, even though the samples are heated up to 500°C. Therefore, the ($2LiNH_2$+Grapite) mixture is decomposed by reaction (3-3), which forms Li_2NH_2 and releases NH_3 regardless of the presence of graphite. It is likely that the proposed reaction (8-1) is difficult to realize, due to the high kinetic energy barrier of C-C bonds.

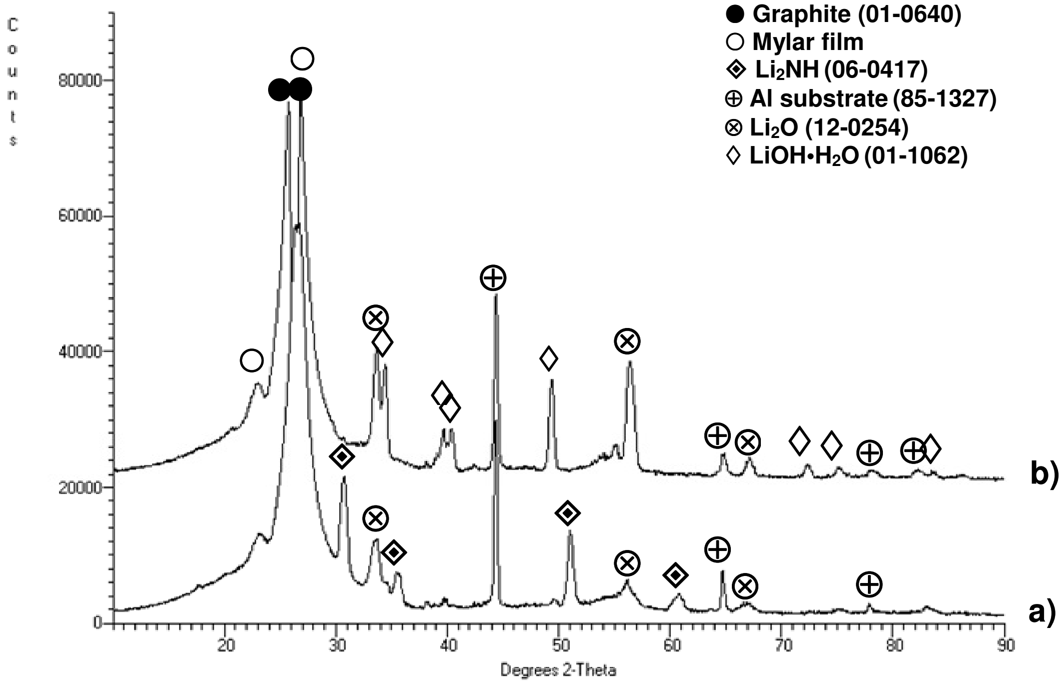

Fig. 8-3 X-ray diffraction patterns of 2:1 molar ratio mixtures of $LiNH_2$ with graphite milled for 25 h heated to various temperatures at a heating rate of 10°C/min in Ar atmosphere (a- 400°C and b- 500°C)

8-2. ($LiNH_2$+1.2LiH) system incorporated with graphite

8-2-1. Morphology and microstructure of powder mixtures

Fig. 8-4 a) shows the backscattered electron (BSE) micrograph of the (($LiNH_2$+1.2LiH)+5 wt.% G (graphite)) mixture after ball milling for 25 h. Fig. 8-4 b) shows the XRD patterns for ($LiNH_2$+1.2LiH) (pattern 1) and (($LiNH_2$+1.2LiH)+5 wt.% G) (pattern 2). The principal diffraction peaks in both patterns belong to both $LiNH_2$ and LiH. Interestingly, there is no graphite peak present in pattern 2, which strongly suggests that graphite transforms into an amorphous form because of high-energy ball milling. It is also interesting to note that both the LiOH and Li_2O diffraction peaks are observed in the mixture without graphite (pattern 1), whereas only the Li_2O peaks are observed in the mixture with 5 wt.% graphite (pattern 2). Possible direct reaction routes that can result in the formation of LiOH when LiH is exposed to air at room temperature are as follows [133]:

$LiH+H_2O = LiOH+H_2$ ΔG = -133.01 kJ/mol (8-2)

$LiH+1/2O_2 = LiOH$ ΔG = -370.24 kJ/mol (8-3)

The absence of the LiOH peaks in diffraction pattern 2 in Fig. 8-4 b) for the mixture with 5 wt.% graphite as opposed to pattern 1 without graphite is clear evidence that the graphite additive indeed formed a hydrophobic coating around the LiH particles that prevented the occurrence of reactions (8-2) and (8-3) in the mixture with graphite.

Li_2O has two possible origins. First, it can be present as a pre-existing impurity in commercial $LiNH_2$ and can lead to the formation of LiOH in the mixture without graphite according to the following reaction [133]:

$Li_2O+H_2O = 2LiOH$ ΔG = -78.06 kJ/mol (8-4)

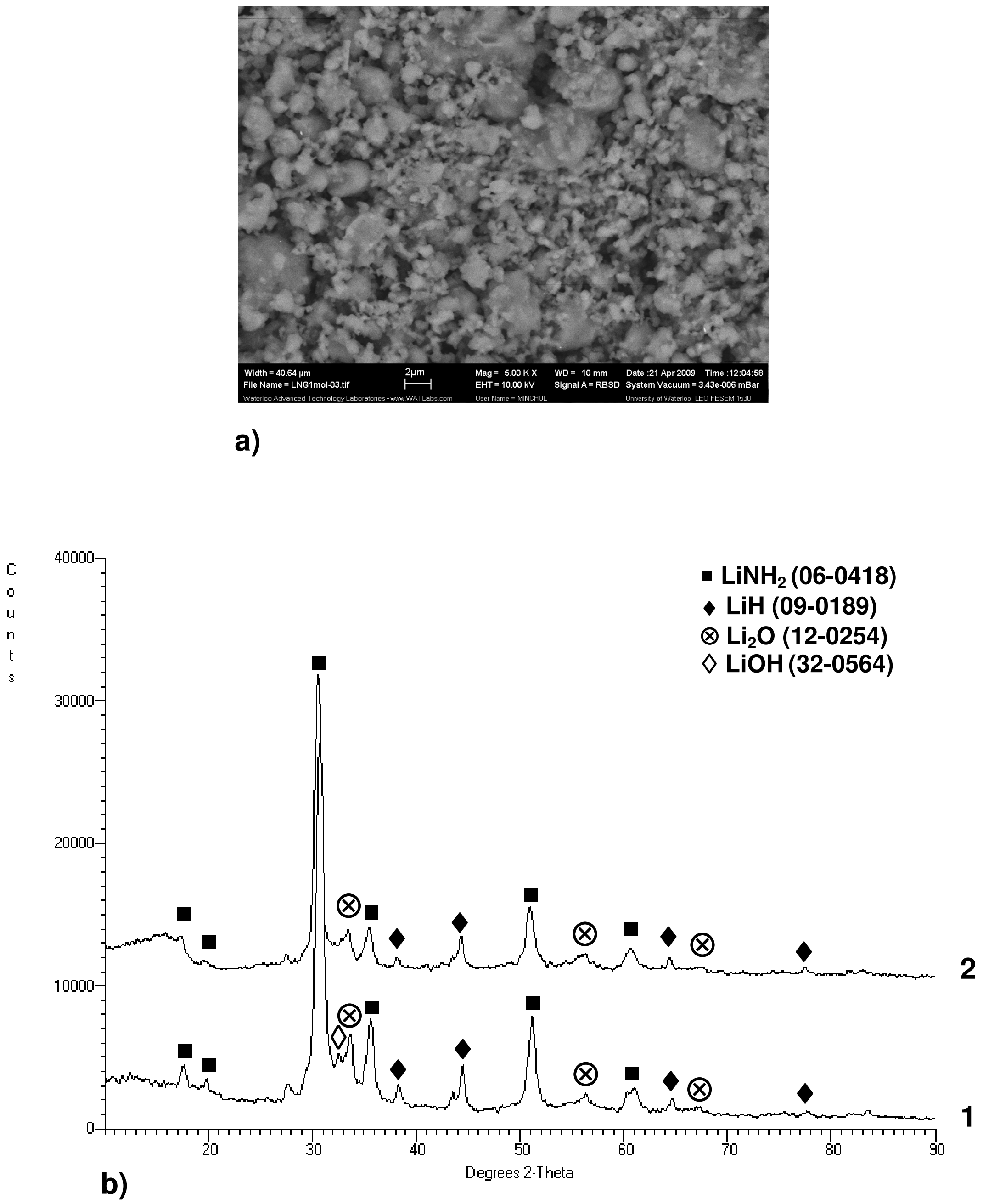

Fig. 8-4 a) Backscattered electron (BSE) micrograph of (($LiNH_2$+1.2LiH)+5 wt.% G) and b) XRD patterns for 1-($LiNH_2$+1.2LiH) and 2-(($LiNH_2$+1.2LiH)+5 wt.% G), both of which were milled for 25 h

Second, Li_2O can be formed at room temperature if there is a small amount of moisture present in the atmosphere according to the following reaction [133]:

$LiH+1/2H_2O = 1/2Li_2O+H_2$ $\Delta G = -93.98$ kJ/mol (8-5)

$LiH+1/4O_2 = 1/2Li_2O+1/2H_2$ $\Delta G = -212.59$ kJ/mol (8-6)

As reported in Chapter 7, the grain size of the principal phases were found from the corresponding XRD peak profile breadths in the ($LiNH_2$+LiH) (1:1) mixture after 25 h of ball milling (IMP67 mode); the grain (crystallite) sizes of $LiNH_2$ and LiH were 23 and 14 nm, respectively, with corresponding lattice strains of 4.62×10^{-3} and 0, respectively. One can reasonably assume that the grain size would be similar after 25 h of milling in the ($LiNH_2$+1.2LiH) mixture with and without 5 wt.% G additive.

8-2-2. Thermal (DSC) behavior

Fig. 8-5 compares the DSC profiles of ($LiNH_2$+1.2LiH) and (($LiNH_2$+1.2LiH)+5 wt.% G) milled for 25 h. Interestingly, the mixture without graphite shows two endothermic peaks, a large peak and a small one, whereas the mixture with graphite shows one large endothermic peak and one small exothermic peak. In the case of ($LiNH_2$+1.2LiH), the first endothermic peak at 234.6°C is related to reaction (3-2), in which hydrogen is released, and the second endothermic peak at 396.2°C is due to the melting of retained $LiNH_2$ in the mixture and the desorption of NH_3 (reaction (3-3)). This retained $LiNH_2$ occurs due to the partial oxidation/hydrolysis of LiH, which renders reaction (3-2) incomplete. For the (($LiNH_2$+1.2LiH)+5 wt.% graphite) mixture, the second endothermic peak disappears, which indicates that graphite can prevent or at least substantially reduce the oxidation/hydrolysis of LiH. Hydrophobic synthetic graphite covers the surface of LiH and $LiNH_2$ and repels water from the surface. Therefore, the hydrolysis/oxidation of LiH can be prevented. The small exothermic peak at 470.9°C for the (($LiNH_2$+1.2LiH)+5 wt.% G) mixture is related to the oxidation and hydrolysis of the Li_2NH phase or the formation of lithiated graphite as discussed above.

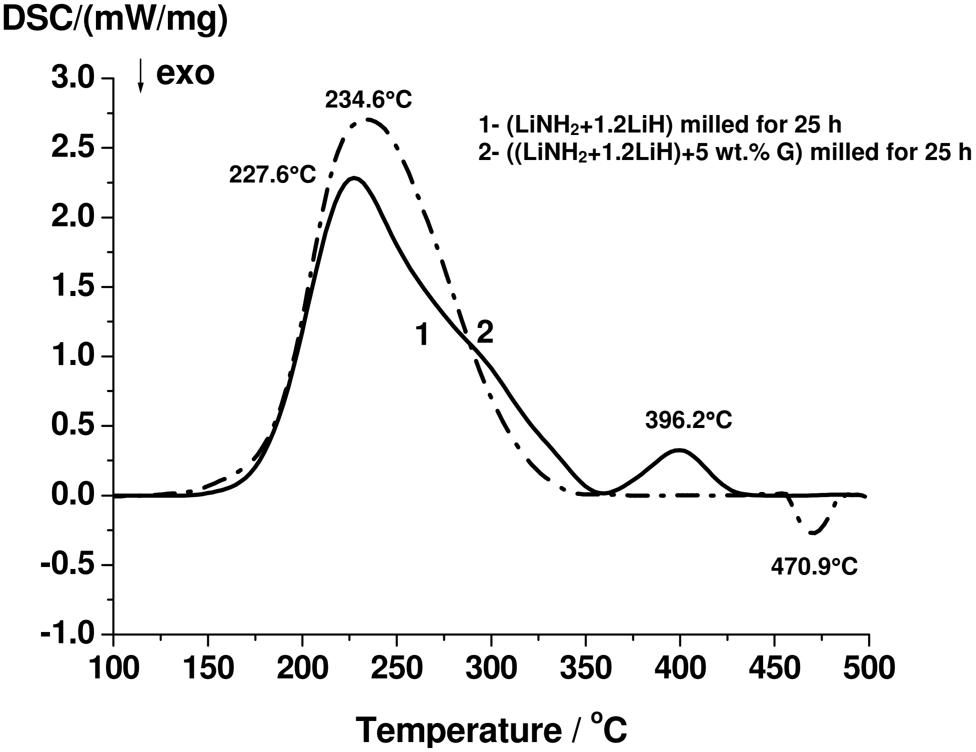

Fig. 8-5 DSC curves at a heating rate of 10°C/min for the ($LiNH_2$+1.2LiH) mixture with and without 5 wt.% graphite, both of which were ball milled for 25 h

The measurements of the apparent activation energy of hydrogen desorption according to reaction (3-2) were collected using two complimentary methods: the Kissinger (Eq. (6-2)) and the JMAK-Arrhenius (Eq. (6-3) and (6-4)) equations.

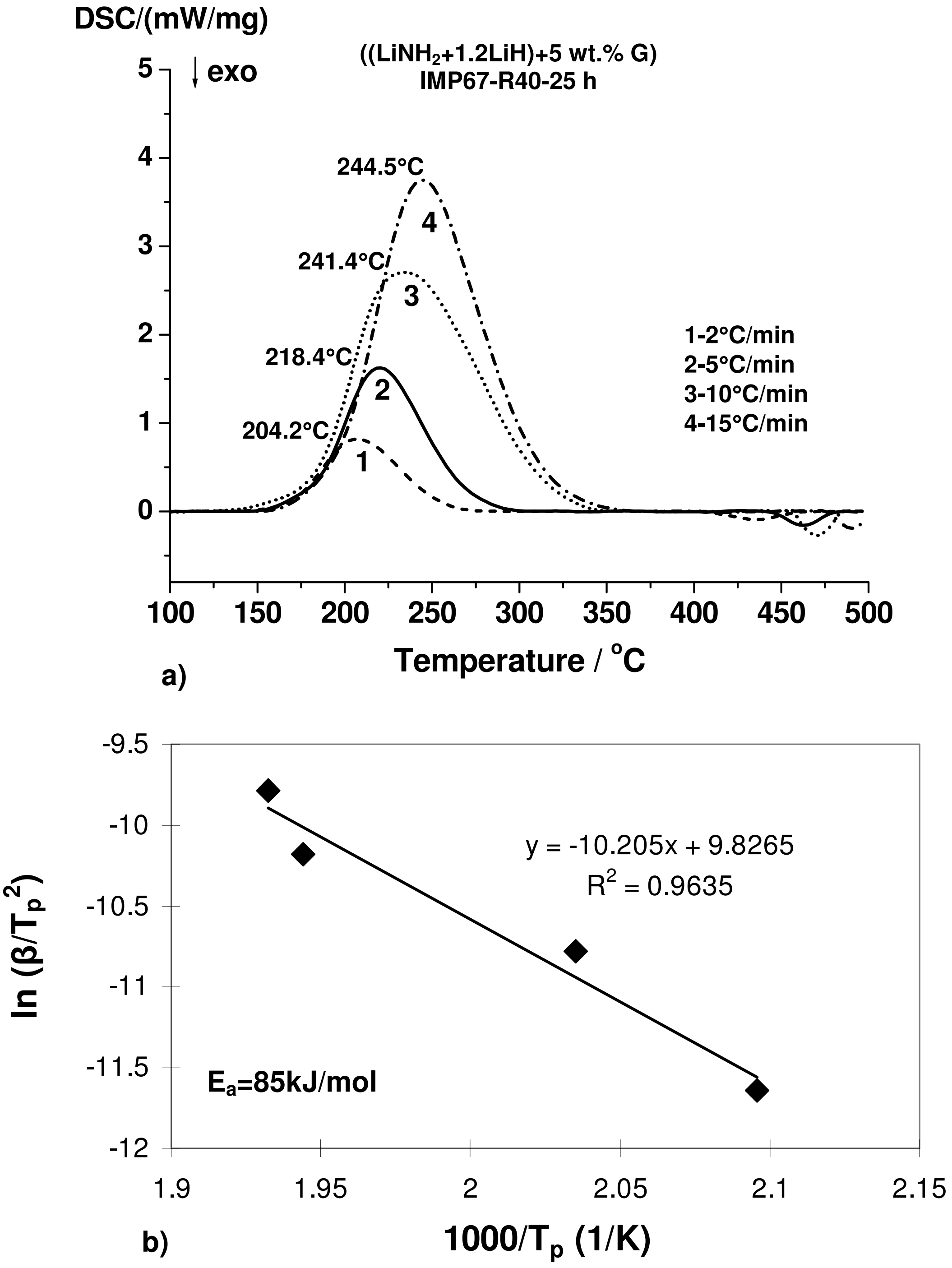

Fig. 8-6 a) DSC curves at various heating rates and b) the Kissinger plot for the apparent activation energy of dehydrogenation (reaction (3-2)) for the milled (($LiNH_2$+1.2 LiH)+5 wt.% G) system

Fig. 8-6 a) shows the effect of varying the heating rate on DSC profiles, which is an underlying principle of the Kissinger method for the milled (($LiNH_2$+1.2LiH) +5wt.% G) system. The corresponding Kissinger plot is shown in Fig. 8-6 b). Excellent correlation coefficients, R^2, are obtained for the Kissinger plots in Fig. 8-6 b), which indicates the accuracy of the method. The apparent activation energy of the mixture with 5 wt.% graphite is 84.9 kJ/mol. Considering the apparent activation energy of ($LiNH_2$+1.2LiH), which is 57.5 kJ/mol, as shown in Chapter 7, the apparent activation energy of the mixture with 5 wt.% graphite becomes relatively high. This behavior can be explained by the fact that the surfaces of $LiNH_2$ and LiH are covered with graphite. Generally, surfaces of the particles after ball milling become notably reactive and are in intimate contact with other reactants. However, if these surfaces are coated with an inactive material, such as graphite, they can become less reactive and the diffusion path and distance can be changed. Therefore, these results suggest that graphite hinders the surface reaction between $LiNH_2$ and LiH.

8-2-3. Isothermal hydrogen storage behavior

Fig. 8-7 a) shows the desorption curves of ($LiNH_2$+1.2LiH) without and with 5 wt.% G milled for 25 h at various temperatures under 1 bar H_2 pressure. At 275°C, 300°C and 325°C, desorption curves for the mixtures with graphite always show higher hydrogen capacity than the same mixtures without graphite. The only exception is the curve at 250°C, which shows a low capacity for H_2 desorbed at this temperature (1 wt.%). This striking capacity difference is probably related to the fact that LiH in the mixture without graphite is partially hydrolyzed/ oxidized.

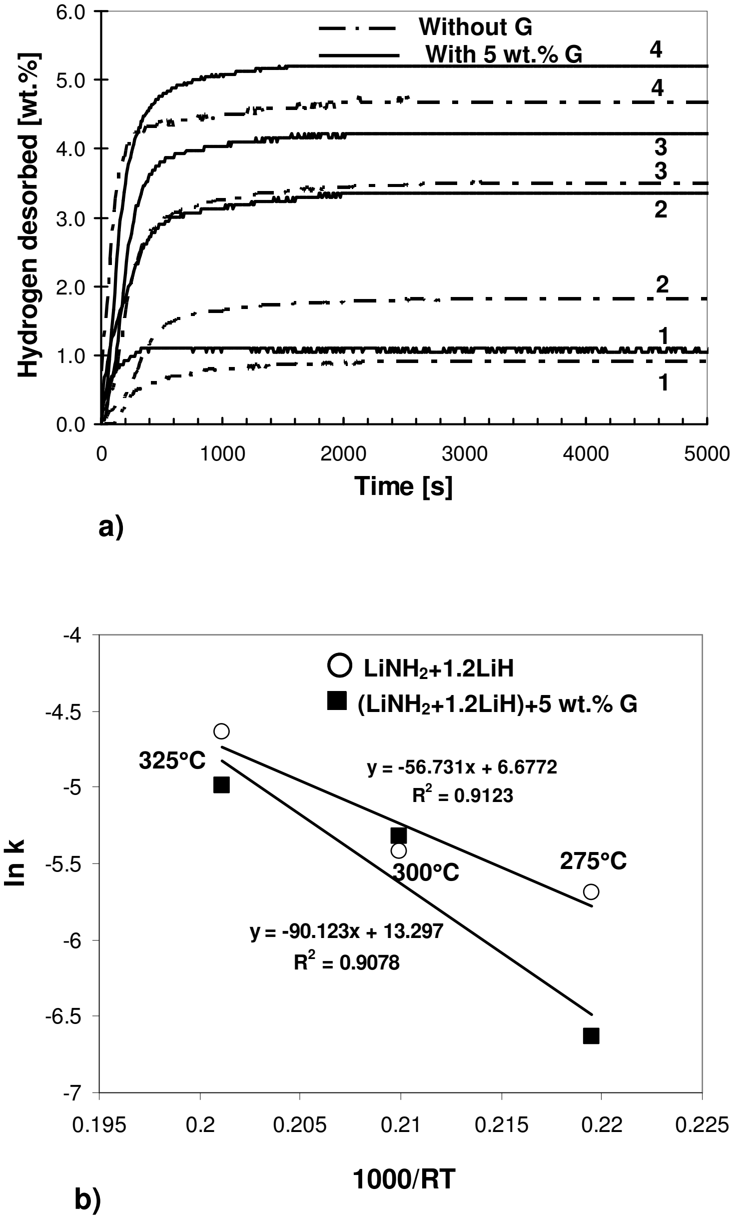

Fig. 8-7 a) Desorption curves of ($LiNH_2$+1.2 LiH) and (($LiNH_2$+1.2 LiH)+5 wt.% G) (1-250°C, 2-275°C, 3-300°C, 4-325°C) under 1 bar H_2 (atmospheric) and milled for 25 h and b) Arrhenius plots for the estimate of the apparent activation energy for mixtures without and with 5 wt.% G

Table 8-1. The calculated and experimental amount of H_2 desorbed from the 1:1.2 molar mixture ($LiNH_2$+LiH) without and with 5 wt.% graphite (G) milled for 25 h

	Theoretical capacity (wt.% H_2)		**Experimental capacity (wt.% H_2) measured at 325°C**
	Purity of starting materials (%)		
	100	**95**	
$LiNH_2$+1.2LiH	6.2	5.9	4.7
($LiNH_2$+1.2LiH)+5 wt.% G	5.9	5.6	5.2

Therefore, $LiNH_2$ does not completely react with LiH, and consequently hydrogen capacity is lost. As shown in Table 8-1, the mixture with graphite shows nearly the same theoretical hydrogen capacity considering the purity of the starting materials. This result provides one more piece of evidence of the benefits of the graphite additive. Fig. 8-7 b) shows the Arrhenius plots for the estimate of the apparent activation energy. The different slopes of the Arrhenius lines indicate a substantial difference in the apparent activation energies for the materials with and without graphite. It is striking that the addition of graphite actually increases the apparent activation energy from 57 to 90 kJ/mol.

Fig. 8-8 compares the apparent activation energies obtained by the JMAK/Arrhenius and Kissinger methods. It is obvious that both the Kissinger and volumetric methods give nearly identical values of the apparent activation energy of desorption according to reaction (3-2).

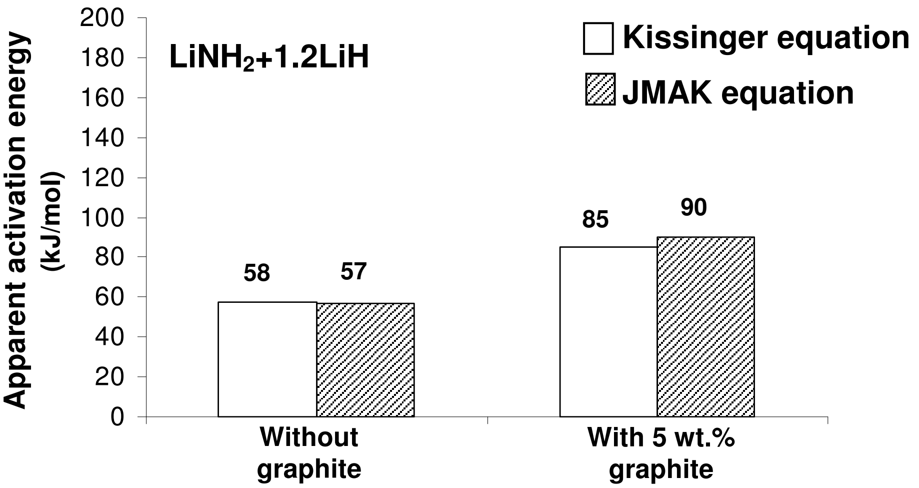

Fig. 8-8 Comparison of apparent activation energies obtained from the Kissinger and Arrhenius methods for the mixtures without and with 5 wt.% G

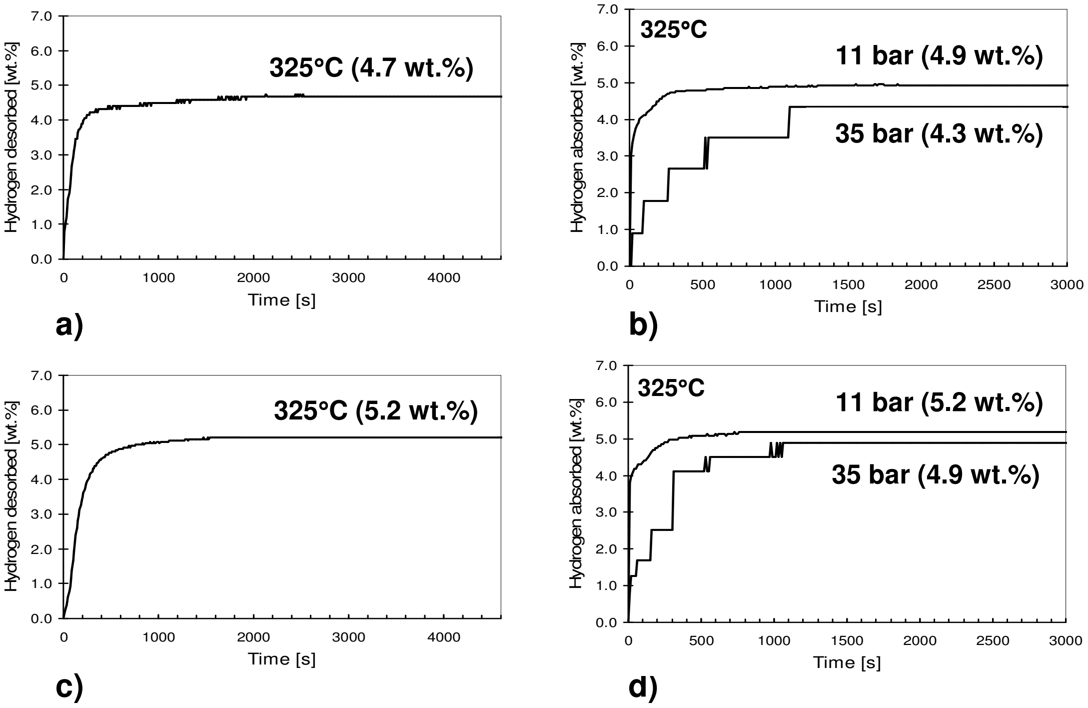

Fig. 8-9 a) Desorption curve at 325°C under 1 bar H_2 pressure and b) corresponding absorption curves at 325°C under 11 and 35 bar H_2 pressure for the ($LiNH_2$+1.2LiH) mixture ball milled for 25 h. c) Desorption curve at 325°C under 1 bar H_2 pressure and d) corresponding absorption curves at 325°C under 11 and 35 bar H_2 pressure for the (($LiNH_2$+1.2LiH)+5 wt.% G) mixture ball milled for 25 h

Fig. 8-9 a) and c) show desorption curves for the mixtures without and with 5 wt.% G, respectively. Fig. 8-9 b) and d) show absorption curves at 325°C under two different hydrogen pressures of 11 and 35 bar for the mixtures without and with graphite, respectively. Absorption behavior is similarly independent of the presence of graphite. Interestingly, the lower absorption hydrogen pressure of 11 bars improves the kinetics of hydrogen absorption compared to the higher hydrogen pressure of 35 bars. It is possible that the high-pressure hydrogen reacts at a high rate with the Li_2NH particle, and, subsequently, a layer of $LiNH_2$ is immediately created on the particle surface as shown in Appendix C. This layer blocks the hydrogen from diffusing into the particle core, which makes the absorption kinetics slower than those used at the lower hydrogen pressure (11 bars).

Fig. 8-10 compares XRD patterns of the mixtures without and with graphite after the desorption test at 325°C. According to JCPDS file No. 06-0418 and 06-0417 for $LiNH_2$ and Li_2NH, respectively, most of the principal diffraction peaks of $LiNH_2$ and Li_2NH overlap except for a couple of peaks at $2\Theta=17.7$ and 19.7° for $LiNH_2$; thus, these peaks can be used as indicators of the presence of the $LiNH_2$ phase in the mixture. It is evident that ($LiNH_2$+1.2LiH) without graphite still exhibits the $LiNH_2$ peak at $2\Theta=19.7°$ (Fig. 8-10a), whereas (($LiNH_2$+1.2LiH)+5 wt.% G) exhibits no retained $LiNH_2$ peaks. The existence of $LiNH_2$ after the desorption process is an indicator of incomplete desorption reactions (3-2) and (3-3). As proposed in Chapter 7, $LiNH_2$ is unable to completely react with LiH, due to the partial hydrolysis and oxidation of LiH according to reactions (8-2), (8-3), (8-5) and (8-6), and, consequently, the unreacted $LiNH_2$ is retained after the desorption process as evidenced by its diffraction peaks in Fig. 8-10 a). This result is additional strong evidence that graphite can improve the stability of LiH because the XRD profile of ($LiNH_2$+1.2LiH) with graphite in Fig. 8-10 b) does not show retained $LiNH_2$ peaks after desorption. However, both mixtures still have LiH peaks after the desorption test. The LiH diffraction peaks in Fig. 8-10 a) for the graphite-free ($LiNH_2$+1.2LiH) mixture arise from the inactive LiH portion due to its hydrolysis/oxidation. In contrast, the LiH diffraction peaks after the desorption test of the (($LiNH_2$+1.2LiH)+5 wt.% G) mixture in Fig. 8-10 b) arise from the unreacted excessive 20% mole LiH added to the mixture with graphite.

In addition, at higher temperatures of desorption, the conversion of LiOH into Li_2O may occur according to reactions (8-7) and (8-8) [66]:

$LiOH + LiH = Li_2O + H_2$ $\Delta G = -49$ kJ/mol (8-7)

$2LiOH = Li_2O + H_2O$ $\Delta G = 97$ kJ/mol (8-8)

Li_2O formed at high temperatures may react with water, and LiOH may reform at room temperature (after cooling) according to reaction (8-4). This mechanism is plausible for the ($LiNH_2$+1.2LiH) mixture (Fig. 8-10 a)), but it is not feasible for the ($LiNH_2$+1.2LiH)+5 wt.% G) mixture (Fig. 8-10 b)) because Li_2O cannot react with water in the latter because water can be repelled from the hydrophobic graphite surface coating around the LiH particles. Additionally, the diffraction peaks of Li_2O observed in Fig. 8-10 b) probably arise from an impurity in commercial $LiNH_2$. To confirm the reversibility of reaction (3-2), XRD analysis for the mixture with graphite (($LiNH_2$+1.2LiH)+5 wt.% G) after desorption and absorption at 325°C under 11 bars was performed as shown in Fig. 8-11 b) and c) and compared to the XRD pattern of a ball milled sample in Fig. 8-11 a). After dehydrogenation, the $LiNH_2$ peaks disappear (Fig. 8-11 b)). The XRD pattern in Fig. 8-11 c) confirms that reaction (3-2) is completely reversible because the Li_2NH phase forms after the hydriding reaction and the $LiNH_2$ and LiH phases re-appear after the dehydriding reaction.

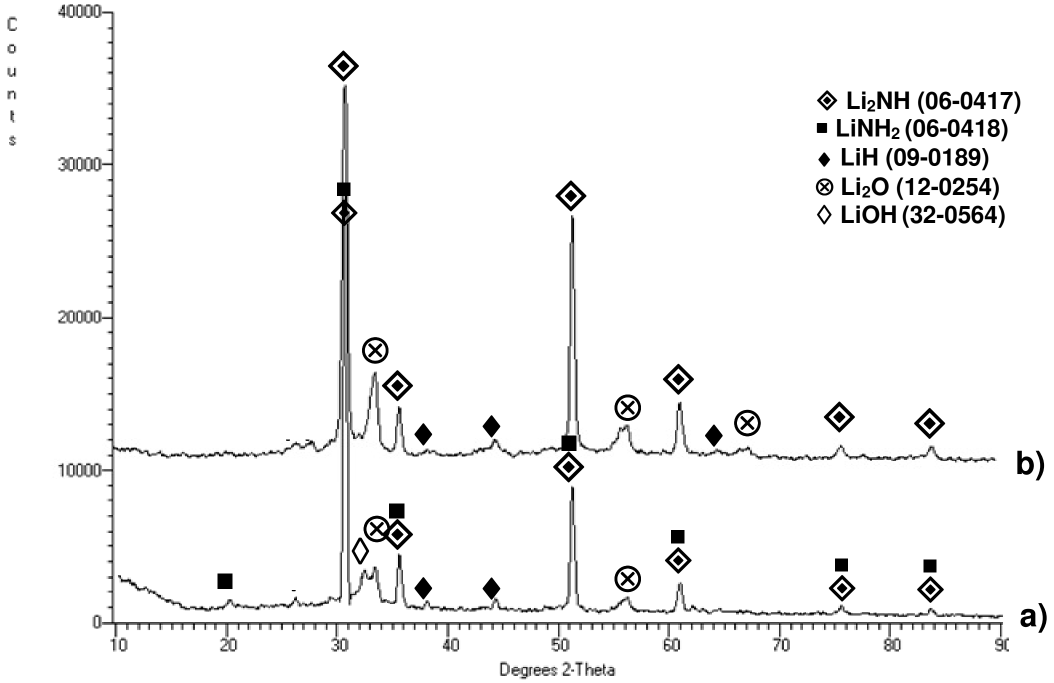

Fig. 8-10 Comparison of XRD profiles for a) ($LiNH_2$+1.2LiH) and b) (($LiNH_2$+1.2LiH)+5 wt.% G), both of which were milled for 25 h and subsequently desorbed at 325°C under 1 bar H_2 pressure

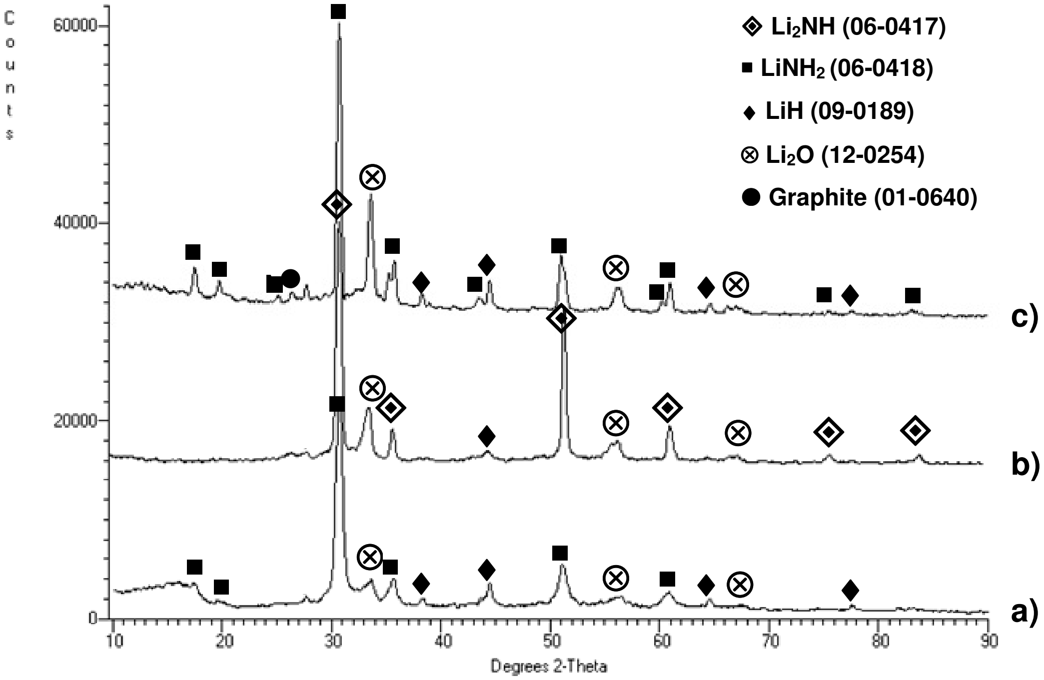

Fig. 8-11 Comparison of XRD profiles for a) ball milled (($LiNH_2$+1.2LiH)+5 wt.% G), b) desorbed at 325°C under 1 bar H_2 pressure after ball milling, and c) absorbed at 325°C under 11 bar H_2 pressure after desorption

8-3. Discussion

8-3-1. Enthalpy and entropy change for the hydrogen desorption reaction

Some controversy in the literature related to the magnitude of the enthalpy change (ΔH) of the dehydrogenation reaction (-44.5 kJ/molH_2 [56] and -65.6 kJ/molH_2 [67]) prompted us to perform experiments using a step-wise desorption method. In this method, every following desorption is carried out on a partially desorbed sample that contains progressively decreasing quantities of hydrogen. In addition, the increase in pressure occurs within a fixed time period during which some desorption may also occur. This method is much faster than the conventional PCT but may not be as accurate as the conventional PCT method, due to the factors mentioned above.

Fig. 8-12 a) and c) show step-wise desorption curves at 275, 285 and 295°C with corresponding equilibrium plateau pressures for the mixtures without and with 5 wt.% G, respectively. The results of the enthalpy and entropy change values obtained from the Van't Hoff relationship (Eq. (2-2)) are shown in Fig. 8-12 b) and d) for the mixtures without and with 5 wt.% G, respectively. As can be seen, the enthalpy and entropy changes of reaction (3-2) are -62.4 kJ/mol and -61.0 kJ/molH_2 and 117.8 and 115.8 J/molK for the ($LiNH_2$+1.2LiH) mixtures without and with 5 wt.% G, respectively. Within the experimental error, there is no measurable effect of graphite additive on the thermodynamic properties.

The enthalpy change values obtained in the present work are slightly lower than those reported elsewhere [67] (-65.6 kJ/molH_2). Excellent coefficients of fit to the Van't Hoff lines in Fig. 8-12 b) and d) give strong evidence that the step-wise method is notably accurate at least for the hydride systems investigated in the present work.

Fig. 8-13 a) and b) show the plateau pressure vs. temperature plots computed from the Van't Hoff relationship (Eq. (2-2)), and the thermodynamic data is shown in Fig. 8-12 b) and d). It is evident that the equilibrium temperature at the atmospheric pressure of hydrogen (0.1 MPa H_2) is 256.8°C and 253.9°C for the ($LiNH_2$+1.2 LiH) mixtures without and with 5 wt.% G milled for 25 h, respectively. Such high equilibrium temperatures also explain the sluggish desorption rate at 250°C observed in Fig. 8-12 a). It is also rather obvious that both of these hydride systems definitely cannot be employed for hydrogen desorption/absorption below 100°C. However, the easily reversible (($LiNH_2$+1.2 LiH)+5 wt.% G) hydride system is a potential candidate for hydrogen storage at higher temperatures, which is relevant for high-temperature fuel cells.

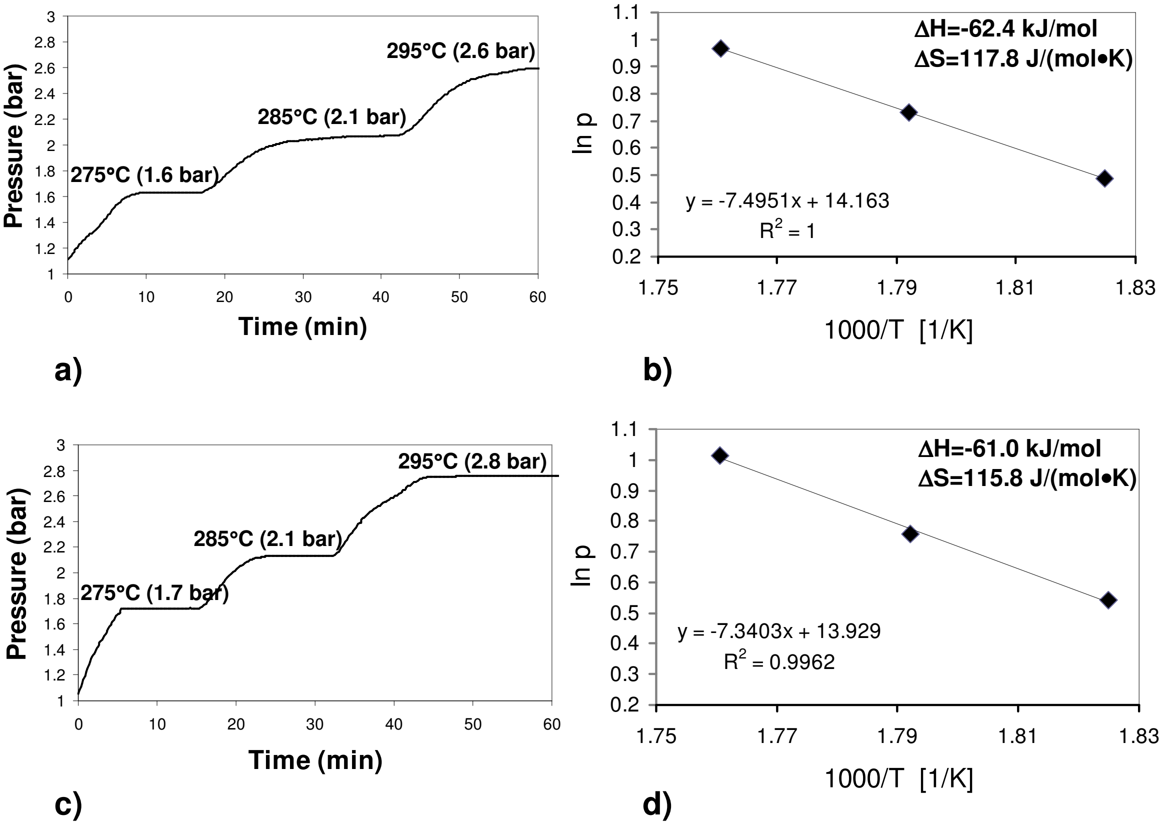

Fig. 8-12 a) Step-wise desorption curves at varying temperatures and b) the corresponding Van't Hoff plot for the (LiNH$_2$+1.2LiH) mixture without graphite. c) Step-wise desorption curve at varying temperatures and d) the corresponding Van't Hoff plot for the (LiNH$_2$+1.2LiH) mixture with 5 wt.% graphite

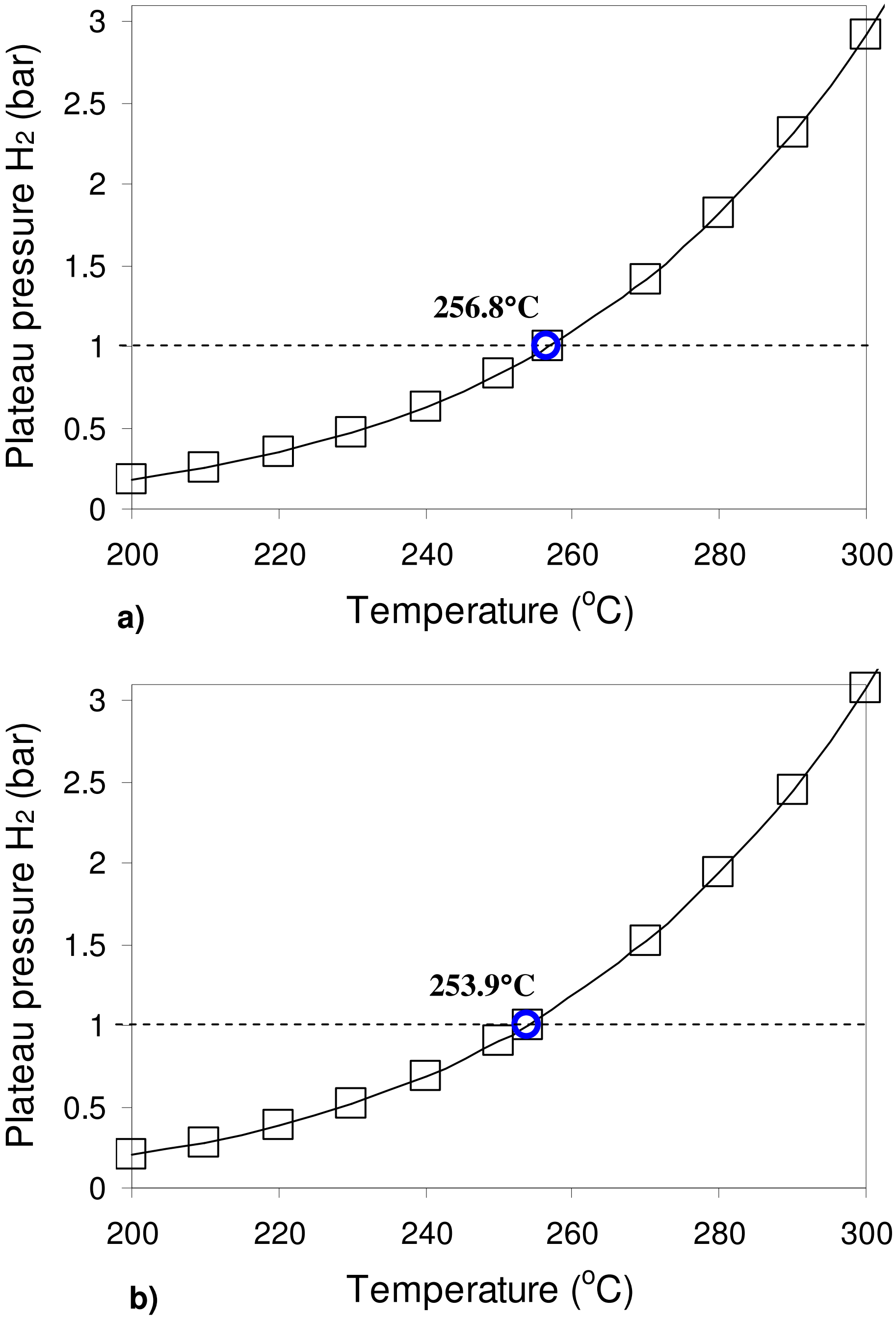

Fig. 8-13 Plateau pressure vs. temperature for a) ($LiNH_2$+1.2LiH) and b) {($LiNH_2$+1.2LiH)+5 wt.% G} mixtures milled for 25 h

9. ($LiNH_2$+nMgH_2) (n=0.55, 0.6, and 0.7)

9-1. ($LiNH_2$+nMgH_2) (n=0.55, 0.6, and 0.7) without catalysts

9-1-1. Effect of milling on the microstructure of hydride mixtures

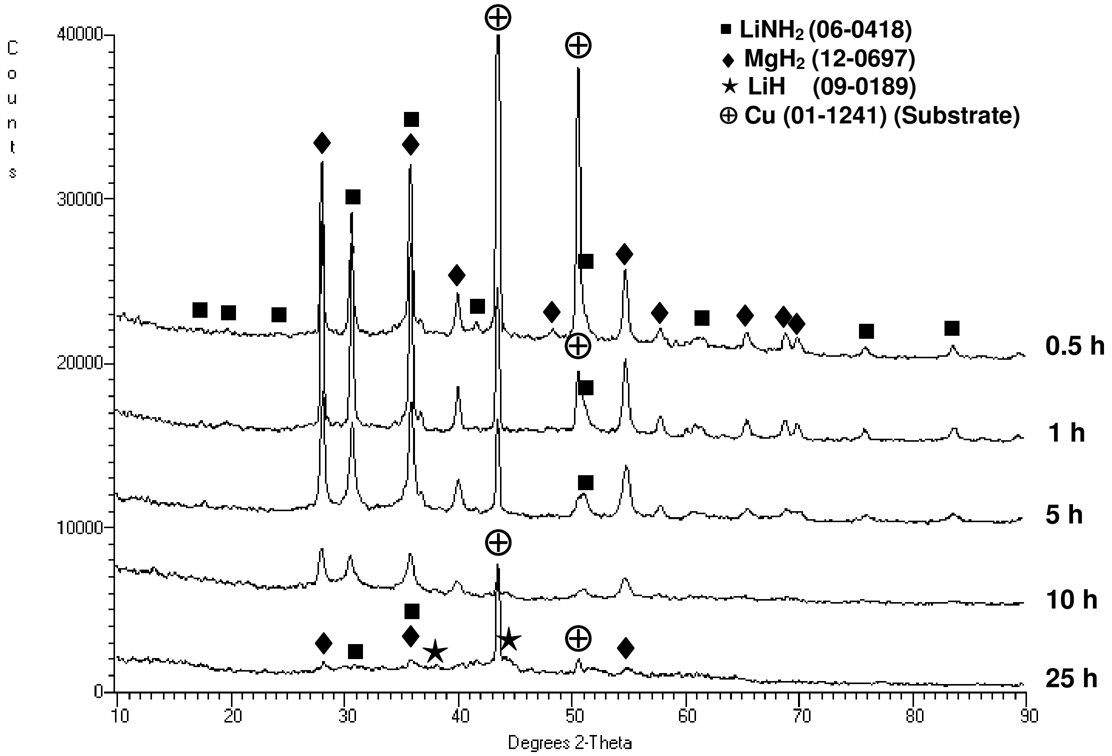

Fig. 9-1 XRD patterns of the ($LiNH_2$+0.7MgH_2) mixtures milled for various milling times (IMP67 mode)

XRD patterns of the ($LiNH_2$+0.7MgH_2) mixtures milled for various milling times are shown in Fig. 9-1. The mixture milled under the IMP67 mode for 10 h still consists of the original $LiNH_2$ and MgH_2 phases. After 25 h of ball milling under the same milling mode, two small new peaks are observed at 38.1 and 44.3° (2θ), which can be assigned to the LiH phase

(JCPDS file No. 09-0189). However, XRD peaks of the $LiNH_2$ and MgH_2 phases are still observed in the XRD pattern. The presence of the LiH phase suggests that a certain quantity of the starting mixture is converted to $Mg(NH_2)_2$ and LiH by the metathesis reaction [102, 107, 108]. However, it is difficult to establish the presence of the $Mg(NH_2)_2$ phase using XRD because this compound is easily deformed into an amorphous state under the energetic ball milling process [107]. Shahi et al. [138] reported the formation of $Mg(NH_2)_2$ and LiH during the ball milling for the ($LiNH_2$+0.55MgH_2) mixture. Therefore, in the ($LiNH_2$+nMgH_2) (n=0.55, 0.6, and 0.7) system, the $LiNH_2$ and MgH_2 phases tend to be converted to $Mg(NH_2)_2$ and LiH by the metathesis reaction depending on the milling duration and energy. In addition, there are no pressure changes during the ball milling. The existence of the $Mg(NH_2)_2$ phase during the ball milling will be shown in Chapter 10 and 11.

9-1-2. Thermal behavior of ($LiNH_2$+nMgH_2) (n=0.55, 0.6, and 0.7)

Fig. 9-2 compares DSC curves of the mixtures with various molar ratios of MgH_2 and $LiNH_2$ milled for a) 1 h and b) 25 h, respectively. As can be seen in Fig. 9-2, the mixtures exhibit three endothermic peaks irrespective of the molar ratios and the milling time, which indicates that the mixtures decompose in a three-step reaction. It is also remarkable that each reaction corresponding to the three endothermic peaks begins at a lower temperature and ends sooner as the molar ratio of MgH_2/$LiNH_2$ and the milling time increase. In particular, peak temperatures for the first and second endothermic reaction for the 1:0.55 $LiNH_2$/MgH_2 mixture are remarkably reduced from 300.9 to 218.8°C and from 401.8 to 344.9°C by increasing the milling time from 1 h to 25 h, respectively. Additionally, the increase of the molar ratio of MgH_2 and $LiNH_2$ can slightly reduce peak temperatures as shown in Fig. 9-2.

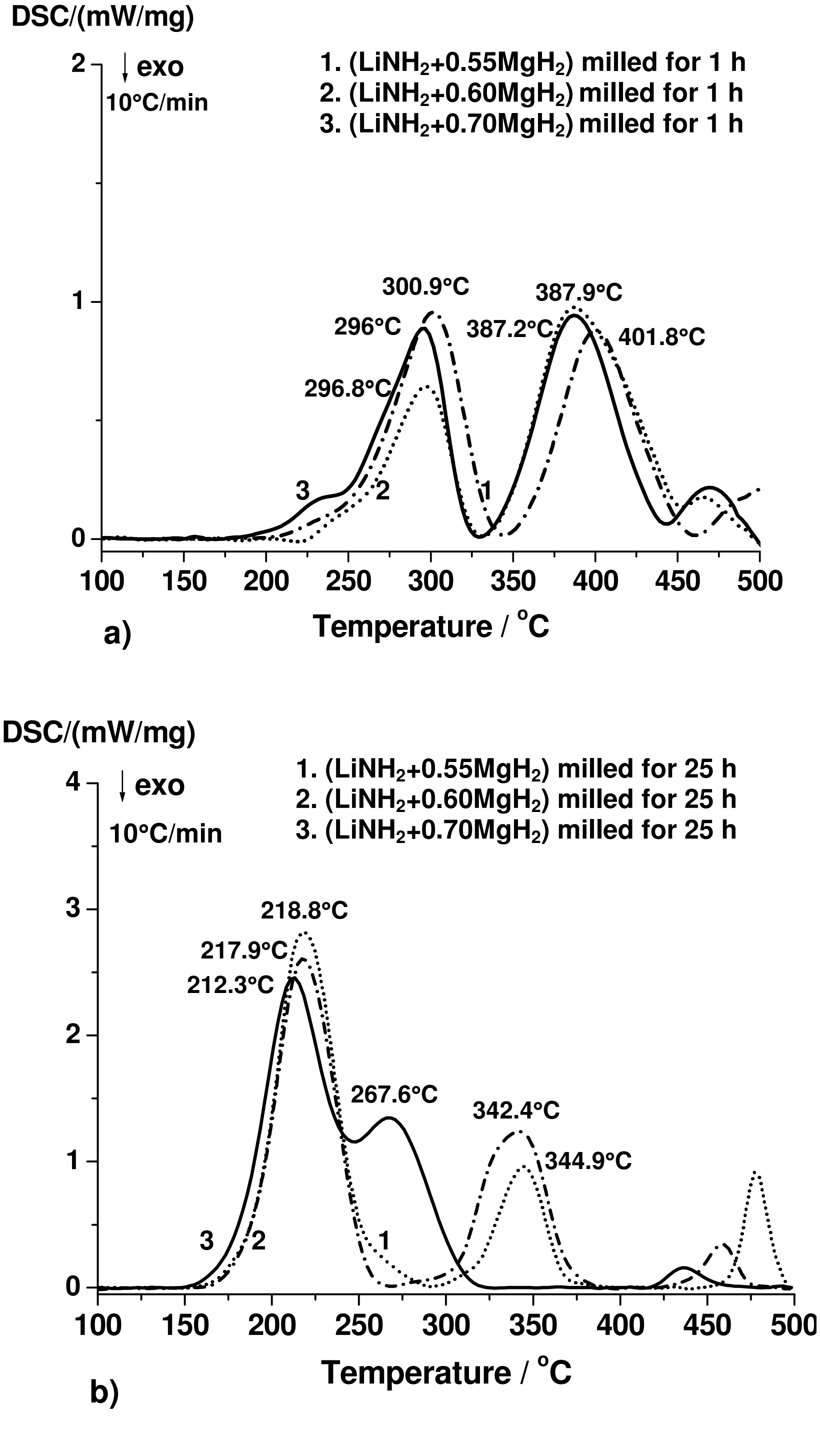

Fig. 9-2 DSC curves of the ($LiNH_2$+nMgH_2) mixtures milled for a) 1 h and b) 25 h: n=0.55, 0.60 and 0.70 (IMP67 mode)

In contrast to n=0.5 and 0.6, the system with n=0.7 milled for 25 h represents the overlap of the first and second endothermic peak. It is also worth highlighting that the intensity of the third endothermic peak decreases as the molar ratio of $MgH_2/LiNH_2$ increases.

Fig. 9-3 shows the dependence of DSC curves on the milling time for the ($LiNH_2$+0.7MgH_2) mixture. The mixture milled for 1 h has three endothermic peaks, and the second and third peaks overlap, whereas the mixture milled for 10 h reveals only two endothermic peaks. However, the third endothermic peak reappears after 25 h of ball milling. It is likely that the third endothermic peak is a result of the incompletion of both reactions corresponding to the first and second endothermic peaks because the second reaction starts before the first reaction is complete in the case of the 25 h milled mixture. Therefore, the retained phases can be decomposed through the endothermic reaction. The reaction pathways corresponding to the three endothermic peaks will be discussed later.

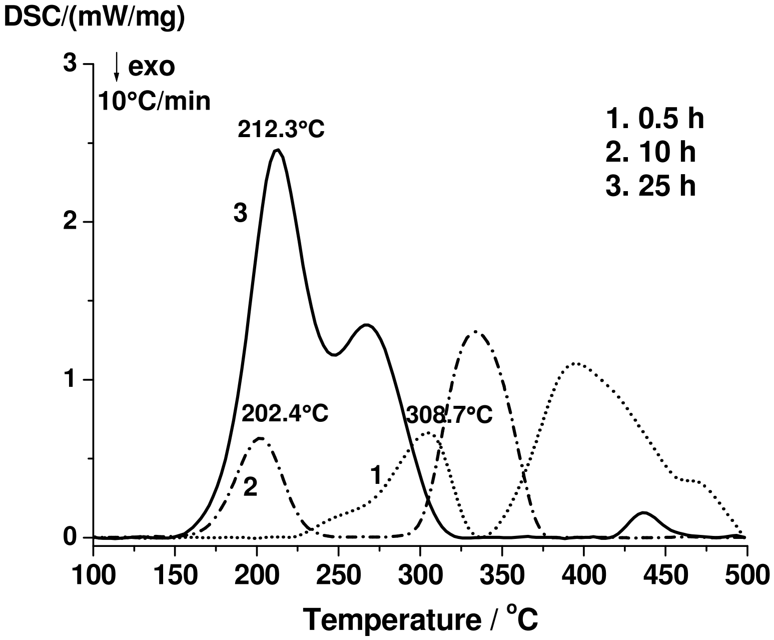

Fig. 9-3 DSC curves of the ($LiNH_2$+0.7MgH_2) mixtures milled for various milling times (IMP67 mode)

9-1-3. Reaction pathways occurring during dehydrogenation

To identify the reaction pathways corresponding to three endothermic peaks for the 25 h milled ($LiNH_2$+0.7MgH_2) mixture as shown in Fig. 9-3, samples at different DSC stages marked in DSC curves as shown in Fig. 9-4 a) were collected and analyzed using both XRD and FT-IR. When the 25 h milled ($LiNH_2$+0.7MgH_2) mixture is heated to 225°C, the diffraction peaks of $Li_2Mg(NH)_2$ phase are shown in Fig. 9-4 b), while XRD peaks of the LiH phase disappear. Further heating of the sample to 350 and 500°C leads to the formation of Mg_3N_2 and LiH phases, while XRD peaks of MgH_2 are no longer detectable. Unfortunately, the strongest Bragg peak ($2\Theta=30.64°$) of $LiNH_2$ and $Li_2Mg(NH)_2$ overlaps (the reader is referred to JCPDS file # 06-0418 and ICSD file # 157493 for $LiNH_2$ and $Li_2Mg(NH)_2$, respectively). This overlap renders the XRD test inconclusive because the presence of $LiNH_2$ cannot be confirmed unambiguously. Therefore, FT-IR analysis was performed to establish clearly the formation of $Li_2Mg(NH)_2$ and the presence of $LiNH_2$ in each heating stage. As shown in Fig. 9-4 c), the FT-IR spectrum of the mixture heated to 350°C reveals characteristic absorption lines at 3180 and 3163 cm^{-1} [131] for $Li_2Mg(NH)_2$ and at 3312 and 3258 cm^{-1} [131] for retained $LiNH_2$. After heating to 500°C, Li_2NH becomes visible at 3180 and 3258 cm^{-1} [67]. The presence of Li_2NH suggests that the decomposition of retained $LiNH_2$ occurs as discussed in Chapter 7. However, there is no $Mg(NH_2)_2$ phase in any heating stages, which indicates that this phase is consumed at the initial heating stage. The results of XRD and FT-IR analyses are summarized in Table 9-1.

To confirm the gaseous species released during heating, a temperature programmed desorption (TPD) test was performed on the mixture of $LiNH_2$-MgH_2 (1:0.7) milled for 25 h, and the result is presented in Fig. 9-5.

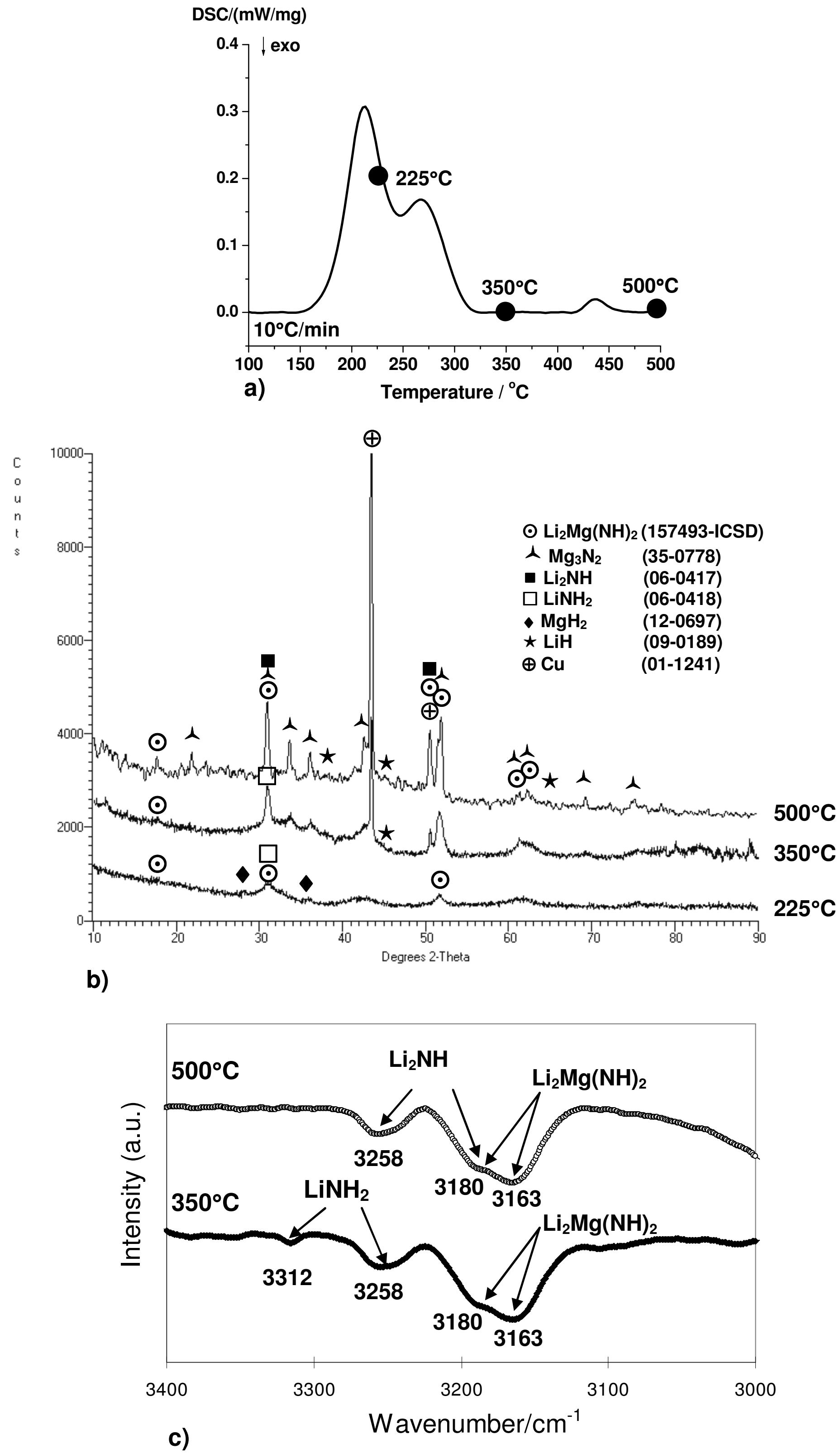

Fig. 9-4 a) DSC curves of the ($LiNH_2$+0.7MgH_2) mixture milled for 25 h (IMP67 mode), b) XRD patterns at three temperatures and c) FT-IR absorption spectra at two temperatures

Table 9-1. Reaction pathways for the ($LiNH_2$+0.7MgH_2) mixtures milled for 25 h (IMP67 mode) (Based on DSC analysis in Fig. 9-4)

T(°C)	$LiNH_2$	MgH_2	$Li_2Mg(NH)_2$	Mg_3N_2	LiH	$Mg(NH_2)_2$	Li_2NH
R.T. (after ball milling)	O	O	-	-	O	O	-
225	O	O	O	-	-	-	-
350	O	-	O	O	O	-	-
500	-	-	O	O	O	-	O

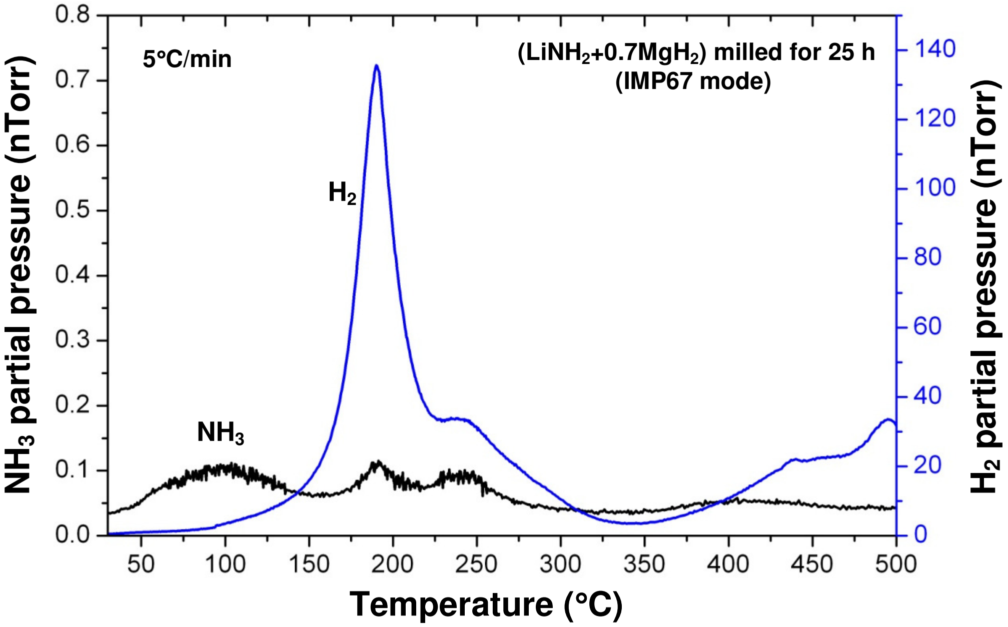

Fig. 9-5 TPD spectra for the ($LiNH_2$+0.7MgH_2) milled for 25 h (IMP67 mode)

When the mixture is heated to 500°C at a rate of 5°C/min, two hydrogen desorption peaks exhibiting a doublet with peak temperatures at 190°C and 240°C are clearly observed up to 340°C, which correspond to the first and second endothermic peaks as shown in Fig. 9-4 a). It clearly indicates that the mixture decomposes in a two-step reaction to release H_2. Moreover, hardly any NH_3 emission (ppm level) is detected in the TPD measurements up to 500°C within our experimental accuracy. However, the result of TPD analysis is beyond our expectation because we expected the release of NH_3 in the temperature range of 420-460°C based on the DSC analysis and the corresponding XRD and FT-IR analysis as shown in Fig. 9-4; the third endothermic peak is clearly shown in the DSC curve (Fig. 9-4 a)), which corresponds to the melting and decomposition reaction of $LiNH_2$ and consequently forms Li_2NH and releases NH_3 according to reaction (3-3). One clue is the heating rate; DSC analysis was performed at a heating rate of 10°C/min, while TPD analysis was processed at a heating rate of 5°C/min. Therefore, it can be understood that if the mixture is heated at a slow rate (5°C/min), then the decomposition reaction of the retained $LiNH_2$ can be avoided, which means that the first and second reaction can be completed.

Markmaitree et al. [131] reported that high-energy ball milling can increase the reaction rates and alleviate the NH_3 emission problem, but their ball milling conditions were not sufficient to solve the NH_3 emission problem of the ($LiNH_2$+ $0.55MgH_2$) mixture. However, it is likely that the problem is not solely due to ball milling conditions. As can be seen in DSC curves of mixtures with n=0.55 and 0.6 (Fig. 9-2 b)), these systems show the third endothermic peak, which has been used as the indicator to show the degree of the completion of the reaction, although they don't have any overlap of the first and second endothermic peaks. It indicates that the above-mentioned reactions are incomplete, due to the kinetic problem between each constituent. Thus, NH_3 can be released during the dehydrogenation, even after high-energy ball milling (IMP67) for 25 h. However, in the case of the ($LiNH_2$+0.7MgH_2) mixture milled for 25 h, it can be surmised that the third endothermic peak does not come from the kinetic problem but rather the overlap of both endothermic peaks because the third endothermic peak is not shown in DSC curve of the 10 h milled ($LiNH_2$+0.7MgH_2) mixture (Fig.9-3), which means that the reaction can be complete even after the shorter milling time. Therefore there are no kinetic issues on this composition. Consequently, to improve the reaction rate and eliminate NH_3 emission, a molar ratio greater than n=0.5, which has been proposed in other studies [83, 86], is needed. Thus, the optimum molar ratio of $MgH_2/LiNH_2$ in our study should be 0.7 in the ($LiNH_2$+nMgH_2) (n=0.55, 0.6, and 0.7) system.

Based on the above analyses, the reaction pathways of hydrogen desorption for the 25 h milled ($LiNH_2$+0.7MgH_2) mixture can be proposed. As mentioned above, $LiNH_2$ is partially converted to $Mg(NH_2)_2$ and LiH by the metathesis reaction with a specific quantity of MgH_2 during ball milling. Thus, at the low temperature range corresponding to the first endothermic peak shown in Fig. 9-4 a), the $LiNH_2$ reacts with MgH_2 as reported by Luo et al.[86] and Xiang et al. [83] ($LiNH_2+0.5MgH_2 \rightarrow 0.5Li_2Mg(NH)_2+H_2$), and, simultaneously newly formed $Mg(NH_2)_2$ reacts with LiH as reported by Barison et al. [135] ($0.5Mg(NH_2)_2+LiH \rightarrow 0.5Li_2Mg(NH)_2+H_2$). Both reactions form $Li_2Mg(NH)_2$ and H_2. Therefore, in the first step (at low temperature), the reaction can be described as follows:

$$[0.5xMg(NH_2)_2+xLiH]+[(1-x)LiNH_2+(0.5-0.5x)MgH_2] \rightarrow \boldsymbol{0.5Li_2Mg(NH)_2+1.0H_2} \qquad (9\text{-}1)$$

where, x is the number of moles of newly formed LiH during the ball milling.

In the second step (performed at high temperatures), $Li_2Mg(NH)_2$ formed through reaction (9-1) reacts with retained MgH_2 to form Mg_3N_2, LiH and H_2 as proposed by Liang et al. [108] and Dolotko et al. [134]:

$$0.5Li_2Mg(NH)_2 + MgH_2 \rightarrow 0.5Mg_3N_2 + LiH + H_2 \tag{9-2}$$

Assuming reaction (9-1) and (9-2) are completed, they can be described by a series of sequential reactions as follows:

$LiNH_2+0.7MgH_2$

$\rightarrow [0.5xMg(NH_2)_2+xLiH]+[(1-x)LiNH_2+(0.7-0.5x)MgH_2]$ (after milling for 25h)

$\rightarrow \boldsymbol{0.5Li_2Mg(NH)_2}+0.2MgH_2+\boldsymbol{H_2}$ (after dehydrogenation at low temp.) (9-3)

$\rightarrow 0.4Li_2Mg(NH)_2+\boldsymbol{0.1Mg_3N_2+0.2LiH+1.2H_2}$ (after dehydrogenation at high temp.)

In total, 2.4 moles of hydrogen atoms can be obtained from the above reaction, which is approximately 5.8 wt.% of hydrogen. Considering 95% purity of the starting materials, the total maximum hydrogen storage capacity is 5.6 wt.% H_2. However, if the above-mentioned reactions cannot be completed, for example, due to the overlap between reaction (9-1) and reaction (9-2) as shown in Fig. 9-4 a), the retained $LiNH_2$ is decomposed as follows:

$$LiNH_2 \rightarrow 0.5Li_2NH + 0.5NH_3 \tag{3-3}$$

Therefore, the above-mentioned reaction (9-3) can be modified as follows:

$LiNH_2+0.7MgH_2$

$\rightarrow [0.5xMg(NH_2)_2+xLiH] + [(1-x)LiNH_2+(0.7-0.5x)MgH_2]$ (after milling for 25h)

$\rightarrow\boldsymbol{(0.5-0.5y)Li_2Mg(NH)_2}+(0.2+0.5y)MgH_2+xLiNH_2+\boldsymbol{(1-y)H_2}$ (reaction (9-1))

$\rightarrow (0.4-0.75y)Li_2Mg(NH)_2 + \boldsymbol{(0.1+0.25y)Mg_3N_2} + \boldsymbol{(0.2+0.5y)LiH} + yLiNH_2$ (9-4)

$+ \boldsymbol{(1.2-0.5y)H_2}$ (reaction (9-2))

$\rightarrow (0.4-0.75y)Li_2Mg(NH)_2 + (0.1+0.25y)Mg_3N_2 + (0.2+0.5y)LiH + (1.2-0.5y)H_2$

$+ \mathbf{0.5yLi_2NH} + \mathbf{0.5yNH_3}$ (reaction (3-3))

where y is the number of moles of retained $LiNH_2$. Therefore, the total amount of desorbed hydrogen reduces to (2.4-y) mol of hydrogen atoms per unit formula of ($LiNH_2$+0.7MgH_2). Moreover, it is worth highlighting that the relative contribution of reaction (9-2) to the total dehydrogenation capacity in reaction (9-4) increases as the amount of the retained $LiNH_2$ increases compared to reaction (9-3). It is clearly shown in reaction (9-4) that the amount of hydrogen released through reaction (9-1) is relatively reduced by 2y mole of hydrogen atoms, whereas it is increased by y mole of hydrogen atoms in reaction (9-2) compared to reaction (9-3). However, it should also be mentioned that the amount of retained $LiNH_2$ can be negligible if the mixture is heated at the low rate as mentioned above; therefore the dehydrogenation reaction pathways are getting closer to reaction (9-3) than to reaction (9-4).

9-1-4. Isothermal hydrogen storage behavior

To verify the proposed reaction pathways, the ($LiNH_2$+0.7MgH_2) mixtures milled for 25 h are dehydrogenated at various temperatures under 1 bar H_2 pressure as shown in Fig. 9-6. As mentioned above, the hydrogen release in this system takes place in a two-step reaction. Based on the TPD analysis and reaction (9-3), the maximum hydrogen-desorption amount is 4.6 wt.% (corrected for 95% purity) for the first step of the reaction in the temperature range of 50-225°C and 0.9 wt.% (corrected for 95% purity) for the second step in the temperature range of 225-340°C, which correspond to 2.0 and 0.4 mol of hydrogen atoms per unit formula of $LiNH_2$/0.7MgH_2, respectively. In total, 5.6 wt.% H_2 (corrected for 95% purity), which is equivalent to 2.4 mol of hydrogen atoms, is released as shown in reaction (9-3). As can be seen in Fig. 9-6, the mixtures desorb 0.3-4.4 wt.% H_2 in the temperature range of

125-225°C under 1 bar of H_2, which corresponds to reaction (9-1). With an increase in temperature, the hydrogen-desorption amount gradually increases. When the temperature is elevated to 400°C, another 0.8 wt.% of hydrogen is desorbed. In total, 5.3 wt.% of hydrogen is released from the sample upon heating. Although this value is still less than the calculated value of 5.6 wt.% H_2 (corrected for 95% purity) from reaction (9-3), it can be in good agreement with the experimental value of 5.3 wt.% H_2 on condition that $LiNH_2$ phase remains after the dehydrogenation up to 400°C, thus the reaction pathways process through reaction (9-4).

Dehydrogenation kinetics has also been studied at 250°C under 1 bar H_2 pressure for all samples to investigate the effect of milling duration. As can be seen in Fig. 9-7, it is clearly observed that the hydrogen desorption kinetics of the 1:0.7 $LiNH_2/MgH_2$ mixture is improved by increasing the milling time. The $LiNH_2/MgH_2$ (1:0.7) mixture milled for 25 h desorbs 4.4 wt.% H_2 at 250°C as shown in Fig. 9-6, which can be considered as the maximum hydrogen capacity at 250°C under 1 bar H_2.

To desorb 4.0 wt.% of H_2 (about 91% of the maximum hydrogen capacity), a mixture milled for 25 h only needs 9.5 min, whereas 84 and 20 min are required for the mixtures milled for 5 and 10 h, respectively. Moreover, the 1:0.7 $LiNH_2/MgH_2$ mixtures milled for 0.5 and 1 h require more than 100 min to desorb 4.0 wt.% of H_2.

Therefore, in our study, the ($LiNH_2$+0.7MgH_2) mixture milled for 25 h under IMP67 mode shows the best kinetic properties.

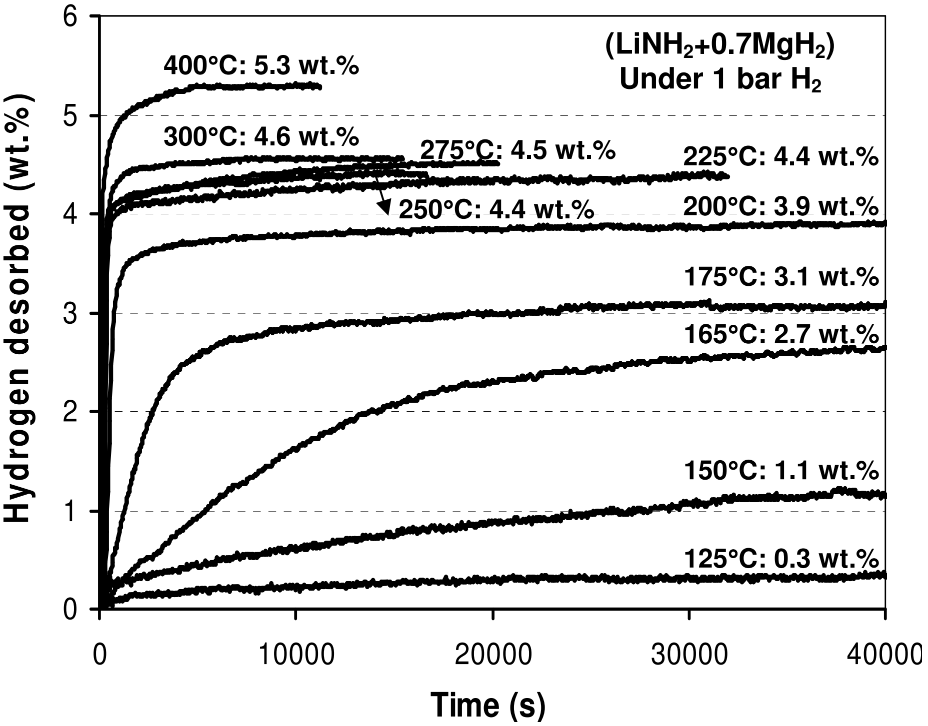

Fig. 9-6 Dehydrogenation curves at various temperatures under 1 bar H_2 for the ($LiNH_2$+0.7MgH_2) mixtures milled for 25 h (IMP67 mode)

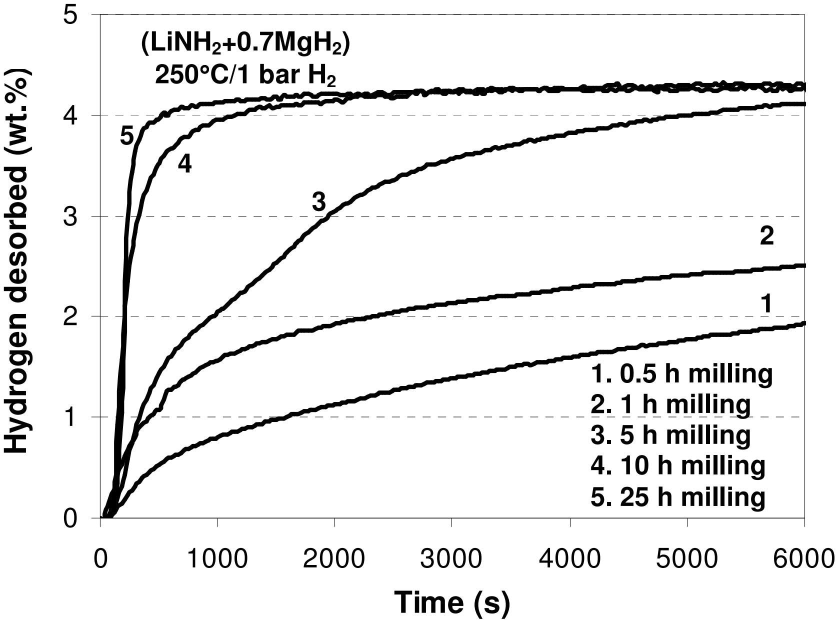

Fig. 9-7 Isothermal dehydrogenation curves at 250°C under 1 bar H_2 for the ($LiNH_2$+0.7MgH_2) mixture milled for various durations (IMP67 mode)

9-2. ($LiNH_2$+0.7MgH_2) mixtures with catalysts

9-2-1. Morphology and microstructure of powder mixtures

Fig. 9-8 shows EDS mappings of the Mg, N, and Ni elements of the 25 h milled ($LiNH_2$+0.7MgH_2) mixture with 5 wt.% n-Ni. Fig. 9-8 b) shows the distribution of Mg element which indicates the MgH_2 and $Mg(NH_2)_2$ phases and Fig. 9-8 c) represents the distribution of the $LiNH_2$ and $Mg(NH_2)_2$ phases. The figure reveals a homogeneous distribution of each constituent. The homogeneous distribution and intimate contact of each phase is the most important parameters in improving the reaction kinetics and show full reversibility; Chen et al. [96] and Barison et al. [135] reported that the reversibility of this system is dominated by a local interaction between reactants.

The grain sizes of $LiNH_2$ and MgH_2 after milling were estimated from XRD patterns for the mixtures without and with 5 wt.% n-Ni in Fig. 9-9 a) and b), respectively. It is evident that the grain sizes of both phases decrease as the milling duration increases, and its behaviors are quite similar independent of the addition of 5 wt.% n-Ni. The crystallite sizes of both $LiNH_2$ and MgH_2 decrease to 10 nm after ball milling for 25 h. It is worth noting that the longer ball-milling process causes grain size reduction; therefore, the reduced grain size results in an increased reaction rate, which is in reasonable agreement with the hydrogen desorption curves of the 1:0.7 $LiNH_2$/MgH_2 mixture shown in Fig. 9-7.

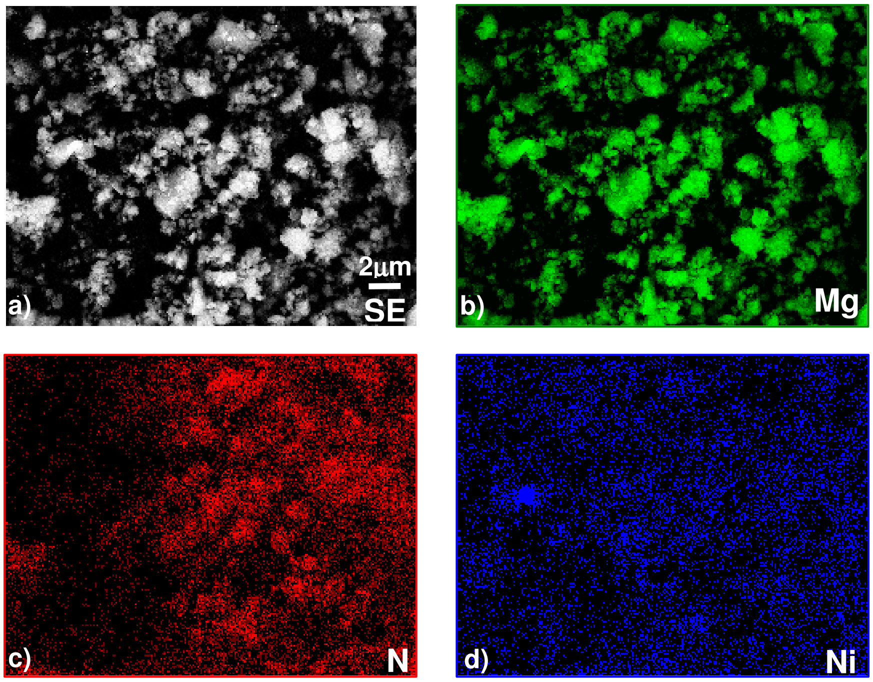

Fig. 9-8 a) Secondary electron (SE) micrograph and energy-dispersive X-ray spectroscopy (EDS) mapping for b) Mg, c) N and d) Ni elements of the ($LiNH_2$+$0.7MgH_2$) mixture with 5 wt.% n-Ni milled for 25 h (IMP67 mode)

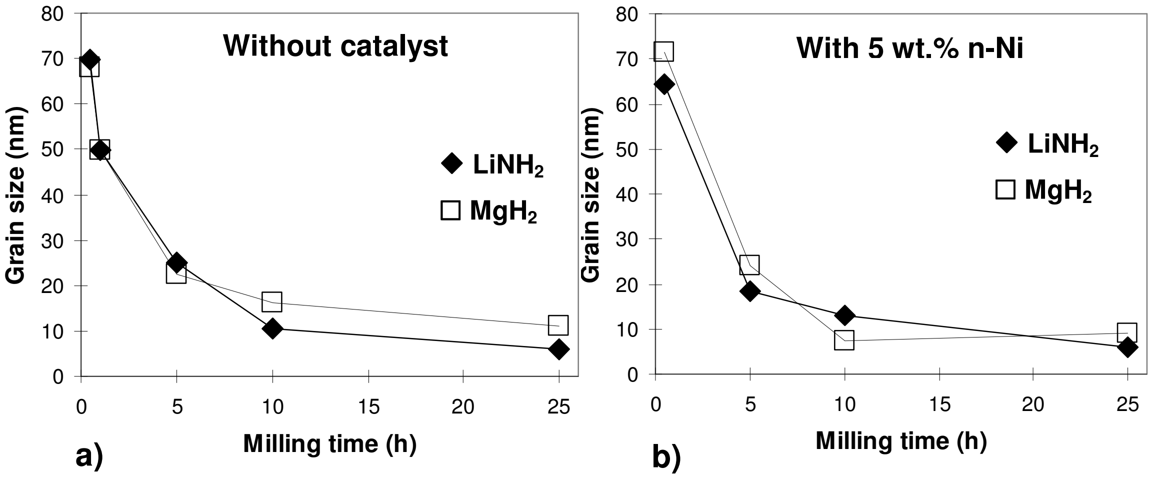

Fig. 9-9 Grain sizes as function of milling times for ($LiNH_2$+$0.7MgH_2$) a) without and b) with 5 wt.% n-Ni (IMP67 mode)

9-2-2. Thermal behavior

Fig. 9-10 represents DSC curves of {($LiNH_2$+0.7MgH_2)+5 wt.% n-Ni} mixtures milled for different amounts of time. It shows that the mixtures have similar thermal behavior to that of the same mixture without n-Ni as shown in Fig. 9-3. However, the reaction of the mixture with 5 wt.% n-Ni starts at lower temperatures and ends faster than that without a catalyst, and the peak temperature is also reduced from 212.3 to 206°C.

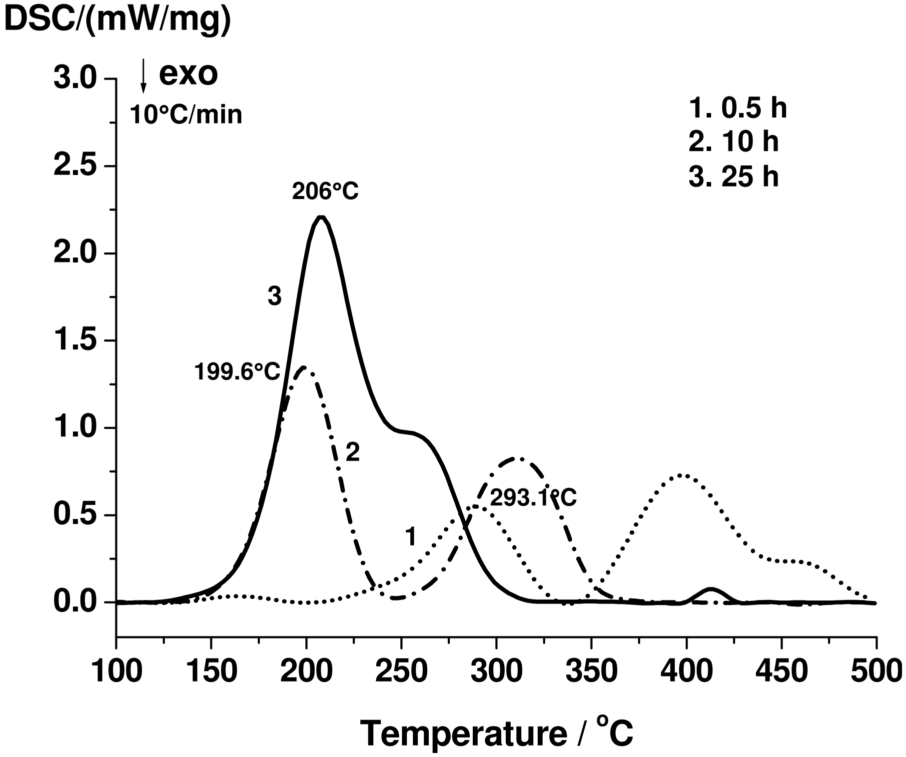

Fig. 9-10 DSC curves for the ($LiNH_2$+0.7MgH_2) mixtures with 5 wt.% n-Ni milled for various durations (IMP67 mode)

The measurements of the apparent activation energy of hydrogen desorption were collected using the Kissinger method (Eq.(6-2)). Fig. 9-11 a) shows the effect of various heating rates on DSC profiles, which is an underlying principle of the Kissinger method. It is interesting to note that in the DSC curve of the mixture heated at 5°C/min, the third endothermic peak is barely noticeable, which is in good agreement with the result of TPD analysis as shown in Fig. 9-5. The corresponding Kissinger plots for reaction (9-1) and reaction (9-2) are shown in Fig. 9-11 b) and c), respectively, for the ($LiNH_2$+0.7MgH_2) mixtures without and with catalysts milled for 25 h. The excellent correlation coefficients, R^2, obtained for the Kissinger plots in Fig. 9-11 b) and c), attest to the accuracy of the method. The apparent activation energies are shown in Fig. 9-12 and 9-13. Three interesting effects on the kinetics in this system are noted from the two figures. First, under the same processing conditions, the apparent activation energies for reaction (3-5), reaction (9-1) and reaction (9-2) decrease dramatically as the molar ratio of MgH_2/$LiNH_2$ increases from 0.55 to 0.7 in Fig. 9-12. Second, the kinetic barrier can be reduced by increasing the milling time as shown in Fig. 9-13. Several studies [92, 136, 137] have already reported that high-energy ball milling reduces the particle and crystallite sizes of powder and increases the powder's specific surface area and defect concentration. Normally, the reduced particle size and increased surface area result in an increased reaction rate, which decreases the apparent activation energy. A change in the apparent activation energy is typically related to changes in the reaction mechanism or in the energy state of the reactant(s). In our study, it is proposed that the reduction in the apparent activation energy results from both the change in the reaction pathway and an increase in the energy states of each constituent induced by high-energy ball milling.

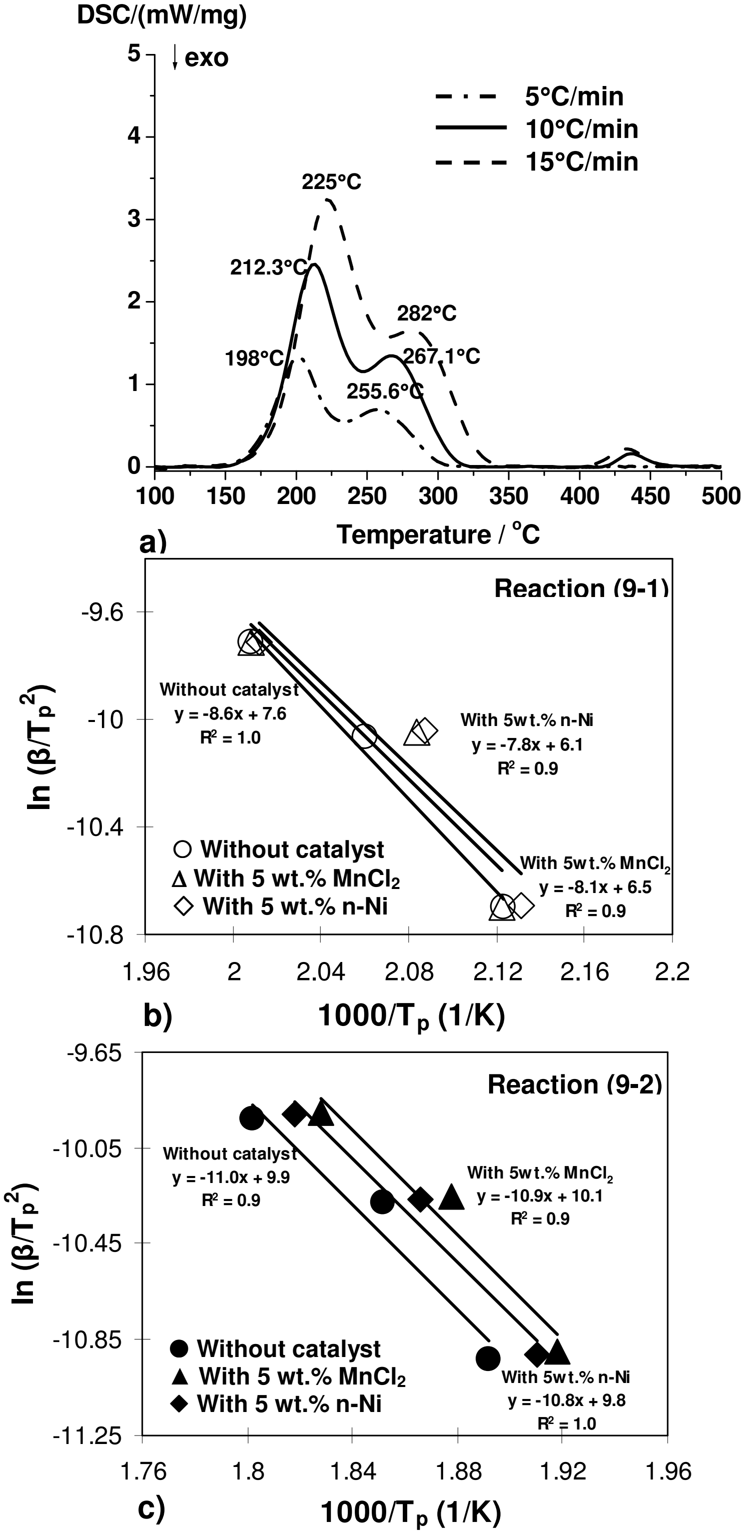

Fig. 9-11 a) DSC curves at various heating rates for the ($LiNH_2$+0.7MgH_2) mixture milled for 25 h (IMP67 mode) and b) and c) the Kissinger plots of the apparent activation energies of reaction (9-1) and reaction (9-2), respectively, after the 25 h milled ($LiNH_2$+0.7MgH_2) mixtures without and with catalysts

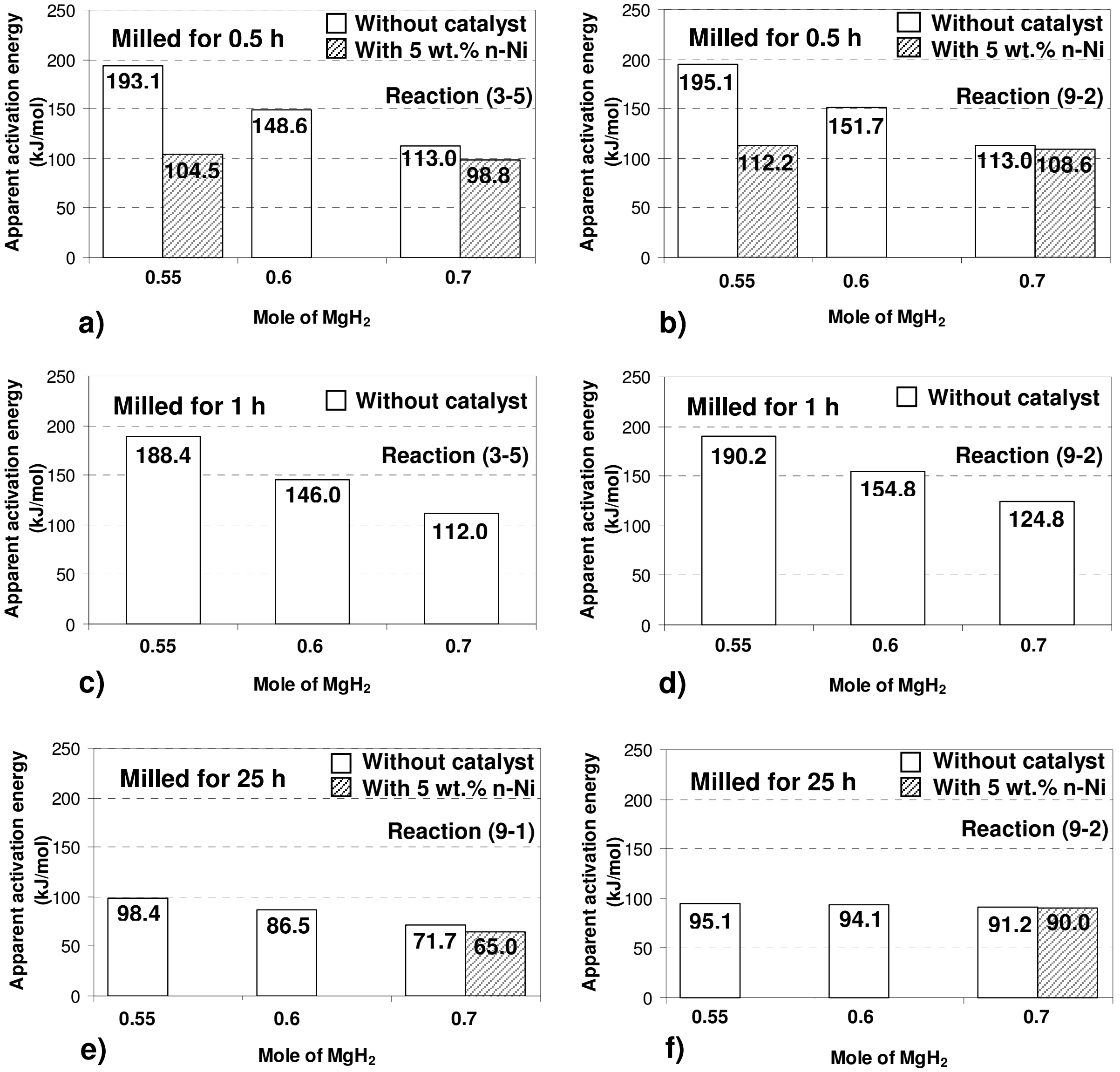

Fig. 9-12 The apparent activation energies for the ($LiNH_2$+nMgH_2) (n= 0.55, 0.60 and 0.70) mixtures milled for various durations (IMP67 mode):

- **Reaction (3-5): $LiNH_2+0.5MgH_2 \rightarrow 0.5Li_2Mg(NH)_2+H_2$**
- **Reaction (9-1): $[0.5xMg(NH_2)_2+xLiH]+[(1-x)LiNH_2+(0.5-0.5x)MgH_2] \rightarrow 0.5Li_2Mg(NH)_2+1.0H_2$**
- **Reaction (9-2): $0.5Li_2Mg(NH)_2+MgH_2 \rightarrow 0.5Mg_3N_2+LiH+H_2$**

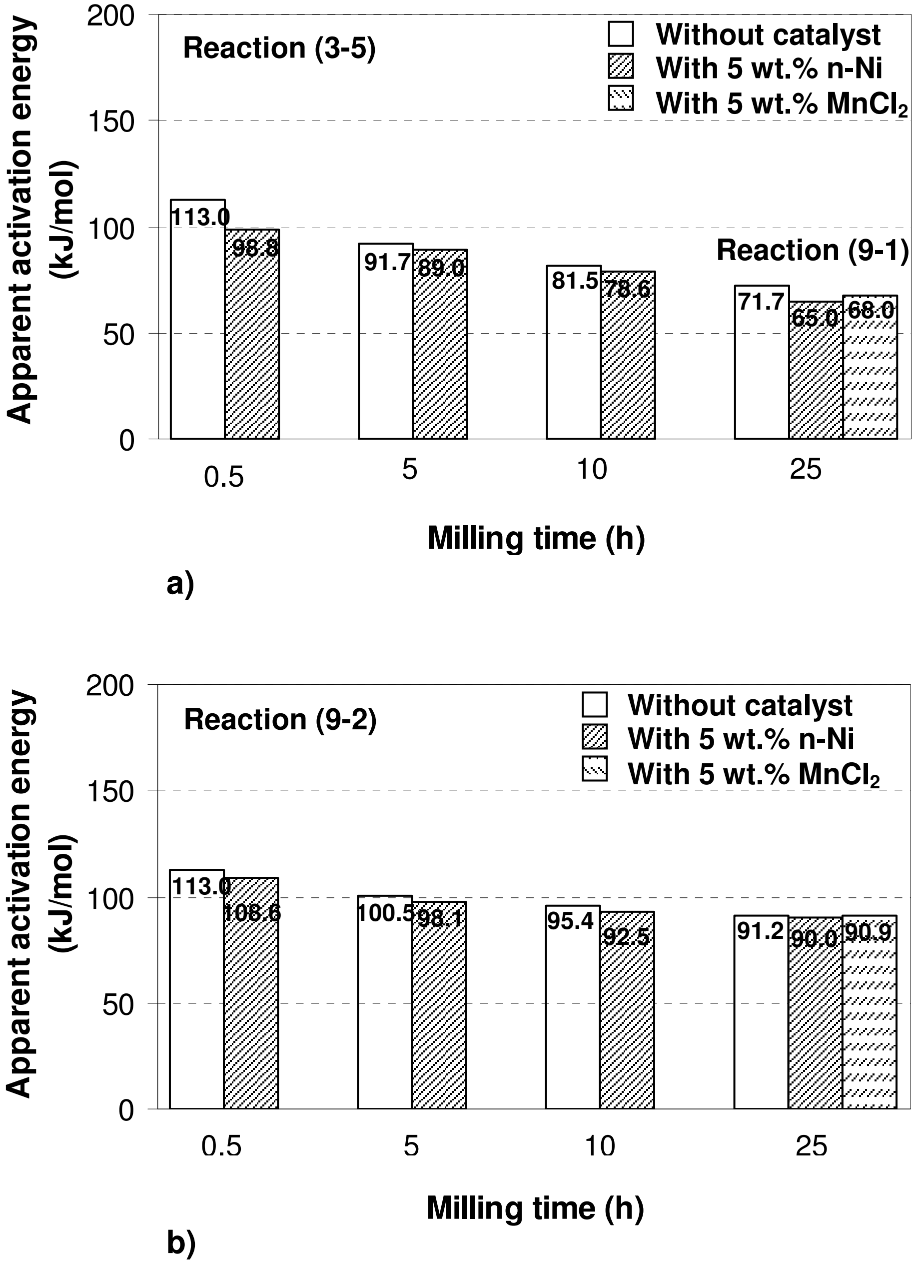

Fig. 9-13 Comparison of the apparent activation energies for the ($LiNH_2$+0.7MgH_2) mixture without and with two types of catalysts (n-Ni and $MnCl_2$) as a function of milling time (IMP67 mode)

The third important feature in Fig. 9-13 is the catalytic effect of n-Ni and $MnCl_2$ on the apparent activation energy of 1:0.7 molar mixtures in different milling stages. This effect clearly indicates that the incorporation of catalysts can reduce the kinetic barrier for the dehydrogenation of the system. In particular, n-Ni is a better catalyst for this mixture than $MnCl_2$ because the apparent activation energy of the ($LiNH_2$+0.7MgH_2) mixture with n-Ni milled for 25 h decreases from 71.7 to 65.0 kJ/mol for reaction (9-1), whereas it is less reduced when $MnCl_2$ is added.

9-2-3. Isothermal hydrogen storage behavior

To verify the catalytic effect on the dehydriding kinetics, ($LiNH_2$+0.7MgH_2) with 5 wt.% n-Ni milled for 25 h was dehydrogenated at various temperatures under 1 bar H_2 pressure as shown in Fig. 9-14. Similarly to the mixture without a catalyst, the hydrogen release in this system takes place in a two-step reaction. Based on reaction (9-3), the hydrogen-desorption amount is approximately 4.4 wt.% (corrected for 95% purity) for the first step of the reaction and 0.9 wt.% (corrected for 95% purity) for the second step, which corresponds to 2.0 and 0.4 mol of hydrogen atoms per unit of the {($LiNH_2$+0.7MgH_2)+5 wt.% n-Ni} mixture, respectively. In total, 5.3 wt.% H_2 (corrected for 95% purity), which is equivalent to 2.4 mol of hydrogen atoms, is released as shown in reaction (9-3). As can be seen in Fig. 9-14, the mixtures dehydrogenated in the temperature range of 125-225°C under 1 bar of H_2 release 0.5-4.5 wt.% H_2, which corresponds to reaction (9-1). With an increase in temperature, the hydrogen-desorption amount gradually increases. When the temperature is elevated to 400°C, another 0.7 wt.% of hydrogen is desorbed. In total, 5.2 wt.% of hydrogen is output from the sample upon heating.

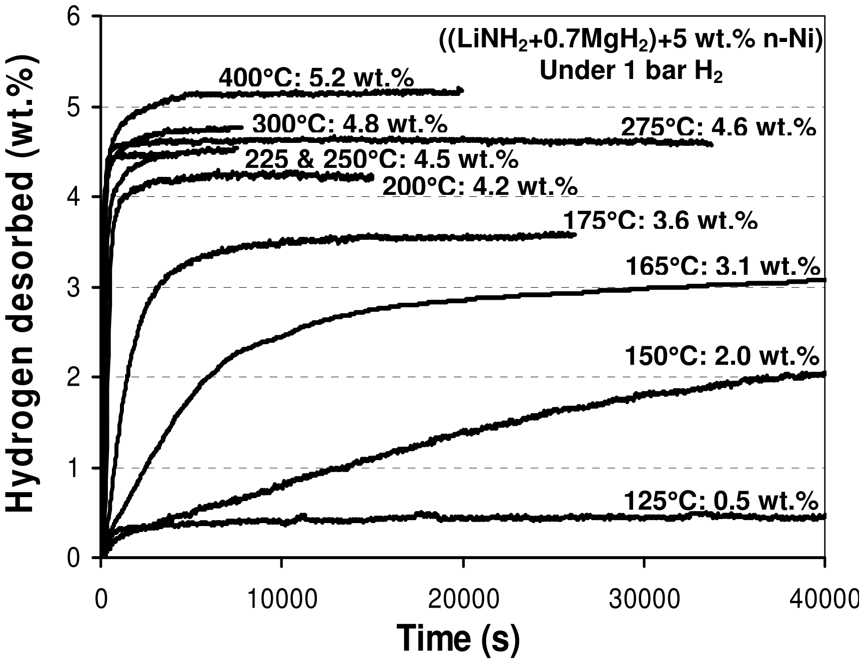

Fig. 9-14 Dehydrogenation curves at various temperatures under 1 bar H_2 for the ($LiNH_2$+0.7MgH_2) mixtures with 5 wt.% n-Ni milled for 25 h (IMP67 mode)

This result is in a good agreement with the amount of hydrogen calculated from equation (9-1) (5.3 wt.% H_2). Therefore, the dehydriding reaction pathways more closely approach those of reaction (9-3) if n-Ni is added. Another finding is that dehydrogenation curves for the mixture with n-Ni always show higher hydrogen capacities than the same mixtures without n-Ni as shown in Fig. 9-6. The only exception is the curve at 400°C, which may be a sufficiently high temperature to overcome kinetic barriers for reaction (9-1) and reaction (9-2). This striking capacity difference is most likely related to the catalytic effect of n-Ni on the dehydriding kinetics. Additionally, Fig. 9-15 represents the comparison of dehydriding curves at various temperatures under 1 bar H_2 for the ($LiNH_2$+ 0.7MgH_2) mixtures without and with 5 wt.% n-Ni and $MnCl_2$ milled for 25 h. As shown in Fig. 9-15 a), the catalytic effect of n-Ni becomes more pronounced at lower temperatures, while, in contrast to n-Ni, the addition of $MnCl_2$ results in no noticeable improvement, as shown in Fig. 9-15 b).

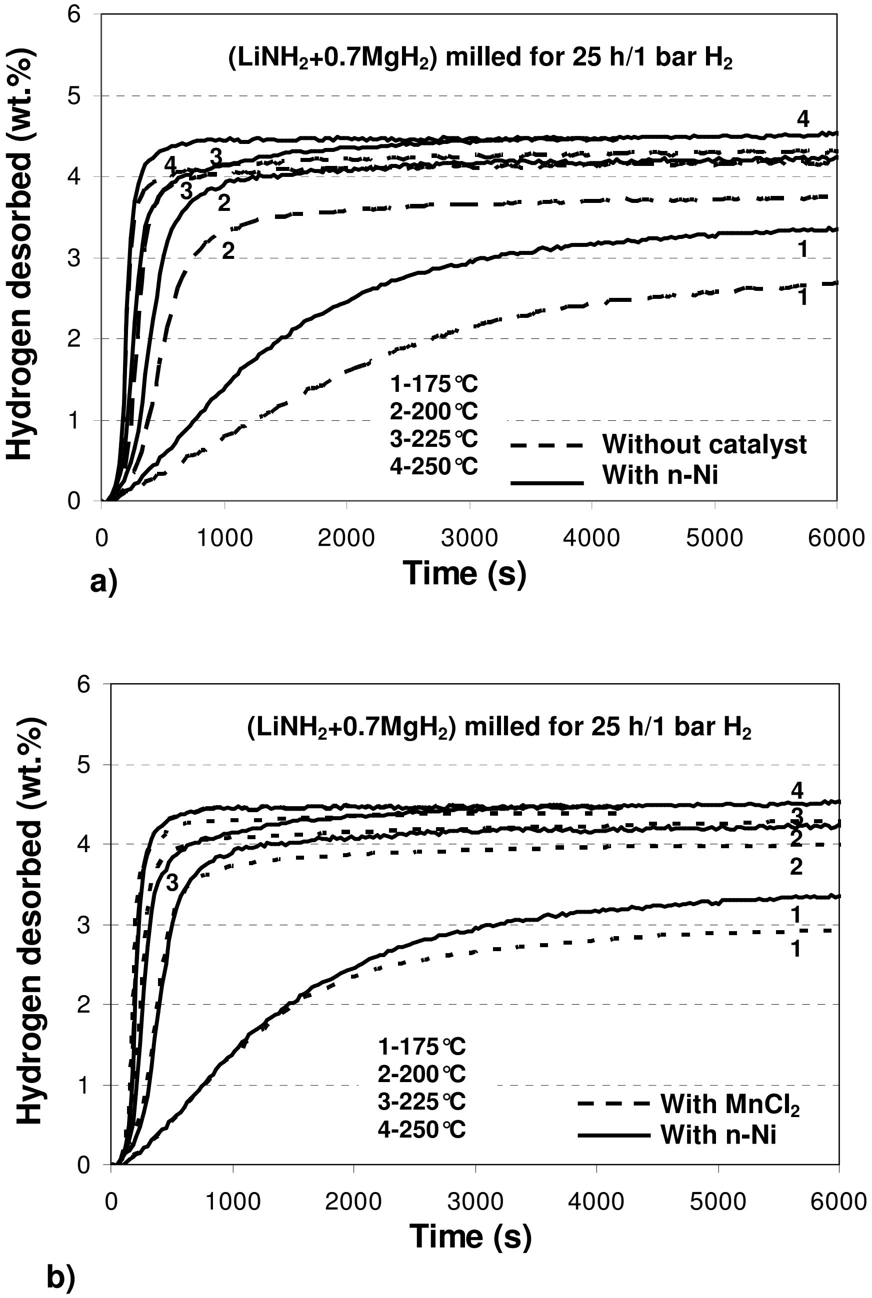

Fig. 9-15 Comparison of dehydrogenation curves at various temperatures under 1 bar H_2 for the ($LiNH_2$+0.7MgH_2) mixtures milled for 25 h (IMP67 mode): a) without and with 5 wt.% n-Ni and b) with 5 wt.% n-Ni/$MnCl_2$

To better understand the reversibility of reaction (9-1) and reaction (9-2), the ($LiNH_2$+0.7MgH_2) mixtures with 5 wt.% n-Ni milled for 25 h were first dehydrogenated at 175 and 400°C under 1 bar of hydrogen, respectively. Next, the differently dehydrogenated samples were hydrogenated under the same conditions of 175°C under 50 bar of hydrogen. Based on the above analyses, the dehydriding reaction at 175°C corresponds to reaction (9-1), whereas both reaction (9-1) and reaction (9-2) occur sequentially at 400°C. Fig. 9-16 a) and b) show the dehydriding/hydriding cycles of the ($LiNH_2$+ 0.7MgH_2) mixture with 5 wt.% n-Ni milled for 25 h at two different dehydrogenation temperatures of 175 and 400°C under 1 bar of hydrogen, respectively. It is seen that the hydrogen desorption/absorption behavior is quite different with different dehydriding temperatures. The mixture dehydrogenated at 175°C and subsequently hydrogenated at 175°C under 50 bar of H_2 shows full reversibility with 3.6 wt.% H_2. However, the mixture dehydrogenated at 400°C releases 5.2 wt.% H_2, but the dehydrogenated sample absorbs only 3.2 wt.% H_2 at 175°C under 50 bar of H_2, which indicates that the dehydrogenated samples cannot be completely converted to their starting states under the present testing conditions. To clarify the reaction pathways of dehydrogenation/hydrogenation, samples at each cycling stage of dehydriding and hydriding were collected and analyzed using XRD as shown in Fig. 9-17 a) and b). Fig. 9-17 a) clearly shows that $Li_2Mg(NH)_2$ is formed by the dehydrogenation of $LiNH_2$-MgH_2 (1:0.7) mixture at 175°C, which corresponds to reaction (9-1). In the subsequent hydrogenation process, $Mg(NH_2)_2$ and LiH appear instead of the $Li_2Mg(NH)_2$ phase. Finally, the $Li_2Mg(NH)_2$ phase reappears during the dehydrogenation of the hydrogenated mixture. The appearance of this phase indicates that the reversible reaction is processed between $Li_2Mg(NH)_2$ and {$Mg(NH_2)_2$ and LiH} rather than {$LiNH_2$ and MgH_2} [83, 86]. Thus, the

$Mg(NH_2)_2/LiH$ system is thermodynamically more favorable than the $LiNH_2/MgH_2$ system, which has already been experimentally proven by Luo et al. [94].

The only difference between Fig. 9-17 a) and b) is the formation of Mg_3N_2 phase after dehydrogenation at 400°C. However, this phase still exists even after the hydrogenation process. Therefore, this phase cannot be hydrogenated under our experimental conditions, which results in the loss of reversibility, as shown in Fig. 9-16 b). XRD results shown in Fig. 9-17 a) and b) are summarized in Table 9-2. With the information obtained from the dehydriding/hydriding cycles and the corresponding XRD analysis, the reversible hydrogenation/dehydrogenation processes can be described by the following reaction:

$$0.5Li_2Mg(NH)_2+H_2 \leftrightarrow 0.5Mg(NH_2)_2+LiH \qquad (3\text{-}6)$$

Assuming that all reactions are completed and that the dehydrogenation is processed at the low temperature range corresponding to the first endothermic peak in the DSC curve shown in Fig. 9-10, it can be described by a series of dehydriding/hydriding reactions as follows:

$[0.5xMg(NH_2)_2+xLiH] +[(1-x)LiNH_2 +(0.7-0.5x)MgH_2]$ (after ball milling)

$\rightarrow \boldsymbol{0.5Li_2Mg(NH)_2} + 0.2MgH_2 + \boldsymbol{H_2}$ (after dehydrogenation) (9-5)

$\leftrightarrow \boldsymbol{0.5Mg(NH_2)_2 + LiH} + 0.2MgH_2$ (after rehydrogenation)

Based on reaction (9-5), the maximum reversible hydrogen amount is approximately 4.4 wt.% (corrected for 95% purity), which corresponds to 2.0 mol of hydrogen atoms per unit of the {($LiNH_2+0.7MgH_2$)+5 wt.% n-Ni} mixture.

However, for dehydrogenation in the high temperature range that corresponds to the second endothermic peak in DSC curve shown in Fig. 9-10, the series of dehydriding/hydriding reactions is as follows:

$[0.5xMg(NH_2)_2+xLiH] +[(1-x)LiNH_2 +(0.7-0.5x)MgH_2]$ (after ball milling)

$\rightarrow \boldsymbol{0.4Li_2Mg(NH)_2+0.1Mg_3N_2+0.2LiH+1.2H_2}$ (after dehydrogenation)

$$0.4Li_2Mg(NH)_2+0.1Mg_3N_2+0.2LiH+\boldsymbol{0.8H_2} \tag{9-6}$$

$\leftrightarrow \boldsymbol{0.4Mg(NH_2)_2+LiH}+0.1Mg_3N_2$ (after rehydrogenation)

It is worth highlighting that 2.4 moles of hydrogen atoms can be desorbed the first time, but only 1.6 moles of hydrogen atoms can be absorbed and be reversible. Considering 95% purity of the starting materials, the ($LiNH_2$+$0.7MgH_2$) mixture without and with 5 wt.% n-Ni can initially desorb 5.5 and 5.3 wt.% H_2, respectively. However, in the subsequent hydrogenation/dehydrogenation process, only 3.7 and 3.5 wt.% H_2 can be absorbed and desorbed for the mixture without and with 5 wt.% n-Ni, respectively. This result is in good agreement with our experimental value of 3.2 wt.% of hydrogen for the ($LiNH_2$+$0.7MgH_2$) mixture with 5 wt.% n-Ni shown in Fig. 9-16 b).

Therefore, the ($LiNH_2$+$0.7MgH_2$) mixture is a completely reversible system in the temperature range corresponding to the first endothermic peak in the DSC curve as shown in Fig. 9-2 and 9-10.

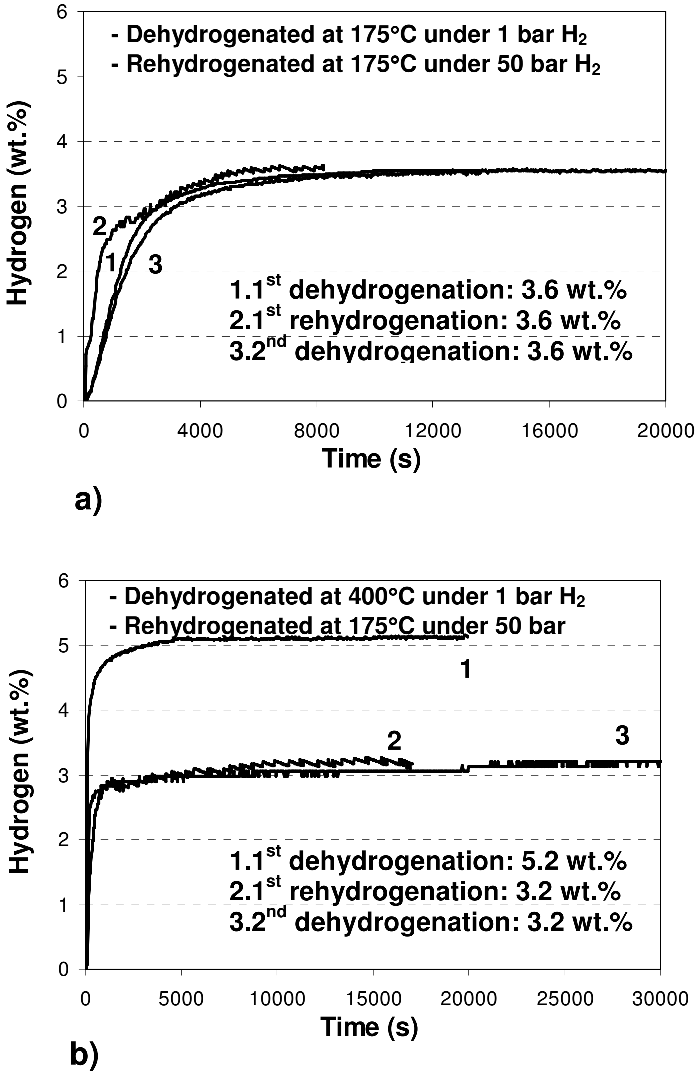

Fig. 9-16 Reversibility for the ($LiNH_2$+0.7MgH_2) mixtures with 5 wt.% n-Ni milled for 25 h (IMP67 mode)

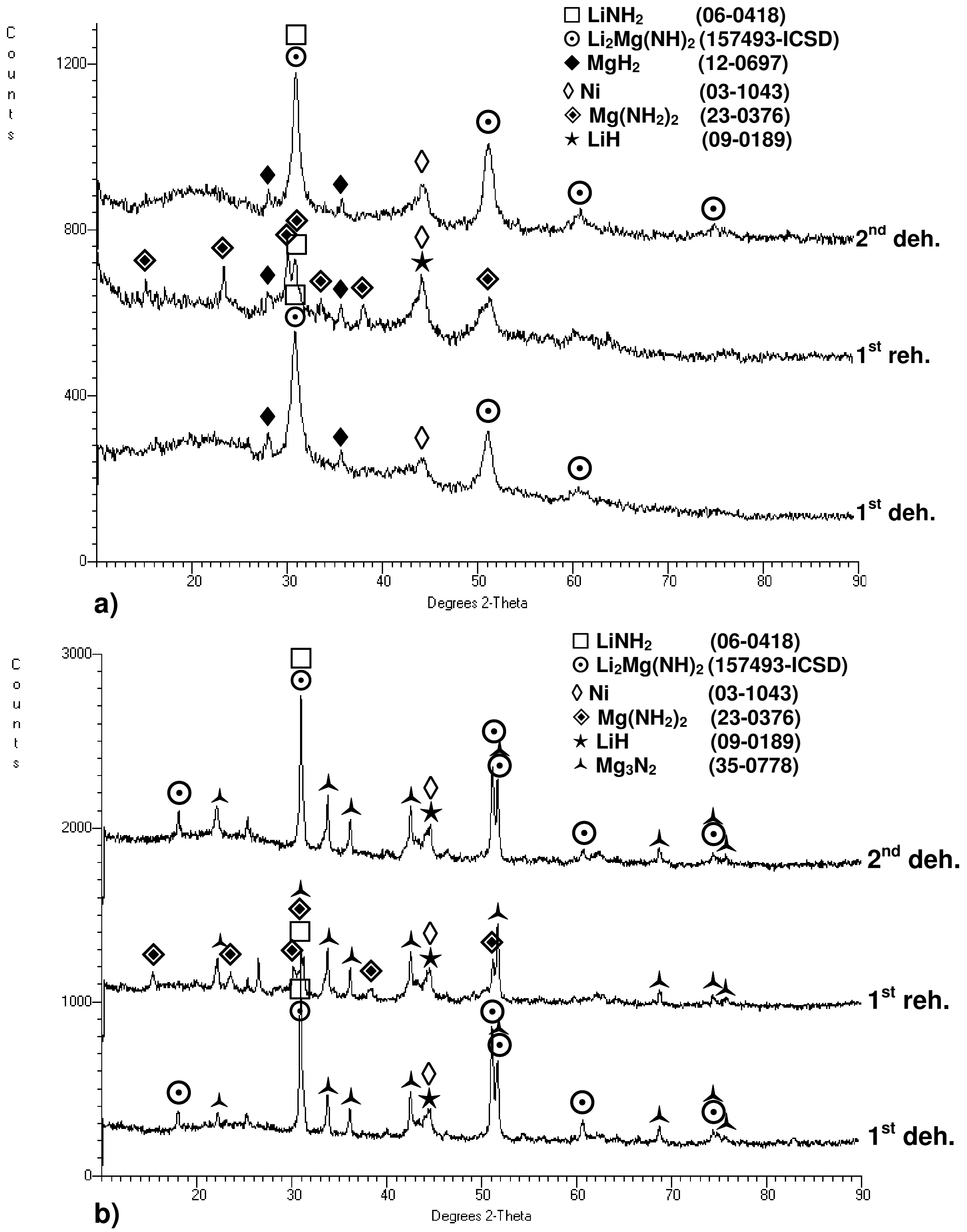

Fig. 9-17 XRD patterns for the ((LiNH$_2$+0.7MgH$_2$)+5 wt.% n-Ni) mixtures milled for 25 h under IMP67 mode and subsequently dehydrogenated at a) 175°C and b) 400°C, respectively, under 1 bar H$_2$ and then rehydrogenated at 175°C under 50 bar H$_2$

Table 9-2. Reversible reaction pathways for the (($LiNH_2$+0.7MgH_2)+5 wt.% n-Ni) mixtures milled for 25 h (IMP67 mode) (Based on Sieverts analysis in Fig. 9-16 and 9-17)

T(°C)	$LiNH_2$	MgH_2	$Li_2Mg(NH)_2$	Mg_3N_2	LiH	$Mg(NH_2)_2$
Dehydrogenated at 175°C under 1 bar H_2	O	O	O	-	-	-
Rehydrogenated at 175°C under 50 bar H_2	O	O	-	-	O	O
Re-dehydrogenated at 175°C under 1 bar H_2	O	O	O	-	-	-
Dehydrogenated at 400°C under 1 bar H_2	O	-	O	O	O	-
Rehydrogenated At 175°C under 50 bar H_2	O	-	-	O	O	O
Re-dehydrogenated at 400°C under 1 bar H_2	O	-	O	O	O	-

9-3. Discussion of thermodynamic properties

At the beginning of the present study, it was mentioned that MgH_2 is substituted for LiH to overcome the thermodynamic barriers of the $LiNH_2$-LiH system; therefore, the ($LiNH_2$+nMgH_2) (n=0.55, 0.60, and 0.70) system is investigated. In this section, the thermodynamic properties of the $LiNH_2$- MgH_2 system are investigated and discussed.

To experimentally confirm the magnitude of the enthalpy change (ΔH) of the dehydrogenation reaction, we performed PCT experiments using a step-wise method (see Chapter 6). Fig. 9-18 a) and c) show step-wise desorption curves at 160, 170 and 180°C with corresponding equilibrium plateau pressures for a 1:0.7 molar ratio $LiNH_2$:MgH_2 mixture without and with 5 wt.% n-Ni milled for 25 h, respectively. The results of the enthalpy and entropy change values obtained from the Van't Hoff relationship (Eq.(2-2)) are shown in Fig. 9-18 b) and d) for the same mixture without and with n-Ni, respectively. It is evident that the enthalpy and entropy changes of reaction (9-1) are -46.7 kJ/mol and -45.9 kJ/molH_2 and 136.1 and 134.5 J/molK for the ($LiNH_2$+0.7MgH_2) mixture without and with 5 wt.% n-Ni, respectively. Within the experimental error, there is no measurable effect of n-Ni on the thermodynamic properties. Moreover, excellent coefficients of fit to the Van't Hoff lines in Fig. 9-18 b) and d) provide strong evidence that the step-wise method is notably accurate, at least for the hydride systems investigated in the present work. However, the values of the enthalpy change obtained in the present work are slightly higher than those reported by Xiong et al. [84] (-38.9 kJ/molH_2) and Barison et al. [135] (-40.4 kJ/molH_2).

Fig. 9-19 a) and b) shows the plateau pressure vs. temperature plots calculated from the Van't Hoff relationship (Eq.(2-2)) and the thermodynamic data in Fig. 9-18 b) and d). It is evident that the equilibrium temperature at atmospheric pressure of hydrogen (1 bar of H_2) is

70.1°C and 68.3°C for the ($LiNH_2$+0.7MgH_2) system without and with 5 wt.% n-Ni milled for 25 h, respectively. It is obvious that both of these hydride systems can be employed for hydrogen desorption/absorption below 100°C.

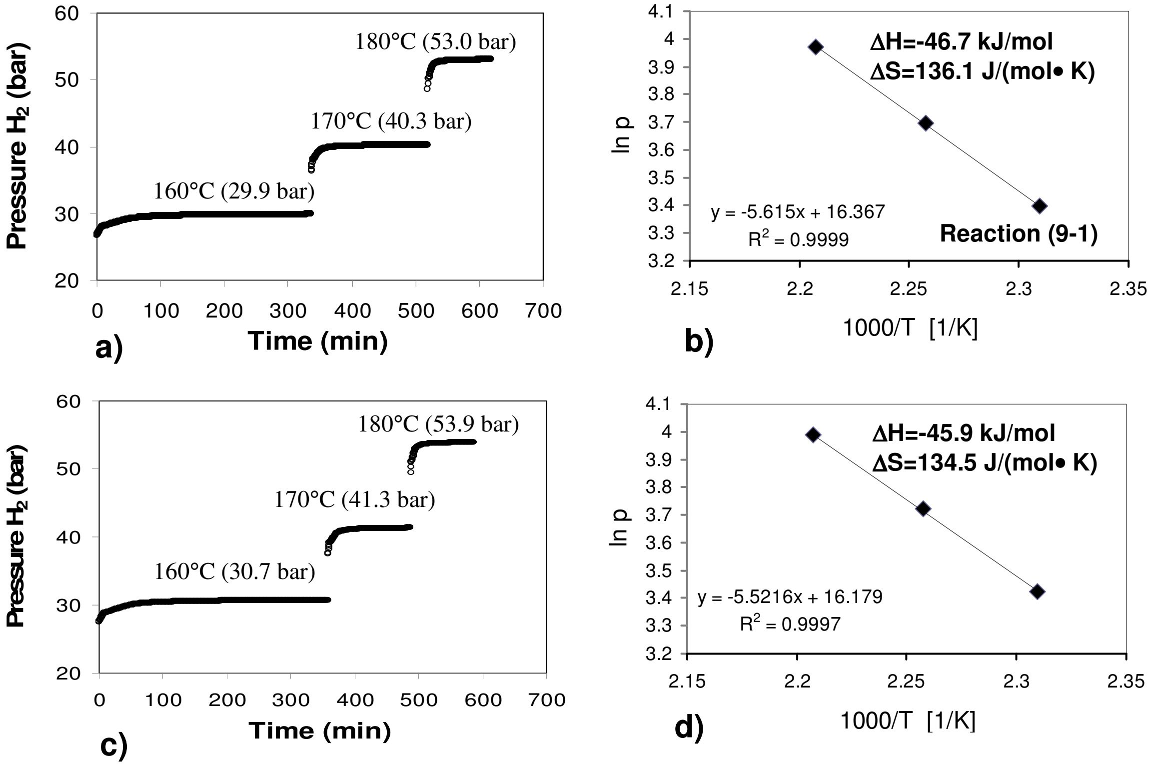

Fig. 9-18 a) & c) Step-wise desorption curves at varying temperatures and b) & d) corresponding Van't Hoff plots for the ($LiNH_2$+0.7MgH_2) mixtures; a) & b) without n-Ni and c) & d) with 5 wt.% n-Ni milled for 25 h (IMP67 mode)

- Reaction (9-1): [$0.5xMg(NH_2)_2+xLiH$] +[$(1-x)LiNH_2$ +$(0.5-0.5x)MgH_2$] → $0.5Li_2Mg(NH)_2+1.0H_2$

Considering the enthalpy change (-62.4 kJ/mol) and the equilibrium temperature at atmospheric pressure of hydrogen (256.8°C) of the $LiNH_2$-LiH system as discussed in Chapter 8, the $LiNH_2/MgH_2$ (1:0.7) mixture has a greater potential for hydrogen storage material when applied to automobiles. However, there are still two main challenges: 1) the low reversible hydrogen capacity (below 5.0 wt.% H_2) and 2) the kinetic issues. Even the catalyzed system desorbs only 0.5 wt.% H_2 at 125°C as shown in Fig. 9-12 b) despite high plateau pressure at that temperature. Therefore, more researches to improve kinetic properties and the reversibility are needed.

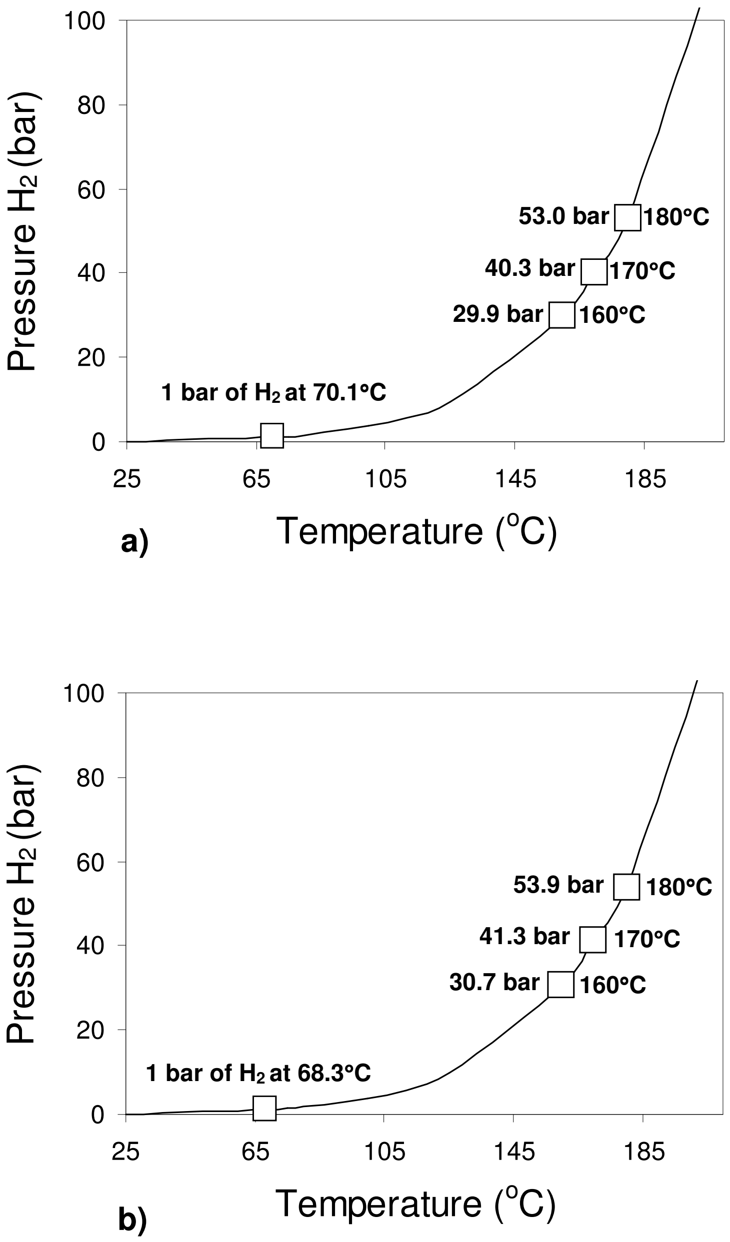

Fig. 9-19 Plateau pressure vs. temperature for the ($LiNH_2$+0.7MgH_2) mixture a) without and b) with 5 wt.% n-Ni milled for 25 h (IMP67 mode)

10. ($LiNH_2$+1.0MgH_2) system

10-1. Hydrogen desorption during ball milling

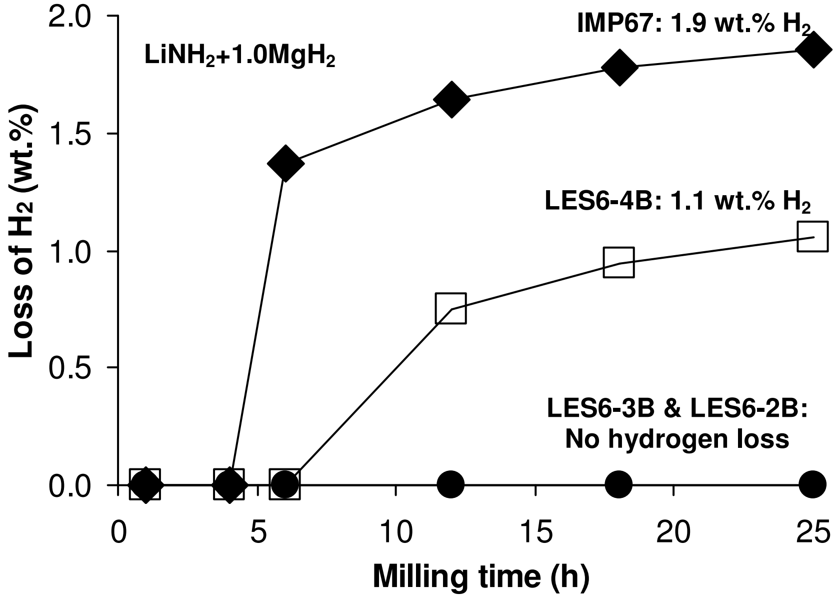

Fig. 10-1 Hydrogen loss of the ($LiNH_2$+1.0MgH_2) during ball milling process in four different milling modes

Fig. 10-1 shows the amount of desorbed hydrogen in the ($LiNH_2$+1.0MgH_2) mixtures during the ball milling process as a function of milling time under different milling modes. The amount of hydrogen released from the starting mixture is calculated using the ideal gas law with the measured gas pressure variations within the ball milling jar as shown in Appendix A-2. It is worth noting that the amount of hydrogen desorbed during the ball milling of $LiNH_2$-MgH_2 system strongly depends on the milling energy and the molar ratio of MgH_2/$LiNH_2$ because the ($LiNH_2$+nMgH_2) (n=0.55, 0.6, and 0.7) mixtures did not show any pressure changes during ball milling under the high energy impact (IMP67) mode for 25 h as shown in Chapter 9. It can be seen from Fig. 10-1 that hydrogen release in the mixture milled under IMP67 mode suddenly begins after milling for 6 h and gradually increases as the ball milling proceeds. After 25 h of milling, 1.9 wt.% H_2 is released from the mixture of $LiNH_2$-MgH_2 (1:1). In contrast to the IMP67 mode, the low-energy shearing (LES6-4B (4 balls)) mode results in the release of 1.1 wt.% H_2 after 25 h milling. This result indicates that hydrogen comes from the chemical reaction between $LiNH_2$ and MgH_2. However, no pressure changes during ball milling are shown under the low-energy shearing (LES6) modes with 2 and 3 balls. Therefore, solid-solid reactions between $LiNH_2$ and MgH_2 occur during ball milling depending on the milling energy as reported by Liu et al. [107] and Liang et al. [108]. To ascertain the chemical process that occurs during the ball milling process, solid residues at different ball milling stages were collected for XRD and FT-IR characterizations. Fig. 10-2 a) and b) show the XRD patterns and FT-IR spectra, respectively, of the ($LiNH_2$+1.0MgH_2) mixtures milled under a high-energy impact (IMP67) mode for various milling times. The mixture milled under the IMP67 mode for 1 h still consists of the original $LiNH_2$ and MgH_2 phases. After 4 h of ball milling under the same milling mode, a small new peak is observed at 44.3° (2θ), which can be assigned to the LiH phase (JCPDS file No. 09-0189), while the diffraction peaks of the $LiNH_2$ phase disappear; however, XRD peaks of the MgH_2 phase still dominates the XRD pattern. Thus, the $LiNH_2$ is completely converted to $Mg(NH_2)_2$ and LiH by the metathesis reaction with MgH_2 [102, 107, 108]. However, it is difficult to establish the presence of the $Mg(NH_2)_2$ phase using XRD because this compound is easily deformed into an amorphous state under the energetic ball milling process [107].

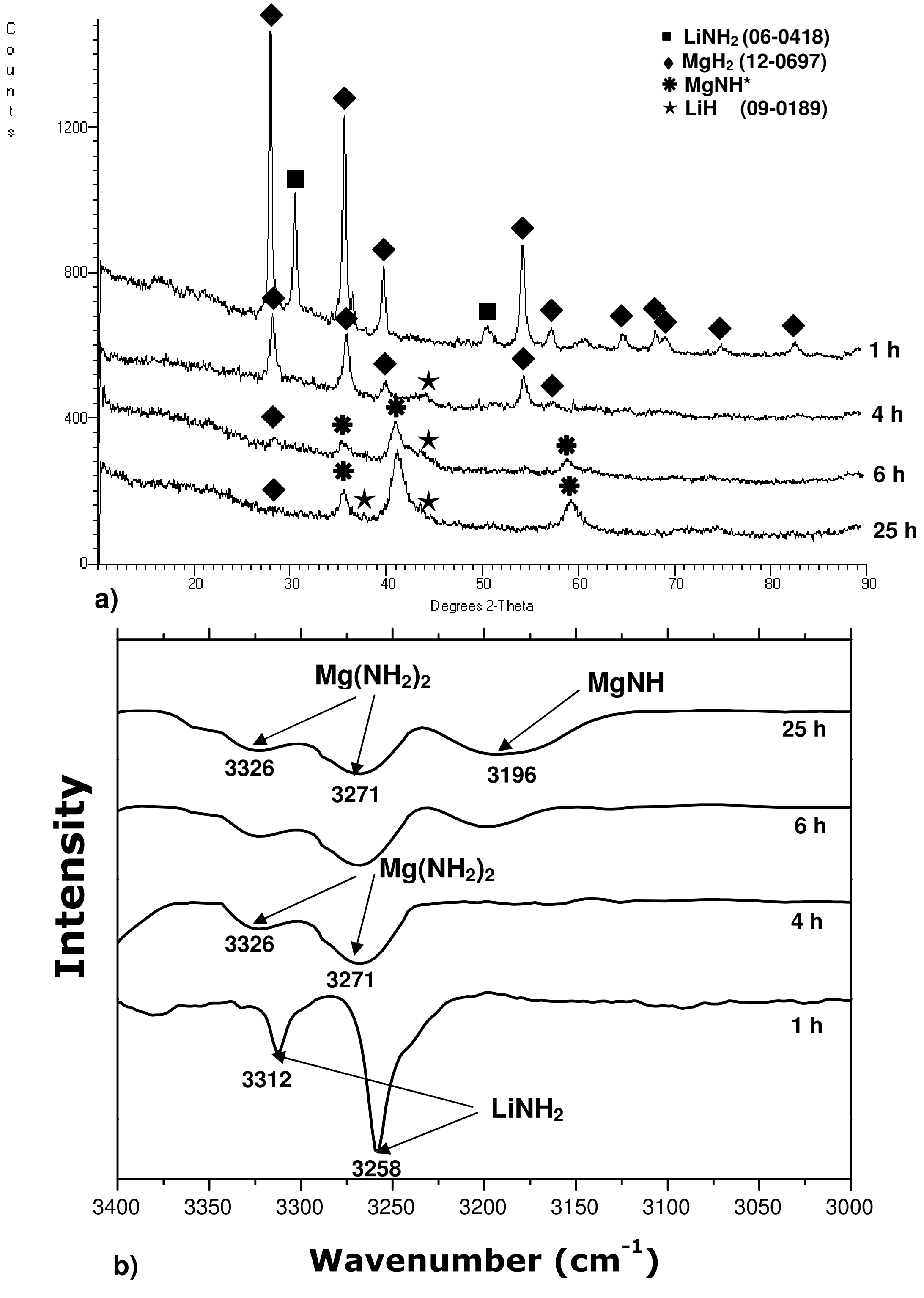

Fig. 10-2 a) XRD patterns and b) FT-IR absorption spectra for the ($LiNH_2$+1.0MgH_2) mixtures milled for various times (IMP67 mode) (*Ref. # 108: Liang et al Chem. Eur. J. 16 (2010) 693-702)

To confirm the presence of the $Mg(NH_2)_2$ phase undetected by XRD in Fig. 10-2 a), FT-IR analysis was performed as shown in Fig. 10-2 b). The figure clearly shows the formation of $Mg(NH_2)_2$ with characteristic absorption lines at 3271 and 3326 cm^{-1} [100] after 4 h milling under the IMP67 mode. When the ball milling is prolonged to 6 and 25 h under IMP67, the formation of new MgNH phase is detected by XRD patterns [99, 100, 108] and the FT-IR spectrum [100], while the intensity of MgH_2 diffraction peaks in XRD pattern becomes lowered, which can be interpreted by the gradual consumption of this phase to form MgNH and H_2.

Fig. 10-3 a) and b) represent the XRD patterns of ($LiNH_2$+1.0MgH_2) mixtures milled under both low-energy shearing (LES6) modes with 2 and 3 balls for 25 h, respectively. The mixture milled under the LES6-2B mode for 25 h consists of the original $LiNH_2$ and MgH_2 phases. Meanwhile, after 25 h ball milling under the LES6-3B mode, two small peaks at 38.1° and 44.3° (2θ) are observed, which can be assigned to the LiH phase and matched with JCPDS file No. 09-0189. However, the diffraction peaks of $LiNH_2$ and MgH_2 phases still dominate the XRD pattern. As mentioned above, the presence of the LiH phase suggests that a certain quantity of the starting mixture is converted to $Mg(NH_2)_2$ and LiH by the metathesis reaction. The results shown in Fig. 10-2 and 10-3 are summarized in Table 10-1.

Based on the above analyses, the following reaction pathways during the ball milling under the high energy impact (IMP67) mode can be proposed. In the first step, $LiNH_2$ is converted to $Mg(NH_2)_2$ and LiH by the metathesis reaction with MgH_2 [102, 107, 108]:

$$LiNH_2 + 0.5MgH_2 \rightarrow 0.5Mg(NH_2)_2 + LiH \qquad (10\text{-}1)$$

In the second step, $Mg(NH_2)_2$ reacts with MgH_2 to form MgNH and H_2, as proposed by Liu et al. [107] and Liang et al. [108]:

$$0.5Mg(NH_2)_2 + 0.5MgH_2 \rightarrow MgNH + H_2 \qquad (10\text{-}2)$$

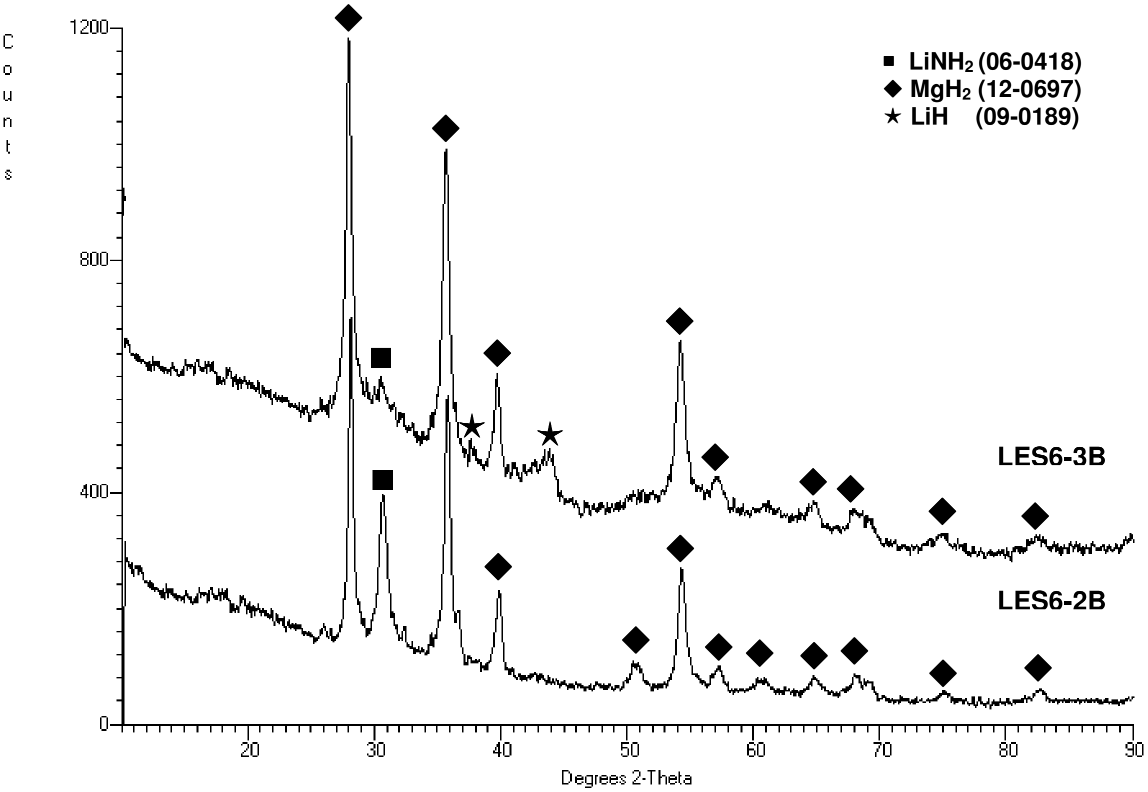

Fig. 10-3 XRD patterns for the ($LiNH_2$ + $1.0MgH_2$) milled for 25 h under two different milling modes

Table 10-1. Summary of XRD results of the ($LiNH_2$+$1.0MgH_2$) mixture milled under various milling modes and times

Milling mode	Milling time (h)	$LiNH_2$	MgH_2	$Mg(NH_2)_2$	LiH	MgNH
IMP67	1	O	O	-	-	-
	4	-	O	O	O	-
	6	-	O	O	O	O
	25	-	O	O	O	O
LES6-2B	25	O	O	-	-	-
LES6-3B	25	O	O	O	O	-

The details to determine reaction pathways occurring during ball milling are shown in Appendix A-4. A series of sequential reactions follows:

$LiNH_2+1.0MgH_2 \rightarrow LiNH_2+MgH_2$ (after 1 h milling)

$\rightarrow \mathbf{0.5Mg(NH_2)_2+LiH}+0.5MgH_2$ (after 4 h milling) (10-3)

$\rightarrow \mathbf{0.352MgNH}+0.324Mg(NH_2)_2+LiH+0.324MgH_2+\mathbf{0.352H_2}$ (after 6 h milling)

$\rightarrow \mathbf{0.5MgNH}+0.25Mg(NH_2)_2+LiH+0.25MgH_2+\mathbf{0.5H_2}$ (after 25 h milling)

It is interesting to note that further hydrogen desorption is possible from a continuous reaction between the remaining $Mg(NH_2)_2$ and MgH_2. Assuming reaction (10-2) can be completed, reaction (10-3) can be modified as follows:

$LiNH_2+1.0MgH_2 \rightarrow \mathbf{MgNH}+LiH+\mathbf{H_2}$ (10-4)

Therefore, 4.1 wt.% H_2 can be released upon the ball milling process, which corresponds to 2.0 mol of hydrogen atoms per unit of the ($LiNH_2+1.0MgH_2$) mixture. Considering 95% purity of the starting materials, the maximum of 3.9 wt.% H_2 can be released.

On the other hand, the following reaction can be proposed for the ($LiNH_2+1.0MgH_2$) mixture milled under low-energy shearing (LES6-3B) mode for 25 h based on the above analyses:

$LiNH_2+1.0MgH_2 \rightarrow \mathbf{0.5xMg(NH_2)_2+xLiH}+(1-0.5x)MgH_2+(1-x)LiNH_2$ (10-5)

where x indicates that only fractions of $LiNH_2$ and MgH_2 are involved in reaction (10-1) because their diffraction peaks are still observed after ball milling as shown in Fig. 10-3 b).

Differences in milling times, milling modes and number of balls can affect the milling energy; therefore, different solid products may result during ball milling depending on the milling energy. Therefore, ball milling conditions significantly affect the reaction pathways of hydrogen desorption in subsequent heating processes.

10-2. Morphology and microstructure of powder mixtures

Fig. 10-4 a) and b) show the backscattered electron (BSE) micrograph of the ($LiNH_2$ $+1.0MgH_2$) mixtures milled for 25 h under low-energy shearing (LES6) modes with 2 and 3 balls, respectively. Even after ball milling under the LES6-2B mode for 25 h, the particles still have a non-uniform particle size distribution with small and large particle populations, whereas the LES6-3B mode results in a more homogeneous particle size distribution with smaller particles. However, its distribution still shows large particle populations in Fig. 10-4 b). This result provides a clue to how the milling mode affects the morphology of the mixture. Furthermore, the specific surface area (SSA) measured from the BET method as shown in Fig. 10-5 shows the dependence of the SSA on the milling mode. SSA dramatically increases, while changing the milling mode from the low-energy shearing (LES6) mode to the high-energy impact (IMP67) mode, which indicates that the IMP67 mode is the most energetic milling mode. The SSA of the mixture milled under the IMP67 mode for 25 h increases by almost 75% compared to that of the LES6-2B mode.

10-3 Thermal behavior

Fig. 10-6 compares the DSC curves of the ($LiNH_2+1.0MgH_2$) mixtures milled under LES6-2B and LES6-3B for 25 h, respectively. Two endothermic peaks appear in the DSC curves, which indicate that the mixtures decompose in a two-step reaction. Both reactions start at lower temperatures and end sooner for the mixture milled under the LES6-3B mode for 25 h than the LES6-2B mode. In particular, the peak temperatures for the first and second reaction are remarkably reduced from 250.1 to 210.1°C and from 357.5 to 298.1°C by increasing the number of balls from 2 to 3, respectively.

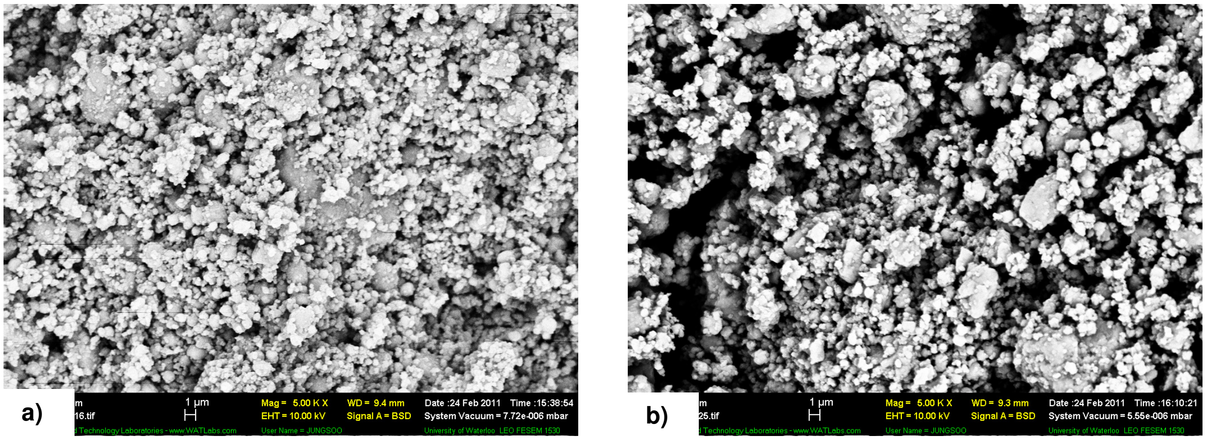

Fig. 10-4 Backscattered electron (BSE) micrographs of the ($LiNH_2$+1.0MgH_2) mixtures milled for 25 h under two different milling modes: a) LES6-2B and b) LES6-3B

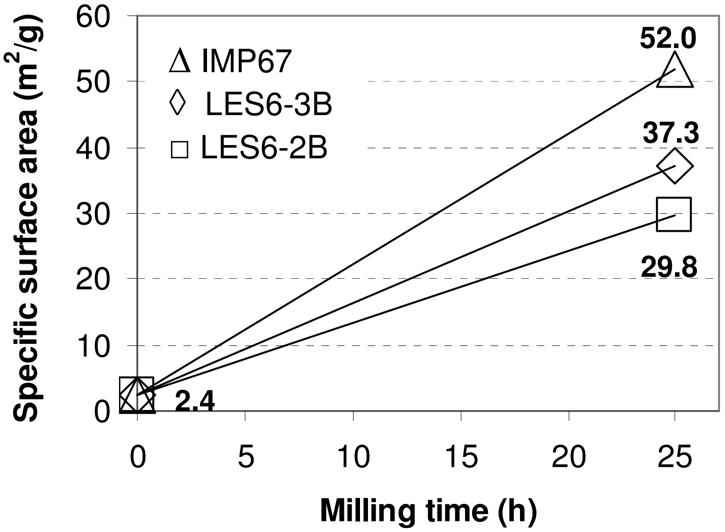

Fig. 10-5 Specific surface areas of the ($LiNH_2$+1.0MgH_2) without and with the milling under various milling modes for 25 h

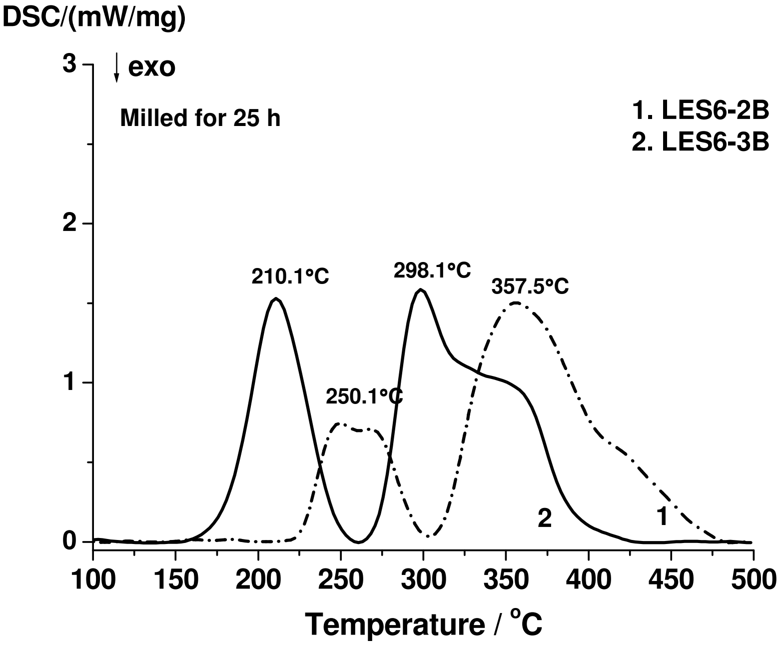

Fig. 10-6 DSC curves at a heating rate of 10°C/min for the ($LiNH_2$+1.0MgH_2) mixtures milled for 25 h under two different milling modes

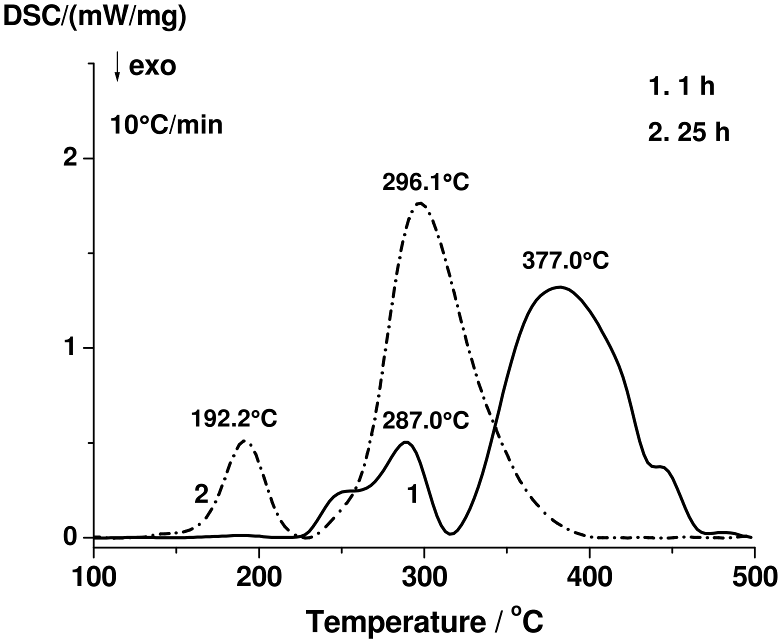

Fig. 10-7 Comparison of DSC curves for the ($LiNH_2$+1.0MgH_2) mixtures milled for 1 h and 25 h (IMP67 mode)

Fig. 10-7 compares the DSC curves of the ($LiNH_2$+1.0MgH_2) mixtures milled under the high-energy impact (IMP67) mode for 1 and 25 h, respectively. As shown in Fig. 10-6 and Fig. 10-7, the mixtures exhibit two endothermic peaks independent of the milling mode and time, which indicates that the mixtures decompose in a two-step reaction. It is also noticeable that the peak temperatures corresponding to two endothermic peaks are reduced from 287.0 to 192.2°C and from 377.0 to 296.1°C by increasing the milling time from 1 to 25 h, respectively.

To confirm the gaseous species released during heating, a TPD test was carried out for the ($LiNH_2$+1.0MgH_2) mixture milled under the LES6-3B mode for 25 h, which is presented in Fig. 10-8. It is evident that the two hydrogen desorption peaks occur below 400°C, while barely any NH_3 emission (ppm level) is detected in the TPD measurements up to 500°C within our experimental accuracy. Thus, the two endothermic peaks shown in Fig. 10-6 correspond to two dehydriding reactions.

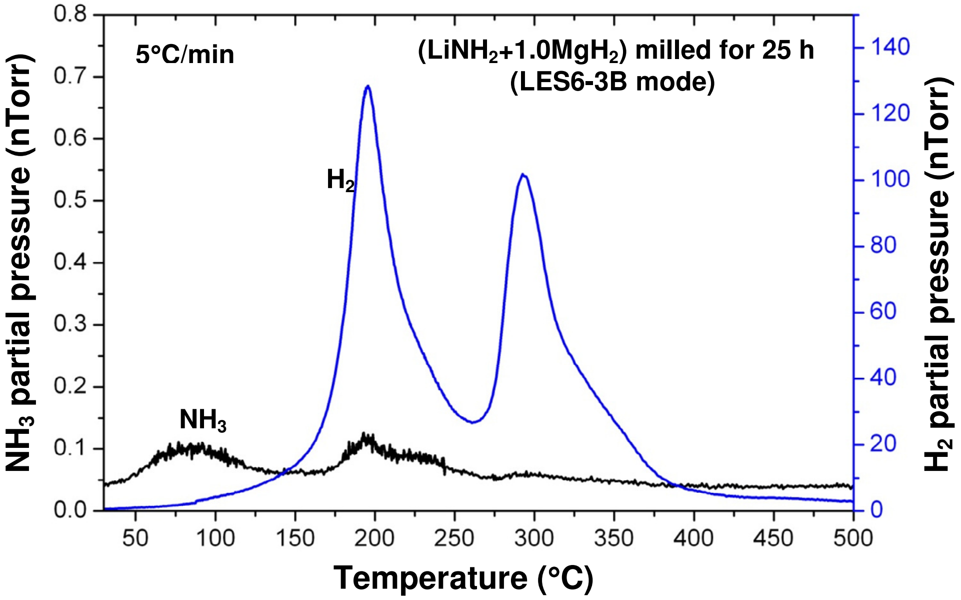

Fig. 10-8 TPD spectra for ($LiNH_2$+1.0MgH_2) milled for 25 h (LES6-3B mode)

10-4. Dehydrogenation behaviors and reaction pathways

Because investigations of the ball-milled $LiNH_2$-MgH_2 (1:1) mixture by several research groups [105-107] resulted in different dehydrogenation processes, the correlation between mechanical ball milling and hydrogen-desorption reactions are elucidated here to understand the underlying mechanisms of the chemical reaction between $LiNH_2$ and MgH_2 with a molar ratio of 1:1.

10-4-1. ($LiNH_2$+1.0MgH_2) mixture milled under the LES6-3B mode for 25 h

Fig. 10-9 a) shows the dehydrogenation curves of the ($LiNH_2$+1.0MgH_2) mixture milled under the LES6-3B mode for 25 h at various temperatures under 1 bar H_2. It is evident that the same mixtures dehydrogenated at 200, 250, 300 and 400°C under 1 bar of H_2 release 3.9, 4.8, 5.6 and 5.8 wt.% H_2, respectively. In particular, the mixture can also desorb 0.5 and 1.3 wt.% H_2 at 125 and 150°C, respectively.

To ascertain the chemical reactions that occur upon dehydrogenation, the residues after dehydrogenating at different temperatures were collected and analyzed using XRD and are summarized in Table 10-2. As can be seen in Fig. 10-9 b), the XRD pattern of the mixture dehydrogenated at 200°C shows the diffraction peaks of the newly formed $Li_2Mg(NH)_2$ phase, whereas XRD peaks of the LiH phase, which was formed after 25 h of ball milling, disappears. As the heating temperature increases, the intensity of MgH_2 diffraction peaks in XRD pattern decreases and finally disappears after dehydrogenation at 400°C. In contrast, the Mg_3N_2 and LiH phases start to form at 250°C, and consequently the diffraction peaks of the Mg_3N_2, LiH and $Li_2Mg(NH)_2$ phases dominate the XRD pattern after dehydrogenation at

400°C. These results clearly indicate that the dehydrogenation of this mixture takes place in two reactions that form $Li_2Mg(NH)_2$ and {Mg_3N_2 and LiH}, respectively.

Based on the above analyses, the following reaction pathways of hydrogen desorption for the ($LiNH_2$+1.0MgH_2) mixture milled under LES6-3B for 25 h can be proposed. As mentioned above, $LiNH_2$ is partially converted to $Mg(NH_2)_2$ and LiH by the metathesis reaction with a specific quantity of MgH_2. Thus, at the low temperature range corresponding to the first endothermic peak shown in Fig. 10-6, newly formed $Mg(NH_2)_2$ reacts with LiH as reported by Barison et al. [135], and, simultaneously, the $LiNH_2$ also reacts with MgH_2 as reported by Luo et al.[86] and Xiang et al. [83]. Both reactions form $Li_2Mg(NH)_2$ and H_2. Therefore, in the first step (at low temperature), the reaction can be described as follows:

$[0.5xMg(NH_2)_2+xLiH] +[(1-x)LiNH_2 +(0.5-0.5x)MgH_2]$

$\rightarrow \boldsymbol{0.5Li_2Mg(NH)_2+1.0H_2}$ (9-1)

In the second step (in the high temperature range, which corresponds to the second endothermic peak shown in Fig. 10-6), the $Li_2Mg(NH)_2$ formed through reaction (9-1) reacts with retained MgH_2 to form Mg_3N_2, LiH and H_2 as proposed by Liang et al. [108] and Dolotko et al. [134]:

$0.5Li_2Mg(NH)_2 + MgH_2 \rightarrow \boldsymbol{0.5Mg_3N_2 + LiH + H_2}$ (9-2)

Assuming reaction (9-1) and (9-2) are complete, a series of sequential reactions occur as follows:

$[0.5xMg(NH_2)_2+xLiH] +[(1-x)LiNH_2 +(1-0.5x)MgH_2]$ (after ball milling)

$\rightarrow \boldsymbol{0.5Li_2Mg(NH)_2}+0.5MgH_2+\boldsymbol{1.0H_2}$ (after dehydrogenation at low temp.) (10-6)

$\rightarrow 0.25Li_2Mg(NH)_2+\boldsymbol{0.25Mg_3N_2+0.5LiH+1.5H_2}$ (after dehydrogenation at high temp.)

In total, 3.0 moles of hydrogen atoms can be obtained from the above reaction, which is approximately 6.1 wt.% of hydrogen. Considering 95% purity of the starting materials, total hydrogen storage capacity is reduced to 5.8 wt.% of H_2. This result is in excellent agreement with our experimental value of 5.8 wt.% of H_2 desorbed at 400°C as shown in Fig. 10-9 a).

Table 10-2. Summary of XRD results of the ($LiNH_2$+1.0MgH_2) mixture milled for 25 h (LES6-3B) and subsequently dehydrogenated under 1 bar H_2 at various temperatures

T(°C)	$LiNH_2$	MgH_2	$Mg(NH_2)_2$	$Li_2Mg(NH)_2$	Mg_3N_2	LiH
R.T. (after ball milling)	O	O	O	-	-	O
200	-	O	-	O	-	-
250	-	O	-	O	O	O
300	-	O	-	O	O	O
400	-	-	-	O	O	O

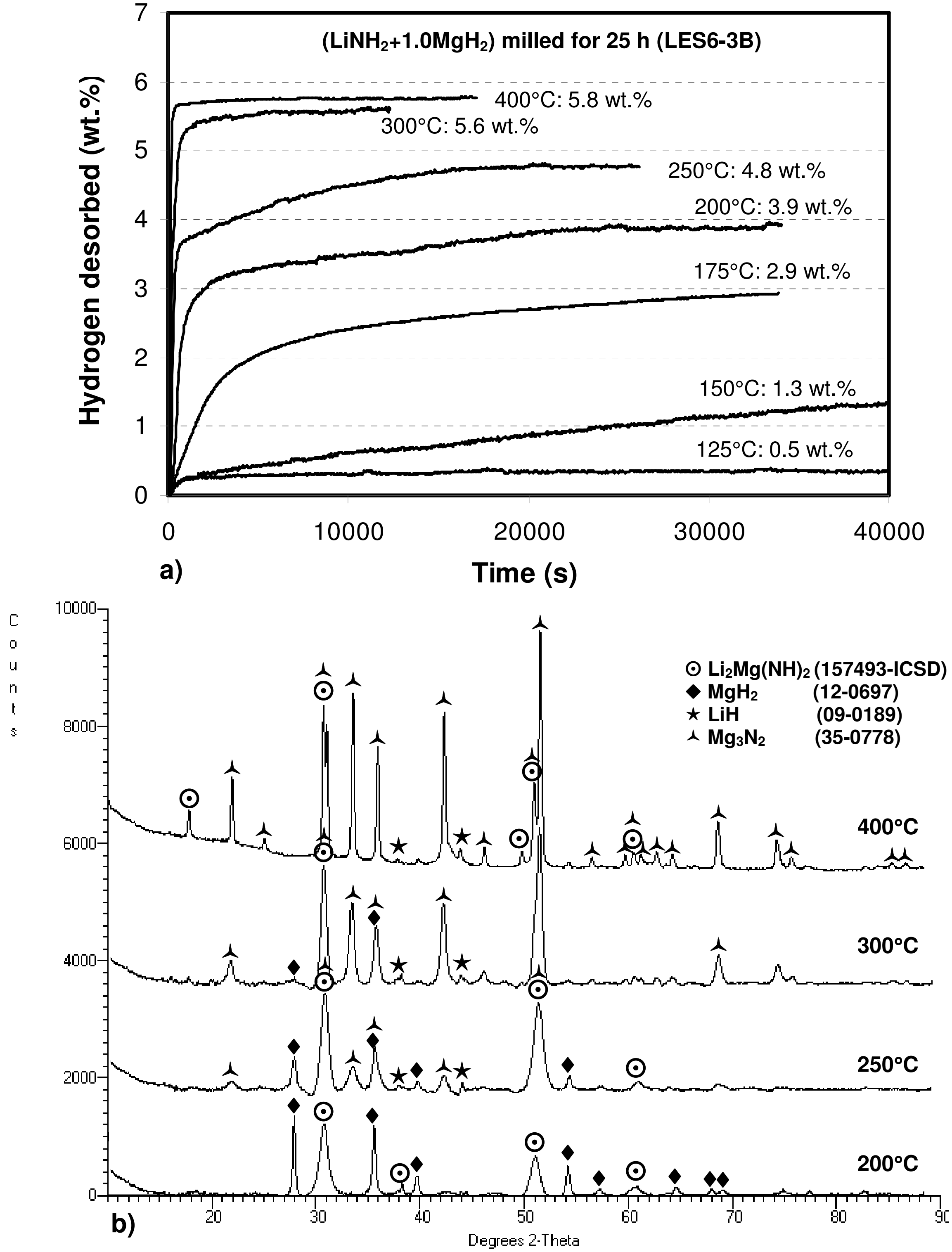

Fig. 10-9 a) Dehydrogenation curves under 1 bar H_2 pressure (atmospheric) at various temperatures and b) the corresponding XRD patterns for the ($LiNH_2$+1.0MgH_2) mixtures milled for 25 h under the LES6-3B mode

10-4-2. ($LiNH_2$+1.0MgH_2) mixture milled under the IMP67 mode for 1 h

Fig. 10-10 a) shows the dehydrogenation curves of ($LiNH_2$+1.0MgH_2) milled under the IMP67 mode for 1 h at various temperatures under 1 bar H_2. It is evident that the same mixtures dehydrogenated at 200, 300 and 425°C under 1 bar of H_2 release 1.3, 5.0 and 5.8 wt.% H_2, respectively. To clarify the chemical reactions that occur during dehydrogenation, samples were collected after dehydrogenation at different temperatures and analyzed using XRD. The results are summarized in Table 10-3. It is evident in Fig. 10-10 b) that the XRD pattern of the mixture dehydrogenated at 200°C shows the diffraction peaks of the newly formed $Li_2Mg(NH)_2$ phase. As the heating temperature increases, the intensity of the MgH_2 diffraction peaks in XRD pattern decreases and this phase completely disappears after dehydrogenation at 425°C. In contrast, the Mg_3N_2 and LiH phase starts to form at 300°C, and consequently the diffraction peaks of the Mg_3N_2, LiH and $Li_2Mg(NH)_2$ phases dominate the XRD pattern after dehydrogenation at 425°C.

The figure also shows that the dehydrogenation of this mixture is processed by a two-step reaction that forms $Li_2Mg(NH)_2$ and {Mg_3N_2 and LiH}, respectively. Therefore, the following reaction pathways of hydrogen desorption for the ($LiNH_2$+1.0MgH_2) mixture milled under IMP67 for 1 h can be proposed. In the first step (in the low temperature range corresponding to the first endothermic peak in Fig. 10-7), $LiNH_2$ reacts with MgH_2 to form $Li_2Mg(NH)_2$ and H_2 as reported by Luo et al. [86] and Xiang et al. [83]:

$$LiNH_2 + 0.5MgH_2 \rightarrow 0.5Li_2Mg(NH)_2 + H_2 \qquad (3\text{-}5)$$

In the second step (in the high temperature range corresponding to the second endothermic peak in Fig. 10-7), the $Li_2Mg(NH)_2$ formed through reaction (3-5) reacts with retained MgH_2 to form Mg_3N_2, LiH and H_2 as proposed by Liang et al.[108] and Dolotko et al. [134]:

$0.5Li_2Mg(NH)_2 + MgH_2 \rightarrow 0.5Mg_3N_2 + LiH + H_2$ (9-2)

Assuming that reactions (3-5) and (9-2) are complete, a series of sequential reactions follows:

$LiNH_2$+1.0MgH_2 (after ball milling)

$\rightarrow$ ***0.5$Li_2Mg(NH)_2$***+0.5MgH_2+***1.0H_2*** (after dehydrogenation at low temp) (10-7)

$\rightarrow$ 0.25$Li_2Mg(NH)_2$+***0.25Mg_3N_2+0.5LiH+1.5H_2*** (after dehydrogenation at high temp)

Finally, approximately 6.1 wt.% of hydrogen is liberated from the mixture, which is equivalent to 3.0 moles of hydrogen atoms per unit formula of the ($LiNH_2$+1.0MgH_2) mixture. Considering the average purity of the starting materials (95%), the total hydrogen storage capacity is 5.8 wt.% of H_2. As shown in Fig. 10-10 a), we obtained the same amount of hydrogen after dehydrogenation at 425°C.

Table 10-3. Summary of XRD results of the ($LiNH_2$+1.0MgH_2) mixture milled for 1 h (IMP67) and subsequently dehydrogenated under 1 bar H_2 at various temperatures

T(°C)	**$LiNH_2$**	**MgH_2**	**$Li_2Mg(NH)_2$**	**Mg_3N_2**	**LiH**
R.T. (after ball milling)	**O**	**O**	**-**	**-**	**-**
200	**O**	**O**	**O**	**-**	**-**
250	**-**	**O**	**O**	**-**	**-**
300	**-**	**O**	**O**	**O**	**O**
350	**-**	**-**	**O**	**O**	**O**
400	**-**	**-**	**O**	**O**	**O**
425	**-**	**-**	**O**	**O**	**O**

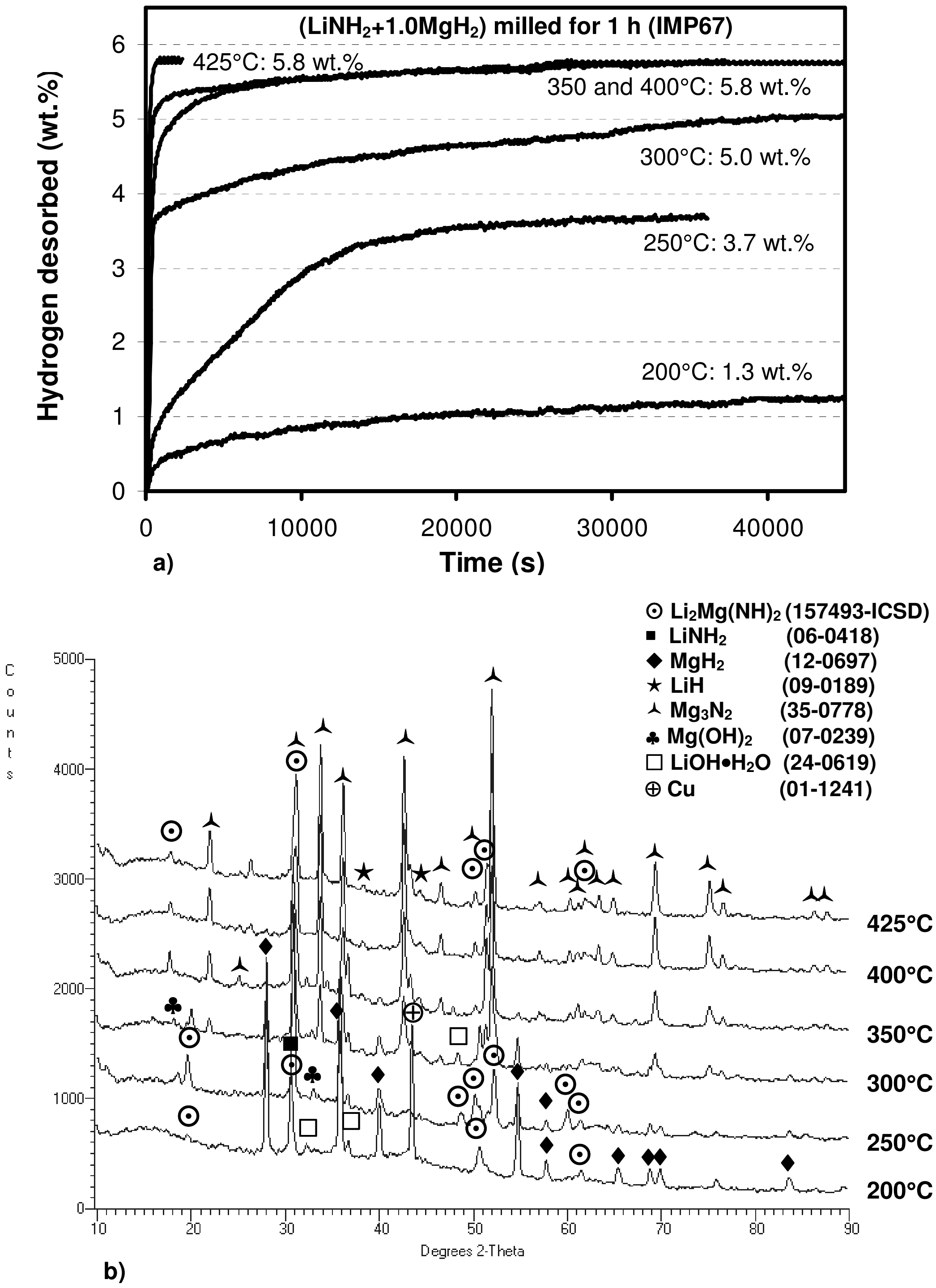

Fig. 10-10 a) Dehydrogenation curves and b) XRD profiles for the ($LiNH_2$+1.0MgH_2) mixtures milled for 1 h (IMP67 mode) and subsequently dehydrogenated under 1 bar H_2 at varying temperatures

10-4-3. ($LiNH_2$+1.0MgH_2) mixture milled under the IMP67 mode for 25 h

Fig. 10-11 a) represents the dehydrogenation curves of ($LiNH_2$+1.0MgH_2) milled under the IMP67 mode for 25 h at various temperatures under 1 bar H_2. The same mixtures dehydrogenated at 175, 200, 300 and 400°C under 1 bar of H_2 release 1.4, 1.9, 3.6 and 4.0 wt.% H_2, respectively. It is remarkable that the maximum hydrogen capacity of this mixture milled under IMP67 mode for 25 h is lower than the mixture milled for 1 h under the same milling mode, due to the hydrogen loss after the ball milling process as shown in Fig. 10-1. To confirm the chemical reactions occurring during dehydrogenation, the residues remaining after dehydrogenation at different temperatures were collected for XRD analysis. The results are summarized in Table 10-4. As shown in Fig. 10-11 b), the XRD pattern of the mixture dehydrogenated at 200°C shows the diffraction peaks of the newly formed $Li_2Mg(NH)_2$ phase. As the heating temperature increases, the intensity of both the MgNH and MgH_2 diffraction peaks decreases, and the two phases completely disappear after dehydrogenation at 400°C. Instead of both MgNH and MgH_2, a Mg_3N_2 phase begins to form at 300°C, and, finally, the diffraction peaks of Mg_3N_2, LiH and $Li_2Mg(NH)_2$ phases are detectable in the XRD pattern after dehydrogenation at 400°C. These results clearly show that the dehydrogenation of this mixture is also processed by a two-step reaction that forms $Li_2Mg(NH)_2$ and Mg_3N_2, respectively.

Based on the XRD analysis, the following reaction pathways of hydrogen desorption for the ($LiNH_2$+1.0MgH_2) mixture milled under IMP67 for 25 h can be proposed. In the first step (in the low temperature range, indicating the first endothermic peak in Fig. 10-7), $Mg(NH_2)_2$ reacts with LiH to form $Li_2Mg(NH)_2$ and H_2 as reported by Barison et al. [135]:

$$0.5Mg(NH_2)_2+LiH \rightarrow 0.5Li_2Mg(NH)_2+H_2 \qquad (3\text{-}6)$$

In the second step (in the high temperature range corresponding to the second endothermic peak in Fig. 10-7), the MgNH which was formed during the milling process reacts with retained MgH_2 to form Mg_3N_2 and H_2 as proposed by Liang et al.[108]:

$MgNH+0.5MgH_2 \rightarrow 0.5Mg_3N_2+H_2$ (10-8)

Assuming reaction (3-6) and reaction (10-8) are complete, a series of sequential reactions follows:

$0.5MgNH+0.25Mg(NH_2)_2+1.0LiH+0.25MgH_2$ (after ball milling)

$\rightarrow \boldsymbol{0.25Li_2Mg(NH)_2}+0.5MgNH+0.5LiH+0.25MgH_2+\boldsymbol{0.5H_2}$ (10-9)

(after dehydrogenation at low temp.)

$\rightarrow 0.25Li_2Mg(NH)_2+ \boldsymbol{0.25Mg_3N_2}+0.5LiH+\boldsymbol{1.0H_2}$ (after dehydrogenation at high temp.)

As a result, 2.0 moles of hydrogen atoms can be obtained from the above reaction, which is approximately 4.2 wt.% of hydrogen. Assuming 95% purity of the starting materials, the maximum hydrogen storage capacity is approximately 4.0 wt.% of H_2, which is in good agreement with the amount of hydrogen after dehydrogenation at 400°C as shown in Fig. 10-11 a).

However, it is worth mentioning that the ternary nitride product, LiMgN, which was predicted by Alapati et al. [103] and Akbarzadeh et al. [104] is not obtained, even though the samples milled under various milling mode and duration are heated up to 400°C in our experiment. Therefore, the dehydrogenation of the ($LiNH_2+1.0MgH_2$) mixture is processed by a two-step reaction that forms $Li_2Mg(NH)_2$ and Mg_3N_2, respectively, independent of the reaction pathways that are affected by the milling energy and duration.

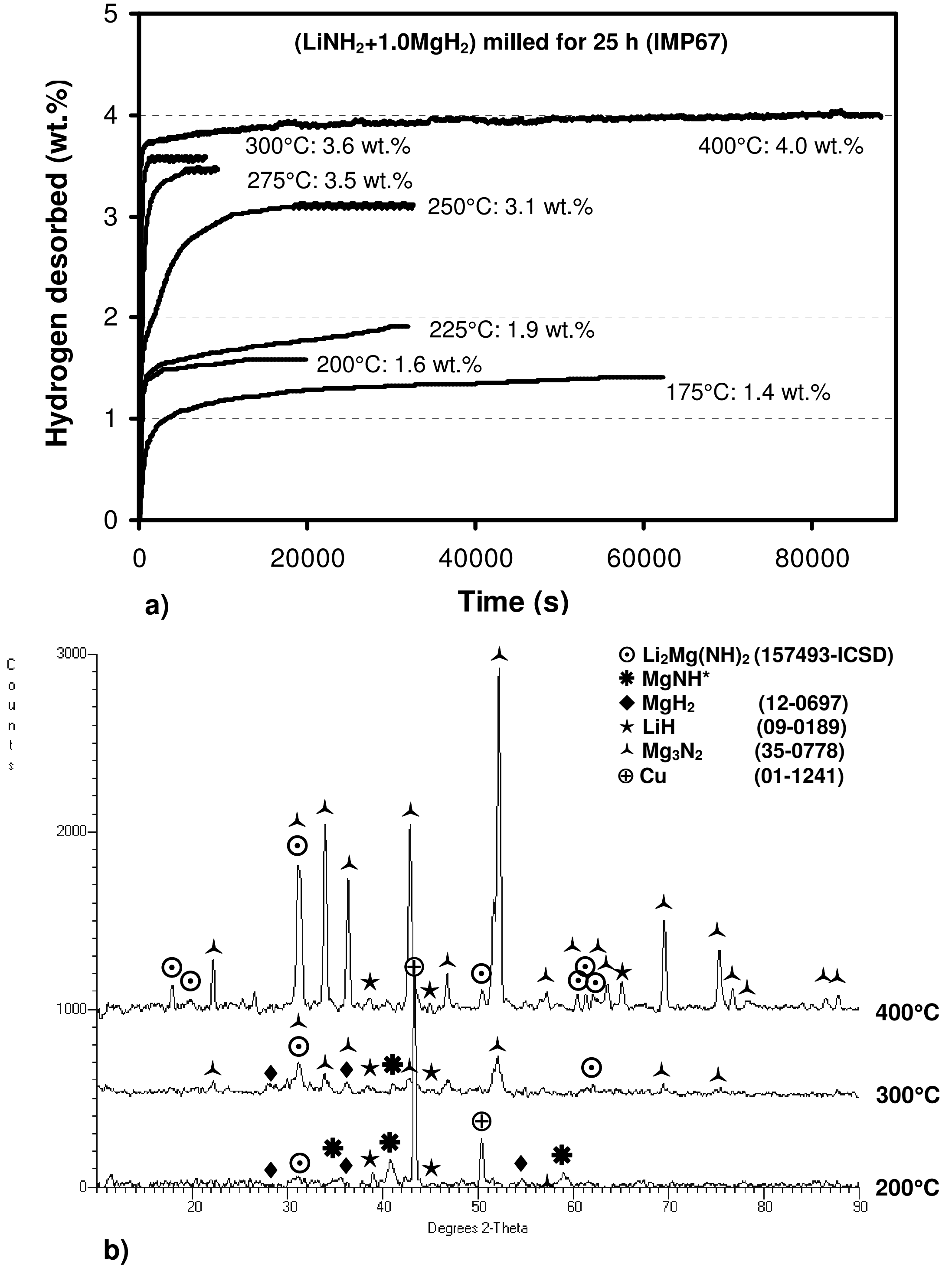

Fig. 10-11 a) Dehydrogenation curves and b) XRD profiles for the ($LiNH_2$ +1.0MgH_2) mixtures milled for 25 h (IMP67 mode) and subsequently dehydrogenated under 1 bar H_2 at varying temperatures (*Ref. # 108: Liang et al Chem. Eur. J. 16 (2010) 693-702)

Table 10-4. Summary of XRD results of the ($LiNH_2$+1.0MgH_2) mixture milled for 25 h (IMP67) and subsequently dehydrogenated under 1 bar H_2 at various temperatures

T(°C)	$LiNH_2$	MgH_2	MgNH	$Mg(NH_2)_2$	$Li_2Mg(NH)_2$	Mg_3N_2	LiH
R.T. (after ball milling)	-	O	O	O	-	-	O
200	-	O	O	-	O	-	O
300	-	O	O	-	O	O	O
400	-	-	-	-	O	O	O

10-5. Reversibility

To understand the reversibility of reaction (9-1) and reaction (9-2), the ($LiNH_2$+1.0MgH_2) mixtures under LES6-3B for 25 h were first dehydrogenated at 175 and 400°C under 1 bar of hydrogen, respectively. Next, the differently dehydrogenated samples were hydrogenated under the same conditions of 175°C at 50 bar of hydrogen. Based on the above analyses, the dehydriding reaction at 175°C corresponds to reaction (9-1), whereas both reaction (9-1) and (9-2) occur sequentially at 400°C. Fig. 10-12 a) and b) show the dehydriding/hydriding cycles of the ($LiNH_2$+1.0MgH_2) mixture milled under LES6-3B for 25 h at two different dehydrogenation temperatures of 175 and 400°C under 1 bar of hydrogen, respectively. The mixture dehydrogenated at 175°C and subsequently hydrogenated at 175°C under 50 bar of H_2 has full reversibility of 2.9 wt.% H_2. However, the mixture dehydrogenated at 400°C releases 5.8 wt.% H_2, but the dehydrogenated sample absorbs only 2.0 wt.% H_2 at 175°C under 50 bar of H_2, which indicates that the dehydrogenated samples cannot be completely converted to their starting states under the present testing conditions. To clarify the reaction pathways of dehydrogenation/hydrogenation, the mixtures at each cycling stage of the dehydriding and hydriding process were collected and analyzed using XRD as shown in Fig. 10-13 a) and b). The results are summarized in Table 10-5. It is very clear that XRD pattern of the mixture dehydrogenated at 175°C shows the diffraction peaks of the $Li_2Mg(NH)_2$ phase, while after hydrogenation, the diffraction peaks of the $Mg(NH_2)_2$ and LiH phases appear instead of that of the $Li_2Mg(NH)_2$ phase as shown in Fig. 10-13 a). Finally, the $Li_2Mg(NH)_2$ phase reappears after dehydrogenation of the hydrogenated mixture. The only difference between Fig. 10-13 a) and b) is the formation of the Mg_3N_2 phase after dehydrogenation at 400°C. However, this phase still exists even after the hydrogenation process. Therefore, this phase cannot be hydrogenated under our experimental conditions and results in a huge loss of reversible hydrogen capacity as shown in Fig. 10-12 b).

With the information obtained from the dehydriding/hydriding cycles and the corresponding XRD analysis, the reversible hydrogenation/dehydrogenation processes can be described by the following reaction:

$0.5Li_2Mg(NH)_2+H_2 \leftrightarrow 0.5Mg(NH_2)_2+LiH$ (3-6)

Assuming that all reactions are complete and that the dehydrogenation is processed in the low temperature range that corresponds to the first endothermic peak in the DSC curve, as shown in Fig. 10-6, a series of dehydriding/hydriding reactions follows:

$0.5xMg(NH_2)_2+xLiH+(1-0.5x)MgH_2+(1-x)LiNH_2$ (after ball milling)

$\rightarrow \boldsymbol{0.5Li_2Mg(NH)_2}+0.5MgH_2+\boldsymbol{1.0H_2}$ (after dehydrogenation) (10-10)

$\leftrightarrow \boldsymbol{0.5Mg(NH_2)_2+1.0LiH}+0.5MgH_2$ (after rehydrogenation)

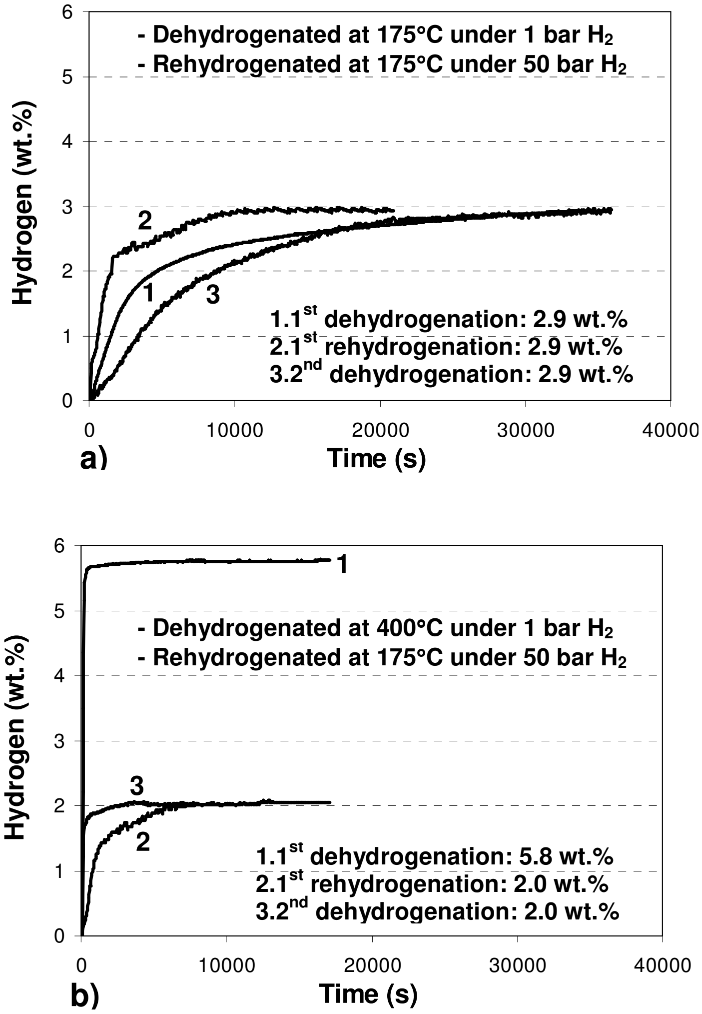

Fig. 10-12 (a) 1st and 2nd dehydrogenation curves at 175°C under 1 bar H_2 pressure and corresponding rehydrogenation curve at 175°C under 50 bar H_2 pressure and (b) 1st and 2nd dehydrogenation curves at 400°C under 1 bar H_2 pressure and corresponding rehydrogenation curve at 175°C under 50 bar H_2 pressure for the ($LiNH_2$+1.0MgH_2) mixtures milled for 25 h under LES6-3B mode

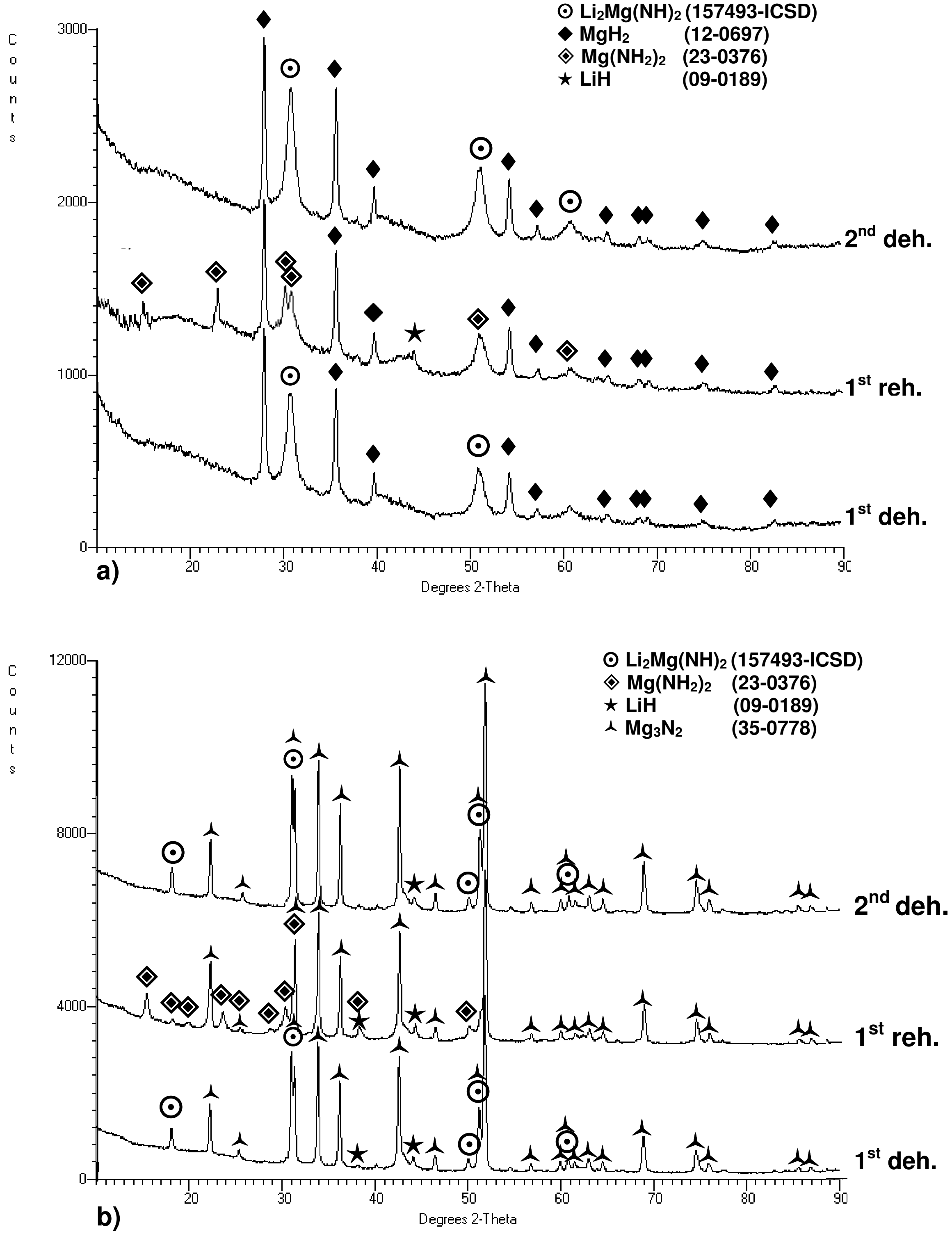

Fig. 10-13 XRD patterns for the ($LiNH_2$+1.0MgH_2) mixtures milled for 25 h under the LES6-3B mode and subsequently dehydrogenated at a) 175°C and b) 400°C, respectively, under 1 bar H_2 and then rehydrogenated at 175°C under 50 bar H_2

Table 10-5. Summary of XRD results of the ($LiNH_2$+1.0MgH_2) mixture milled for 25 h (LES6-3B) and subsequently dehydrogenated under 1 bar H_2 at 175°C and 400°C, respectively, and rehydrogenated under 50 bar H_2 at 175°C

T(°C)	MgH_2	$Li_2Mg(NH)_2$	Mg_3N_2	LiH	$Mg(NH_2)_2$
Dehydrogenated At 175°C under 1 bar H_2	O	O	-	-	-
Rehydrogenated At 175°C under 50 bar H_2	O	-	-	O	O
Re-dehydrogenated At 175°C under 1 bar H_2	O	O	-	-	-
Dehydrogenated At 400°C under 1 bar H_2	-	O	O	O	-
Rehydrogenated At 175°C under 50 bar H_2	-	-	O	O	O
Re-dehydrogenated At 400°C under 1 bar H_2	-	O	O	O	-

Based on reaction (10-10), the maximum reversible hydrogen amount is about 4.1 wt.%, which corresponds to 2.0 mol of hydrogen atoms per unit of the ($LiNH_2$+1.0MgH_2) mixture.

However, in case of dehydrogenation in the high temperature range, which corresponds to the second endothermic peak in the DSC curve, as shown in Fig. 10-6, the reaction pathways can be described by a series of dehydriding/hydriding reactions as follows:

$0.5xMg(NH_2)_2+xLiH+(1-0.5x)MgH_2+(1-x)LiNH_2$ (after ball milling)

$\boldsymbol{\rightarrow 0.25Li_2Mg(NH)_2+0.25Mg_3N_2+0.5LiH+1.5H_2}$ (after dehydrogenation)

$0.25Li_2Mg(NH)_2+0.25Mg_3N_2+0.5LiH \boldsymbol{+0.5H_2}$ (10-11)

$\leftrightarrow \boldsymbol{0.25Mg(NH_2)_2+1.0LiH}+0.25Mg_3N_2$ (after rehydrogenation)

As a result, 3.0 moles of hydrogen atoms can be desorbed the first time, but only 1.0 mole of hydrogen atoms can be absorbed and is reversible. Assuming 95% purity of the starting materials, the ($LiNH_2$+1.0MgH_2) mixture can initially desorb 5.8 wt.% H_2. However, in the subsequent hydrogenation/dehydrogenation process, only 2.0 wt.% H_2 can be absorbed and be reversible for the mixture. This result is in a good agreement with our experimental value of 2.0 wt.% of hydrogen for the ($LiNH_2$+0.7MgH_2) mixture as shown in Fig. 10-12 b).

Therefore, the ($LiNH_2$+1.0MgH_2) mixture milled under LES6-3B for 25 h is a completely reversible system only in the temperature range that corresponds to the first endothermic peak in the DSC curve as shown in Fig. 10-6.

10-6. Apparent activation energies

The measurements of the apparent activation energy of hydrogen desorption according to various reaction pathways were collected using the Kissinger method (Eq. (6-2)). Fig. 10-14 a) and c) show the effect of various heating rates on DSC profiles, which is an underlying principle of the Kissinger method. The corresponding Kissinger plots for each reaction are shown in Fig. 10-14 b) and d) for the ($LiNH_2$+1.0MgH_2) mixtures milled under the IMP67 mode for 1 and 25 h and under the LES6-3B mode for 25 h, respectively. The excellent correlation coefficients, R^2, obtained for the Kissinger plots in Fig. 10-14 b) and d) attest to the accuracy of the method.

The apparent activation energies of each mixture milled under different milling conditions are not comparable because they have different phases after the ball milling, which results in different dehydrogenation reaction pathways. Compared to the ($LiNH_2$+nMgH_2) (n=0.55, 0.6 and 0.7) mixtures discussed in Chapter 9, the effect of the milling duration on the apparent activation energy is not pronounced. However, it is remarkable that the apparent activation energies of the ($LiNH_2$+1.0MgH_2) mixtures milled under the IMP67 mode for 1 h are lower than those of the ($LiNH_2$+nMgH_2) (n=0.55, 0.6 and 0.7) mixtures milled under the same conditions. As discussed in Chapter 9, the apparent activation energy decreases from 188.4 to 112.0 kJ/mol as the molar ratio increases from 0.55 to 0.7 for the reaction (3-5). In this study, further increasing the molar ratio to 1.0 results in an apparent activation energy of 99.4 kJ/mol, which is shown in Fig. 10-15. It remains interesting that the high molar ratio of MgH_2/$LiNH_2$ can improve the kinetic properties of this system.

In this study, there are two interesting findings: 1) hydrogen can be desorbed during the ball milling process given appropriate milling energy and duration, and 2) milling energy and duration can affect the reaction pathways for the dehydrogenation of this mixture. It is also worth highlighting that $Li_2Mg(NH)_2$ and Mg_3N_2 are formed by dehydrogenation at low and high temperatures, respectively, regardless of the reaction pathways. However, the ternary nitride product, LiMgN, which was predicted by Alapati et al. [103] and Akbarzadeh et al. [104], is not obtained in our study. Therefore, the research on a higher molar ratio of MgH_2/$LiNH_2$ system can be motivated for obtaining further understanding of the reaction pathways of the $LiNH_2$-MgH_2 system.

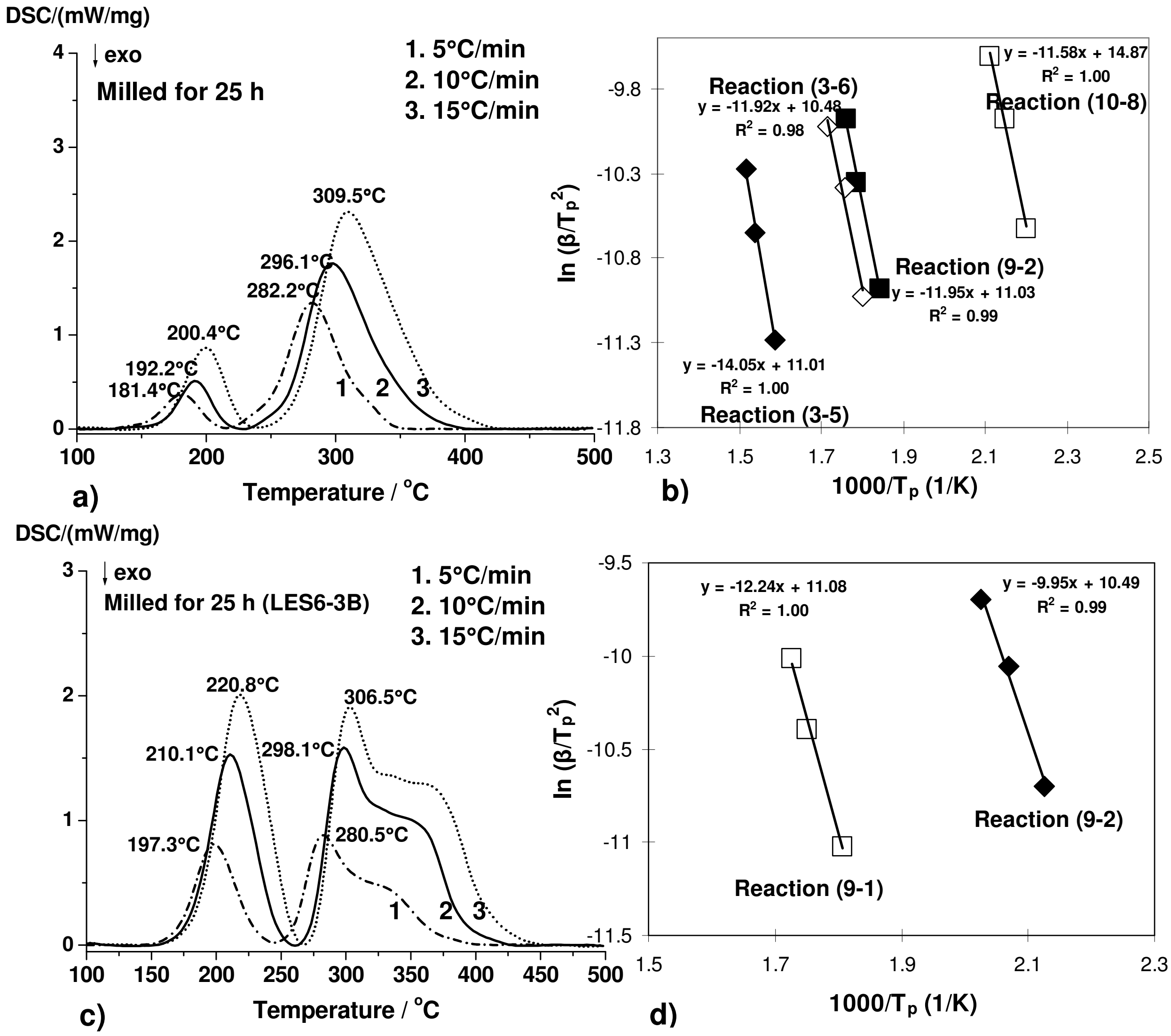

Fig. 10-14 a) DSC curves at various heating rates for the ($LiNH_2$+1.0MgH_2) mixtures milled for 25 h and b) the corresponding Kissinger plots of the apparent activation energies for the mixtures milled for 1 h (closed) and 25 h (open), respectively (IMP67 mode). c) DSC curves at various heating rates and d) the Kissinger plots of the apparent activation energies for the ($LiNH_2$+1.0MgH_2) mixtures milled for 25 h in the LES6-3B mode

- **Reaction (3-5): $LiNH_2+0.5MgH_2 \rightarrow 0.5Li_2Mg(NH)_2+H_2$**
- **Reaction (9-1): $0.5xMg(NH_2)_2+xLiH+(0.5-0.5x)MgH_2+(1-x)LiNH_2 \rightarrow 0.5Li_2Mg(NH)_2+H_2$**
- **Reaction (3-6): $0.5Mg(NH_2)_2+LiH \leftrightarrow 0.5Li_2Mg(NH)_2+H_2$**
- **Reaction (9-2): $0.5Li_2Mg(NH)_2+MgH_2 \rightarrow 0.5Mg_3N_2+LiH+H_2$**
- **Reaction (10-8): $MgNH+0.5MgH_2 \rightarrow 0.5Mg_3N_2+H_2$**

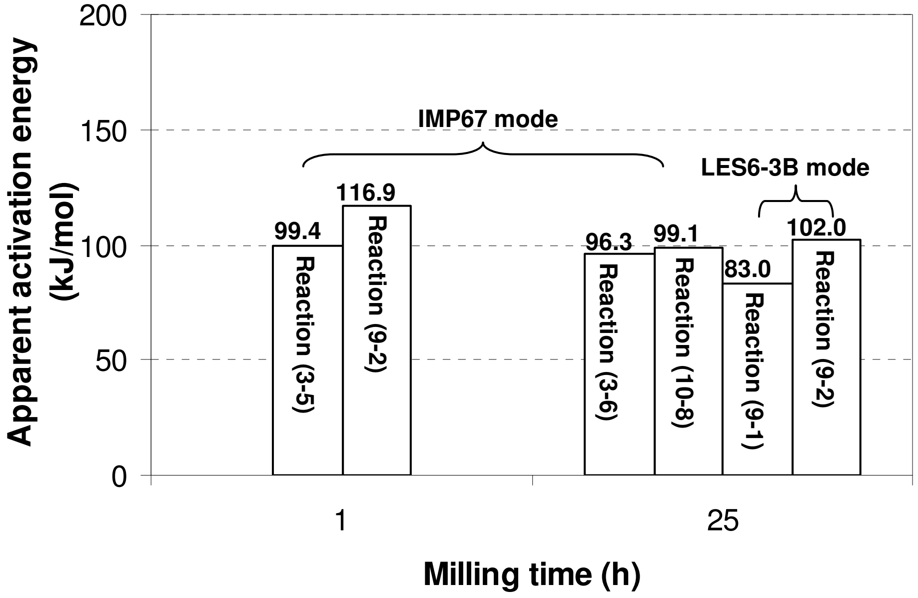

Fig. 10-15 Comparison of the apparent activation energies for ($LiNH_2$+1.0MgH_2) milled for 1 h and 25 h under IMP67 mode and for 25 h under the LES6-3B mode, respectively

11. ($LiNH_2$+1.5MgH_2) system

11-1. Hydrogen desorption during ball milling

Fig. 11-1 shows the amount of hydrogen desorption exhibited by the ($LiNH_2$+1.5MgH_2) mixtures during the ball milling process under different milling modes as a function of milling time.

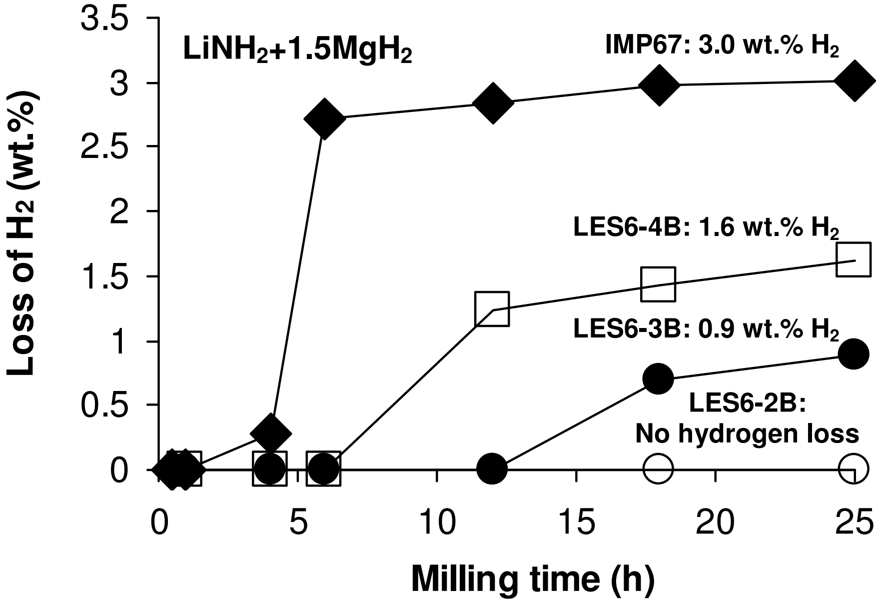

Fig. 11-1 Hydrogen loss of the ($LiNH_2$+1.5MgH_2) during ball milling process under four different milling modes

The amount of hydrogen released from starting materials is calculated by using the ideal gas law with the measured gas pressure variations within the ball milling jar as shown in Appendix A-2. As can be seen in Fig. 11-1, under the high-energy impact (IMP67) mode, the release of hydrogen begins and is accelerated after milling for 4 h and is almost saturated after 6 h of ball milling. After 25 h of milling, 3.0 wt.% H_2 is released from the 1:1.5 molar ratio mixture. In contrast to the IMP67 mode, the low-energy shearing (LES6) modes with 4 and 3 balls result in the release of 1.6 and 0.9 wt.% H_2 after 25 h milling, respectively. However, any pressure changes during ball milling are not shown under the low-energy shearing mode with 2 balls (LES6-2B). This result clearly indicates that the amount of hydrogen desorbed during the ball milling of $LiNH_2$-MgH_2 system strongly depends on the milling energy and the molar ratio of $MgH_2/LiNH_2$ because more hydrogen in the mixture of $LiNH_2$-MgH_2 (1:1.5) is desorbed during the ball milling under the same conditions compared to the mixture of $LiNH_2$-MgH_2 (1:1) as discussed in Chapter 10. Therefore, hydrogen comes from the chemical reaction between $LiNH_2$ and MgH_2 [107, 108], and its chemical reaction between both starting materials during ball milling can be accelerated as the molar ratio of $MgH_2/LiNH_2$ increases.

To determine the reaction pathways that occur during the ball milling process, solid residues at different ball milling stages were collected for both XRD and FT-IR characterizations. Fig. 11-2 a) and b) show the XRD patterns and FT-IR spectra of the ($LiNH_2$+1.5MgH_2) mixtures milled under the IMP67 mode for various milling times, respectively. The mixture milled under the high-energy impact (IMP67) mode for 1 h still consists of the original $LiNH_2$ and MgH_2 phases. After 4 h of ball milling under the same milling mode, the XRD peaks of the newly formed MgNH [99, 100] and LiH phases are shown in XRD pattern, while the diffraction peaks of $LiNH_2$ phase disappear, and the diffraction peaks of MgH_2 phase still dominate the XRD pattern. As mentioned in Chapter 10, this result indicates that $LiNH_2$ is completely converted to $Mg(NH_2)_2$ and LiH by the metathesis reaction with MgH_2 [102, 107, 108], and the newly formed $Mg(NH_2)_2$ partially reacts with MgH_2 to form MgNH and H_2.

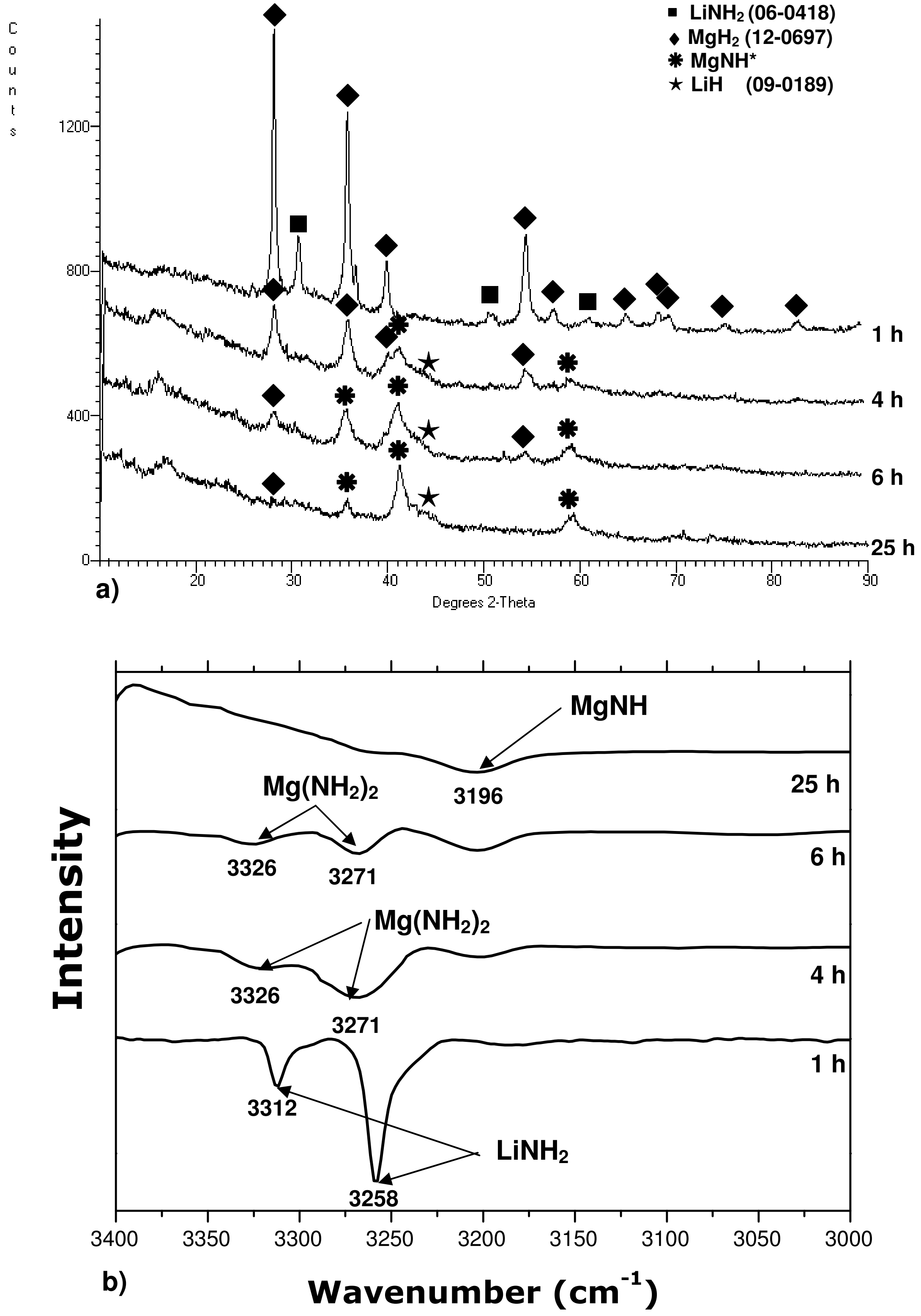

Fig. 11-2 a) XRD patterns and b) FT-IR absorption spectra for the ($LiNH_2$+1.5MgH_2) milled for various milling times (IMP67 mode) (*Ref. # 108: Liang et al Chem. Eur. J. 16 (2010) 693-702)

Because it is difficult to establish the presence of the $Mg(NH_2)_2$ phase by XRD, due to its amorphous state under the energetic ball milling process [107], FT-IR analysis was performed as shown in Fig. 11-2 b). The analysis clearly shows the formation of $Mg(NH_2)_2$ with the characteristic absorption lines at 3271 and 3326 cm^{-1} [100] after 4 h of ball milling under the IMP67 mode. When the ball milling is prolonged to 6 h under IMP67 mode, the diffraction peaks and the absorption spectrums of MgNH phase dominates the XRD pattern and FT-IR spectrum [100], whereas the intensity of the MgH_2 diffraction peaks and the characteristic absorption lines of $Mg(NH_2)_2$ in the FT-IR spectrum decrease. Finally, after 25 h of ball milling, the characteristic absorption lines of $Mg(NH_2)_2$ phase finally disappear; only MgNH, MgH_2 and LiH phases are detectable in Fig. 11-2 a) and b). One interesting finding is that the MgNH phase forms earlier in the mixture of $LiNH_2$-MgH_2 (1:1.5) than the the mixture of $LiNH_2$-MgH_2 (1:1.0), all of which were milled under the same milling mode. This phase begin to form after 4 h of ball milling under the IMP67 mode in the ($LiNH_2$+ 1.5MgH_2) mixture; in the ($LiNH_2$+1.0MgH_2) mixture, the MgNH phase began to form after 6 h of ball milling in the same milling mode as shown in Chapter 10. This result is clear evidence that increasing the molar ratio of MgH_2/$LiNH_2$ can accelerate the solid-solid reactions during ball milling; consequently, a 1:1.5 mixture milled under the IMP67 mode releases more hydrogen than a 1:1 mixture milled in the same milling conditions.

Fig. 11-3 a) and b) represent the XRD patterns of the ($LiNH_2$+1.5MgH_2) mixtures milled under both low-energy shearing (LES6) modes with 2 and 3 balls for 25 h, respectively. It is evident that the mixture milled under the LES6-2B mode for 25 h consists of the original $LiNH_2$/MgH_2 phases and LiH, which indicates that a specific quantity of the starting mixture is converted to $Mg(NH_2)_2$ and LiH by the metathesis reaction mentioned above.

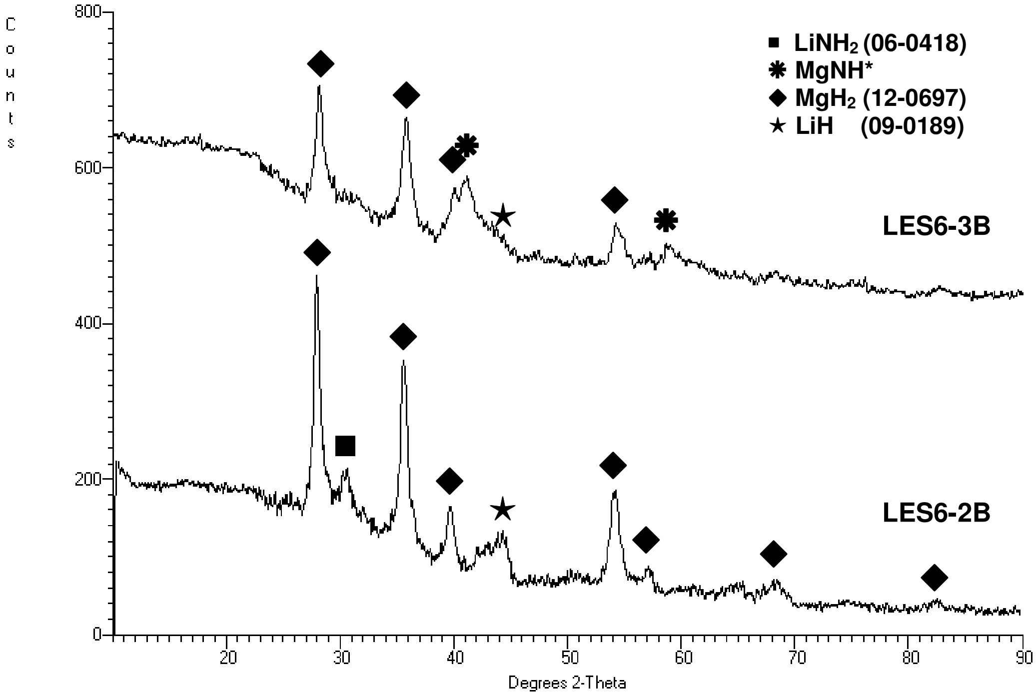

Fig. 11-3 XRD patterns for the ($LiNH_2$ + $1.5MgH_2$) mixture milled for 25 h under two different milling modes (*Ref. # 108: Liang et al Chem. Eur. J. 16 (2010) 693-702)

Table 11-1. Summary of XRD results of the ($LiNH_2$+$1.5MgH_2$) mixture milled for various milling modes and times

Milling Mode	Milling time (h)	$LiNH_2$	MgH_2	$Mg(NH_2)_2$	LiH	MgNH
IMP67	1	O	O	-	-	-
	4	-	O	O	O	O
	6	-	O	O	O	O
	25	-	O	-	O	O
LES6-2B	25	O	O	O	O	-
LES6-3B	25	-	O	O	O	O

In contrast to LES6-2B, the diffraction peaks of newly formed MgNH phase are detected in XRD pattern of the mixture milled under the LES6-3B mode for 25 h, while $LiNH_2$ peaks disappear in the XRD pattern. This result clearly indicates that $LiNH_2$ is completely consumed to form the $Mg(NH_2)_2$ and LiH phases and that a certain quantity of newly formed $Mg(NH_2)_2$ phase reacts with the original MgH_2 phase to form MgNH and H_2. These results are summarized in Table 11-1.

Based on the above analyses, the following reaction pathways during ball milling under the high-energy impact (IMP67) mode can be proposed. In the first step, $LiNH_2$ is converted to $Mg(NH_2)_2$ and LiH by the metathesis reaction with MgH_2 [107, 108]:

$$LiNH_2 + 0.5MgH_2 \rightarrow 0.5Mg(NH_2)_2+LiH \qquad (10\text{-}1)$$

In the second step, $Mg(NH_2)_2$ reacts with MgH_2 to form MgNH and H_2 as proposed by Liu et al. [107] and Liang et al. [108]:

$$0.5Mg(NH_2)_2 +0.5MgH_2 \rightarrow MgNH+H_2 \qquad (10\text{-}2)$$

Based on reaction (10-1) and reaction (10-2) and the quantity of hydrogen desorption during ball milling, as shown in Fig. 11-1, a series of sequential reactions follows:

$$\begin{aligned}
&LiNH_2+1.5MgH_2 \rightarrow LiNH_2+1.5MgH_2 \text{ (after 1 h milling)}\\
&\rightarrow \mathbf{0.09MgNH+0.455Mg(NH_2)_2+LiH}+0.955MgH_2+\mathbf{0.09H_2} \text{ (after 4 h milling)}\\
&\rightarrow \mathbf{0.884MgNH}+0.058Mg(NH_2)_2+LiH+0.558MgH_2+\mathbf{0.884H_2} \text{ (after 6 h milling)} \qquad (11\text{-}1)\\
&\rightarrow \mathbf{MgNH} + LiH+0.5MgH_2+\mathbf{1.0H_2} \text{ (after 25 h milling)}
\end{aligned}$$

The details to determine reaction pathways occurring during ball milling are shown in Appendix A-4. It is interesting to note that reaction (10-2) is completed after 25 h of ball milling. Therefore, 3.2 wt.% H_2 can be released during the ball milling process, which corresponds to 2.0 mol of hydrogen atoms per unit of the ($LiNH_2$+1.5MgH_2) mixture. Considering 95% purity of the starting materials, the maximum 3.0 wt.% H_2 can be released.

On the other hand, the following reaction is proposed for the ($LiNH_2$+1.5MgH_2) mixture milled under the low energy shearing (LES6-2B) mode for 25 h based on the above analyses:

$$LiNH_2+1.5MgH_2 \rightarrow \mathbf{0.5xMg(NH_2)_2+xLiH}+(1.5-0.5x)MgH_2+(1-x)LiNH_2 \qquad (11\text{-}2)$$

where x indicates that only fractions of $LiNH_2$ and MgH_2 are involved in reaction (10-1) because their diffraction peaks are still observed after ball milling as shown in Fig. 11-3.

Different milling times, milling modes and number of balls can affect the milling energy; therefore, different solid products may result during ball milling depending on the milling energy. Therefore, these parameters significantly affect the reaction pathways of hydrogen desorption in subsequent heating processes.

11-2. Thermal behavior

Fig. 11-4 compares the DSC curves of the ($LiNH_2$+1.5MgH_2) mixtures milled under the LES6-2B mode for 25 h and the IMP67 mode for 1 and 25 h, respectively. Two endothermic peaks are shown in the DSC curves of the 1:1.5 mixture milled under the LES6-2B mode for 25 h and IMP67 mode for 1 h, respectively, while the same mixture milled under IMP67 mode for 25 h has only one endothermic peak, which starts at 230°C and ends at 380°C. It is worth noting that the milling mode (energy) can change the reaction pathways from a two-step reaction to a one-step reaction.

To clarify the gaseous species released during heating, a TPD test was carried out for the ($LiNH_2$+1.5MgH_2) mixture milled under the LES6-2B mode for 25 h, and the result is presented in Fig. 11-5. Three hydrogen desorption peaks are observed below 400°C, while nearly no NH_3 emission (ppm level) is detected in the TPD measurements up to 500°C within our experimental accuracy. It is likely that the first and second hydrogen desorption peaks correspond to the first endothermic peak in its DSC curve (Fig. 11-4) and that the third peak is related to the second endothermic peak as shown in Fig. 11-4. Moreover, it should be noted that the intensity of the third desorption peak of H_2 is higher than that of the other peaks.

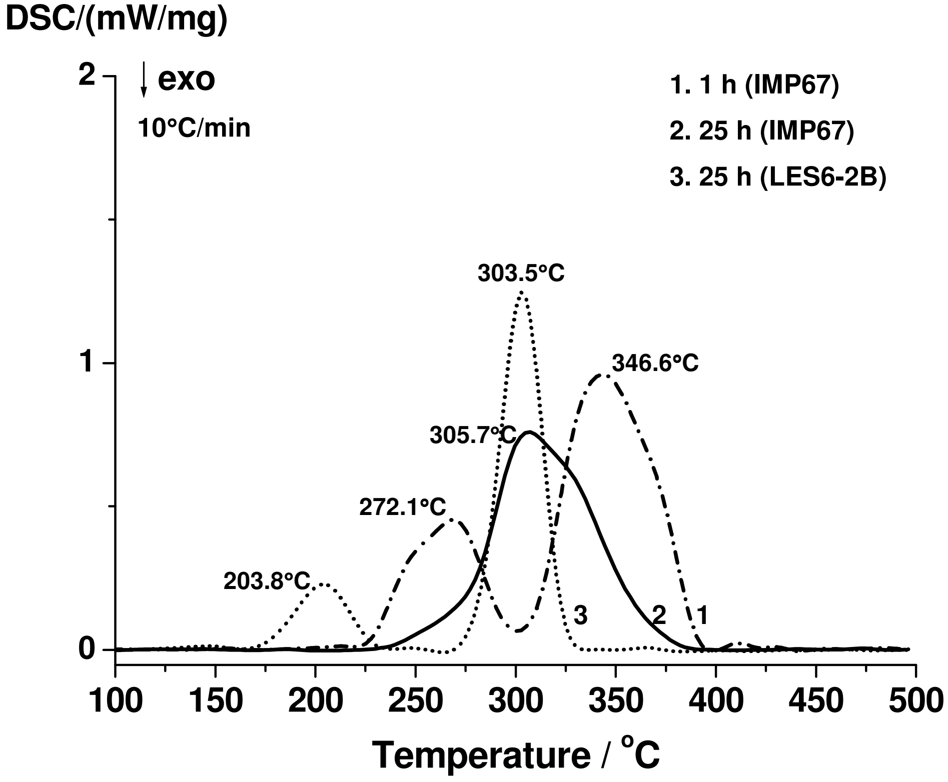

Fig. 11-4 Comparison of DSC curves for the ($LiNH_2$+$1.5MgH_2$) mixtures milled for 1 h and 25 h under IMP67 mode and for 25 h under the LES6-2B mode

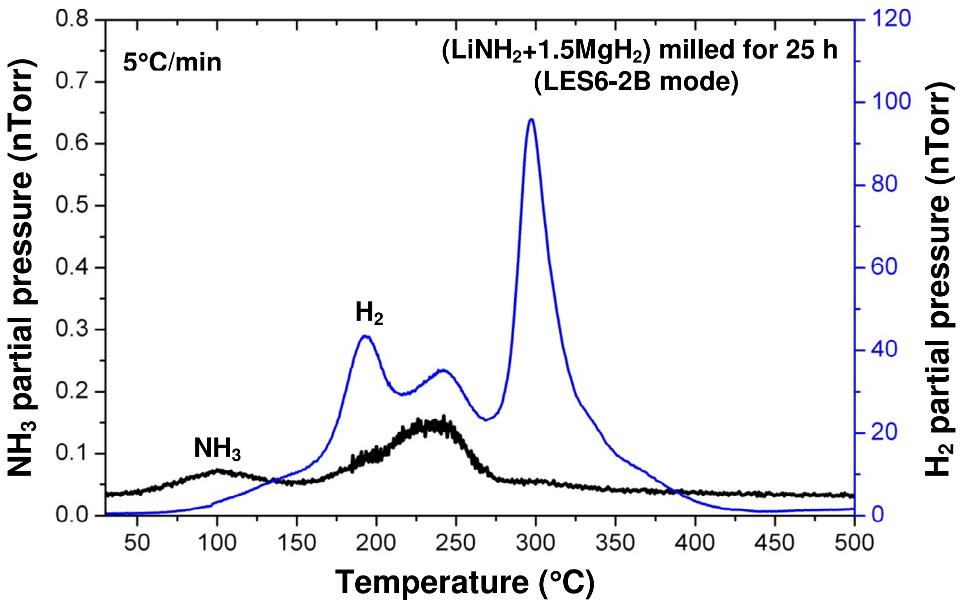

Fig. 11-5 TPD spectra for the ($LiNH_2$+1.5MgH_2) milled for 25 h (LES6-2B mode)

11-3. Reaction pathways occurring during dehydrogenation

To further understand the reaction pathways of the $LiNH_2$-MgH_2 system, the correlation between mechanical ball milling and hydrogen-desorption reactions is investigated for the mixture of $LiNH_2$-MgH_2 (1:1.5).

11-3-1. The ($LiNH_2$+1.5MgH_2) milled under the LES6-2B mode for 25 h

The dehydrogenation curves of ($LiNH_2$+1.5MgH_2) milled under the LES6-2B mode for 25 h at various temperatures under 1 bar H_2 are shown in Fig. 11-6 a). It is evident that the same mixtures dehydrogenated at 200, 250, 300 and 400°C under 1 bar of H_2 release 3.1, 4.9, 5.8 and 6.1 wt.% H_2, respectively. In particular, this mixture can also desorb 0.4 and 1.0 wt.% H_2 at the relatively low temperatures of 125 and 150°C, respectively.

Solid residues were collected after dehydrogenating at different temperatures and analyzed using XRD to ascertain the chemical reactions that occur upon dehydrogenation. As seen in

Fig. 11-6 b), the desorption at low temperatures below 250°C results in the formation of the $Li_2Mg(NH)_2$ phase, while the diffraction peaks of the Mg_3N_2 and LiH phases dominate the XRD pattern after dehydrogenation at high temperatures. The $Li_2Mg(NH)_2$ and MgH_2 peaks in the XRD patterns finally disappear after dehydrogenation at 400°C. This result clearly indicates that the $Li_2Mg(NH)_2$ and MgH_2 phases are completely consumed to form the Mg_3N_2 and LiH phases. This result is summarized in Table 11-2.

Based on the above analyses, the following reaction pathways of hydrogen desorption for the ($LiNH_2+1.5MgH_2$) mixture milled under LES6-2B for 25 h are proposed. As mentioned above, hydrogen desorption follows a two-step reaction. In the first step, which corresponds to the first endothermic peak shown in Fig. 11-4, $Li_2Mg(NH)_2$ and H_2 are formed through reaction (9-1) [83, 86, 135]. In the second step, which is related to the second endothermic peak shown in the DSC curve, Mg_3N_2, LiH and H_2 are formed through reaction (9-2) [134].

Assuming reaction (9-1) and (9-2) are complete, a series of sequential reactions follows:

$[0.5xMg(NH_2)_2+xLiH]+[(1-x)LiNH_2+(1.5-0.5x)MgH_2]$ (after ball milling)

$\rightarrow \mathbf{0.5Li_2Mg(NH)_2}+MgH_2+\mathbf{1.0H_2}$ (after dehydrogenation at low temp.) (11-3)

$\rightarrow \mathbf{0.5Mg_3N_2+LiH+2.0H_2}$ (after dehydrogenation at low temp.)

In total, 4.0 moles of hydrogen atoms can be obtained from the above reaction, which is approximately 6.5 wt.% of hydrogen. Assuming 95% purity of the starting materials, the maximum hydrogen storage capacity decreases to 6.1 wt.% of H_2. This result is in excellent agreement with our experimental value of 6.1 wt.% of H_2 obtained after dehydrogenation at 400°C as shown in Fig. 11-6 a).

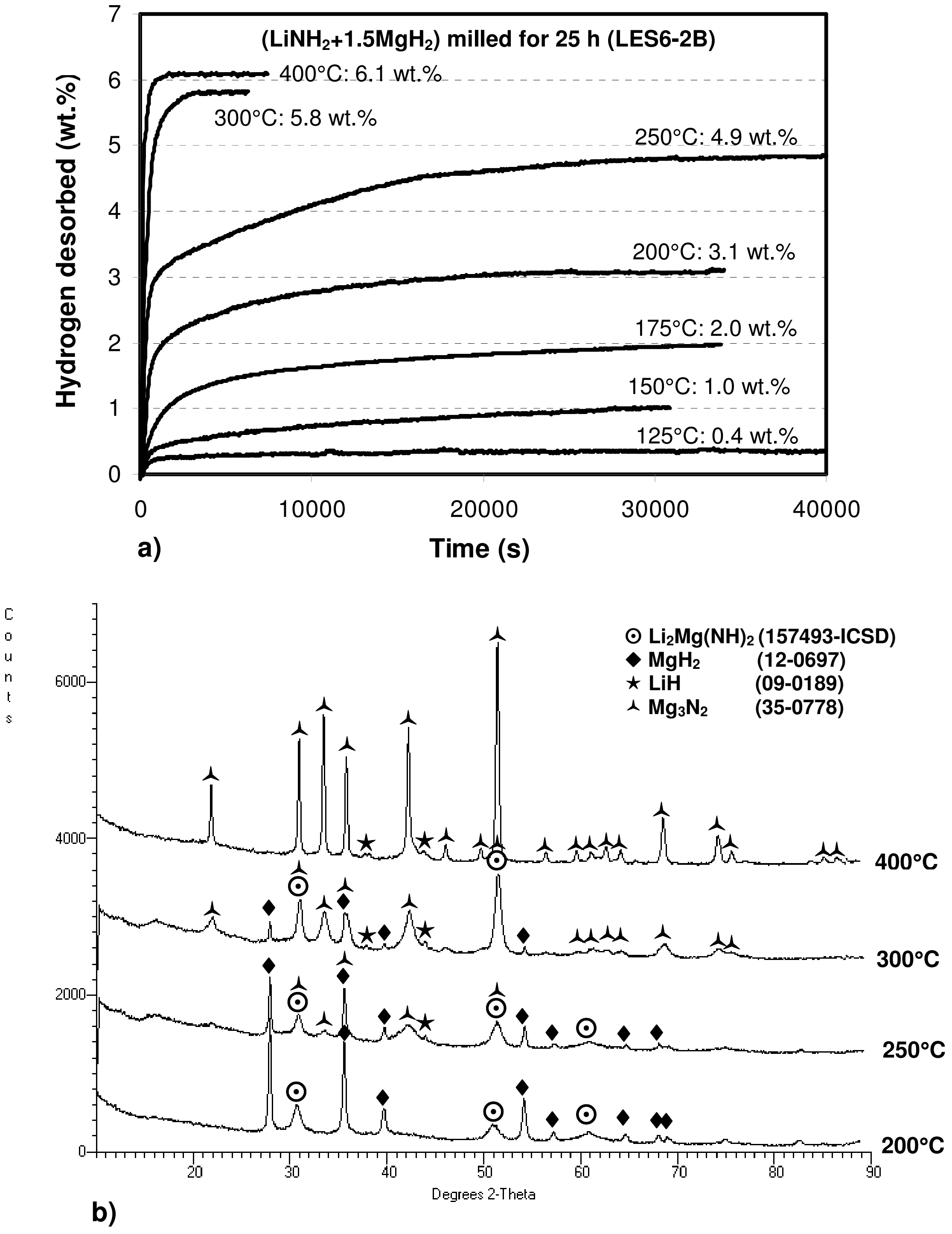

Fig. 11-6 Dehydrogenation curves under 1 bar H_2 pressure (atmospheric) at various temperatures and b) the corresponding XRD patterns for the ($LiNH_2$+1.5MgH_2) mixtures milled for 25 h under the LES6-2B mode

Table 11-2. Summary of the XRD results of the ($LiNH_2$+1.5MgH_2) mixture milled for 25 h (LES6-2B) and subsequently dehydrogenated under 1 bar H_2 at various temperatures

T (°C)	$LiNH_2$	MgH_2	$Mg(NH_2)_2$	$Li_2Mg(NH)_2$	Mg_3N_2	LiH
R.T. (after ball milling)	O	O	O	-	-	O
200	-	O	-	O	-	-
250	-	O	-	O	O	O
300	-	O	-	O	O	O
400	-	-	-	-	O	O

11-3-2. The ($LiNH_2$+1.5MgH_2) milled under the IMP67 mode for 1 h

Fig. 11-7 a) shows dehydrogenation curves of ($LiNH_2$+1.5MgH_2) milled under the high-energy impact (IMP67) mode for 1 h at various temperatures under 1 bar H_2. It is evident that the same mixtures dehydrogenated at 250, 300 and 425°C under 1 bar of H_2 release 3.1, 5.0 and 6.1 wt.% H_2, respectively. To clarify the chemical reactions that occur during dehydrogenation, the reactants and products after dehydrogenation at different temperatures were collected and analyzed using XRD. As shown in Fig. 11-7 b), the XRD pattern of the mixture dehydrogenated at 250°C shows the diffraction peaks of the $Li_2Mg(NH)_2$ phase. As the heating temperature increases, the intensity of both the MgH_2 and $Li_2Mg(NH)_2$ diffraction peaks decreases, and the two phases completely disappear after dehydrogenation at 400°C. The Mg_3N_2 and LiH phases start forming at 300°C and the diffraction peaks of the Mg_3N_2 and LiH phases dominate the XRD patterns after dehydrogenation above 400°C. It is clear that the dehydrogenation of this mixture is processed by both reactions, which form $Li_2Mg(NH)_2$ and {Mg_3N_2 and LiH}, respectively. This result is summarized in Table 11-3.

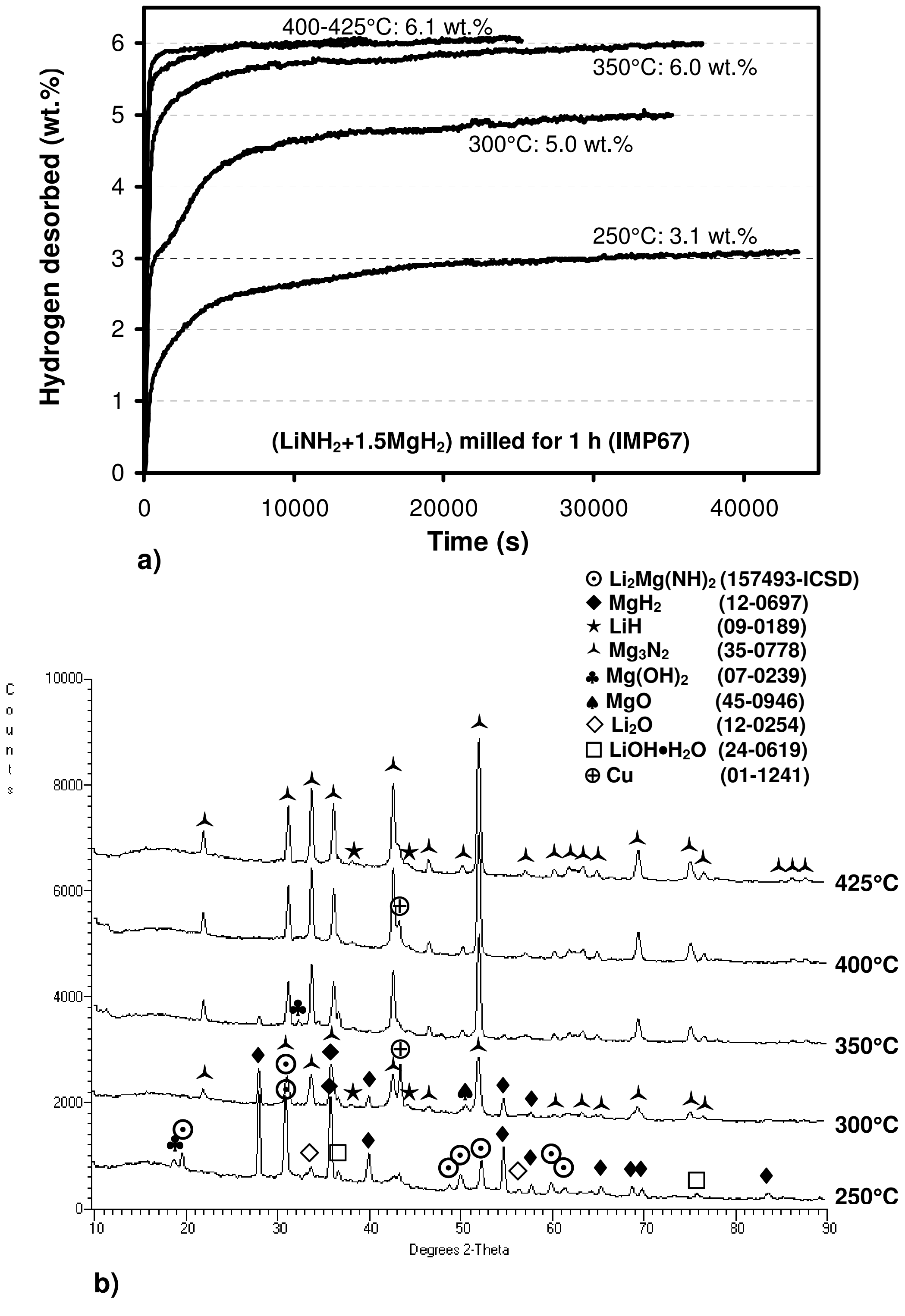

Fig. 11-7 a) Dehydrogenation curves and b) XRD patterns for 1 h milled ($LiNH_2$+1.5MgH_2) mixtures (IMP67 mode) and subsequently dehydrogenated under 1 bar H_2 at varying temperatures

Table 11-3. Summary of XRD results of the ($LiNH_2$+1.5MgH_2) mixture milled for 1 h (IMP67) and subsequently dehydrogenated under 1 bar H_2 at various temperatures

T(°C)	$LiNH_2$	MgH_2	$Li_2Mg(NH)_2$	Mg_3N_2	LiH
R.T. (after ball milling)	O	O	-	-	-
250	-	O	O	-	-
300	-	O	O	O	O
350	-	O	O	O	O
400	-	-	-	O	O
425	-	-	-	O	O

Therefore, reaction (3-5) and reaction (9-2), as discussed in Chapter 10, occur sequentially and can be described by a series of sequential reactions as follows:

$LiNH_2$+1.5MgH_2 (after ball milling)

→ **0.5$Li_2Mg(NH)_2$**+MgH_2+**1.0H_2** (after dehydrogenation at low temp.) (11-4)

→ **0.5Mg_3N_2+LiH+2.0H_2** (after dehydrogenation at high temp.)

Finally, approximately 6.5 wt.% of hydrogen is liberated from the mixture, which is equivalent to 4.0 moles of hydrogen atoms per unit of the ($LiNH_2$+1.5MgH_2) mixture. Considering the average purity of the starting materials (95%), the total hydrogen storage capacity is 6.1 wt.% of H_2. As shown in Fig. 11-7 a), we obtained the exact same amount of hydrogen after dehydrogenation at 425°C.

11-3-3. The ($LiNH_2$+1.5MgH_2) milled under the IMP67 mode for 25 h

Fig. 11-8 a) represents dehydrogenation curves of ($LiNH_2$+1.5MgH_2) milled under the IMP67 mode for 25 h at various temperatures under 1 bar H_2. It is evident that the same mixtures dehydrogenated at 250, 300 and 400°C under 1 bar of H_2 release 2.7, 3.0 and 3.2 wt.% H_2, respectively. It should be noted that the hydrogen capacity of this mixture under the IMP67 mode for 25 h is lower than the mixture milled for 1 h in the same milling mode, due to the hydrogen loss after the ball milling process shown in Fig. 11-1. To confirm the chemical reactions that occur during dehydrogenation, the solid residues were collected after dehydrogenation at different temperatures and analyzed using XRD. As shown in Fig. 11-8 b), the XRD pattern of the mixture dehydrogenated at 250°C shows the diffraction peaks of the newly formed Mg_3N_2 phase. As the heating temperature increases, the intensities of both MgNH and MgH_2 diffraction peaks decrease, and the two phases completely disappear after dehydrogenation at 400°C. The XRD peaks of the Mg_3N_2 and LiH phases dominate the XRD pattern after dehydrogenation at 400°C. This result clearly shows that the dehydrogenation of this mixture is processed by a one-step reaction that forms Mg_3N_2. This result is summarized in Table 11-4.

Therefore, this reaction will be followed by reaction (10-8) as discussed in Chapter 10 and can be described as follow:

$MgNH+LiH+0.5MgH_2$ (after ball milling) (11-5)

$\rightarrow \mathbf{0.5Mg_3N_2}+LiH+\mathbf{1.0H_2}$ (after dehydrogenation)

As a result, 2.0 moles of hydrogen atoms can be obtained from the above reaction, which is approximately 3.3 wt.% of hydrogen. Considering 95% purity of the starting materials, the maximum hydrogen storage capacity is around 3.2 wt.% of H_2, which is in a good agreement with the amount of hydrogen after dehydrogenation at 400°C as shown in Fig. 11-8 a).

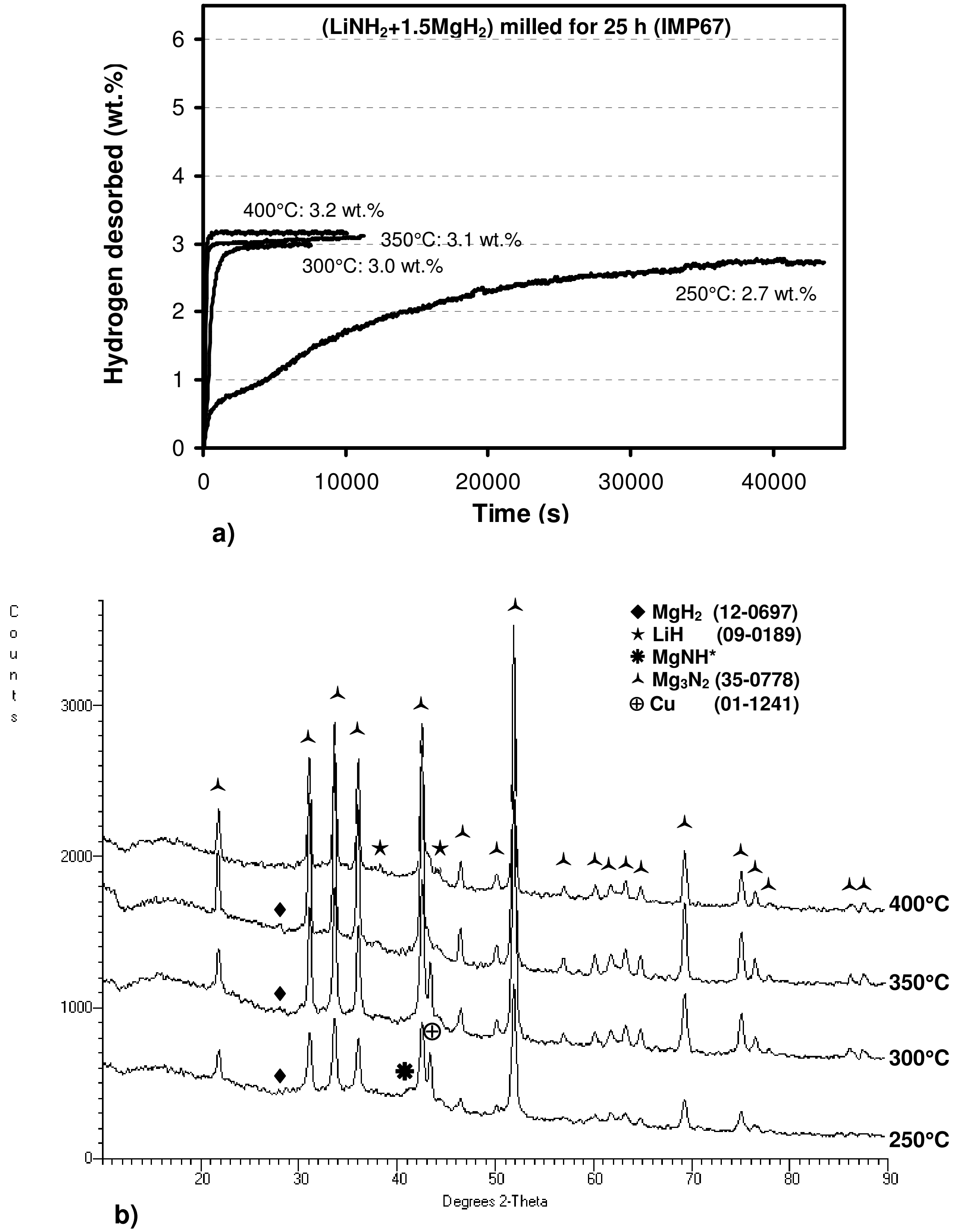

Fig. 11-8 a) Dehydrogenation curves and b) XRD patterns for 25 h milled ($LiNH_2$+1.5MgH_2) mixtures (IMP67 mode) that are subsequently dehydrogenated under 1 bar H_2 at various temperatures (*Ref. # 108: Liang et al Chem. Eur. J. 16 (2010) 693-702)

Table 11-4. Summary of XRD results of the ($LiNH_2$+1.5MgH_2) mixture milled for 25 h (IMP67) and subsequently dehydrogenated under 1 bar H_2 at various temperatures

T(°C)	$LiNH_2$	MgH_2	MgNH	$Mg(NH_2)_2$	$Li_2Mg(NH)_2$	Mg_3N_2	LiH
R.T. (after ball milling)	-	O	O	-	-	-	O
250	-	O	O	-	-	O	O
300	-	O	O	-	-	O	O
350	-	O	O	-	-	O	O
400	-	-	-	-	-	O	O

11-4. Reversibility

To understand the reversibility of reaction (9-1) and reaction (9-2), the ($LiNH_2$+1.5MgH_2) mixtures under LES6-2B for 25 h were first dehydrogenated at 175 and 400°C under 1 bar of hydrogen, respectively. The differently dehydrogenated samples were hydrogenated under the same conditions of 175°C under 50 bar of hydrogen. Based on the above analyses, the dehydriding reaction at 175°C corresponds to reaction (9-1), whereas both reaction (9-1) and reaction (9-2) occur sequentially at 400°C. Fig. 11-9 a) and b) show the reversibility of the ($LiNH_2$+1.5MgH_2) mixture milled under LES6-2B for 25 h at two different dehydrogenation temperatures of 175 and 400°C under 1 bar of hydrogen, respectively. The mixture dehydrogenated at 175°C and sequently hydrogenated at 175°C under 50 bar of H_2 reversibly desorbs and absorbs 2.0 wt.% H_2. However, after dehydrogenation at 400°C for the same mixture, there is no hydrogenation/dehydrogenation, due to the irreversibility of the Mg_3N_2 phase as discussed in Chapters 9 and 10.

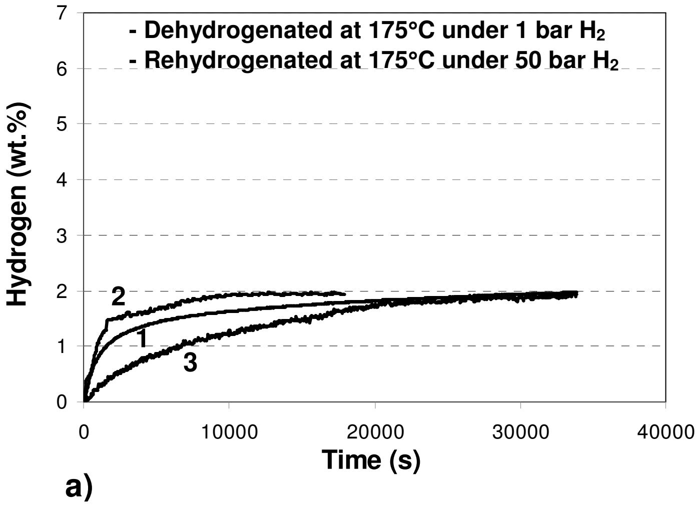

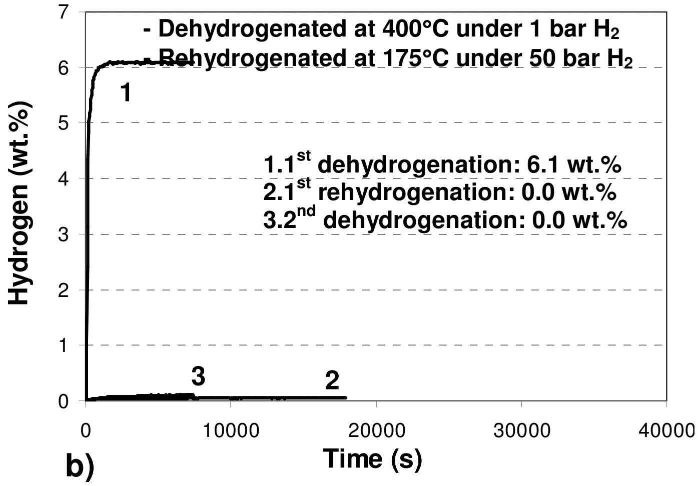

Fig. 11-9 (a) 1st and 2nd dehydrogenation curves at 175°C under 1 bar H_2 pressure and corresponding rehydrogenation curve at 175°C under 50 bar H_2 pressure and (b) 1st and 2nd dehydrogenation curves at 400°C under 1 bar H_2 pressure and corresponding rehydrogenation curve at 175°C under 50 bar H_2 pressure for the ($LiNH_2$+1.5MgH_2) mixtures milled for 25 h under the LES6-2B mode

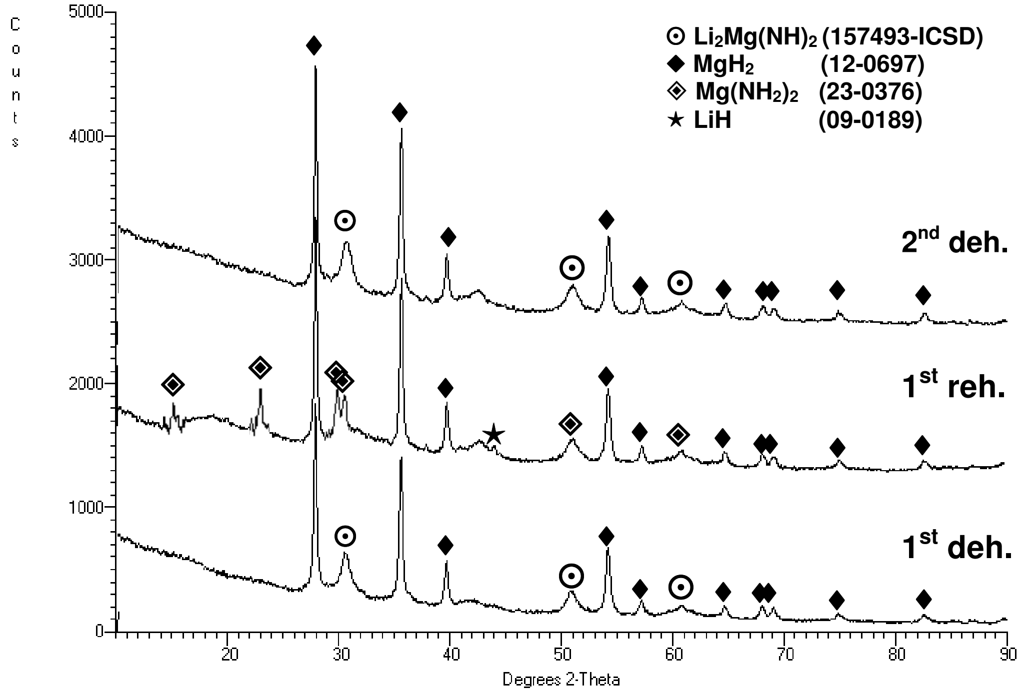

Fig. 11-10 XRD patterns for the ($LiNH_2$+1.5MgH_2) mixtures milled for 25 h under the LES6-2B mode and subsequently dehydrogenated at 175°C under 1 bar H_2 and rehydrogenated at 175°C under 50 bar H_2

Table 11-5. Summary of XRD results of the ($LiNH_2$+1.5MgH_2) mixture milled for 25 h (LES6-2B) and subsequently dehydrogenated under 1 bar H_2 at 175°C and rehydrogenated under 50 bar H_2 at 175°C

T(°C)	MgH_2	$Li_2Mg(NH)_2$	Mg_3N_2	LiH	$Mg(NH_2)_2$
Dehydrogenated at 175°C under 1 bar H_2	O	O	-	-	-
Rehydrogenated at 175°C under 50 bar H_2	O	-	-	O	O
Re-dehydrogenated at 175°C under 1 bar H_2	O	O	-	-	-

To clarify the reaction pathways of dehydrogenation/hydrogenation, the reactants and products after Sieverts analysis were collected and analyzed using XRD as shown in Fig. 11-10. The results are summarized in Table 11-5 and clearly indicate that the reversible reaction is processed between $Li_2Mg(NH)_2$ and {$Mg(NH_2)_2$ and LiH} as discussed in Chapters 9 and 10.

Assuming that all reactions are complete and the dehydrogenation is processed in the low temperature range that corresponds to the first endothermic peak in DSC curve as shown in Fig. 11-4, a series of dehydriding/hydriding reactions is proposed as follows:

$0.5xMg(NH_2)_2+xLiH+(1.5-0.5x)MgH_2+(1-x)LiNH_2$ (after ball milling)

$\rightarrow$ **$0.5Li_2Mg(NH)_2$**$+1.0MgH_2+$**$1.0H_2$** (after dehydrogenation) (11-6)

$\leftrightarrow$ **$0.5Mg(NH_2)_2+1.0LiH$**$+1.0MgH_2$ (after rehydrogenation)

Based on reaction (11-6), the maximum reversible hydrogen amount is approximately 3.2 wt.%, which corresponds to 2.0 mol of hydrogen atoms per unit formula of the ($LiNH_2+1.5MgH_2$) mixture. Considering 95% purity of the starting materials, the maximum reversible hydrogen amount reduced to 3.0 wt.% H_2.

However, for the dehydrogenation in the high temperature range that corresponds to the second endothermic peak in the DSC curve as shown in Fig. 11-4, the reaction pathways can be described by a series of dehydriding/hydriding reactions as follows:

$0.5xMg(NH_2)_2+xLiH+(1-0.5x)MgH_2+(1-x)LiNH_2$ (after ball milling)

$\rightarrow$ **$0.5Mg_3N_2+1.0LiH+2.0H_2$** (after dehydrogenation) (11-7)

$\rightarrow$ **No absorption** (after rehydrogenation)

As a result, it is worth highlighting that 4.0 moles of hydrogen atoms can be desorbed the first time but no hydrogen atoms can be absorbed subsequently, which indicates that the Mg_3N_2 phase cannot be hydrogenated under our experimental conditions.

11-5. Apparent activation energies

Measurements of the apparent activation energy of hydrogen desorption according to various reaction pathways were conducted using the Kissinger method (Eq. (6-2)). Fig. 11-11 a) and c) show the effect of various heating rates on DSC profiles, which is an underlying principle of the Kissinger method. The corresponding Kissinger plots for each reaction are shown in Fig. 11-11 b) and d) for the ($LiNH_2$+1.5MgH_2) mixtures milled under the IMP67 mode for 1 and 25 h and the LES6-2B mode for 25 h, respectively. The excellent correlation coefficients, R^2, obtained for the Kissinger plots in Fig. 11-11 b) and d) attest to the accuracy of the method.

As can be seen in Fig. 11-12, the apparent activation energies of each mixture milled in different milling conditions are not comparable, due to the different reaction pathways. However, it is remarkable that the apparent activation energies of ($LiNH_2$+1.5MgH_2) mixtures milled for 1 h under the IMP67 mode are approximately the same as those of ($LiNH_2$+1.0MgH_2) mixtures milled in the same conditions as shown in Chapter 10. Thus, a further increase of the MgH_2 molar ratio to 1.5 does not lead to any further decrease in the apparent activation energy.

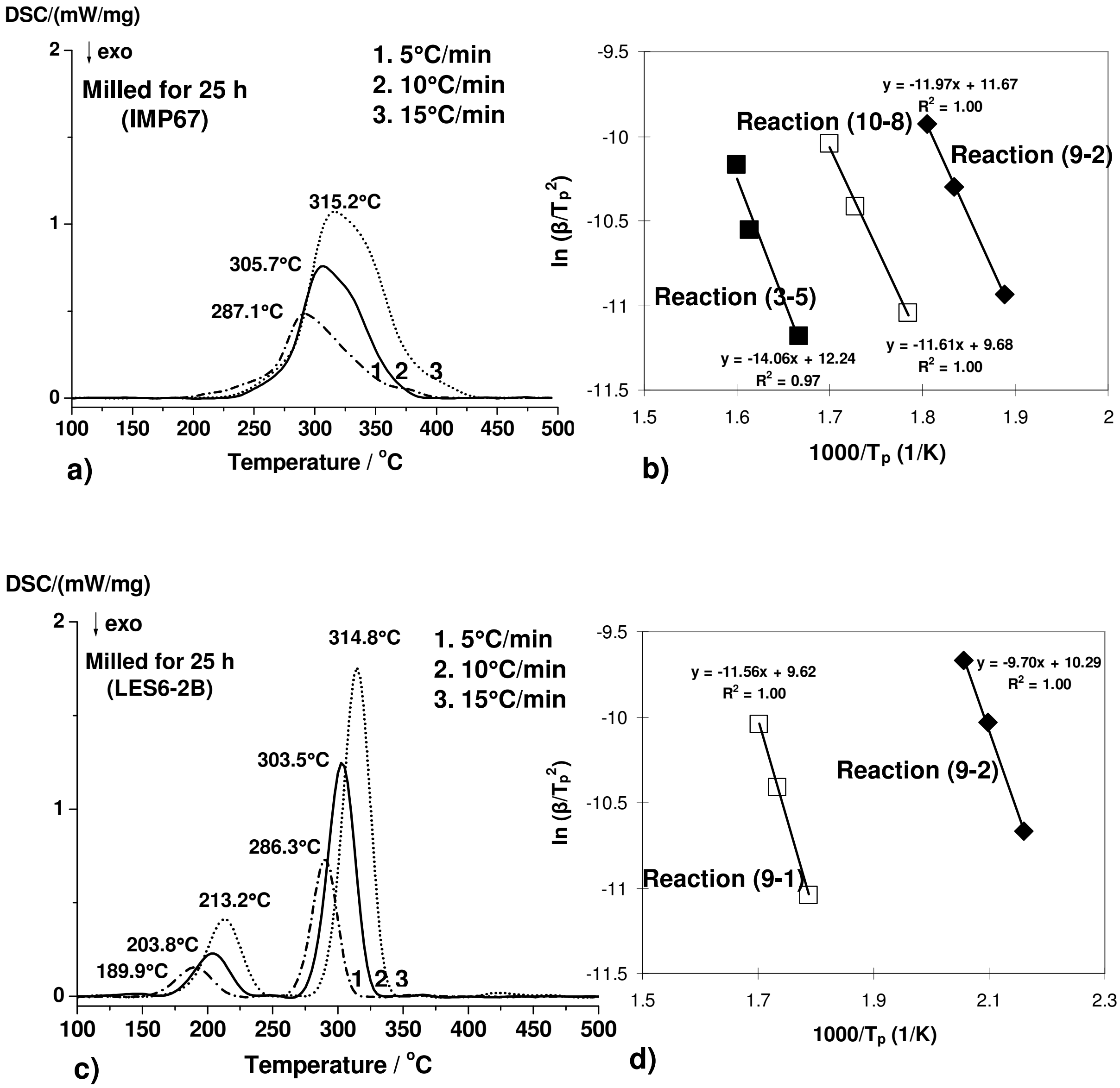

Fig. 11-11 a) DSC curves at various heating rates and b) the corresponding Kissinger plots of the apparent activation energies for the ($LiNH_2$+1.5MgH_2) mixtures milled for 1 h (closed) and 25 h (open) (IMP67 mode). c) DSC curves at various heating rates and d) the Kissinger plots of the apparent activation energies for the ($LiNH_2$+1.5MgH_2) mixtures milled for 25 h under LES6-2B mode

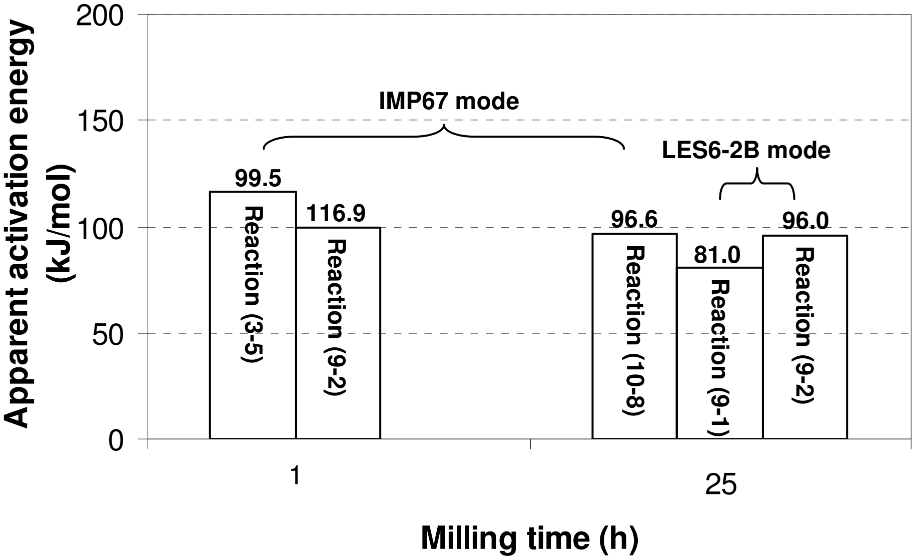

Fig. 11-12 Comparison of the apparent activation energies for the ($LiNH_2$+1.5MgH_2) milled for 1 h and 25 h under IMP67 and for 25 h under the LES6-2B mode:

- **Reaction (3-5): $LiNH_2 + 0.5MgH_2 \rightarrow 0.5Li_2Mg(NH)_2 + H_2$**
- **Reaction (9-1): $0.5xMg(NH_2)_2 + xLiH + (0.5-0.5x)MgH_2 + (1-x)LiNH_2 \rightarrow 0.5Li_2Mg(NH)_2 + H_2$**
- **Reaction (9-2): $0.5Li_2Mg(NH)_2 + MgH_2 \rightarrow 0.5Mg_3N_2 + LiH + H_2$**
- **Reaction (10-8): $MgNH + 0.5MgH_2 \rightarrow 0.5Mg_3N_2 + H_2$**

12. Discussion of ($LiNH_2$+nMgH_2) (n=0.55, 0.6, 0.7, 1.0 and 1.5)

Because several research groups [81, 83, 87, 97] have shown that composition changes can enhance the hydrogen-storage capacity of the Li-Mg-N-H system, due to changes in the dehydrogenation/hydrogenation reaction pathways, we were motivated to understand the underlying mechanisms of the chemical reaction between $LiNH_2$ and MgH_2 with various molar ratios. In this study, we discuss the effect of the molar ratio of $MgH_2/LiNH_2$ on the reaction pathways and the kinetic properties.

12-1. Effect of the molar ratio of MgH_2 and $LiNH_2$ on the reaction pathways

The reaction pathways of the ($LiNH_2$+nMgH_2) mixtures (0.55, 0.6, 0.7, 1.0 and 1.5) during the ball milling and dehydrogenation/hydrogenation are summarized in Table 12-1. There are two interesting findings. First, increasing the molar ratio of $MgH_2/LiNH_2$ can accelerate the solid-solid reactions during ball milling depending on the milling mode (energy); therefore, a 1:1.5 mixture milled under IMP67 mode for 25 h releases more hydrogen than a 1:1 mixture milled in the same milling conditions. As discussed above, the following reaction pathways during the ball milling can be proposed. In the first step, $LiNH_2$ is converted to $Mg(NH_2)_2$ and LiH by the metathesis reaction with MgH_2 without H_2 release [107, 108]:

$$LiNH_2 + 0.5MgH_2 \rightarrow 0.5Mg(NH_2)_2 + LiH \qquad (10\text{-}1)$$

In the second step, $Mg(NH_2)_2$ reacts with MgH_2 to form MgNH with H_2 release, as proposed by Liu et al. [107] and Liang et al.[108]:

$$0.5Mg(NH_2)_2 + 0.5MgH_2 \rightarrow MgNH + H_2 \qquad (10\text{-}2)$$

Table 12-1. Summary of the reaction pathways

	Ball milling				**Dehydrogenation**		**Rehydrogenation***	
	Milling		**H_2 released**	**Reaction**	**Reaction pathway (Reaction product)**		**Reaction pathway (Reaction product)**	
	Mode	**Time (h)**			**Low temp.**	**High temp.**	**Desorption low temp.**	**Desorption high temp.**
$LiNH_2$+0.55MgH_2	**IMP67**	**25**	N/A	Reaction (10-1)	Reaction (9-1) **($Li_2Mg(NH)_2$ & H_2)**	Reaction (9-2) **(Mg_3N_2 & LiH & H_2)**	Reaction (3-6) ($Mg(NH_2)_2$ & LiH)	
$LiNH_2$+0.6MgH_2			N/A	Reaction (10-1)				
$LiNH_2$+0.7MgH_2			N/A	Reaction (10-1)				
$LiNH_2$+1.0MgH_2	**IMP67**	**1**	N/A	N/A	Reaction (3-5) **($Li_2Mg(NH)_2$ & H_2)**			
	LES6-3B	**25**	N/A	Reaction (10-1)	Reaction (9-1) **($Li_2Mg(NH)_2$ & H_2)**			
	IMP67	**25**	**1.9 wt.% H_2 released**	Reaction (10-2)	Reaction (3-6) **($Li_2Mg(NH)_2$ & H_2)**	Reaction (10-8) **(Mg_3N_2 & H_2)**		
$LiNH_2$+1.5MgH_2	**IMP67**	**1**	N/A	N/A	Reaction (3-5) **($Li_2Mg(NH)_2$ & H_2)**	Reaction (9-2) **(Mg_3N_2 & LiH & H_2)**	Reaction (3-6) **($Mg(NH_2)_2$ & LiH)**	N/A
	LES6-2B	**25**	N/A	Reaction (10-1)	Reaction (9-1) **($Li_2Mg(NH)_2$ & H_2)**			N/A
	IMP67	**25**	**3.0 wt.% H_2 released**	Reaction (10-2)	N/A	Reaction (10-8) **(Mg_3N_2 & H_2)**	N/A	N/A

***Comments: Only $Li_2Mg(NH)_2$ can be reversible under 5.0 MPa at 175°C, while Mg_3N_2 cannot be reversible in the same conditions**

It must be noted that hydrogen can be released through reaction (10-2) during ball milling at nearly ambient temperature without subsequent heating processes depending on the milling modes and the molar ratio of $MgH_2/LiNH_2$.

Second, the dehydrogenation of the $LiNH_2$-MgH_2 system is processed by a two-step reaction that forms $Li_2Mg(NH)_2$ and Mg_3N_2, respectively, independent of the molar ratio of $MgH_2/LiNH_2$ and reaction pathways that are affected by the milling energy and duration. The only exception is the ($LiNH_2$+1.5MgH_2) mixture milled under IMP67 for 25 h, which shows a one-step reaction that forms Mg_3N_2 at the high temperature range. Although Alapati et al. [103] and Akbarzadeh et al. [104] predicted LiMgN as a product during the dehydrogenation of the ($LiNH_2$+1.0MgH_2) mixture, this ternary nitride product was not observed, even though the samples milled under various milling modes and durations were heated up to 400°C in our study.

Therefore, the molar ratio of $MgH_2/LiNH_2$ can significantly affect mechano-chemical reactions during ball milling, which results in different reaction pathways of hydrogen desorption in subsequent heating processes. However, its product is the same, independent of different molar ratios of $MgH_2/LiNH_2$.

Assuming that no hydrogen is released during ball milling, the available hydrogen capacity depending on the molar ratio of $MgH_2/LiNH_2$ can be calculated based on the previously mentioned reaction pathways. As mentioned above, the $LiNH_2$-MgH_2 system is dehydrogenated by a two-step reaction. The first step occurs at low temperatures, while the second is processed at high temperatures.

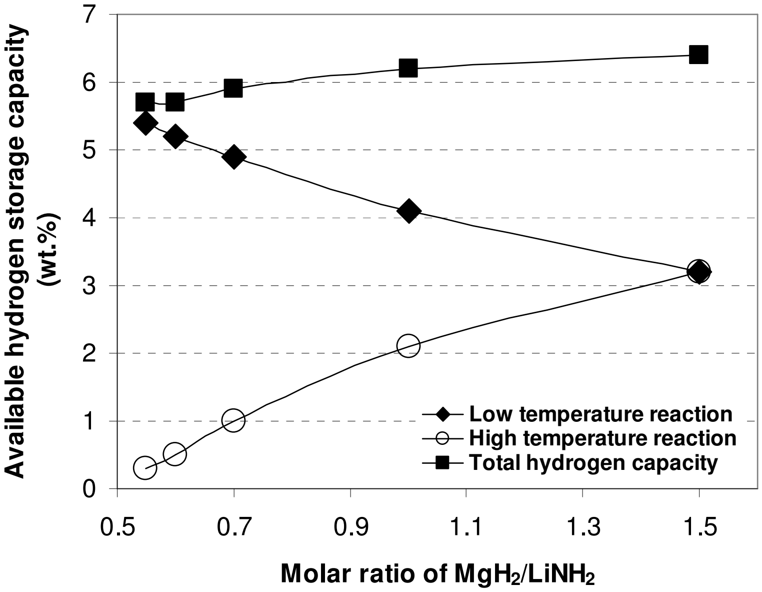

Fig. 12-1 Available hydrogen storage capacity as a function of the molar ratio of $MgH_2/LiNH_2$

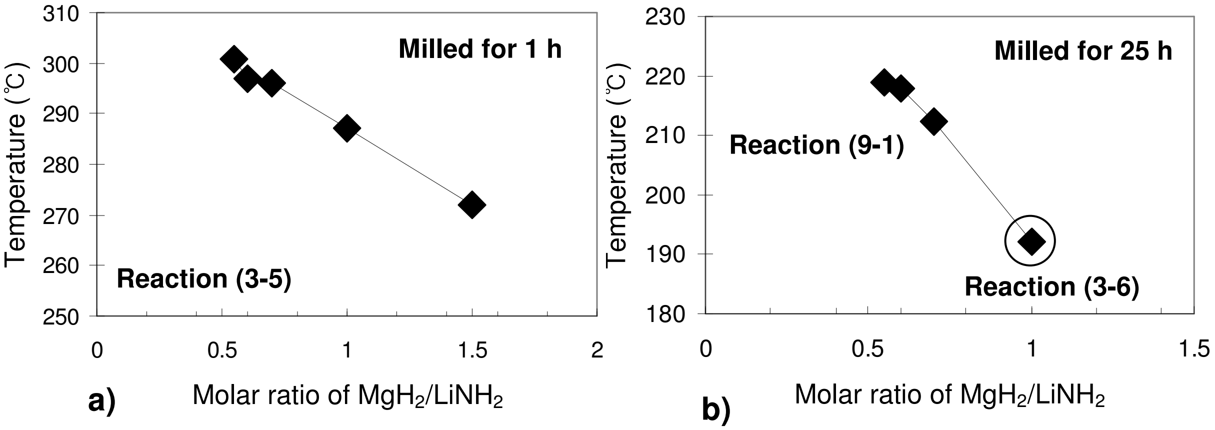

Fig. 12-2 The peak temperatures corresponding to the first endothermic peak in each DSC curve as a function of various molar ratios of $MgH_2/LiNH_2$ mixtures milled for a) 1 h and b) 25 h (IMP67 mode)

As can be seen in Fig. 12-1, the hydrogen capacity desorbed by the first reaction decreases as the molar ratio of $MgH_2/LiNH_2$ increases, while increasing the MgH_2 molar ratio in the system causes the amount of hydrogen released through the second to increase; therefore, the total hydrogen capacity gradually increases from 5.7 to 6.4 wt.% H_2. However, it must be noted that the reversible hydrogen storage capacity decreases from 5.4 to 3.2 wt.% H_2 as its molar ratio increases from 0.55 to 1.5 because only the first reaction is reversible as discussed above.

Therefore, there is no reason to increase the molar ratio of $MgH_2/LiNH_2$ to enhance the hydrogen storage capacity of the $LiNH_2$-MgH_2 system. However, it must be noted that the 1:0.55 and 1:0.6 molar ratio mixtures have the kinetic problems as discussed in Chapter 9. Therefore, the first and the second reactions cannot be completed and consequently, the hydrogen storage capacities for the 1:0.55 and 1:0.6 molar ratio mixtures must be less than the calculated values shown in Fig. 12-1. To determine the optimum composition of the $LiNH_2$-MgH_2 system, the kinetic properties must be considered.

12-2. Effect of the molar ratio of MgH_2 and $LiNH_2$ on kinetics

To investigate further the role of MgH_2 in this system, the peak temperatures and the apparent activation energies vs. the molar ratio of $MgH_2/LiNH_2$ are shown in Fig. 12-2 and 12-3, respectively.

Fig. 12-2 a) and b) present the peak temperatures that correspond to the first endothermic peak in DSC curves of $LiNH_2$-MgH_2 system milled under the IMP67 mode for 1 h and 25 h, respectively. The peak temperatures dramatically decrease as the molar ratio of $MgH_2/LiNH_2$ increases; for example, the peak temperature of the mixture milled under IMP67 mode for 1 h is reduced from 300.9 to 272.1°C as its molar ratio increases from 0.55 to 1.5. In Fig. 12-3 a) and b), the corresponding apparent activation energies are plotted vs. the molar ratio of MgH_2 to $LiNH_2$ in the mixtures milled under the IMP67 mode for 1 h and 25 h, respectively. For the mixture milled for 1 h, it is clear that increasing the MgH_2 molar ratio to 1.0 results in a more significant reduction of the apparent activation energy. However, a further increase of the MgH_2 molar ratio to 1.5 does not lead to further decreases of the apparent activation energy, suggesting that excessive MgH_2 may be present at the $1LiNH_2$:1.5 MgH_2 molar ratio. The lowest apparent activation energy is observed for the ($LiNH_2$+0.7MgH_2) mixture milled under IMP67 for 25 h, but in the ($LiNH_2$+1.0MgH_2) mixture milled at the same conditions, it increases, due to the different reaction pathway. Therefore, in our study, considering the reversible hydrogen storage capacity and the kinetic properties, the optimum molar ratio of MgH_2/$LiNH_2$ is 0.7 in the $LiNH_2$–MgH_2 system.

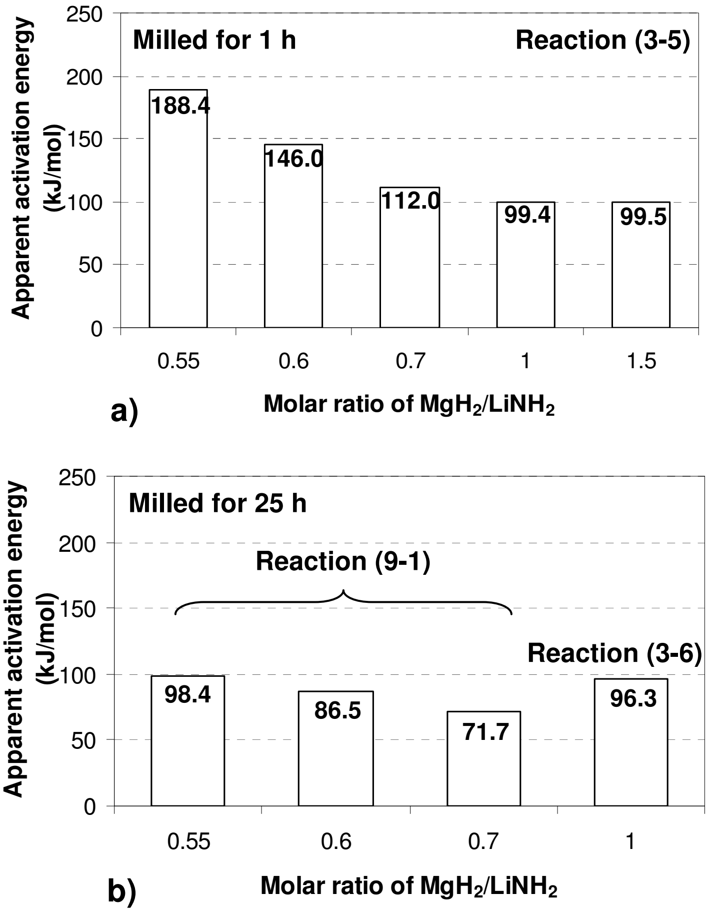

Fig. 12-3 The apparent activation energies as functions of the molar ratio of the $MgH_2/LiNH_2$ (IMP67 mode)

13. Summary and Conclusions

13-1. Li-N-H system

(1) High-energy ball milling was applied to mixtures of $LiNH_2$ and LiH with molar ratios of 1:1, 1:1.2 and 1:1.4 LiH.

(2) During high-energy ball milling of the 1:1 molar ratio mixture, the grain (crystallite) size of $LiNH_2$ and LiH decreases monotonically with increasing milling time. Conversely, the specific surface area (SSA) of the powder increases as the milling time increases to 25 h and subsequently decreases as the milling time continues to increase to 100 h, due to the excessive agglomeration of powder.

(3) Single-phase $LiNH_2$ decomposes through melting and the release of ammonia (NH_3). A just mixed ($LiNH_2$+LiH) mixture still mostly decomposes through the melting of $LiNH_2$ and the release of NH_3. For the hydrogen to be effectively released from the mixture of ($LiNH_2$+LiH), high-energy ball milling is necessary, which creates intimate contact between both components.

(4) The apparent activation energy for hydrogen desorption from the ball milled mixture of ($LiNH_2$+LiH) decreases as the SSA of powders increases up to 26 m^2/g and subsequently levels off as the SSA continues to increase. For the ball milled mixture of $LiNH_2$ and LiH, the lowest apparent activation energy is observed for the 1:1.2 LiH molar ratio.

(5) The major impediment to hydrogen desorption from the ball milled mixture ($LiNH_2$+LiH) system is the hydrolysis and oxidation of a fraction of the LiH because it is inactive in the intermediate reaction, $NH_3+LiH \rightarrow LiNH_2+H_2$. Therefore, a $LiNH_2$-LiH system will always release NH_3 as long as part of the LiH becomes inactive, due to the hydrolysis/oxidation, and does not take part in the intermediate reaction.

13-2. Li-N-C-H system with graphite

(1) To prevent LiH from undergoing hydrolysis/oxidation during desorption/absorption, 5 wt.% graphite was incorporated in the ($LiNH_2$+1.2LiH) hydride system.

(2) After ball milling for 25 h, graphite is transformed into an amorphous form.

(3) DSC analysis shows that graphite can prevent or at least substantially reduce the oxidation/hydrolysis of LiH because the melting peak of the retained $LiNH_2$ is not observed.

(4) Both the DSC and Sieverts tests show that adding graphite increases the apparent activation energy of desorption from 57-58 to 85-90 kJ/mol. However, the graphite additive significantly increases the desorbed/absorbed capacity of hydrogen at 275°C, 300°C and 325°C.

(5) The (($LiNH_2$+1.2LiH)+5 wt.% graphite) system is fully reversible and desorbs/absorbs ~5 wt.% H_2 at 325°C in the following reaction: ($LiNH_2 + LiH \leftrightarrow Li_2NH + H_2$).

(6) Step-wise desorption tests show that the enthalpy and entropy changes of this reversible reaction are -62.4 kJ/mol and -61.0 kJ/molH_2 and 117.8 and 115.8 J/molK for the ($LiNH_2$+1.2LiH) mixtures without and with 5 wt.% graphite, respectively. Within the experimental error, there is no measurable effect of graphite additive on the thermodynamic properties of the reaction.

(7) The Van't Hoff analysis of the obtained thermodynamic data shows that the equilibrium temperature at atmospheric pressure of hydrogen (0.1 MPa H_2) is 256.8°C and 253.9°C for ($LiNH_2$+1.2LiH) mixtures without and with 5 wt.% graphite milled for 25 h, respectively. Given such high equilibrium temperatures, it is obvious that both of these hydride systems cannot be employed for hydrogen desorption/absorption below 100°C.

13-3. ($LiNH_2$+nMgH_2) (n=0.55, 0.6 and 0.7)

(1) To overcome the thermodynamic and kinetic barriers associated with the $LiNH_2$/LiH system, LiH was substituted with MgH_2.

(2) The ($LiNH_2$+nMgH_2) (n=0.55, 0.6 and 0.7) system is partially converted to $Mg(NH_2)_2$ and LiH by the metathesis reaction upon ball milling.

(3) In DSC, the systems show three endothermic peaks that correspond to the following reactions:

- 1st end. peak: $[0.5xMg(NH_2)_2+xLiH]+[(1-x)LiNH_2+(0.5-0.5x)MgH_2]\rightarrow 0.5Li_2Mg(NH)_2+1.0H_2$
- 2nd end. peak: $0.5Li_2Mg(NH)_2+ MgH_2\rightarrow 0.5Mg_3N_2+LiH+H_2$
- 3rd end. peak: $LiNH_2 \rightarrow 0.5Li_2NH+0.5NH_3$

(4) H_2 is released through reaction (9-1) and reaction (9-2), while the NH_3 in reaction (3-3) results from the incompletion of reaction (9-1) and reaction (9-2). In case of n=0.7, reaction (3-3) results from two overlapping endothermic peaks, while it comes from the lack of reactivity between $LiNH_2$ and LiH in case of n=0.55 and 0.6 because the two peaks are totally separated.

(5) The lowest apparent activation energy of 71.7 kJ/mol is also observed for the molar ratio of 1:0.7MgH_2 milled for 25 h.

(6) The incorporation of n-Ni can reduce the kinetic barrier for reaction (9-1) and (9-2); therefore, the apparent activation energy of the ($LiNH_2$+0.7MgH_2) mixture with n-Ni milled for 25 h is reduced from 71.7 to 65.0 kJ/mol for reaction (9-1).

(7) Step-wise desorption tests show that the enthalpy and entropy change of reaction (9-1) is 46.7 kJ/molH_2 and 136.1 J/(molK), respectively. The Van't Hoff analysis of the obtained

thermodynamic data shows that the equilibrium temperature at atmospheric pressure of hydrogen (0.1 bar H_2) is 70.1°C.

(8) ($LiNH_2$+0.7MgH_2) mixture is fully reversible and desorb/absorb 3.6 wt.% H_2 at 175°C in the reaction ($Li_2Mg(NH)_2+2H_2 \leftrightarrow Mg(NH_2)_2+2LiH$). However, at a high temperature, the mixture first desorbs 5.2 wt.% H_2 at 400°C under 1 bar H_2 but only absorbs 3.2 wt.% H_2 at 175°C under 50 bar H_2 and desorbs 3.2 wt.% H_2 at 400°C under 1 bar H_2. This difference is a result of the formation of Mg_3N_2 during dehydrogenation at a high temperature, and this phase cannot be hydrogenated under our experimental conditions. Therefore, the maximum reversible H_2 capacity for the ($LiNH_2$+0.7MgH_2) mixture is 4.6 wt.% H_2, considering the average purity of the materials (95%).

13-4. ($LiNH_2$+nMgH_2) (n=1.0 and 1.5)

(1) The molar ratio of $MgH_2/LiNH_2$ was increased to 1.0 and 1.5 to increase the limit of stored hydrogen in ($LiNH_2$+nMgH_2) (n=0.55, 0.6 and 0.7) system. It has been reported that composition changes are able to enhance the hydrogen storage capacity, due to changes in the dehydrogenation/hydrogenation reaction pathways.

(2) However, the theoretically predicted LiMgN is not observed, even after dehydrogenation at 400°C. Instead of this phase, $Li_2Mg(NH)_2$ and Mg_3N_2 are obtained after dehydrogenation at low and high temperatures, respectively, regardless of the milling mode.

(3) ($LiNH_2$+1.0MgH_2) desorbs only 5.8 wt.% H_2 at 400°C under 1 bar H_2 in contrast to the theoretically predicted 8.2 wt.% H_2.

(4) The reaction pathways for the dehydrogenation/hydrogenation of ($LiNH_2$+nMgH_2) (n=1.0 and 1.5) systems depend strongly on the milling modes and times because the initial ball

milling induces a metathesis reaction between $LiNH_2$ and MgH_2 to yield $Mg(NH_2)_2$ and LiH without H_2 evolution, and $Mg(NH_2)_2$ reacts with MgH_2 to release hydrogen and form MgNH as the ball milling proceeds.

(5) In the high-energy milling mode (IMP67), systems with n=1.0 and 1.5 release 1.9 and 3.0 wt.% H_2 after 25 h, respectively, while in the relatively low-energy milling mode (LES6-2B or 3B), both systems produce $Mg(NH_2)_2$ and LiH without H_2 after 25 h.

(6) The n=1.0 system milled in the low-energy milling mode (LES6-3B) desorbs approximately 0.5 and 1.3-3.9 wt.% H_2 at 124 and 150-200°C, respectively, and the n=1.5 system milled under LES6-2B mode is capable of desorbing 0.4 and 1.0-3.1 wt.% H_2 at 125 and 150-200°C, respectively.

(7) The low-energy ball milled systems with n=1.0 and 1.5 fully reversibly desorb and absorb 2.9 and 2.0 wt.% H_2 at 175°C, respectively, according to the reversible reaction $Li_2Mg(NH)_2+2H_2 \leftrightarrow Mg(NH_2)_2+2LiH$. However, the reversible capacity decreases as the dehydrogenation temperature increases due to the formation of Mg_3N_2, which cannot be hydrogenated under our experimental conditions. The maximum reversible H_2 capacity for systems with n=1.0 and 1.5 are only 3.9 and 3.1 wt.% H_2 (purity corrected), respectively. Therefore, there is no reason to increase the molar ratio of $MgH_2/LiNH_2$ to achieve greater hydrogen capacity.

References

[1] R. A. Varin, T. Czujko, Z. S. Wronski, Nanomaterials for Solid State Hydrogen Storage, Springer Science+Business Media, New York, NY 10013, USA, 2009

[2] A. Andreassen, Ph.D. Thesis in Riso National Laboratory (December, 2005)

[3] United Nations Populations Division, World population prospects: The 2004 revision population database (June 2005)

URL http://esa.un.org/unpp/

[4] J. H. Wood, G. R. Long, D. F. Morehouse, Long-Term World Oil Supply Scenarios, Energy Information Administration (August 2004)

URL http://www.eia.doe.gov/pub/oil gas/petroleum/feature articles/2004/-worldoilsupply/oilsupply04.html

[5] B. J. Fleay, Climaxing oil: How will transport adapt?, Institute for Science and Technology Policy Murdoch University, Western Australia (November 1998)

URL http://wwwistp.murdoch.edu.au/teaching/N212/n212content/topics/-topic5/00content.html

[6] BP Distribution Services, BP Statistical Review of World Energy 2004 (June 2004)

URL http://www.bp.com/statisticalreview2004

[7] M. E. Mann, R. S. Bradley, M. K. Hughes, Geophys. Res. Lett. 26 (1999) 759-762

[8] M. E. Mann, R. S. Bradley, M. K. Hughes, Nature 392 (1998) 779-787

[9] E. Friis-Christensen, K. Lassen, Science 254 (1991) 698-700

[10] IPCC special report of working group III, Emission scenarios, Summary for policymakers, International Panel on Climate Change 2000

URL http://www.ipcc.ch

[11] P. P. Edwards, V. L. Kuznetsov, W. I. F. David, Phil. Trans. R. Soc. A 365 (2007) 1043-1056

[12] J. A. Turner, Science 285 (1999) 687-689

[13] M. Schrope, Nature 414 (2001) 682-684

[14] R. F. Service, Science 305 (2004) 958-961

[15] J. A. Ritter, A. D. Ebner, J. Wang, R. Zidan, Materialstoday 6 (2003) 18-23

[16] A. Züttel, Materialstoday 6 (2003) 24-33

[17] I. Dincer, Renewable and Sustainable Energy Reviews 4 (2004) 157-175

[18] T. N. Veziroglu, Int. J. Hydrogen Energy 22 (1997) 551-556

[19] S. Dunn, Int. J. Hydrogen Energy 27 (2002) 235-264

[20] U. Wagner, B. Geiger, H. Schaefer, Int. J. Hydrogen Energy 23 (1998) 1-6

[21] M. Momirlan, T. N. Veziroglu, Renewable and Sustainable Energy Reviews 6 (2002) 141-179

[22] L. Schlapbach, MRS Bull. 27 (2002) 675-676

[23] L. Zhou, Renewable and Sustainable Energy Reviews 9 (2005) 395-408

[24] A. M. Seayad, D. M. Antonelli, Adv. Mater. 16 (2004) 765-777

[25] M. Conte, P. P. Prosini, S. Passerini, Materials Science and Engineering B108 (2004) 4-8

[26] L. Schlapbach, A. Züttel, Nature 414 (2001) 353-358

[27] A. Züttel, Materials Today 9 (2003) 24-33

[28] L. Schlapbach (Ed.), Hydrogen in Intermetallic Compounds II, Vol. 67 of Topics in Applied Physics, Springer-Verlag, 1992

[29] J. Bloch, J. Alloys Comps. 312 (2000) 135-153

[30] C. S. Wang, H. Wang, Q. Lei, P. Chen, Q. D. Wang, Int. J. Hydrogen Energy 21 (1996) 471-478

[31] M. Martin, G. Gommel, C. Borkhardt, E. Fromm, J. Alloys Comps. 238 (1996) 193-201

[32] G. Sandrock in Y. Yurum (Ed.), Hydrogen Energy System-Production and Utilization of Hydrogen and Future Aspects, Kluwer Academics, Dordrecht, (1995)135-166

[33] Targets for On-board Hydrogen storage systems in Hydrogen, Fuel Cells and Infrastructure Technology Program. USDOE.

URL http://www.eere.energy.gov/hydrogenandfuelcells/storage/current_technology.html

[34] B. Bogdanovi, G. Sandrock, MRS Bull. 27 (9) (2002) 712–716

[35] F. Schüth, B. Bogdanovi, M. Felderhoff, Chem. Commun. (Camb) 21 (2004) 2249–2258

[36] A. M. Seayad, D. M. Antonelli, Adv. Mater. 16 (2004) 765–777

[37] M. Fichtner, Adv. Eng. Mater. 7 (2005) 443–455

[38] D. Chandra, J. J. Reilly, R. Chellapa, JOM 58 (2) (2006) 26–32

[39] B. Bogdanovi, U. Eberle, M. Felderhoff, F. Schüth, Scripta Mater. 56 (2007) 813–816

[40] S. I. Orimo, Y. Nakamori, J. R. Eliseo, A. Züttel, C. M. Jensen, Chem. Rev. 107 (2007) 4111–4132

[41] W. Grochala, P. P. Edwards, Chem. Rev. 104 (2004) 1283–1315

[42] G. Sandrock , J. Alloys Compd. 293–295 (1999) 877–888

[43] D. K. Slattery, M. D. Hampton, In Proceedings of the 2002 U.S. D.O.E. Hydrogen Program Review NREL/CP-610–32405, Golden, CO

[44] B. Bogdanovic, M. Schwickardi, J. Alloys Compd. 1 (1997) 253-254

[45] R. A. Varin, T. Czujko, Z. Wronski, Nanotechnology 17 (2006) 3856–3865

[46] R. A. Varin, S. Li, A. Calka, J. Alloys Compd. 376 (2004) 222–231

[47] R. A. Varin, T. Czujko, Mater. Manuf. Proc. 17 (2002) 129–156

[48] R. A. Varin, T. Czujko, C. Chiu, Z. Wronski, J. Alloys Compd. 424 (2006) 356–364

[49] R. A. Varin, S. Li, C. Chiu, L. Guo, O. Morozova, T. Khomenko, Z. Wronski, J. Alloys Compd. 404–406 (2005) 494–498

[50] R. A. Varin, T. Czujko, E. B. Wasmund, Z. S. Wronski, J. Alloys Compd. 446–447 (2007) 63–66

[51] A. Zaluska, L. Zaluski, J. O. Ström-Olsen, Appl. Phys. A 72 (2001) 157–165

[52] H. Imamura H, K. Masanari, M. Kusuhara, H. Katsumoto, T. Sumi, Y. Sakata, J. Alloys Compds. 386 (2005) 211–216

[53] L. Zaluski, A. Zaluska, J. O. Ström-Olsen, J. Alloys Compds. 253–254 (1997) 70–79

[54] M. Zhu, H. Wang, L. Z. Ouyang, M. Q. Zeng, Int. J. Hydrogen Energy 31 (2006) 251–257

[55] A. Zaluska, L. Zaluski, J. O. Ström-Olsen, J. Alloys Compds. 288 (1999) 217–225

[56] P. Chen, Z. Xing, J. Luo, J. Lin, K.L. Tan, Nature 420 (2002) 302-304

[57] L. L. Shaw, R. Ren, T. Markmaitree, W. Osborn, J. Alloys Compd. 448 (2008) 263-271

[58] T. Ichikawa, S. Isobe, N. Hanada, H. Fujii, J. Alloys Compd. 365 (2004) 271-276

[59] J. H. Yao, C. Shang, K.F. Aguey-Zinsou, Z.X. Guo, J. Alloys Compd. 432 (2007) 277-282

[60] T. Markmaitree, R. Ren, L.L. Shaw, J. Phys. Chem. B 110 (2006) 20710-20718

[61] J. Lu, Z.Z. Fang, H.Y. Sohn, Inorg. Chem. 45 (2006) 8749-8754

[62] W. I. F. David, M. O. Jones, D. H. Gregory, C. M. Jewell, S. R. Johnson, A. Walton, P. P. Edward, J. Am. Chem. Soc., 129 (2007) 1594-1601

[63] J. Z. Hu, J. H. Kwak, Z. Yang, W. Osborn, T. Markmaitree, L. L. Shaw, J. Power Sources 181 (2008) 116-119

[64] L. Xie, J. Zheng, Y. Liu, Y. Li, X. Li, Chem. Mater. 20 (2008) 282-286

[65] Y. Kojima, Y. Kawai, Chem. Commun., 19 (2004), 2210-2211

[66] K. F. Aguey-Zinsou, J. Yao, Z. X. Guo, J. Phys. Chem. B 111 (2007) 12531-12536

[67] Y. Kojima, Y. Kawai, J. Alloys Compd. 395 (2005) 236-239

[68] L. L. Shaw, W. Osborn, T. Markmaitree, X. Wan, J. Power Sources 177 (2008) 500-505

[69] R. Ren, A. L. Ortiz, T. Markmaitree, W. Osborn, L. L. Shaw, J. Phys. Chem. B 110 (2006) 10567-10575

[70] P. Chen, Z. Xiong, J. Z. Luo, J. Y. Lin, K. L. Tan, J. Phys. Chem. B 107 (2003) 10967–10970

[71] Y. H. Hu, E. Ruckenstein, Ind. Eng. Chem. Res. 42 (2003) 5135–5139

[72] Y. H. Hu, E. Ruckenstein, J. Phys. Chem. A 107 (2003) 9737–9739

[73] T. Ichikawa, N. Hanada, S. Isobe, H. Leng, H. Fujii, J. Phys. Chem. B 108 (2004) 7887–7892

[74] S. Orimo, Y. Nakamori, G. Kitahara, K. Miwa, N. Ohba, T. Noritake, S. Towata, Appl. Phys. A 79 (2004) 1765–1767

[75] T. Ichikawa, N. Hanada, S. Isobe, H. Leng, H. Fujii, Mater. Trans. 46 (2005) 1–14

[76] Y. H. Hu, E. Ruckenstein, Ind. Eng. Chem. Res. 43 (2004) 2464–2467

[77] H. Y. Leng, T. Ichikawa, S. Isobe, S. Hino, N. Hanada, H. Fujii, J. Alloys Compd. 404–406 (2005) 443–447

[78] G. P. Meisner, F. E. Pinkerton, M. S. Meyer, M. P. Balogh, M. D. Kundrat, J. Alloys Compd. 404–406 (2005) 24–26

[79] S. Isobe, T. Ichikawa, N. Hanada, H. Y. Leng, M. Fichtner, O. Fuhr, H. Fujii, J. Alloys Compd. 404–406 (2005) 439–442

[80] T. Ichikawa, N. Hanada, S. Isobe, H. Y. Leng, H. Fujii, J. Alloys Compd. 404–406 (2005) 435–438

[81] H. Y. Leng, T. Ichikawa, S. Hino, N. Hanada, S. Isobe, H. Fujii, J. Phys. Chem. B 108 (2004) 8763–8765

[82] H. Y. Leng, T. Ichikawa, S. Hino, T. Nakagawa, H. Fujii, J. Phys. Chem. B 109 (2005) 10744–10748

[83] Z. Xiong, G. Wu, J. Hu, P. Chen, Adv. Mater. 16 (2004) 1522–1525

[84] Z. Xiong, J. Hu, G. Wu, P. Chen, W. Luo, K. Gross, J. Wang, J. Alloys Compd. 398 (2005) 235–239

[85] Z. Xiong, G. Wu, J. Hu, P. Chen, W. Luo, J. Wang, J. Alloys Compd. 417 (2006) 190–194

[86] W. Luo, J. Alloys Compd. 381 (2004) 284–287

[87] W. Luo, E. Ronnebro, J. Alloys Compd. 404–406 (2005) 392–395

[88] Y. Nakamori, G. Kitahara, K. Miwa, N. Ohba, T. Noritake, S. Towata, S. Orimo, J. Alloys Compd. 404–406 (2005) 396–398

[89] Y. Nakamori, G. Kitahara, S. Orimo, J. Power Sources 138 (2004) 309–312

[90] Z. G. Yang, L. L. Shaw, Nanostruct. Mater. 7 (1996) 873–886

[91] L. L. Shaw, J. Villegas, H. Luo, D. Miracle, Acta Mater. 51 (2003) 2647–2663.

[92] A. L. Ortiz, L. Shaw, Acta Mater. 52 (2004) 2185–2197

[93] Y. Nakamori, S. Orimo, J. Alloys. Compd. 370 (2004) 271–275

[94] W. Luo, S. Sickafoose, J. Alloys. Compd. 407 (2006) 274–281

[95] H. Y. Leng, T. Ichikawa, H. Fujii, J. Phys. Chem. B 110 (2006) 12964–12968

[96] Y. Chen, C. Z. Wu, P. Wang, H. M. Cheng, Int. J. Hydrogen Energy 31 (2006) 1236–1240

[97] Y. Nakamori, G. Kitahara, K. Miwa, S. Towata, S. Orimo, Appl. Phys. A 80 (2005) 1–3

[98] M. Aoki, T. Noritake, G. Kitahara, Y. Nakamori, S. Towata, S. Orimo, J. Alloys. Compd. 428 (2007) 307–311

[99] J. Hu, Z. Xiong, G. Wu, P. Chen, K. Murata, K. Sakata, J. Power Sources 159 (2006) 120–125

[100] J. Hu, G. Wu, Y. Liu, Z. Xiong, P. Chen, K. Murata, J. Phys. Chem. B 110 (2006) 14688–14692

[101] Z. G. Yang, L. Shaw, Nanostruct. Mater. 7 (1996) 873–886

[102] W. Lohstroh, M. Fichtner, J. Alloys. Compd. 446–447 (2007) 332–335

[103] S. V. Alapati, J. K. Johnson, D. S. Sholl, J. Phys. Chem. B 110 (2006) 8769 – 8776

[104] A. R. Akbarzadeh, V. Ozolins, C. Wolverton, Adv. Mater. 19 (2007) 3233 – 3239

[105] W. Osborn, T. Markmaitree, L. L. Shaw, J. Power Sources 172 (2007) 376 – 378

[106] J. Lu, Z. Z. Fang, Y. J. Choi, H. Y. Sohn, J. Phys. Chem. C 111 (2007) 12129 – 12134

[107] Y. Liu, K. Zhong, M. Gao, J. Wang, H. Pan, Q. Wang, Chem. Mater. 20 (2008) 3521–3527

[108] C. Liang, Y. Liu, K. Luo, B. Li, M. Gao, H. Pan, Q. Wang, Chem. Eur. J. 16 (2010) 693–702

[109] J. J. Vajo, G. L. Olsen, Scripta Materialia 56 (2007) 829-834

[110] K. Miwa, N. Ohba, S. Towata, Y. Nakamori, S. Orimo, Phys. Rev. B 69 (2004) 245120-1~8

[111] F. E. Pinkerton, G. P. Meisner, M. S. Meyer, M. P. Balogh, M.D. Kundrat, J. Phys. Chem. B. 109 (2005) 6-8

[112] J. J. Vajo, F. Mertens, C. C. Ahn, R.C. Bowman Jr., B. Fultz, J. Phys. Chem. B 108 (2004) 13977-13983

[113] J. J. Vajo, S. L. Skeith, F. Mertens, J. Phys. Chem. B 109 (2005) 3719–3722

[114] J. J. Vajo, T. T. Salguero, A. F. Gross, S. L. Skeith, G. L. Olson, J. Alloys Compd. 446–447 (2007) 409–414

[115] J. Graetz, Y. Lee, J. J. Reilly, S. Park, T. Vogt, Phys. Rev. B 71 (2005) 184115

[116] E. Wiberg, E. Amberger, Hydrides of the Elements of Main Groups I–IV, Elsevier, Amsterdam, 197

[117] R. C. Bowman Jr., S. J. Hwang, C. C. Ahn, J. J. Vajo, Mater. Res. Soc. Symp. Proc. 837 (2005), N3.6.1–N3.6.6

[118] J. J. Reilly, R. H. Wiswall, Inorg. Chem. 6 (1967) 2220–2223

[119] G. Liang, R. Schulz, J. Mater. Sci. 39 (2004) 1557–1562

[120] A. J. Maeland, J. Less Common Met. 89 (1983) 173

[121] E. Veleckis, J. Less Common Met. 73 (1980) 49–60

[122] E. G. Baburaj, F. H. Froes, V. Shutthanandan, S. Thevuthasan, Interfacial Chemistry and Engineering Annual Report, Pacific Northwest National Laboratory, Oak Ridge,Tenn, USA, 2000

[123] R. Schulz, S. Boily, L. Zaluski, A. Zaluka, P. Tessier, J. O. Strőm-Olsen, Innovation in Metallic Materials, pp. 529–535, 1995

[124] S. H. Joo, S. J. Choi, I. Oh, et al., Nature 412 (2001) 169–172

[125] M. U. Niemann, S. S. Srinivasan, A. R. Phani, A. Kumar, D. Y. Goswami, E. K. Stefanakos, J. Nanomaterials, Review article (2008) 1-9

[126] H. Gleiter. Z. Metallkd. 86 (1995) 78-83

[127] A. Zaluska, L. Zaluski, J.O. Strőm-Olsen. J. Alloys Compd. 298 (2000) 125-134

[128] A. Calka, R. A. Varin, Processing and Fabrication of Advanced Materials IX. (2000) 263-265

[129] Patents: WO9104810, US5383615, CA2066740, EP0494899, AU643949

[130] H. P. Klug, L. Alexander, X-ray Diffraction Procedures for Polycrystalline and Amorphous Materials, John Wiley & Sons, New York, 1974, pp. 618–708

[131] T. Markmaitree, W. Osborn, L. L. Shaw, Int. J. Hydrogen Energy 33 (2008) 3915-3924

[132] S. V. Alapati, J. K. Johnson, D. S. Sholl, Phys. Chem. Chem. Phys. 9 (2007) 1438-1452

[133] R. Ren, A. L. Ortiz, T. Markmaitree, X. Wan, J. Power Sources 177 (2008) 500-505

[134] O. Dolotko, N. Paulson, V. K. Pecharsky, Int. J. Hydrogen Energy 35 (2010) 4562–4568

[135] S. Barison, F. Agresti, S.L. Russo, A. Maddalena, P. Palade, G. Principi, G. Torzo, J. Alloys Compd. 459 (2008) 343-347

[136] H. J. Fecht, Nanostructed Mater. 1 (1992) 125-130

[137] L. L. Shaw, Z. G. Yang, R. M. Ren, Mater. Sci. Eng. A 244 (1998) 113–126

[138] R. R. Shahi, T. P. Yadav, M. A. Shaz, O. N. Srivastava, Int. J. Hydrogen Energy 33 (2008) 6188-6194

Appendix A

A-1. Controlled milling modes by changing position of magnets in Uni-Ball Mill 5

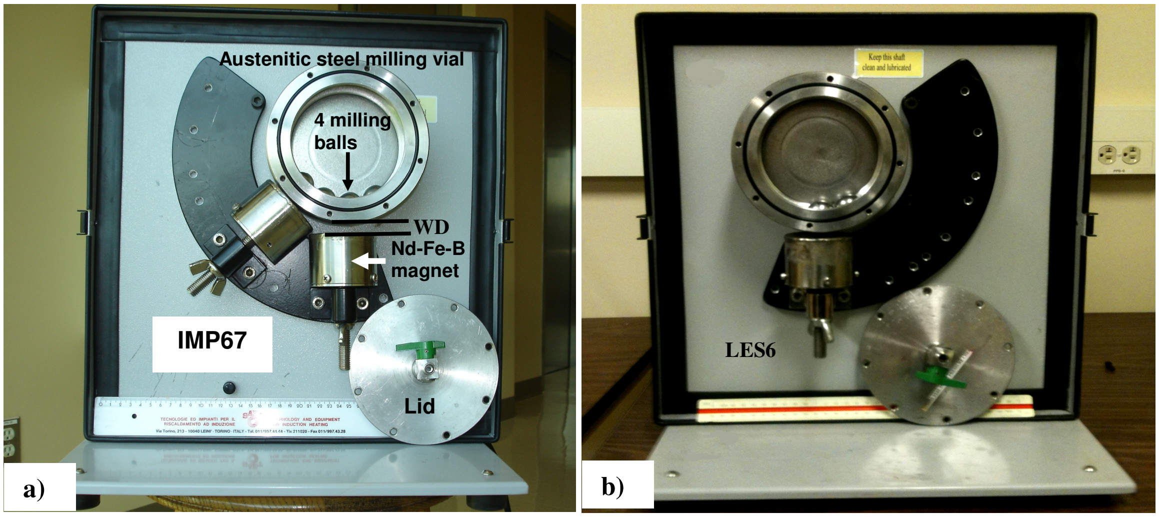

Fig. A-1 Milling modes with two magnets in Uni-Ball Mill 5: (a) high energy impact mode with magnets at 6 and 7 o'clock positions (IMP67 mode) and (b) low energy shearing mode with magnets at 6 o'clock position (LES6 mode)

A-2. Hydrogen storage capacity estimated by pressure variations during milling using a volumetric method

Assuming hydrogen behave as ideal gas, one can estimate the mass of absorbed hydrogen from:

$$\Delta P V_{eff} = (m/M_H)RT \qquad \text{(A-1)}$$

where ΔP is the total pressure changes of H_2 in a milling period

V_{eff} is the effective volume of the vial (m^3)

(V_{eff} = absolute volume – volume of balls – volume of the material)

m is weight of absorbed H_2 (g)

M_H is molar mass of H_2 (g/mol)

T is the temperature (K)

R is the gas constant (8.314J $(mol)^{-1}K^{-1}$

and **hydrogen capacity (wt.% H_2) = $m/M_p \times 100\%$** (A-2)

where M_p is the initial powder mass (g)

A-3. Kinetic curves determination by volumetric method in a Sieverts-type apparatus

The Sieverts-type apparatus consist of: a calibrated volume determined physically, a reactor whose temperature is controlled by the temperature control system and the cooling system, a vacuum system, a pressure monitoring system, valves and source of hydrogen and argon delivery. The quantity of desorbed hydrogen (number of molls) is calculated using ideal gas low:

$$PV = nRT \qquad \text{(A-3)}$$

where P–gas pressure, V–gas volume, n–number of moles of gas, T–absolute temperature of gas, R–the universal gas constant. The value and units of R depend on the units used in determining P, V, n and T

- The quantity of gas, n, is normally expressed in moles
- The units chosen for pressure and volume are typically atmospheres (atm) and liters (L), however, other units may be chosen

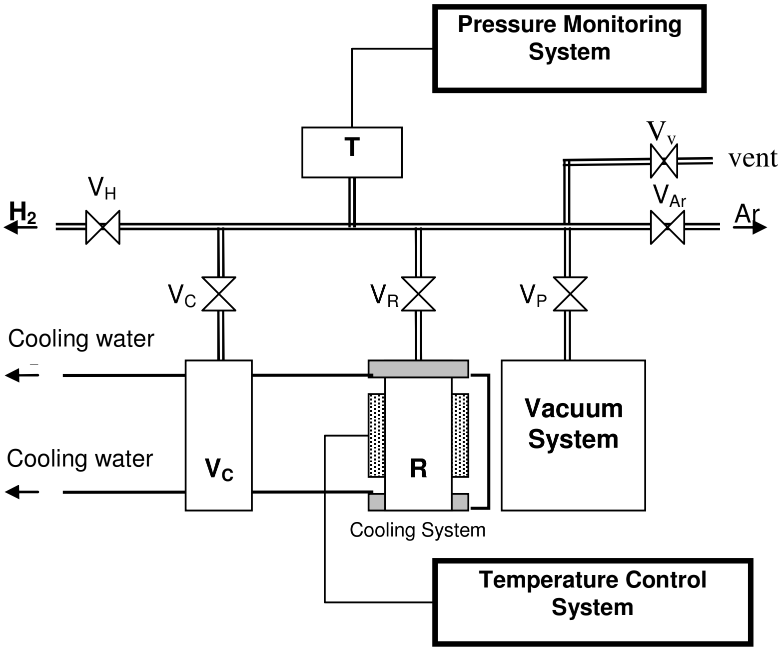

Fig. A-2 Scheme of Sieverts-type apparatus where: T- transducer, V_H – hydrogen cut off valve, V_{Ar}–argon cut off valve, V_P–vacuum system cut off valve, V_R–reactor cut off valve, V_C–calibrated volume and its cut off valve, V_v-vent valve, R–reactor

Therefore, R can be expressed for example in L·atm/mol·K where R=0.08206. Let us assume that we can treat hydrogen as an ideal gas. Before beginning of absorption or desorption the relation between pressure of hydrogen in a system and number of moles of hydrogen at temperature T of the analyzed process can by described by:

$$P_1 V = n_1 RT \qquad \text{(A-4)}$$

After desorption or absorption we have:

$$P_2V = n_2RT \qquad \text{(A-5)}$$

where $P_1 > P_2$ for absorption and $P_1 < P_2$ for desorption

Rearranging Eq. A-4 and A-5, we obtain:

$$n_1 = \frac{P_1V}{RT} \qquad n_2 = \frac{P_2V}{RT} \qquad \text{(A-6)}$$

Therefore, the difference between number of moles of hydrogen in the system resulting from absorption or desorption is:

$$\Delta n = n_1 - n_2 = \Delta P \frac{V}{RT} \qquad \text{(A-7)}$$

where $\Delta P = P_1 - P_2$.

The mass of absorbed or desorbed hydrogen can be calculated using number of moles of gas and molecular mass of hydrogen: $m_H = 2.016 \cdot \Delta n$ which finally gives us:

$$m_H = 2.016 \Delta P \frac{V}{RT} \qquad \text{(A-8)}$$

When change in hydrogen mass is known using Eq. A-8, we can easily calculate hydrogen capacity using Eq. A-2.

A-4. Determination of reaction pathways occurring on ball milling process

$LiNH_2+1.0MgH_2$

$\rightarrow \underline{0.5Mg(NH_2)_2+LiH}+0.5MgH_2$ (after 4 h milling)

$\rightarrow \underline{0.352MgNH}+0.324Mg(NH_2)_2+LiH+0.324MgH_2+\underline{0.352H_2}$ (after 6 h milling)

The reaction pathways of ($LiNH_2+MgH_2$) occurring after 6 h of ball milling under IMP67 mode can be determined as follows:

- The experimental amount of hydrogen:1.37 wt.% H_2 (after 6 h milling)
- Considering the purity of the starting materials,

The theoretical amount of hydrogen: 1.37 wt.% × 0.95 (the average purity)=1.44 wt.% H_2

- Hydrogen is released during the ball milling by the following reaction:

$$0.5Mg(NH_2)_2+0.5MgH_2 \rightarrow MgNH+H_2 \qquad (10\text{-}2)$$

- Based on the above reaction, the number of moles of hydrogen can be determined

$$\text{Hydrogen capacity (wt.\% } H_2) = m/M_p \times 100\% \qquad (A\text{-}2)$$

where M_p is the initial powder mass (g)

1.44 wt.% = (total weight of hydrogen)/(total molar weight of reactants) × 100%

∴ The number of moles of hydrogen is $0.352H_2$

- Based on the number of moles of hydrogen, the stoichiometry of each phase ($Mg(NH_2)_2$, MgH_2, and MgNH) can be also determined as follows:

$$0.5Mg(NH_2)_2+0.5MgH_2 \rightarrow MgNH+H_2$$

$$0.5 : 0.5 = 1 : 1$$

$$\therefore \quad a : b = c : 0.352$$

∴ a= 0.5*0.352=0.176, b=0.5*0.352=0.176, and c=1*-.352=0.352

∴ *0.176*$Mg(NH_2)_2$+*0.176*MgH_2 → *0.352*MgNH+ *0.352*H_2

∴ ***Newly formed phases:*** *0.352*MgNH+ *0.352*H_2

The retained phases: 0.324$Mg(NH_2)_2$+LiH+0.324MgH_2

- Therefore, the reaction pathways of ($LiNH_2$+MgH_2) occurring after 6 h of ball milling under IMP67 mode can be described as follows:

$LiNH_2$+1.0MgH_2 → 0.352MgNH+0.324$Mg(NH_2)_2$+LiH+0.324MgH_2+0.352H_2

Appendix B. Characteristic absorption lines in FT-IR spectra

- FT-IR spectroscopy is an absorption technique
- It is a kind of vibrational spectroscopy
- This instrument covered the wavelength range from 2.5 μm to 15 μm (wavenumber range 4000 cm^{-1} to 660 cm^{-1})
- The **wavenumber** is a property of a wave, its spatial frequency, that is proportional to the reciprocal of the wavelength

  $$k = \frac{2\pi}{\lambda} = \frac{2\pi\nu}{v_p} = \frac{\omega}{v_p} \ ,$$

  where v is the frequency of the wave, λ is the wavelength, $\omega = 2\pi v$ is the angular frequency of the wave, and v_p is the phase velocity of the wave
- When IR light interacts with the molecule, it absorb the energy and vibrates faster
- The infrared spectrum of a sample is collected by passing a beam of infrared light through the sample. Examination of the transmitted light reveals how much energy was absorbed at each wavelength. This can be done with a monochromatic beam, which changes in wavelength over time, or by using a Fourier transform instrument to measure all wavelengths at once. From this, a transmittance or absorbance spectrum can be produced, showing at which IR wavelengths the sample absorbs. Analysis of these absorption characteristics reveals details about the molecular structure of the sample
- Infrared spectroscopy exploits the fact that molecules have specific frequencies (wavenumber) at which they rotate or vibrate corresponding to discrete energy levels (vibrational modes). These resonant frequencies are determined by the shape of the

molecular potential energy surfaces, the masses of the atoms and, by the associated vibronic coupling. In order for a vibrational mode in a molecule to be IR active, it must be associated with changes in the permanent dipole. The frequency of the vibrations can be associated with a particular bond type.

- There are six different ways for vibration: symmetrical and antisymmetrical stretching, scissoring, rocking, wagging and twisting

Table B-1. Summary of the characteristic absorption lines

	Characteristic absorption lines (cm^{-1})	**References #**
$LiNH_2$	3258 / 3312	131
Li_2NH	3180 / 3250	67
$Li_2Mg(NH)_2$	3163 / 3180	131
$Mg(NH_2)_2$	3272 / 3326	100
MgNH	3196	131

Appendix C. Rehydrogenation behaviour of ($LiNH_2$+LiH) system depending on applied hydrogen pressure

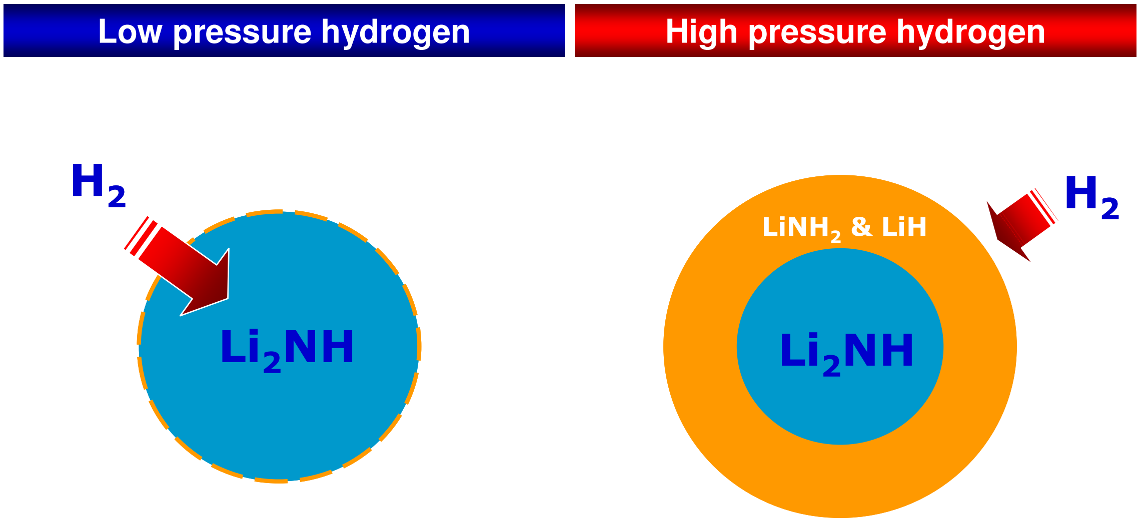

Fig. C-1 Scheme of rehydrogenation behaviours of ($LiNH_2$+LiH) mixture depending on applied hydrogen pressure

Possibly, the high pressure hydrogen reacts at a high rate with the Li_2NH particle and subsequently a layer of ($LiNH_2$+LiH) mixture is immediately created on the particle surface. This layer blocks the hydrogen from diffusing into the particle core which makes the absorption kinetics slower than those when using lower hydrogen pressure (11 bars).